UNIVERSITÉ DE GENÈVE

Département de physique

nucléaire et corpusculaire

FACULTÉ DES SCIENCES

Dr. Alessandro Bravar

Development of the Scintillating Fiber Detector for Timing Measurements in the Mu3e Experiment

THÈSE

présentée à la Faculté des sciences de l'Université de Genève
pour obtenir le grade de Docteur ès sciences, mention physique

par

ANTOANETA DAMYANOVA

de

Pleven (Bulgarie)

THÈSE N$^\circ$ 5380

GENÈVE

2019

DOCTORAT ÈS SCIENCES, MENTION PHYSIQUE

Thèse de Madame Antoaneta DAMYANOVA

intitulée :

«Development of the Scintillating Fiber Detector for Timing Measurements in the Mu3e Experiment»

La Faculté des sciences, sur le préavis de Monsieur A. BRAVAR, docteur et directeur de thèse (Département de physique nucléaire et corpusculaire), Monsieur F. SANCHEZ NIETO, professeur ordinaire (Département de physique nucléaire et corpusculaire), Monsieur C. GRAB, professeur (ETHZ - Swiss Federal Institute of Technology in Zurich, Department of Physics, Zürich, Switzerland), Madame A. PAPA, docteure (PSI - Paul Scherrer Institute, Villigen, Switzerland), autorise l'impression de la présente thèse, sans exprimer d'opinion sur les propositions qui y sont énoncées.

Genève, le 9 septembre 2019

Thèse - 5380 -

Le Doyen

ABSTRACT

Mu3e is an experiment designed to search for charged lepton flavor violation in the $\mu \to eee$ process. During the first phase of its operation, it targets a sensitivity of 1 in 10^{15} muon decays - an improvement to the current experimental limit by three orders of magnitude. Since the $\mu \to eee$ decay is heavily suppressed within the Standard Model, observing a signal at that level will be an unambiguous sign of new Physics. To achieve this goal, the experiment relies on a high rate of muons being detected in a spectrometer with a wide kinematic acceptance, excellent momentum and vertex resolutions and precise timing information.

The subject of this thesis is the development and characterization of one of the timing sub-systems - namely the Scintillating Fiber detector. Prototypes of staggered scintillating fibers with a diameter of 250 μm are constructed in two distinct readout configurations within the scope of the present work. Silicon photomultipliers with different geometries are further explored for the optical readout of the fibers. The prototypes are then characterized in accelerated proton and electron beams, as well as with radioactive strontium sources. To evaluate their performance, the author developed dedicated data acquisition systems featuring established instruments for nuclear physics experiments and novel digitizing electronics.

Following a comprehensive analysis, a time resolution better than 280 ps and an efficiency above 95 % were measured with the produced scintillating fiber ribbons. Thus, their feasibility for the Mu3e experiment has been proven. The design of the fiber detector is refined based on the observed results and the experience gained in handling and producing these prototypes.

Mu3e est une expérience conçue pour étudier la violation de la saveur des leptons chargés dans le processus $\mu \rightarrow$ eee. Au cours de la première phase de son exploitation, elle cible une sensibilité de 1 sur 10^{15} désintégrations des muons - une amélioration de trois ordres de grandeur par rapport à la limite expérimentale actuelle. Comme la désintégration $\mu \rightarrow$ eee est fortement supprimée dans le modèle standard de la physique des particules, l'observation d'un signal serait un signe sans ambiguïté d'une nouvelle physique. Pour atteindre cet objectif, l'expérience requiert de détecter un grand nombre de muons à l'aide du spectromètre, qui doit inclure une large acceptation cinématique, une excellente résolution de l'impulsion et des vertex d'interactions, ainsi que des informations précises sur la synchronisation.

Le sujet de cette thèse est le développement et la caractérisation d'un des sous-systèmes de mesure temporelle du spectromètre, à savoir le détecteur à fibre scintillante. Dans le cadre de ce travail, des prototypes de rubans de fibres scintillantes de diamètre 250 μm sont construits dans deux configurations de prises de données distinctes. Des photomultiplicateurs en silicium de différentes géométries sont explorés pour la lecture optique des fibres. Les prototypes sont ensuite caractérisés par des faisceaux accélérés de protons et d'électrons, ainsi que par des sources radioactives de strontium. Pour évaluer leur performance, l'auteur a mis au point des systèmes d'acquisition de données dédiés comportant des instruments éprouvés pour les expériences de physique nucléaire et de nouveaux systèmes électroniques.

Après une analyse complète, une résolution temporelle meilleur de 280 ps et une efficacité supérieure à 95 % ont été mesurées avec les rubans de fibres scintillantes produits, demontrant la faisabilité de leur utilisation pour l'expérience Mu3e. La conception du détecteur de fibres est améliorée en fonction des résultats observés et de l'expérience acquise dans la manipulation et la production des ces prototypes.

Contents

CONTENTS

1

Phenomenology of Charged Lepton Flavor Violation

The Standard Model (SM) is an elaborate theory unifying present day's knowledge of elementary particles and their interactions. Despite being astonishingly accurate in predicting numerous experimental observations it is incomplete. Neutrino masses, gravitational interactions and matter-antimatter asymmetry are amidst some phenomena the SM fails to explain. In pursuit of more complete models, experiments are probing diverse processes for hints of *New Physics*.

The current chapter presents a brief introduction to the SM and some of its shortcomings. Following is a discussion on the lepton flavor violation as a source of new Physics with emphasis on neutrinoless muon to electron conversions. Finally, the experimental situation in exploring charged lepton flavor violating processes is summarized.

1.1 THE STANDARD MODEL

In the second half of the twentieth century, the joined efforts of a large scientific community lead to the formulation of what presently is known as the Standard Model of Elementary Particles, or simply the Standard Model [1, 2]. This is a sophisticated and greatly successful quantum field theory born from the interplay between theoretical predictions and unexpected experimental observations. It has been subjected to rigorous testing and until recently, a single particle predicted by the model was still eluding detection. However, with the discovery of the Higgs boson [3] by the ATLAS [4] and CMS [5] experiments at CERN in 2012 all pieces have
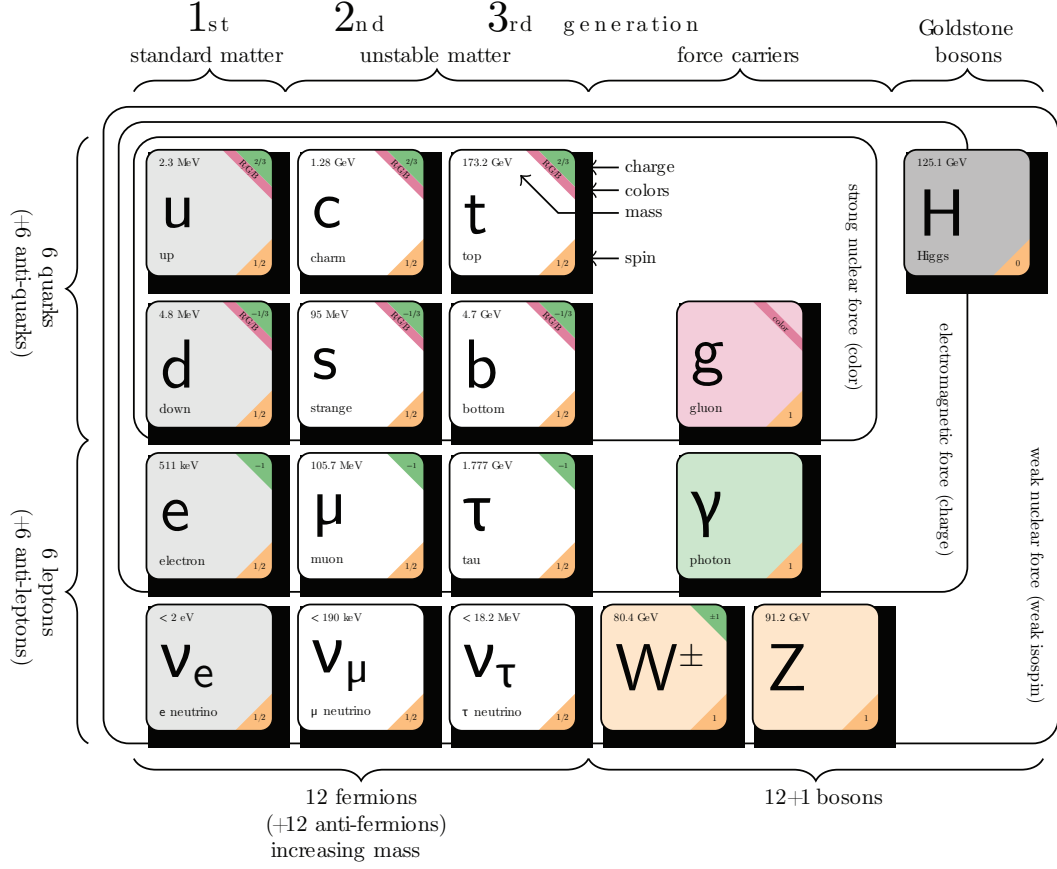
Figure 1.1 – Summary of the Standard Model constituents. Figure adopted from [6]

been revealed. Fig. 1.1 presents a summary of the SM constituents.

All visible matter is defined by means of twelve elementary particles and their anti-particles. They interact amongst each other via three of four known fundamental forces, namely the strong, electromagnetic and weak interactions. The last force, gravity, cannot be consistently unified with any renormalizable quantum field theory, thus it is excluded from the model. Within the SM terminology interactions are mediated by gauge bosons, often referred to as force carriers. Eight of them are called gluons (g) and they mediate the strong interaction. A photon (γ) is the boson that transfers the electromagnetic force, while the W^+, W^- and Z^0 are the bosons responsible for the weak interaction. The matter particles, on the other hand, are fermions (spin 1/2). They are further classified into *quarks* and *leptons* based on their interactions with the other particles. The quarks couple with bosons of all three forces, while the leptons lack a color charge, hence they cannot participate in any strong interactions. Additionally, there are two groups of leptons: the electron, muon and tau leptons are electrically charged and they are susceptible to both the electromagnetic and the weak forces; the corre-

sponding neutrinos, however, are electrically neutral and they interact only through the W and Z bosons. Particles located in the same row in Fig. 1.1 possess identical electrical charges. All three upper quarks (u, c, t) have a fractional electric charge equal to $+2/3\ e$, while the three lower quarks (d, s, b) are characterized with an electric charge of $-1/3\ e$. Accordingly, the charged leptons possess a charge of $-1\ e$, while the neutral ones have none. The leptons are further grouped by their weak flavor[1] in three generations labeled 1ST, 2ND and 3RD.[2]. It is accepted that masses of the particles in one generation are lower than those of the particles in the next generation.[3] Furthermore, the lack of evidence for the existence of a decay that transforms leptons from one generation into another [11] inspired the addition of a new conserved quantity in the SM, namely the lepton flavor (LF) number. In each generation such a number is assigned to the corresponding fermions denoted by L_e, L_μ and L_τ, respectively. Table 1.1 summarizes the values of the LF numbers. Every particle within the SM is complemented by an anti-particle which has the same mass but opposite quantum numbers e.g. charge, lepton flavor, magnetic moment, etc.

	$\mathbf{L_e}$	$\mathbf{L_\mu}$	$\mathbf{L_\tau}$	**Generation**
e^- / e^+	1 / -1	0 / 0	0 / 0	I
$\nu_e / \bar{\nu}_e$	-1 / 1	0 / 0	0 / 0	I
μ^- / μ^+	0 / 0	1 / -1	0 / 0	II
$\nu_\mu / \bar{\nu}_\mu$	0 / 0	-1 / 1	0 / 0	II
τ^- / τ^+	0 / 0	0 / 0	1 / -1	III
$\nu_\tau / \bar{\nu}_\tau$	0 / 0	0 / 0	-1 / 1	III

Table 1.1 – Lepton flavor numbers attributed to fermions in each generation. The absolute values are identical for both particles and anti-particles but the sign changes. According to the conventional notation positively charged leptons and the neutrinos denoted as $\bar{\nu}$ are the anti-particles.

1.2 LEPTON FLAVOR VIOLATION

While most conserved quantities in the SM arise as symmetries under gauge transformation, there isn't a fundamental argument preserving the lepton flavor. In fact, it has been violated in the neutral sector where neutrinos oscillate between different flavors [7–10]. Analogously to

---

[1]The names of the particles correspond to their flavor as seen by the weak interaction.

[2]The quarks are also grouped in three families, but they are classified by their strong interaction eigenstates.

[3]While the neutrinos are massless within the original version of the SM, the existence of neutrino oscillations [7–10] show that they are massive, thus the model has been extended to accommodate them. This broader version of the SM is often referred to as νSM. The absolute value of the neutrino masses, however, are not known and neither is their ordering.
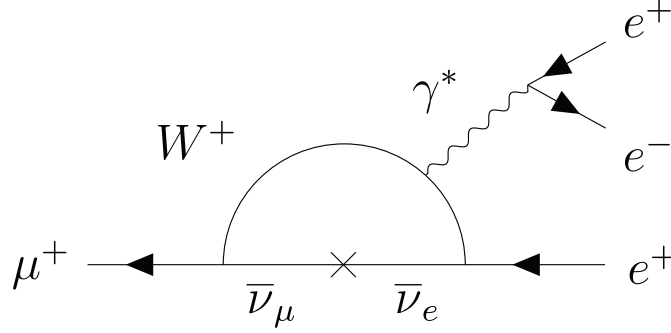
Figure 1.2 – A νSM diagram with neutrino oscillating in a loop (penguin diagram) leading to cLFV in the process μ → eee

.

the quark mixing expressed via the Cabibbo-Kobayashi-Maskawa matrix (CKM matrix) [12], the neutrino (ν_1, ν_2, ν_3) mass eigenstates rotate into flavor eigenstates (ν_e, ν_μ, ν_τ) under the unitary Pontecorvo-Maki-Nakagawa-Sakata matrix U_{li}, ($l = e, \mu, \tau$, $i = 1, 2, 3$) [13]. As a result, charged lepton flavor violating (cLFV) decays such as μ → eee and μ → eγ become accessible within the νSM via neutrinos oscillating in a loop, e.g. Fig. 1.2.

The probability that any of these processes occurs, nonetheless, is extremely small. Its branching fraction $\mathcal{B}_{SM}$ is proportional in quadrature to the ratio between the neutrino mass differences squared ($\Delta m^2 \lesssim 2.5\ 10^{-3}$ eV [14]) and the squared mass of the W boson ($m_W \approx 80.4$ GeV [15]):

$$\mathcal{B}_{SM}(\mu \to eee, \mu \to e\gamma, \mu N \to eN) \propto \left| \sum_{i=2,3} U_{\mu i}^* U_{ei} \frac{\Delta m_{i1}^2}{m_W^2} \right|^2 < 10^{-54} \qquad (1.1)$$

The sensitivity of state-of-the-art experiments currently in operation or planned in the foreseeable future is more than 30 orders of magnitude smaller than the νSM estimate. Hence, while theoretically possible, cLFV emerging from neutrino oscillations is practically unobservable.

Various experiments, however, hint that despite being remarkably detailed and precise in its predictions, the SM is incomplete, even with the inclusion of massive neutrinos.[4] Cosmological observations studying the expansion of the universe and the Cosmological Microwave Background (CMB) conclude that only 5 % of the matter in the Universe can be described with SM particles [16]. The remainder comprises of what today is called dark matter and dark energy in fractions of about 25 % and 70 %, respectively. Moreover, according to the SM, matter and anti-matter are created in equal amounts and annihilate when placed in contact with each

---

[4]Hereafter SM refers to the extended version of the Standard model with massive neutrinos

other. Nevertheless, there is an imbalance between the two with the matter outweighing its counterpart and so far no viable explanation for this asymmetry exists. The number of fermion generations is another puzzle that remains unsolved in the SM. It is an experimentally established fact but no theoretical constrain forbids the existence of more than three generations. In addition, the exact values of the neutrino masses[5], as well as their ordering and the mechanism under which they are generated are not defined within the SM.

A broad spectrum of theories beyond the Standard model (BSM) attempt to provide solutions to these observed deviations, albeit at the expense of additional parameters. However, none of these models are confirmed by measurements. To constrain the space of allowed parameter values and operators, the search for new Physics centers around three experimental approaches. At the so called *energy frontier* currently pursued by the LHC experiments, new particles are directly searched for in collisions with the highest possible center of mass energy. With this approach the properties of new particles can be unambiguously investigated. The scale accessible for direct searches nowadays is 13 TeV. A complimentary *precision/intensity* studies program focuses on detecting the smallest deviations in quantities predicted by the SM. These discrepancies are indirectly sensitive to new Physics at a much higher energy scale than any direct searches can reach in the near future [17], see Fig. 1.4 and Eq. 1.2. Examples of unexplained anomalies include e.g. the proton charge radius determined in muonic and atomic spectroscopy [18] and in electron-proton scattering [19]; the anomalous magnetic moment of the muon whose experimental value differs by more than 3σ from the SM prediction [15]; additionally, recent results on the branching fractions of B meson decays [20] suggest non-universal couplings between fermions in different generations and the force carriers. If this is indeed the case, cLFV should be observable with larger branching fractions. Lastly, studies of high energy *cosmic particles* investigate possible dark matter candidates.

Since many of the observed anomalies involve fermions in the lepton family, experiments probing the lepton flavor are particularly appealing in the quest for new physics. According to some BSM theories, cLFV manifests naturally if supersymmetric particles or new interaction bosons exist [21, 22]. Fig. 1.3 presents Feynman diagrams of possible $\mu^+ \to e^+ e^- e^+$ processes.

Depending on the model, different lepton flavor violating processes result in stronger constrains to the particular parameter space. Hence, to assess the advantages of one experimental design over another, a model independent approach is preferred.
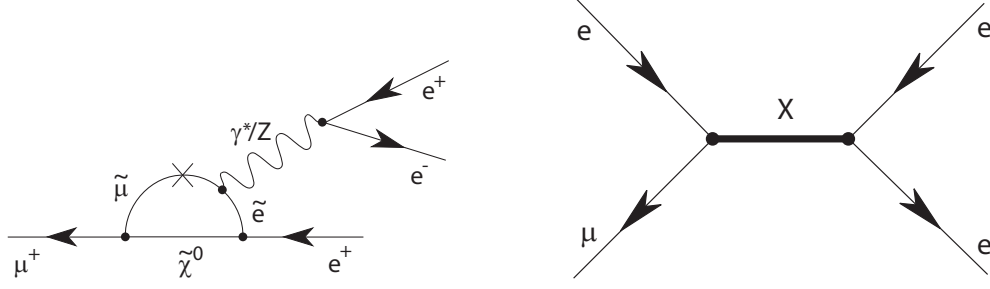
---

[5]In the extended version of the SM

Figure 1.3 – First order diagrams of $\mu \to eee$ processes arising in BSM theories. Supersymmetric particles oscil-
lating in a loop are proposed by SUSY models (Left). Tree-like diagrams with new bosons coupling
to the muon and electron are expected in e.g. extended Higgs models (Right).

1.2.1 cLFV in Effective Field Theories

An effective field theory is a simplified model for physical processes that occur below a
certain energy scale Λ. High energy degrees of freedom reflecting a more complex underlying
Physics are integrated out at low energies[6] as they contribute negligibly to the phenomena
under investigation. As a consequence, a model independent parametrization can be used to
search for new Physics.

Mass Scale Reach

The effective Lagrangian shown in Eq. 1.2 provides means to compare the mass scales of
underlaying physics processes that can affect cLFV decays of the muon [17, 23].

$$\mathcal{L}_{\text{cLFV}} = \left[\frac{m_\mu}{(\kappa + 1)\Lambda^2} \bar{\mu}_R \sigma_{\mu\nu} e_L F^{\mu\nu} + h.c. \right]_{\gamma-\text{penguin}}$$
$$+ \left[\frac{\kappa}{(\kappa + 1)\Lambda^2} (\bar{\mu}_L \gamma^\mu e_L)(\bar{e}_L \gamma_\mu e_L) \right]_{\text{tree}} \tag{1.2}$$

The two processes are compared at a common mass scale Λ. The only relevant contributions
arise from the penguin and tree diagrams shown in Fig. 1.3. The ratio between the amplitudes
for the two types of interactions are parametrized by the term κ. Fig. 1.4 illustrates the limits
on the common mass scale as a function of κ. For small values of κ (dipole interactions) the
$\mu \to e\gamma$ decay is sensitive to processes occurring at higher mass scales. It is however not
sensitive at all to four fermion interactions (large κ). The $\mu \to eee$ decay, on the other hand, is
well suited for probing new Physics in case it manifests via tree-like diagrams[7] Already with

---

[6] Accessible by experiments.

[7] The sensitivity of $\mu \to eee$ to dipole interactions is suppresses by a factor of $\mathcal{O}(\alpha_s)$ with respect to $\mu \to e\gamma$

a sensitivity of 10^{-14} the Mu3e experiment can probe for new phenomena at the PeV scale.
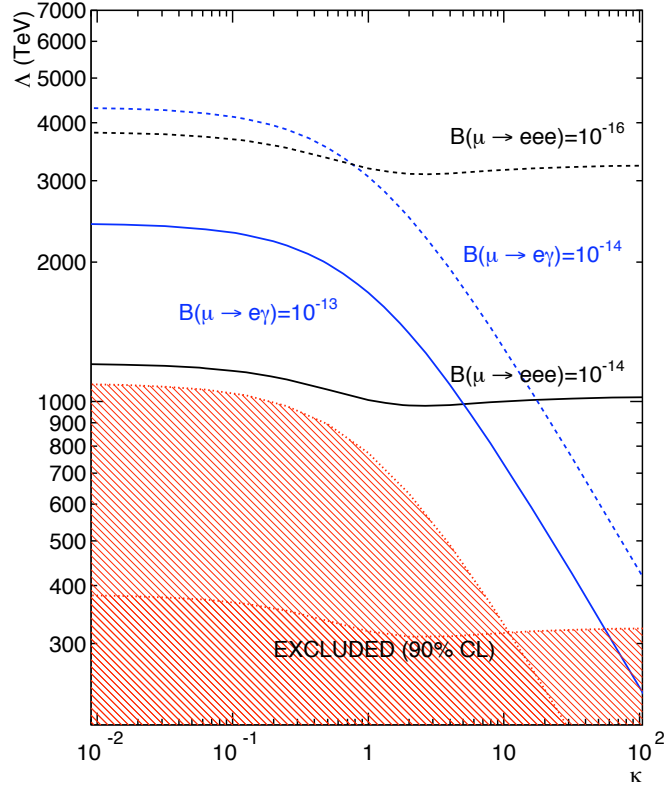

Figure 1.4 – Experimental limits on the mass scale reach of $\mu \rightarrow eee$ and $\mu \rightarrow e\gamma$ searched as a function of the parameter κ. Figure source [17].

7

AN ALTERNATIVE APPROACH

In a recent analysis of lepton flavor violating muon to electron transitions [24] the following effective Lagrangian is formulated:

$$\mathcal{L}_{eff} = \mathcal{L}_{\text{QCD}} + \mathcal{L}_{\text{QED}}$$
$$+ \frac{1}{\Lambda^2} \left[C_{\text{L}}^{\text{D}} \mathcal{O}_{\text{L}}^{\text{D}} + \sum_{f=q,l} \left(C_{ff}^{\text{V LL}} \mathcal{O}_{ff}^{\text{V LL}} + C_{ff}^{\text{V LR}} \mathcal{O}_{ff}^{\text{V LR}} + C_{ff}^{\text{S LL}} \mathcal{O}_{ff}^{\text{S LL}} \right) \right. $$
$$\left. + \sum_{f=q,\tau} \left(C_{hh}^{\text{T LL}} \mathcal{O}_{hh}^{\text{T LL}} + C_{hh}^{\text{S LR}} \mathcal{O}_{hh}^{\text{S LR}} \right) + C_{gg}^{\text{L}} \mathcal{O}_{gg}^{\text{L}} + \text{L} \leftrightarrow \text{R} \right]$$
$$+ \text{ h.c.}$$

(1.3)

The mass scale Λ below which the approximation is valid is $m_W > \Lambda \gg m_b$, where m_W is the mass of the W boson and m_b, $\mathcal{O}(4\text{ GeV})$, is the mass of the heaviest participating quark, namely the b quark. The electroweak term of the SM Lagrangian is irrelevant for the processes under study at that scale, hence only the QED and QCD Lagrangians remain. The coefficients C^β are called Wilson coefficients and they encode the targeted energy scale for a given process. Contrary to the Lagrangian in 1.2, the mass scale of the underlying Physics is not explicitly apparent. Depending on the type of operators they belong to, $\beta = \{\text{S, V, T}\}$ denotes scalar, vector or tensor, while L and R label the handedness of the particles the operators act upon. The effective field operators $\mathcal{O}$ of dimension six are defined as follows:

$$\mathcal{O}_{\text{L}}^{\text{D}} = \text{e} \cdot \text{m}_\mu (\bar{e}\sigma^{\mu\nu} P_{\text{L}}\mu) F_{\mu\nu}$$
$$\mathcal{O}_{ff}^{\text{V LL}} = (\bar{e}\gamma^\mu P_{\text{L}}\mu)(\bar{f}\gamma_\mu P_{\text{L}}f)$$
$$\mathcal{O}_{ff}^{\text{V LR}} = (\bar{e}\gamma^\mu P_{\text{L}}\mu)(\bar{f}\gamma_\mu P_{\text{R}}f)$$
$$\mathcal{O}_{ff}^{\text{S LL}} = (\bar{e}P_{\text{L}}\mu)(\bar{f}P_{\text{L}}f)$$
$$\mathcal{O}_{hh}^{\text{S LR}} = (\bar{e}P_{\text{L}}\mu)(\bar{h}P_{\text{R}}h)$$
$$\mathcal{O}_{hh}^{\text{T LL}} = (\bar{e}\sigma_{\mu\nu} P_{\text{L}}\mu)(\bar{h}\sigma^{\mu\nu} P_{\text{L}}h)$$
$$\mathcal{O}_{gg}^{\text{L}} = \alpha_s m_\mu G_{\text{F}}(\bar{e}P_{\text{L}}\mu)G_{\mu\nu}^a G_a^{\mu\nu}$$

(1.4)

$P_{\text{R/L}} = (\mathbb{I} \pm \gamma^5)/2$ are the right(+)- and left(-)-handed projection operators. $F^{\mu\nu}$ and $G_a^{\mu\nu}$ are the photon and gluon field strength tensors, respectively. All charged fermion fields with masses below the decoupling scale m_W are denoted as f, while $h = \{u, d, c, s, b, \tau\}$ contains the permitted quarks and only the τ lepton. γ^μ are the gamma-matrices while $\sigma^{\mu\nu} = \frac{i}{2}[\gamma^\mu, \gamma^\nu]$.

e is the elementary electric charge, m_μ - the muon mass, α_s is the strong coupling constant and G_F - the Fermi coupling constant.

While for the $\mu \to e\gamma$ and $\mu \to eee$ processes the energy scale is $\mathcal{O}(m_\mu)$, muon conversions in the vicinity of nuclei $\mu N \to eN$ occur at about 1 GeV, hence to compare the three cLFV transitions the Wilson coefficients are calculated at the m_W scale. In this regime operators with quarks and τ fields contribute not only to the $\mu N \to eN$, but also to the $\mu \to eee$ decay. Accordingly, vector and scalar operators participate also in $\mu \to e\gamma$ decays. The effects arise due to mixing of the Wilson coefficients when they are propagated to the Λ energy scale through evolution of the renormalization group.

The strengths of the three processes to constrain the parameter space are evaluated under the assumption that for any BSM Physics all but two of the operators vanish. Fig. 1.5 and Fig. 1.6 illustrate results presented by [24] for select pairs of operators.

Figure 1.5 – Parameter space constrains in the $C_{ee}^{S\,LL}$-$C_{ee}^{V\,RR}$ plane. Current (solid) and future (dashed) experimental limits set by the three $\mu - e$ conversion channels. Figure source [24].

The allowed values of $C_{ee}^{V\,RR}$ and $C_{ee}^{S\,LL}$ are the most strictly confined by the $\mu \to eee$ process. In this case, interactions between the three electrons occur at tree level and they are mediated by vector and scalar operators. The operator associated with the $C_{bb}^{S\,LR}$ term, on the other hand, is most pronounced in $\mu - e$ conversions where quarks participate in both the initial and final states. Hence, the most stringent limits for this parameter are achieved by $\mu N \to eN$ experiments.

It is already evident from these two examples that a single decay channel cannot efficiently probe for charged lepton flavor violation. Thus, complementary studies exploring all accessible processes are necessary.
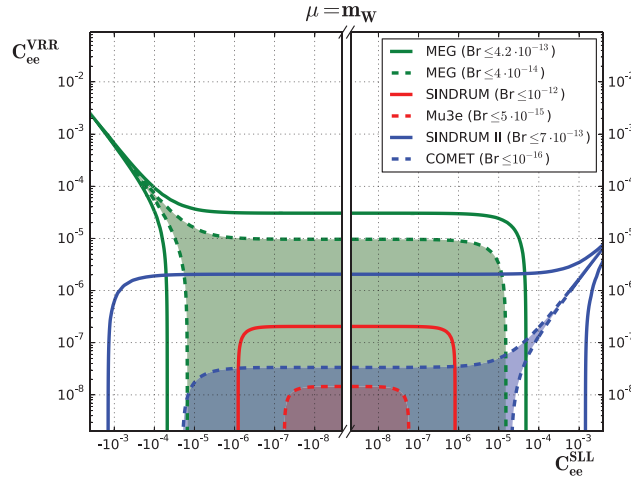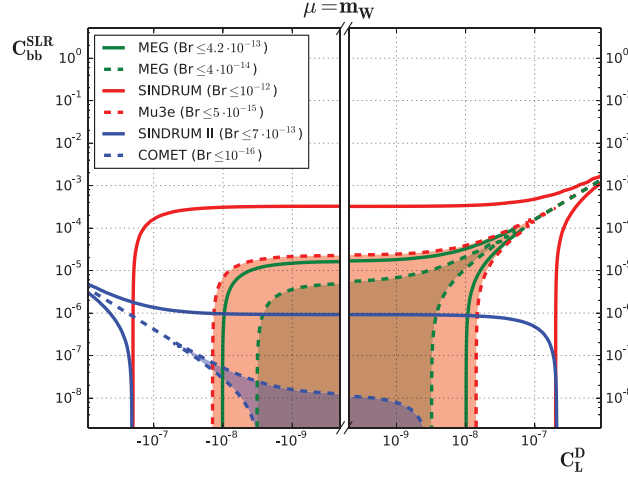
Figure 1.6 – Parameter space constrains in the C_L^D-$C_{bb}^{S\,LR}$ plane. Current (solid) and future (dashed) experimental limits set by the three $\mu - e$ conversion channels. Figure source [24].

Fig. 1.7 is a chronological summary of the progress achieved in searching for cLFV through muon or tau decays over the last seventy years. Planned experiments with their design sensitivity are also marked.

1.3 Experiments Probing for cLFV in Muon Decays

While flavor violating decays of the neutral Higgs and Z bosons provide further options to explore cLFV [26, 27], the relative abundance of low momentum muons in high intensity beams drive the development of new instruments investigating all three muon channels. Table 1.2 summarizes the present-day upper limits set on the branching ratios of cLFV processes with muons converting to electrons. At least one experiment aiming to push the boundaries for each of them is currently under construction or being upgraded, see Table 1.3.

Process	Experiment	$\mathcal{B}_{\mathbf{CL=90\%}}^{\mathbf{UpperLimit}}$	Year	Facility	Reference
$\mu^+ \rightarrow e^+\gamma$	MEG	4.2×10^{-13}	2016	PSI	[28]
$\mu^+ \rightarrow e^+e^-e^+$	SINDRUM	1.0×10^{-12}	1988	PSI	[29]
$\mu^-\,\text{Au} \rightarrow e^-\,\text{Au}$	SINDRUM II	7×10^{-13}	2006	PSI	[30]

Table 1.2 – Experimental upper limits at 90% confidence level on cLFV in $\mu - e$ processes. The year of publication and the laboratory at which the experiments are conducted are also shown.
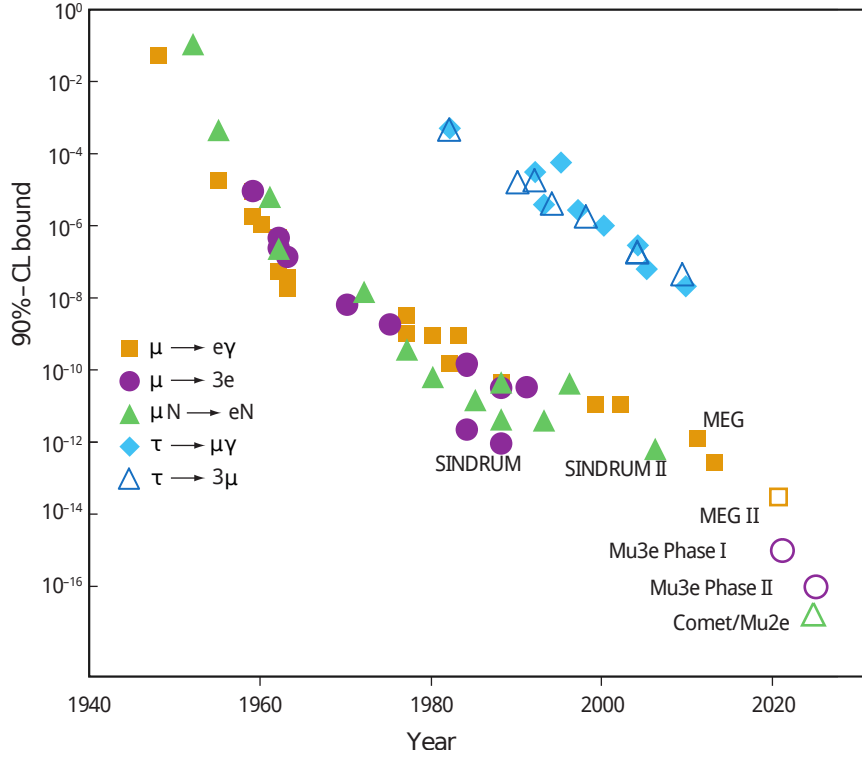
Figure 1.7 – History of cLFV experimental searches. Figure source [25]

$\mu N \to eN$

The experimental signature of cLFV in muons converting to electrons in the vicinity of nuclei is very distinct: a single mono-energetic electron with momentum approaching the muon rest mass. A small fraction of the momentum is absorbed in the recoiling nucleus. The main source of backgrounds to this process are electrons from pion decays originating along the beam line. A pulsed beam with high muon purity is used to efficiently suppress them. Several experiments in this class are under preparation at J-PARC in Japan [31, 32] and FNAL in the USA [33] (see Table 1.3). The prompt signal topology combined with lack of irreducible backgrounds stemming from SM decays drive the wide program in this channel.

$\mu \to e\gamma$

The most recent results for the $\mu^+ \to e^+\gamma$ searches are reported by the MEG experiment [28]. It is the sole apparatus currently investigating that particular transition. It is installed at the Paul Scherrer Institute (PSI) and benefits from the available high intensity $\mathcal{O}(10^7 \; \mu/\text{sec})$

Process	Experiment	Sensitivity	Facility	Reference
$\mu^+ \to e^+\gamma$	MEG II	(*)6×10^{-14}	PSI	[34]
$\mu^+ \to e^+e^-e^+$	Mu3e Phase I	2×10^{-15}	PSI	[35]
	Mu3e Phase II	1×10^{-16}	PSI	[35]
μ^- SiC $\to e^-$ SiC	DeeMe	2×10^{-14}	J-PARC	[32]
μ^- Al $\to e^-$ Al	COMET	2.7×10^{-17}	J-PARC	[36]
	Mu2e	2.9×10^{-17}	FNAL	[37]

Table 1.3 – Projected single event sensitivity (SES) of planned $\mu - e$ experiments. (*) - projected upper limit of the branching ratio $\mathcal{B}$ at 90 % CL. The facilities hosting the experiments and providing the muon beams are also indicated.

beam line providing a continuous source of low momentum muons. The idea of the experiment is to stop positive muons in a thin target at the core of the detector where they undergo decay at rest. The event topology of the process consists of a positron and a photon emitted simultaneously back to back with momenta exactly equal to half the muon mass. A liquid Xenon calorimeter measures precisely the time and energy of the photons while a drift chamber complemented by a timing detector based on scintillating bars and fibers[8] determines the properties of the positrons. All subsystems are currently being upgraded to improve the sensitivity of the detector by approximately one order of magnitude in the upcoming MEG II setup.

$\mu \to eee$

The latest limits set on the $\mu \to eee$ branching ratio date back to 1988 and were achieved by the SINDRUM experiment [29]. The successor of this experiment is Mu3e. With state-of-the-art detectors and fast data acquisition system, it aims to improve the sensitivity on the measurement by four orders of magnitude. Detailed description of experiment follows in chapter 2.

---

[8]Square scintillating fibers with a cross-section of 5×5 mm^2.

2

The Mu3e Experiment

Mu3e is a novel experiment aiming to search for cLFV in the $\mu^+ \rightarrow e^+e^-e^+$ channel. It is organized in two stages with the goal of reaching single event sensitivity of 2×10^{-15} and 1×10^{-16} in its *Phase I* and *Phase II*, respectively. The research conducted in the present work is within the scope of Phase I, which will become operational in the coming years at PSI. The expected sensitivity will improve on the latest measurements of the $\mathcal{B}(\mu \rightarrow eee)$ by three orders of magnitude.

This chapters presents the physical challenges in measuring the $\mu \rightarrow eee$ signal followed by the conceptual design of the Mu3e apparatus. Section 2.2.6 is dedicated to specifics on the scintillating fiber detector - the main subject of this thesis.

2.1 Mu3e Signal and Background Processes

All three particles in the final state of the $\mu^+ \rightarrow e^+e^-e^+$ process are detectable defining a clean kinematic signature. In Mu3e the muons[1] stop in a thin target before decaying. Following the laws of energy and momentum conservation, the momenta of the three daughter electrons[2] are coplanar and their total energy equals the muon rest mass m_μ = (105.658 374 5 $\pm$ 0.000 002 4) MeV/c^2 [15]. Additionally, since the decay proceeds promptly all products are

---

[1] Hereafter muons refer to the positive muon leptons which will be used in the Mu3e experiment
[2] In the current text electrons refers to both positrons and electrons when used in a plural form.

created instantaneously and originate from a single vertex in space.

$$\vec{p}_{\text{tot}} = \sum_{i=1}^{3} \vec{p}_i = \vec{0}$$

$$E_{\text{tot}} = \sum_{i=1}^{3} E_i = m_\mu \tag{2.1}$$

$$t = t_1 = t_2 = t_3$$

The signal topology along with the main sources of backgrounds that mimic it are illustrated in Fig. 2.1. Irreducible and accidental backgrounds are the two types of contamination that should be suppressed below the target sensitivity.
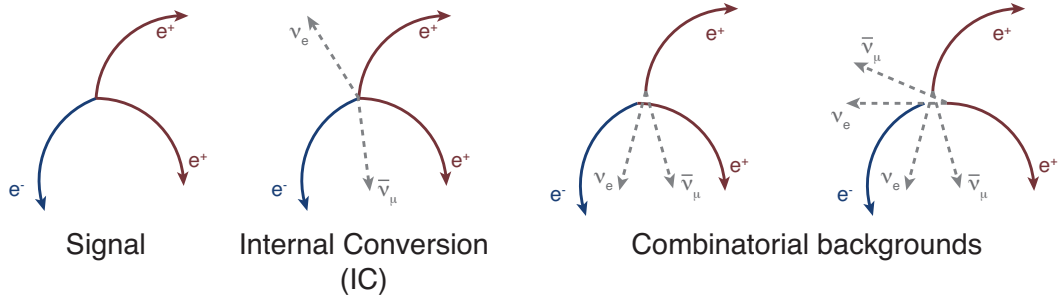

Figure 2.1 – Signal topology for the $\mu^+ \rightarrow e^+ e^- e^+$ decay. The SM internal conversion decay mimics the signal since the two neutrinos are undetectable. Misreconstruction of electrons originating from different events can also lead to topologies imitating the signal.

The first one is generated by the SM internal conversion (IC) decay $\mu^+ \rightarrow e^+ e^- e^+ \nu_e \bar{\nu}_\mu$. It has two extra neutrinos that cannot be detected and manifest as missing energy. This process occurs with a branching ratio $\mathcal{B} = (3.4 \pm 0.4) \times 10^{-5}$ [15]. Since the three electrons appear simultaneously in time and space, the only means of suppressing this background are high momentum and energy resolutions. Fig. 2.2 shows the contamination of the signal arising from IC decays as a function of the reconstructed mass resolution. In order to achieve a sensitivity of 2×10^{-15} at 2σ level, the momentum resolving power of the apparatus should be below 1.0 MeV/c.

The second type of background is accidental and occurs as a combination of an electron and two positron tracks generated by distinct sources. Ordinary muon decays[3] $\mu^+ \rightarrow e^+ \nu_e \bar{\nu}_\mu$ which have a branching fraction close 100 % are the main contributors of positrons, while the electrons emerge in Bhabha scattering, photon conversion or Compton scattering. Bhabha scattering vertices are located mainly in the target and the surrounding detector material as

---

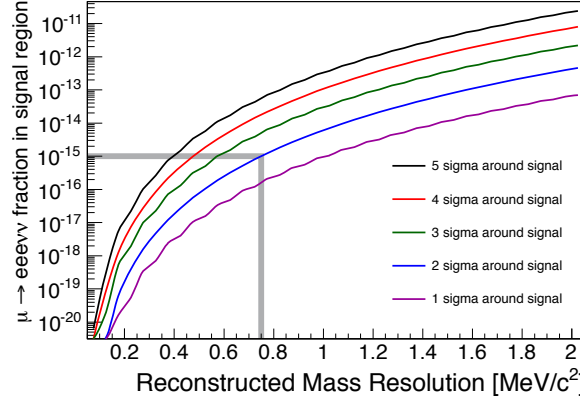[3]The dominant decay mode of the muons is also called Michel decay.

Figure 2.2 – Suppression of the IC background as a function of the reconstructed mass resolution. Figure source [38]

well as in the mechanical supports. They are the predominant source of contamination. Additionally, photons created in the radiative muon decay $\mu^+ \rightarrow e^+ \gamma \nu_e \bar{\nu}_\mu$ or via bremsstrahlung can convert to e^+-e^- pair and also provide an electron. There are various combinations of three independent or two correlated and one independent particle that mimic the signal. Moreover, inefficiencies in the reconstruction of tracks, wrong charge identification or fake tracks increase the accidental backgrounds. The probability of combinatorial contamination scales with the beam intensity. Hence, the high muon stopping rates necessary to achieve a sensible measurement within a reasonable time scale $\mathcal{O}(1\ \text{year})$ should be counteracted by precise momentum, vertex and time resolutions in order to suppress the accidental backgrounds.

2.2 DETECTOR CONCEPT

The MU3E detector is a high-resolution spectrometer for low energy electrons emitted in muons decays at rest. It is placed in a magnetic field in order to determine the momenta of charge particles based on the curvature of their trajectories. Dedicated timing detectors record the instances when each particle traverses them. The time information is then utilized for reducing the accidental backgrounds.

A longitudinal and a transverse view of the experiment with respect to the beam line are shown in Fig. 2.3. The whole system is placed in a 1 T magnetic field parallel to the beam line. Low momentum muons are transported to the central part of the spectrometer and stopped in the material volume of a hollow double cone target. The long lifetime of the muons 2.2 μs ensures their survival until reaching the target such that when they decay their momentum is already zero. A cylindrical pair of thin silicon pixel trackers is located immediately around

15

the target at radiuses of 2 cm and 3 cm, respectively. Its close proximity to the muon decay points is crucial for the resolution of the vertex reconstruction. Another set of double pixel tracker layers with an inner radius of 7 cm and a displacement of about 1 cm between the two layers provides a second set of measurements for the particles' trajectory. Since the electrons follow helical paths inside the magnetic field, the outer tracker layers are further duplicated on both sides of the central region to improve the momentum resolution of tracks leaving the area. The outer stages are called *recurl stations* after the electrons which curl back towards the beam axis. Two types of timing detectors - scintillating fibers and scintillating tiles - are foreseen for the central part and the recurl stations, respectively. The former are optimized for thickness and placed between the tracker layers. The latter, on the other hand, deliver superior time resolution at the expense of more material. Both detectors are positioned at a radius about 6 cm.
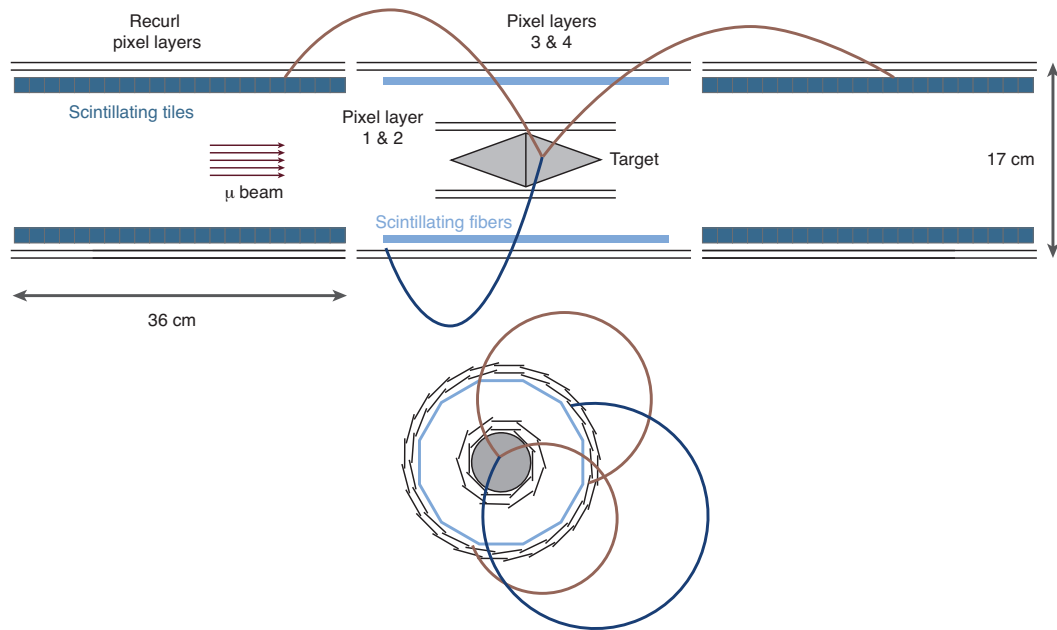
Figure 2.3 – Schematic of the Phase I MU3E experiment.

2.2.1 MOMENTUM OPTIMIZATION

The MU3E experiment is optimized for precise momentum resolution at high particle rates. As it relies on reconstructing particle tracks to extract the momentum, the material budget of all detectors should be minimized in order to avoid multiple Coulomb scattering. For thin layers, the central 98 % of the scattering angular distribution can be approximated by a Gaussian

with a width θ_{MS} dependent on the deflected particle momentum:

$$\theta_{\text{MS}} = \frac{13.6\,\text{MeV}}{\beta c p} z \sqrt{\frac{x}{X_0}} \left[1 + 0.038 \ln\left(\frac{xz^2}{X_0 \beta^2}\right)\right] \tag{2.2}$$

The momentum, velocity and charge number of the incident particle are denoted as p, βc and z, respectively. The thickness of the scattering medium x/X_0 is defined in terms of radiation lengths X_0. In a first order approximation when traversing a thin layer of material only the direction of the particles changes and not their momentum.

The resolution is further affected by the uncertainty on the position measurement, hence smaller pixel sizes with respect to the scattering angle are preferred, see Fig. 2.4.
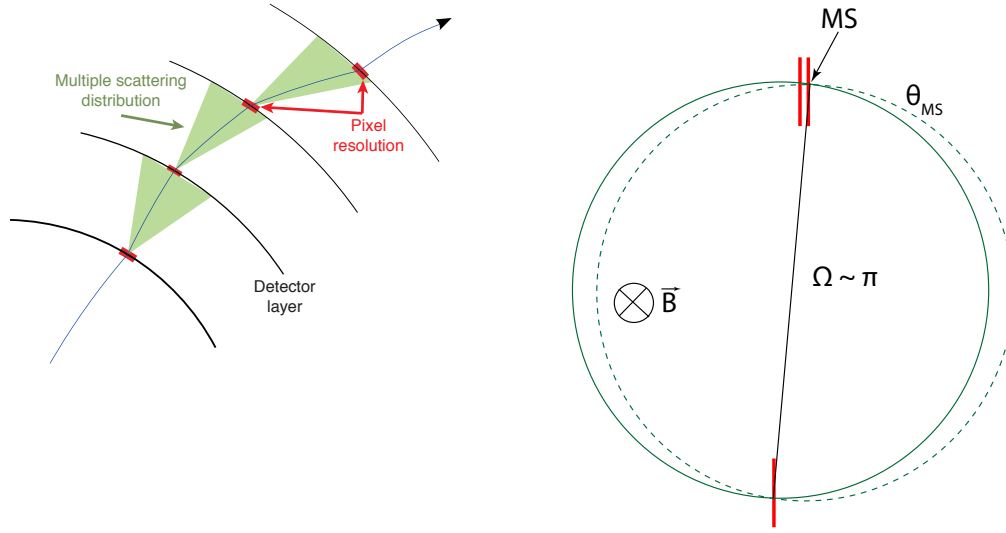
Figure 2.4 – Illustration of momentum resolution measurement dominated by multiple scattering (Left) and the benefits of determining the trajectory using half turn points to cancel the multiple scattering effect at first order (Right). Figures source [35].

When the predominant source of uncertainties is multiple scattering, the momentum resolution is proportional to the track deflection Ω:

$$\frac{\sigma_p}{p} \propto \frac{\theta_{\text{MS}}}{\Omega} \tag{2.3}$$

An interesting property is observed if the trajectories are measured again at about half a turn, as illustrated in Fig. 2.4. The uncertainties generated by the multiple scattering cancel at first order and the momentum is determined with a higher precision. The Mu3e spectrometer is hence designed with the intention of exploiting these benefits for tracks detected twice with deflection $\Omega = \pi$ between the two points.

2.2.2 BEAM LINE

MU3E will be installed in the πE5 channel of the PSI facility which delivers the highest intensity continuous muon beam available nowadays - $\mathcal{O}(10^8$ muons/s). A 1.3 MW cyclotron accelerates protons to 590 MeV kinetic energy at a current of up to 2.4 mA [39]. The protons then impinge on a primary target, TgE , made of polycrystalline graphite and produce pions. Some of them decay close to the surface of the target producing the so called *surface* muons whose momentum distribution peaks at approximately 28 MeV/c. This value approaches the kinematic edge of a two-body decay spectrum observed when pions decay at rest. A dedicated beam line, see Fig. 2.5, selects particles with 28 MeV/c momenta and transports them to the MU3E experiment.
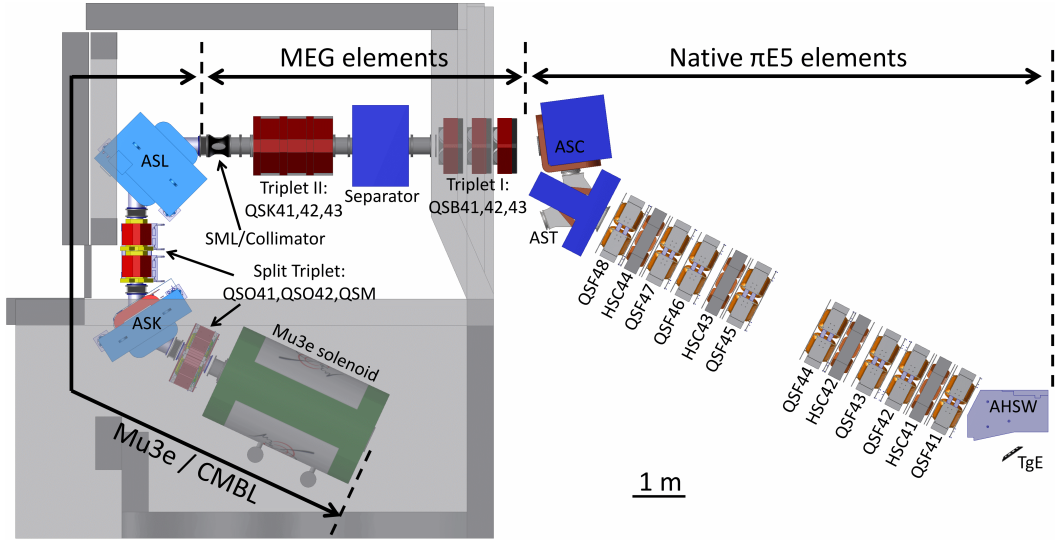

Figure 2.5 – A CAD model of the full πE5 channel and CMBL. Positive muons produced in the TgE target (bottom right) are transported via existing πE5 elements, the beam line section shared with the MEG II experiment, and the dedicated CMBL to the MU3E solenoid. Figure source [40]

Since MU3E and the MEG II experiment will share the same πE5 channel, an additional compact muon beam line (CMBL) [40] section is specifically constructed to divert muons towards the MU3E detector. Only one of the experiments will use the high intensity muon beam at a given time. Besides muons, there is a significant fraction of positrons and electrons in the beam line. They originate either from muon decays along the beam line or from electron-positron showers generated by photons emitted in π^0 decays at the production target. A Wien filter separator exploiting the properties of orthogonal electric and magnetic fields separates the muons by their velocity from the rest of the beam constituents with a purity of 99 % Following the upgrades of the beam line in 2018, a maximal yield of 1.1×10^8 μ/s is observed at

the injection point of the Mu3e solenoid [38]. The beam momentum is further reduced by a 600 µm Mylar degrader and a 35 µm Mylar vacuum window before reaching the Mu3e target in order to achieve about 90 % stopping efficiency. The aperture of the beam is narrowed down to 40 mm in diameter due to mechanical constrains arising from the inner pixel layers support structure. Taking into account all factors affecting the beam intensity the expected muon stopping rate in the Mu3e target is 6.2×10^7 µ/s at 2.4 mA proton current [38]. By using an alternative TgE target the rate at the Mu3e stopping target can increase up to about 8×10^7 µ/s at 2.4 mA with the existing beam line.

2.2.3 TARGET

The Mu3e stopping target is designed with the intention of maximizing the stopping efficiency along the beam direction while minimizing the material thickness along the path of electrons emitted in the muon decays. The latter is directly correlated with increased Bhabha and multiple scattering probabilities. Additionally, the decay vertices should be distributed as wide as possible to minimize overlaps in the reconstruction phase. Furthermore, utilizing low Z materials decreases the probabilities of photon conversion and multiple scattering. The shape of the target is modeled after the SINDRUM double cone hollow target which fulfills the previously stated requirements, see Fig. 2.6.

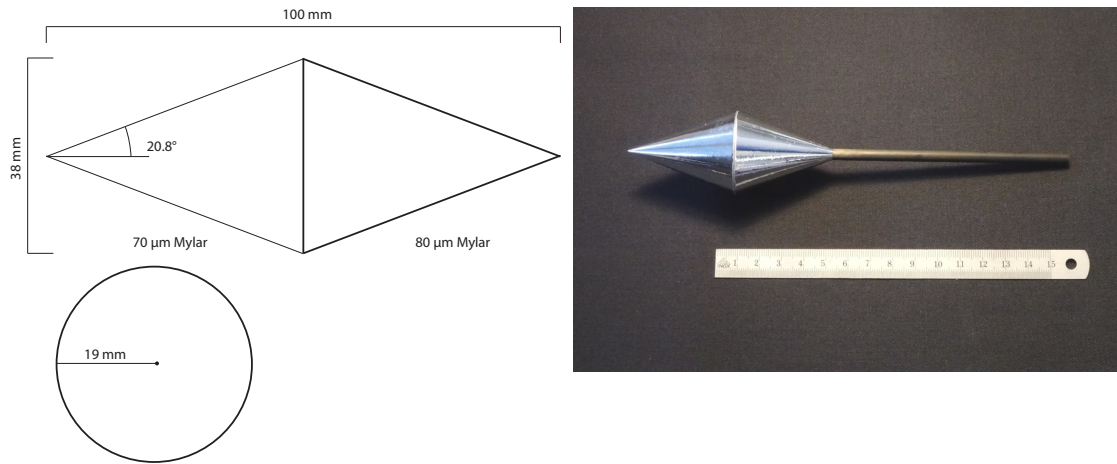
Figure 2.6 – A schematic of the Mu3e stopping target (Left) and a full model (Right) produced by PSI. Figure source [38].

It consists of thin Mylar foils glued together to a total thickness of 70 µm at the front part and 80 µm in the back. The length of the target is 100 mm and its radius is 19 mm. The 20.8 °cone aperture is equivalent to a thickness of 197 µm and 225 µm seen by the muons

along the beam in the front and back parts, respectively. A thin layer of aluminum is vaporized on the inner and outer surfaces of the target. The aluminum is in contact with a conductive carbon support tube in order to avoid charge accumulation due to the high stopping rate of positive muons.

2.2.4 MAGNET

The MU3E magnet generates a homogeneous 1 T magnetic field throughout the full volume of the experiment with field lines oriented along the beam axis. The field strength is chosen such that electrons with transverse momentum between 10 MeV/c and 53 MeV/c reach the outer pixel layers and recurl back at least once. The largest electron trajectory radius is chosen below 38 cm in order to keep the production cost for the magnet in reasonable scale. Field stability $\Delta B/B = 10^{-4}$ over 100 days of operation is required to ensure good momentum resolution. The magnet is currently in production by an external company. Options for field strength variations between 0.5 T and 2 T are foreseen to allow further acceptance studies. The warm bore of the solenoid is closed on both sides to insulate the helium atmosphere of the experiment from the external environment.

2.2.5 PIXEL TRACKER

The technology chosen for the MU3E pixel tracker is based on high voltage monolithic active pixel sensors (HV-MAPS) [41]. They offer large geometrical fill factors by integrating the readout electronics and placing it in deep N-wells directly on top of each pixel diode, see Fig. 2.7.
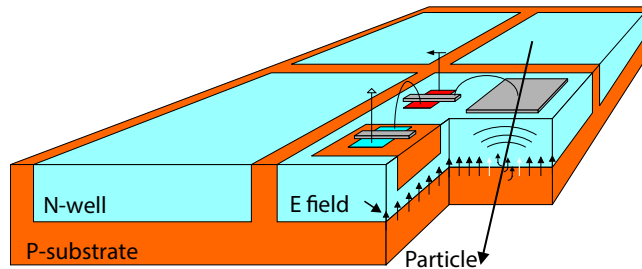
Figure 2.7 – Schematic of HV-MAPS sensor. The readout electronics is integrated into each pixel diode structure, shielded by a deep N-well. Figure source [41]

Reverse biasing the diodes at 60 V results in a highly sensitive depleted region with a width of approximately $15 - 30$ μm and charge collection in the order of a few nanoseconds. Consequently, the total thickness of the sensor can be reduced to 50 μm translating to a radiation

length of $x/X_0 = 0.054$ %. The aluminum traces for the signals in and out of the chip are also included in the thickness. Dedicated chips called MuPix are developed specifically for the Mu3e experiment. They are fabricated in a commercial 180 nm HV-CMOS process. A single pixel covers an active area of 80×80 μm^2, while one sensor consists of 250×250 pixels incorporated on a surface of 20×20 mm^2. Additional 3 mm on the one side are reserved for memory cells for each pixel, comparators, voltage regulators and digital logic. The power consumption is in the order of 300 mW/cm^2. Test beam measurements with the eight generation MuPix8 demonstrate detection efficiencies above 99 % with negligible noise rates $\mathcal{O}(<$ 1 Hz/pixel) and time resolution of 13 ns [42].

The individual chips are assembled in long ladders and glued directly onto high density interconnects. They link the sensors to all external electrical circuits for data transmission and slow control systems. The overall thickness in terms of radiation length is kept within 0.1 % X_0. Fig. 2.8 illustrates the geometry of the pixel tracker in the central region of the Mu3e experiment.
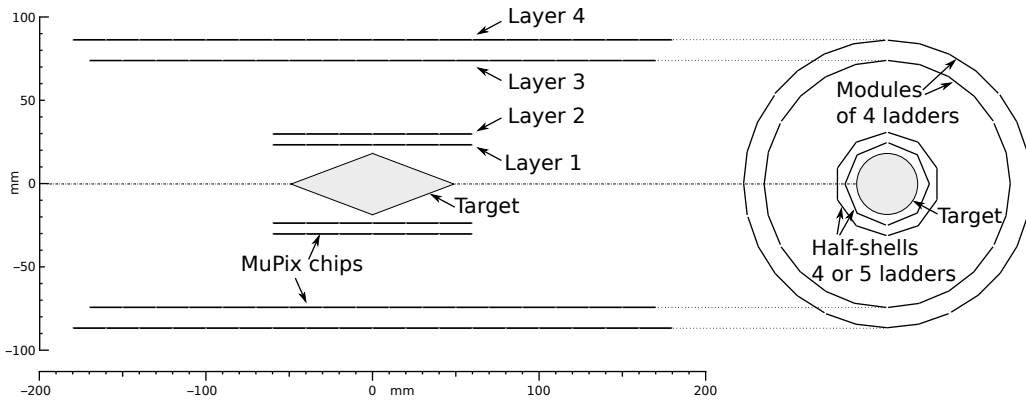

Figure 2.8 – Geometry of the central Mu3e pixel tracker. Figure source [38]

Two pixel layers are located in close proximity to the target and fully cover its surface. Their length is 12 cm and their radii are 2.3 cm and 3.0 cm. Another pixel tracker doublet is installed at radii of 7.4 cm and 8.6 cm allowing the measurement of electrons with minimum 10 MeV/c transverse momentum. The outer layers position is a compromise between momentum resolution and detector acceptance. Larger radii would provide better momentum resolution but it would also limit the minimal energy of the electrons reaching the tracker. While reducing the magnetic field would in principle allow higher acceptance, the maximal bending radius increases. As it is not feasible to produce a solenoid with a homogeneous magnetic field and the desired long-term stability, the specified geometry of the pixel layers is chosen. The lengths of the two outer modules are 34 cm and 36 cm, respectively.

Two recurl stations equipped with tracker doublets at radii identical to the outer layers are foreseen on both sides of the central section.

2.2.6 Timing Detectors

A timing system consisting of scintillating fiber and scintillating tile detectors is used to suppress the accidental backgrounds. Since the amount of material in the central region is critical for achieving the projected momentum resolution of < 1 MeV/c, a very thin scintillating fiber detector is foreseen for this section. At the recurl stations on the other hand, the momentum measurements are completed and a thicker scintillating tile detector can be installed under the pixel tracker to provide superior time information. Both systems are optically coupled to silicon photomultiplier (SiPM) sensors, albeit in different configurations. The scintillating tiles employ distinct single channel devices arranged in a matrix, while the fibers are coupled to monolithic arrays with 128 column shaped channels per single package. More details about the SciFi detector are provided in chapter 4. A dedicated ASIC - the MuTRiG chip [43] - is under development for the readout of both systems, see section 5.3 for more details.

2.2.6.1 Scintillating Tiles

The tile detector is located between the recurl pixel layers and the beam pipe. Part of this already tight space is reserved for data transmission, powering, cabling and cooling systems. Hence, while restrictions from the momentum measurement are lifted, the dimensions of the tiles should be small enough to fit in the available geometry. The tiles are made of Eljen technology EJ-228 plastic scintillator and the size of one tile is $6.3 \times 6.2 \times 5.0$ mm^3. Each tile is individually wrapped in Enhanced Specular Reflector (ESR) foil. A small 3×3 mm^2 opening is cut into the foil at the bottom of the tile for coupling to the Hamamatsu S13360-3050PE SiPM sensors with the same size. Fig. 2.9 shows a submodule with connected readout electronics. Seven such modules assemble in a ring under the pixel layers transverse to the beam direction. Longitudinally, 14 rings stack next to each other for a total of 56 tiles in each row along the recurl station.

The time resolution recorded in test beam measurements with the tile detector is approximately 50 ps [38], while the detection efficiency is above 99 %. he time resolution is well below the required 100 ps in the Mu3e research proposal.

2.2.6.2 Scintillating Fibers

The overall position of the Mu3e scintillating fiber (SciFi) detector is determined by the following physics constrains. Any material added on the outside of the fourth pixel layer
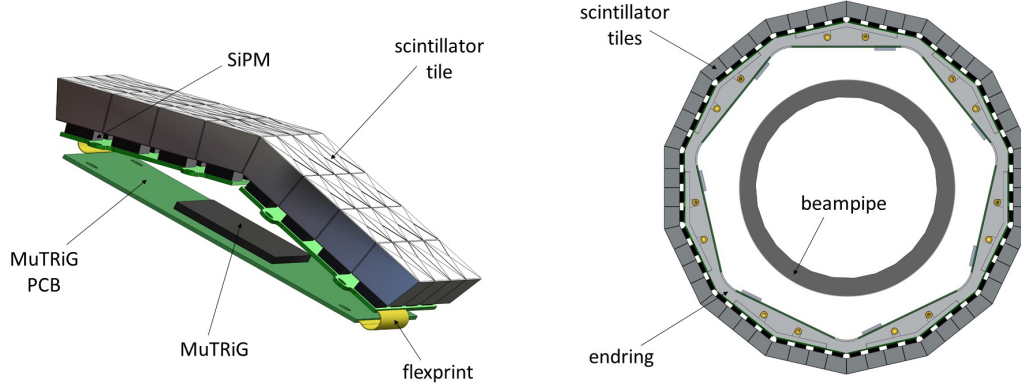
Figure 2.9 – A submodule of the Mu3e tiles detector. Seven such modules arrange in a ring around the beam pipe. The ring structure is replicated 14 times along the beam direction in both recurl stations. Figure source [38]

deteriorates the momentum resolution since no tracking detector is immediately available to account for the additional multiple scattering. Hence the fiber detector should lie on the inner side of the pixel tracker. Since the third and fourth, and first and second pixel layers are displaced by about 10 mm, no other detectors can fit between each pair. On the other hand, to optimize the momentum resolution the fiber tracker should be as close as possible to one of the pixel layers. There are two possible locations that fulfill the above requirements: either immediately outside the second pixel layer or directly inside the third pixel layer. The latter option is preferred due to the larger radius that leads to lower detector occupancy and pile up events. The baseline design consists of twelve 32.5-mm wide fiber ribbons arranged in a cylindrical shape. The length (along the beam axis) of each ribbon is 30 cm and it is constructed by staggered 250 μm thick fibers with circular cross-section. Both ribbon ends are equipped with SiPM arrays whose signals are digitized with the MuTRiG ASIC (see section 5.3). Fig. 2.10 shows a submodule of the SciFi detector and a circular cross-section view of the support structure for the detector. A detailed discussion on the mechanical integration of the latest design is presented in chapter 8.

2.2.7 DATA ACQUISITION

The Mu3e experiment uses a state-of-the-art data acquisition (DAQ) to handle information coming from all sub-detectors in a triggerless mode of operation. The DAQ system is organized in three logical and physical layers, see Fig. 2.11.

The first layer consists of front-end field programmable gate arrays (FPGA) processing raw
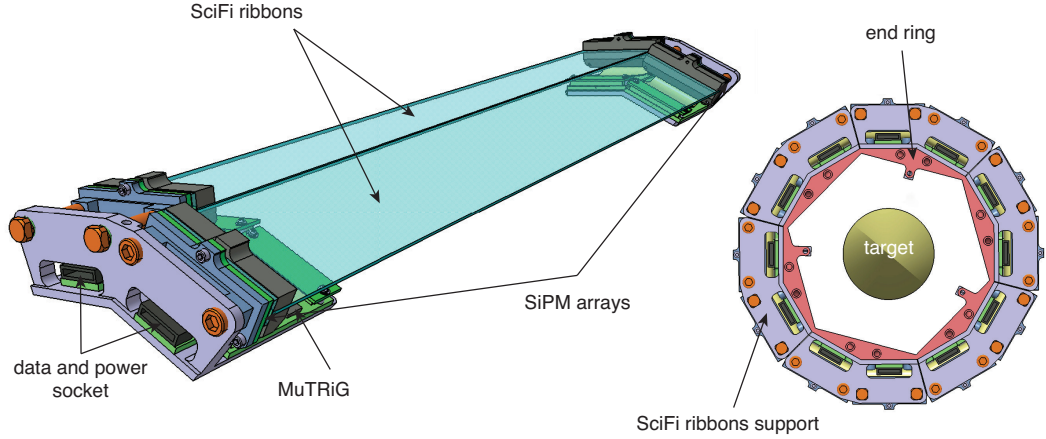
Figure 2.10 – A submodule of the Mu3e SciFi detector. Six such module assemble in a cylinder below the third pixel layer in the central part of the detector.

data from all sub-detectors. Each detector transfers hit information to its corresponding FPGA over 1.25 Gbps low voltage differential signaling (LVDS) links. For the Phase I of the experiment, the expected data rate in this layer is $\mathcal{O}$(105 Gbps). The FPGAs are programmed to sort and group the hit information in frames of 50 ns. Additionally, dedicated clustering algorithms are applied on the fiber detector data in order to suppress the outgoing amount of data to the next layer.

The packets from the front-end FPGAs are delivered to a set of switching boards over optical links with 6 Gbps bandwidth per link. These are dedicated boards that combine the information from all modules of a given sub-detector system and distribute it to FPGAs in an event filter farm. Each PC in the filter farm has access to data from all the detectors during a specific time slice. The data transfer between the switching boards and the filter farm is realized over 10 Gbits optical links.

The first component in the event filter farms are the FPGAs that execute event building, buffering and preliminary sorting and clustering operations. They communicate with the filter farm PCs over PCIe lines. The event data from the FPGAs is copied to the memory of high-performance graphics processing units (GPUs) using Direct Memory Access (DMA). A dedicated tracking and vertex reconstruction algorithm processes the incoming data online. It selects only event topologies close to the Mu3e signals reducing the output by a factor of 100 [44]. The results are delivered to a central DAQ computer running the Maximum Integrated Data Acquisition System (MIDAS) software [45]. From there the data is stored to discs for offline analysis. The expected data rate between the filter farm and the final DAQ PC is in the order of 50-100 MByte/s, hence a gigabit ethernet link will be sufficient for the last DAQ stage.
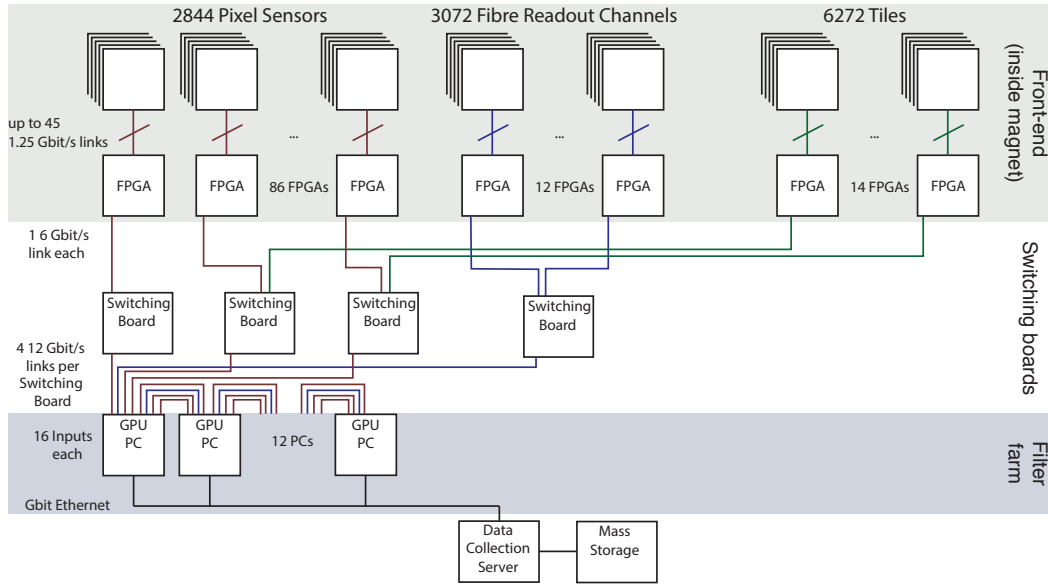
Figure 2.11 – Overall readout scheme of the Mu3e detectors.

2.2.8 Cooling

Most of the hardware components - e.g. silicon pixels, MuTRiG ASICs, front-end electronics (FEE) - generate significant amount of heat. Without a dedicated cooling system none of the sub-detectors will be operational. A water cooling system regulates the temperature of the electronic components outside the active volume. These include all front-end readout boards and electronics for the timing detectors. Gaseous helium flow cools the pixel sensors in the sensitive region of the experiment. The lower density of the helium is required in order to minimize the multiple scattering. Laboratory studies have been conducted in [46, 47].

2.3 The Fiber Detector Requirements

The Mu3e simulation framework is used to evaluate the impact of the timing detectors on the background suppression and the overall performance of the experiment. It serves to quantify also the requirements for the Mu3e fiber detector. Characterization studies performed in [48–51] and the present work are used as input to define the fiber detector properties in the simulation. Specifics on how the individual fiber detector components are implemented in the software can be found in [51].

2.3.1 OVERVIEW OF THE MU3E SIMULATION FRAMEWORK

A dedicated simulation software based on the GEANT4 toolkit is developed within the MU3E collaboration. Physics processes, environmental conditions, detector responses and digitization are all taken into account. After the initial particle propagation through the experimental volume, information about the hits in each detector is stored. This data is subsequently used to evaluate the parameters of track and vertex reconstruction algorithms as well as to study the performance requirements of the various detector subsystems.

Tracks are first reconstructed with data from the pixel sensors. Afterwards they are propagated to the fiber or tile detector planes and assigned time stamps based on their proximity to the hits in the corresponding time system. Depending on the number of pixel layers the tracks originate from they are classified into 4-, 6-, and 8-hit tracks as shown in Fig. 2.12. When a vertex satisfying the energy and momentum constrains for a $\mu \to eee$ event is found (Eq. 2.1), the timestamp of each track is used to discriminate accidental backgrounds. Only "long" tracks with 6 or 8 hits are considered for signal events due to the superior momentum resolution achieved in half turn measurements where the multiple scattering effects cancel at first order.
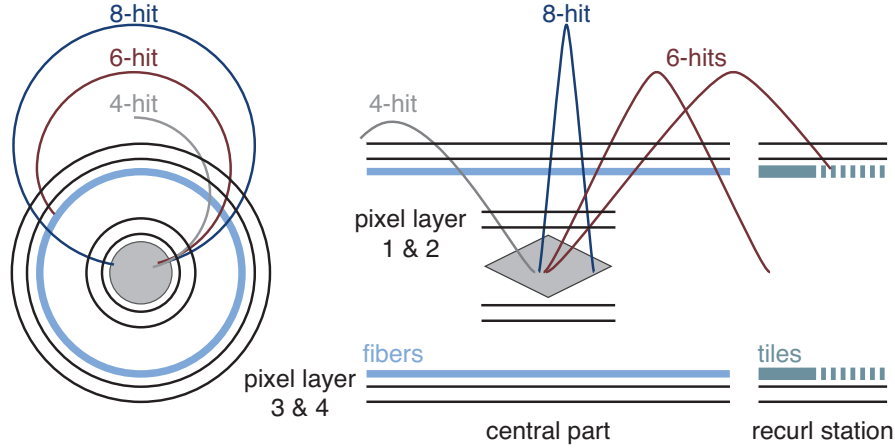
Figure 2.12 – Classification of track candidates based on the number of hits in the pixel detector.

2.3.2 FIBER DETECTOR IMPACT

If all three tracks from a given vertex are successfully matched to either a fiber or a tile detector hit, the accidental background can be suppressed by a factor of 75 given a time resolution of 260 ps for the fiber detector, see Fig. 2.13. If due to inefficiencies of the timing detectors not all tracks obtain a timestamp the suppression factor is in the order of 50.

Figure 2.13 – Suppression of the accidental backgrounds as a function of the fiber detector resolution. A conservative 90 % efficiency is assumed for the fiber detector. The resolution of the tiles detector is fixed at 50 ps and their efficiency is 100 %. The solid lines are obtaine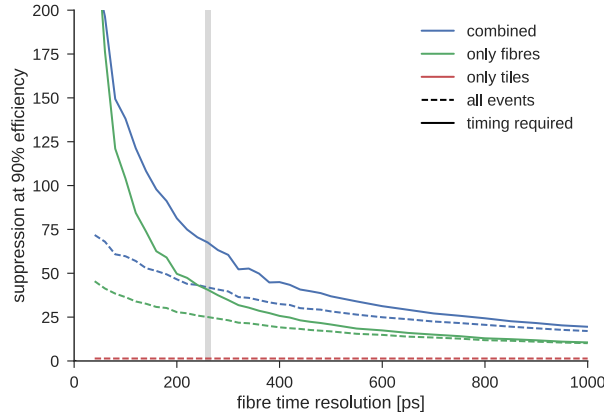d with events in which all three tracks have time stamps assigned. The dashed lines, on the other hand, include also tracks without time information, hence the background suppression is worse. Figure source [51].

Additionally, a fiber detector with a resolution in the order of 300 ps can be used to distinguish between electrons and positrons. Particles with opposite charges curve in the opposite directions when moving in a magnetic field. Thus, the sign of the time difference between two consecutive crossings in the fiber detector as a function of the trajectory length can identify the direction of the particle trajectory and hence determine its electric charge. Fig. 2.14 illustrates the potential of the fiber detector in identifying wrongly assigned particle charges in eight hit tracks.

Clearly, the better the time resolution of the fiber detector is, the more significant its power to suppress undesirable effects is. However, the more precise time resolution is correlated with an increase in the thickness of the fiber material which in turn degrades the momentum resolution. Fig. 2.15 shows the impact of the fiber ribbon thickness on the momentum resolution of a single track. The 6- and 8-hit tracks are significantly less affected by the presence of the fibers with respect to the 4-hit tracks. Because of that the short tracks are excluded from the $\mu \rightarrow eee$ event reconstruction in the experiment. The thickness of 0.9 mm is noted as the upper limit of acceptable fiber detector thickness. It corresponds to a ribbon with four staggered fiber layers.

2.3.3 ALTERNATIVE DESIGN OPTIONS

In the early days of the present work, 24 fiber ribbons, 16-mm wide, were foreseen for the fiber detector. The designed evolved due to the commercial production of 32 mm wide SiPM
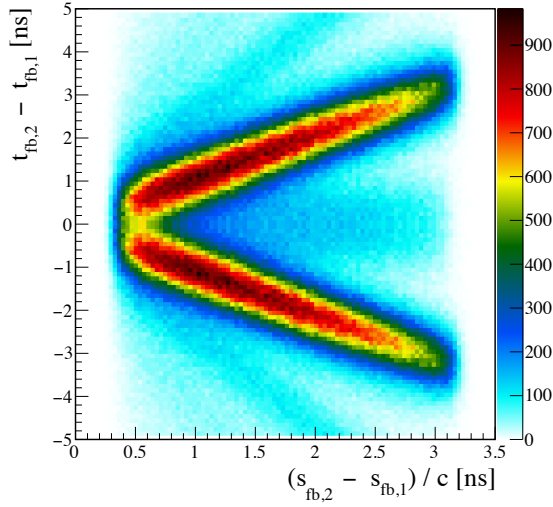
Figure 2.14 – Charge identification using the time difference between cluster hits in 8-hit tracks as a function of the time of flight (trajectory length divided by speed of light c). The upper branch corresponds to correct charge assignment while events in the lower branch have the wrong assignment. Figure source [38].
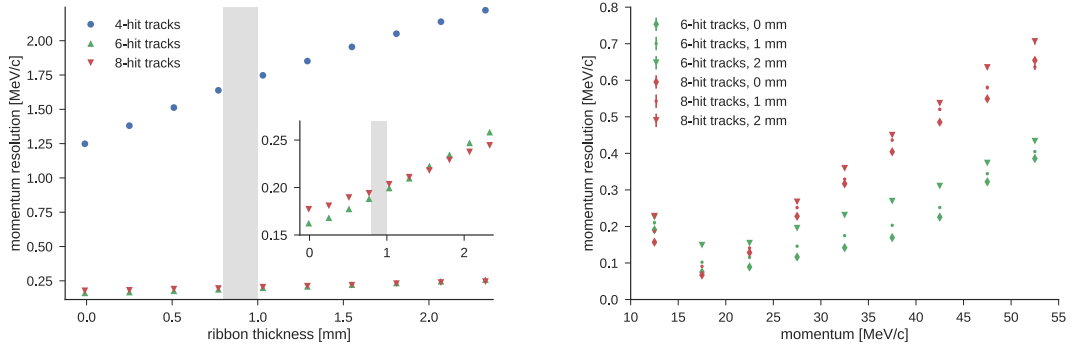
Figure 2.15 – Impact of the fiber ribbon thickness on the momentum resolution of single tracks at fixed momentum value (Left). A thickness of 0 mm, 1 mm or 2 mm is considered for the momentum scan plot (Right). Figure source [51].

arrays driven by the LHCB experiment [52].

An alternative readout scheme with each individual fiber mapped to a separate SiPM channel was also considered, see section 3.2. While, the latter solution offers higher granularity, the technological challenges in producing such modules combined with poorer time resolution and efficiency observed in the current work, lead to the conclusion that the single fiber readout is not feasible for the MU3E experiment.

In both configurations a critical parameter remains the number of fiber layers per ribbon. It

directly affects the time resolution and efficiency of the fiber detector as well as the momentum resolution of the pixel tracker.

3

Scintillating Fibers

The inner timing detector of the Mu3e experiment is constructed of staggered scintillating fibers with a diameter of 250 μm. This section introduces the working principle and materials used in the scintillating fibers evaluated in the scope of the current work. Following, is a description of the production methodology used in constructing scintillating fiber ribbons for two different readout configurations.

3.1 Scintillation Mechanism

Materials that emit light as a result of ionizing particles or γ- / X-rays depositing energy into their volume are called scintillators. Depending on the scintillation mechanism they are classified as organic or inorganic. In the latter, the energy transferred during an interaction excites electrons to the conduction band of the crystal. Impurities in the lattice shift the relaxation path of the electrons by introducing an intermediate energy level. As a result, the electrons transition to the ground state in several steps. The photons emitted in the process have longer wavelengths with respect to the absorption ones, hence they are not reabsorbed afterwards. In organic scintillators, on the other hand, the scintillation mechanism is an intrinsic property of the polymer molecules embedded in the material.

3.1.1 Organic Molecules

A base constituent of the organic polymers are benzene ring molecules (C_6H_6) whose atomic structure is illustrated in Fig. 3.1.

σ – bonds
sp^2 hybrydised orbitals

π – bonds
2p orbitals

delocalized π – electrons
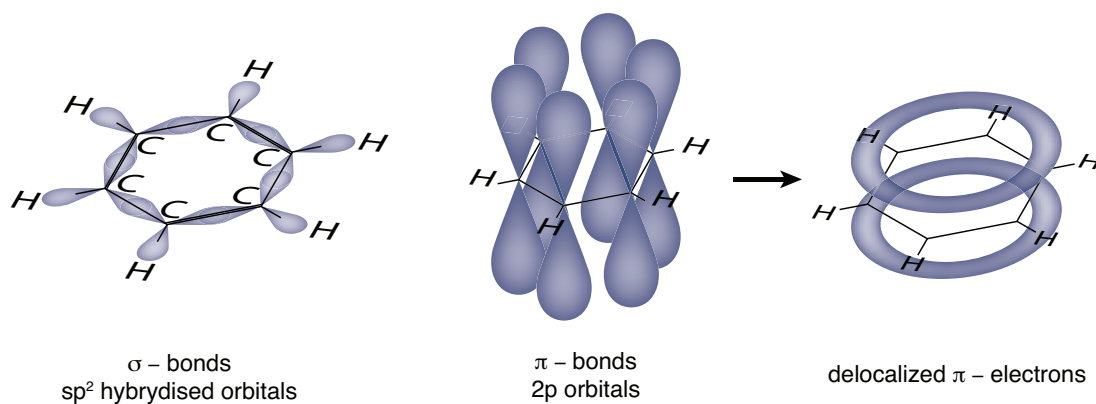
Figure 3.1 – Structure of a benzene molecule. The six carbon and six hydrogen atoms compose a planar ring with 12 σ-bonds. The remaining six electrons from the carbon atoms participate in π-bonds and are delocalized around the ring.
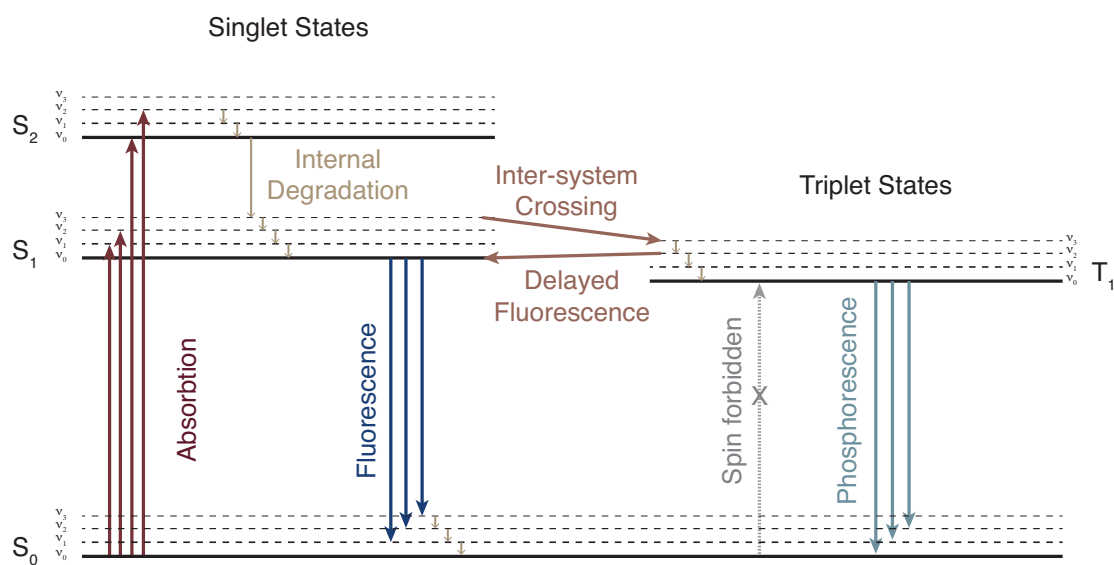
Figure 3.2 – Fluorescence and phosphorescence mechanism in an organic scintillator. The scintillation is a result of transitions between energy levels in the π electron system of benzene. Figure adapted from [53].

Three of the four valence electrons in each carbon atom (C) are in the sp^2 orbitals and participate in single covalent bonds (σ-bonds) with the two neighboring carbon atoms and a hydrogen atom (H). They establish a planar ring structure. The fourth electron, on the other hand, is in a $2p$ orbital and overlaps with a $2p$ electron from one of the adjacent carbon atoms to form a π-bond. These six electrons remain delocalized and can transition between the energy levels of the π-bonds (see Fig. 3.2) to trigger luminescence in the organic scintillator. The energy levels are divided into singlets S_i and triplets T_i with S_0 denoting the ground state. Each state additionally splits in finer level ν_k due to vibrational and rotational modes of the molecule. A typical spacing between the S_0 and S_1 levels is in the order of $\mathcal{O}(3 \text{ eV})$ while the distance between the fine vibrational excitations is in the order of $\mathcal{O}(0.1 \text{ eV})$. Energy deposited by ionizing radiation excites both the π-electrons and the vibrational modes of the molecule. Since direct transitions from the ground state to one of the higher triplet states are spin forbidden, electron excitations occur only to one of the $S_{i>0}$ states. Thermal relaxation of the vibrational ν_i states to the nearest ν_0 level proceeds at a very short time scale compared to transitions between the S_i levels. Additionally, higher vibrational levels of lower S_{i-1} states often overlap with the ν_0 of the current S_i level resulting in very fast thermal transitions to the S_1 level. This process of rapid non-radiative relaxation is known as *internal degradation* or *internal conversion*. The radiative transition from S_1 to one of the vibrational states in S_0 proceeds with the emission of a *fluorescence* photon. Since thermal relaxation to the ν_0 - S_0 state proceeds instantaneously, the energy of the photon is insufficient for it to be reabsorbed and excite electrons to any of the S_1 levels. The phenomenon of moving the emission spectrum towards higher wavelengths with respect to the absorption spectrum is called *Stoke's shift*. Besides *fluorescence*, two more luminescence processes are observed in the benzene energy scheme, namely *phosphorescence* and *delayed fluorescence*. For the former to occur electrons in the singlet state first transition to the triplet T_1 state via thermal relaxation in a process called *inter-system crossing*. *Phosphorescence* is realized in the decay of the T_1 level to S_0. The T_1 level is metastable due to spin conservation and it's lifetime is in the order of $\mathcal{O}(10^{-4} \text{ to } 10 \text{ s})$. Consequently, it is possible for an electron in the T_1 state to transition back into a singlet state and relax to the ground level via *delayed fluorescence* emission.

3.1.2 PLASTIC SCINTILLATORS

Since fluorescence is an inherent property of the benzene molecules, organic scintillators can be produced in various shapes, sizes and states - solid, liquid and gaseous. In plastic scintillators, for example, polyvinyl-toluene (PVT) or polystyrene (PS) are often used as the carrier polymer substances. Their quantum efficiency, however, is low and the wavelengths of the
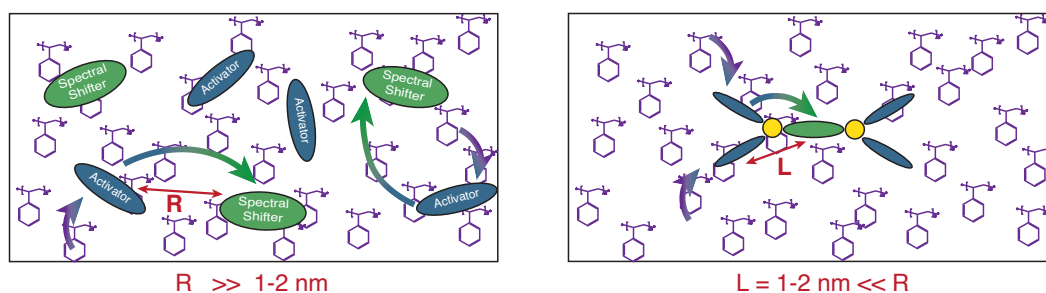
Figure 3.3 – Schematic representation of a plastic scintillator based on polystyrene with traditional activator and spectral shifter luminophores (Left). The novel NOL molecules combine both the activator and the shifter in a single nanostructure increasing the efficiency of the wavelength shifting process. Figure adapted from [55]

emitted photons by PS are in the range 280 - 400 nm. Around the peak of the emission spectrum, which lie at approximately 330 nm, photons are quickly absorbed back by the PS due to various effects of Rayleigh scattering and molecular vibrations. To mitigate these inefficiencies an organic fluorescent dye with properly matched energy levels is added to the base polymer. It is called an *activator* and is typically used in concentrations of about $\mathcal{O}(1 \%)$ by weight such that the molecules of the dye and the benzene rings are no further than $\mathcal{O}(1 \text{ nm})$ apart. As a result, energy from the benzene excitation is quickly transferred to the activator via non-radiative dipole couplings (Förster transfer). The emission spectrum of the activator is chosen to shift the photon wavelengths away from the peaks of PS absorption. Depending on the dye and especially when fast decay times $\mathcal{O}(< 1 \text{ ns})$ are required the fluorescent photons have wavelengths in the UV spectrum and above. A second dye, referred to as *wavelength shifter*, is often added in concentrations of about $\mathcal{O}(0.05 \%)$. It absorbs the UV photons and shifts their wavelengths to higher values in order to both increase the transparency of the scintillator and to match the absorption spectrum of the available photosensors. Each step of shifting up the wavelengths introduces inefficiencies in the scintillation output and leads to low overall efficiency in converting the deposited ionizing energy to light.

Recent developments have introduced a new class of luminophores in the polystyrene matrix - the so-called Nanostructured Organosilicon Luminophores (NOL) [54]. They bind the activator and the wavelength shifting dye via a silicon atom and allow non-radiative intramolecular energy transfer between the two through the Förster mechanism, see Fig. 3.3. As a result, the wavelengths of scintillation photons are shifted faster and more efficiently. These materials are not yet commercially available as R&D activities are still ongoing, however some samples were procured by the fiber group at University of Geneva for evaluation.
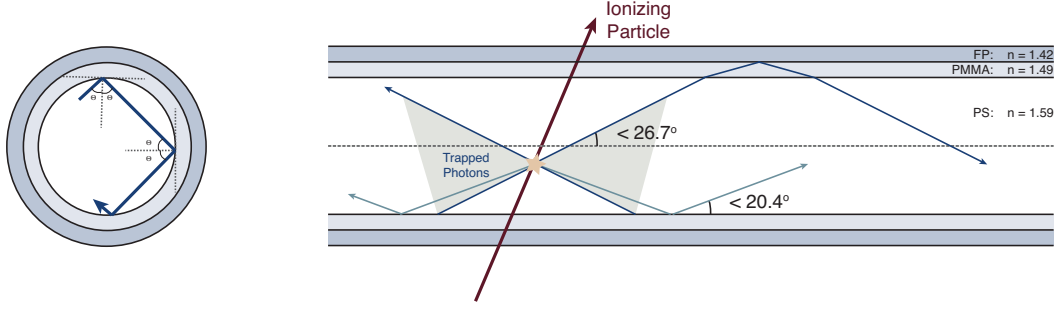
Figure 3.4 – Illustration of the light trapping in scintillating fibers. (Right) Cross section of a fiber with helical path of the trapped photon. (Left) A longitudinal view of the trapping efficiency for a multiclad fiber. The additional cladding increases the internal reflection angle.

3.2 SCINTILLATING FIBERS

In general, a scintillating fiber consists of a core scintillating material e.g. a plastic scintillator, surrounded by one or more cladding layers with a decreasing refractive index. As a consequence of this configuration the detector serves a dual purpose: on one hand it converts energy from ionizing particles to light, and on the other, it guides the emitted photons towards its extremities. The last property is significant for the Mu3e fiber detector as the photosensors can be placed outside of the active volume thus keeping the thickness of the timing detector at a minimum. Additionally, using fibers with a diameter of only 250 µm increases the granularity and ensures a better spacial resolution.

When energy is deposited in the fiber core, the scintillation photons are emitted isotropically around the interaction point. A fraction of the light is trapped inside the fiber if the requirements of full internal reflection are fulfilled. Namely if $\Theta > \Theta_c = \arcsin\left(\frac{n^{\text{cladding}}}{n^{\text{core}}}\right)$, where Θ is the photon incidence angle relative to the normal of the surface upon which the photon reflects (Fig. 3.4) The principle of light propagation within the scintillating fiber is identical to that of optical fibers used in communications. While it it possible to manufacture fibers with various shapes, most common are the ones with circular and square cross-sections. The accent of the current work is on the former and detailed evaluation of the latter is given in [50]. Contrary to the square fibers, with round ones the critical angle is invariant of the position in the cross-section where the reflection occurs (Fig. 3.4). By adding more layers of cladding with decreasing refractive indices the critical angle, as seen from the core, decreases leading to a higher trapping efficiency. The majority of fibers tested in this work are produced by Kuraray and have two cladding layers each with a thickness of $\leq 3\%$ of the fiber diameter. The core material is polystyrene with n^{PS} = 1.59, covered by a cladding of poly-methylmethacrylate (PMMA) with n^{PMMA} = 1.49 and finished with a layer of fluorinated polymer (FP)

- n^{FP} = 1.42. With this composition of materials, the trapping efficiency of a fiber with only the PMMA cladding would be $\varepsilon_{\text{s}}^{\text{trap}} = d\Omega/4\pi$ = 3.1% (Θ_c = 20.4°), while including the FP layer results in $\varepsilon_{\text{d}}^{\text{trap}}$ = 5.3% (Θ_c = 26.7°).[1] Mechanical instabilities and increased absorption prohibit the construction of fiber with PS core and a single FP cladding.

3.2.1 Main Characteristics

For the Mu3e fiber detector the most important characteristics are the efficiency and the time resolution of the system. The signal amplitude in terms of number of photons reaching the fiber extremities directly affects the efficiency while the decay constant of the scintillation process determines the achievable time resolution. The system output for a given energy ΔE deposited into the fibers can be expressed as:

$$N^{\text{out}} \;=\; Y_s \;\cdot\; \varepsilon^{\text{trap}} \;\cdot\; \varepsilon^{\text{trans}} \;\cdot\; PDE \;\cdot\; \Delta E \tag{3.1}$$

The ionization light yield $Y_s(\lambda)$ is an intrinsic property of the scintillator and depends on the core material, concentration and type of dissolved dyes and their spectral matching and quantum efficiency. The last term, $PDE(\lambda)$, is the photo-detection efficiency of the optical sensor that will be used to readout the fiber. Both terms are a function of the photon wavelength. From the remaining two factors, $\varepsilon^{\text{trap}}$ is the trapping efficiency described previously and $\varepsilon^{\text{trans}}(\lambda)$ reflects the signal attenuation during light transport in the fiber. The latter can be characterized by a wavelength dependent function $\Lambda(\lambda)$ called attenuation length which is defined as the distance d along the fiber after which $1/e$ of the initial number of photons survives. Imperfections in the cladding and core surfaces, as well as absorption in the scintillation material are the main causes for light attenuation. The light intensity along the fiber at a distance d from the interaction point can be approximated as:

$$I(\lambda, d) \;=\; I_0^{\text{long}}(\lambda) \cdot e^{\frac{-d}{\Lambda^{\text{long}}(\lambda)}} \;+\; I_0^{\text{short}}(\lambda) \cdot e^{\frac{-d}{\Lambda^{\text{short}}(\lambda)}} \tag{3.2}$$

where $I_0^{\text{long}}(\lambda) + I_0^{\text{short}}(\lambda)$ is the initial intensity of the wavelength λ.

3.2.2 Fiber Materials Used for Prototyping

All fiber prototypes emerging from this work are constructed with round fibers of diameter 250 µm and double cladding. The samples with single fiber readout (see section 3.3) utilize only

---

[1]The trapping efficiency is estimated for photons crossing the fiber axis. It is also possible to trap photons with non-meridional trajectories i.e. photons that do not traverse the fiber axis. They contribute positively to the total trapping efficiency, however their helical paths are too long and they are often lost in the multiple reflections between the claddings due to imperfections in the surfaces.

	SCSF-78	KURARAY SCSF-78	NOL-11	SAINT-GOBAIN BCF-12	
Cross-section		round		round	square
Core		PS		PS	
Inner Cladding		PMMA		PMMA	
Outer Cladding		FP		FP	
Size [μm]		250		250	
Cladding Thickness [%]		3 - 3		3 - 1	4 - 2
Refractive Index		1.59 - 1.49 - 1.42		1.60 - 1.49 - 1.42	
Trapping efficiency [%]		5.4		5.6	7.3
Emission Peak [nm]	437	450	435	435	
Decay Time [ns]	2.4	2.8	1.3	3.2	
Attenuation Length [m]	>3.5	>4.0	>2.5	>2.5	

Table 3.1 – Properties of scintillating fiber materials utilized for the production of ribbon samples evaluated in this work. The NOL-11 fibers are still in the R&D phase and the reported parameter values might change in the future.

SCSF-81MJ fibers by KURARAY which were initially chosen due to their short decay time. For the column readout, on the other hand, an extensive study is performed using all blue light emitting fibers from KURARAY, namely SCSF-81MJ, SCSF-78MJ and NOL-11[2][56], as well as BCF-12 fiber from SAINT-GOBAIN [57]. Additionally, one sample with aluminized square BCF-12 fibers have been provided by the PSI fiber group for evaluation with the column readout.

Table 3.1 summarizes the properties of the fiber materials assessed within the present work.

3.3 FIBER RIBBONS DESIGN AND PRODUCTION

The criteria imposed on the fiber detector by the baseline MU3E design are discusses hereafter from the perspective of ribbons construction. Most notably, the detector geometry and assembly should be optimized for minimal material budget, maximal efficiency and high granularity. Design specifications and modifications implemented in the ribbon production as well as the actual manufacturing of the samples tested in this work are carried out by the author.

3.3.1 MINIMAL MATERIAL BUDGET

This requirement implies that the active volume of the detector should be maximized while any excess passive materials such as binding epoxy, coatings and support structures inside the sensitive area should be minimized.

---

[2]The first samples of NOL-11 fibers with sufficient length to produce a fiber ribbon became available after the conclusion of the single fiber readout studies.
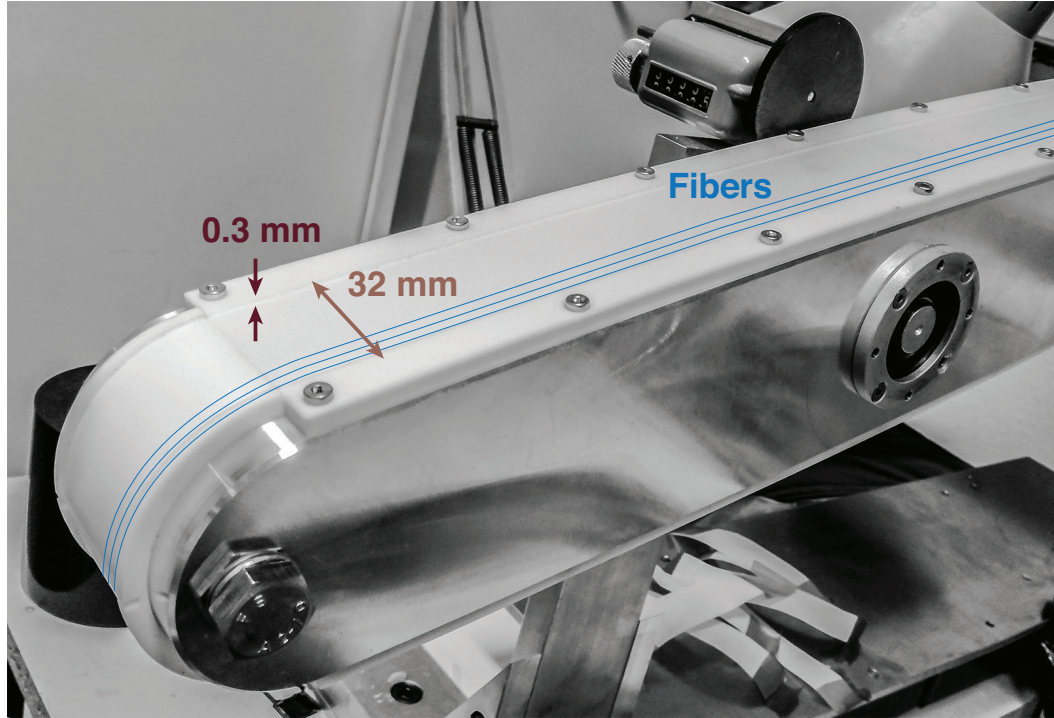
Figure 3.5 – U-channel with a depth of 0.3 mm and width of 32 mm machined in 5 mm thick Teflon™.

The fibers are pulled from a spool and aligned layer by layer in a flat U-shaped channel via winding. The goal is to achieve the tightest possible configuration with minimum dead material. Close up photo of a U-channel with a width of 32 mm is shown in Fig. 3.5, while the full ribbon winding station is pictured in Fig. 3.6.

Consecutive layers use the pattern on the surface of the previous ones to maintain the fiber alignment. The width is chosen to fit the desired number of fibers placed at an average distance of ≈255 μm, offering a tolerance of 5 μm with respect to the mean fiber diameter. For example, if the target width is 32 mm than 126 fibers with a diameter of 250 μm will be placed in the first layer. Since the length of the Mu3e ribbons is in the order of 30 cm a two-sided rotating frame is used, thus producing two ribbons at a time.

To facilitate lifting off of the completed ribbons, the U-channel is machined in 5 mm thick Teflon™ plates attached on top of the frame. The depth of the channel is 0.5 mm and it is further coated with a thin layer of wax-based spray Trennspray P6 before starting a new ribbon. The wax prevents resin from sticking to the bottom of the channel and aids in smoothly extracting the ribbon.

In the proposed construction method each fiber layer is wound after the epoxy on the previous one has hardened. After a few iterations using flat surfaces for the two sides of the frame,
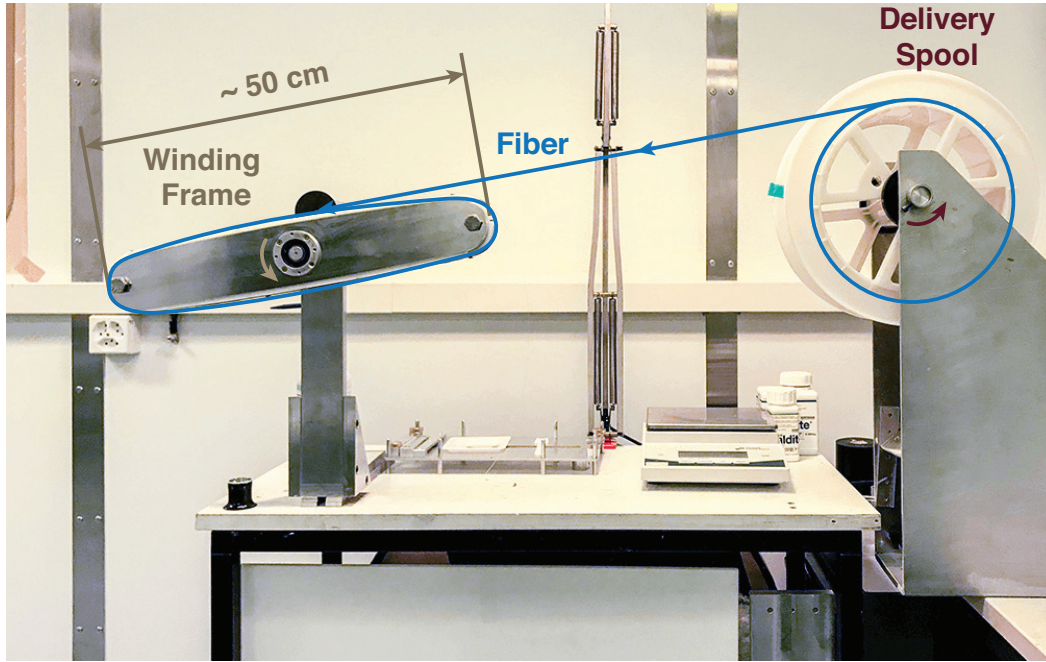
Figure 3.6 – Fibers are drawn from the delivery spool (Right) and alined next to each other in a U-shaped channel (Left) machined in a specially designed frame. Ribbons are assembled by winding one layer at a time.

it was concluded that a minimal curvature would help keeping the fibers under tension and tightly laying at the bottom of the U-channel. This is important in order to avoid air gaps at the base of the ribbon in which small epoxy drops can form before the ribbon is completely dry. When hardened, the blobs can damage the fibers due to the mechanical tension exerted upon them during application of the subsequent layers.

To further minimize the passive substances, the excess adhesive is absorbed with a soft cloth immediately after the completion of each layer.

When preparing the ribbons, the viscosity and the density of the glueing mixture also affect the overall amount of dead material. With the intention of minimizing it, several two component epoxy adhesives with varying viscosity were tested. A critical criterion, for them is to have a pot life of at least 40 minutes in order to be able to complete a full layer of 32 fibers without the need of preparing a new mixture. For ribbons with larger number of fibers per layer, a pot life $\mathcal{O}(2$ hours) is preferred. Table 3.2 summarizes the properties of the resins used in this work.

The first samples were produced with PROCHIMAE-30 resin. While it was useful for proving that a ribbon of three or four layers with a length of 40 cm and a width of 8 mm to 16 mm is sufficiently rigid to be handled without additional support layers, the E-30 is highly viscose - about 1300 mPa·s and little information is available about its properties when operated at

	Prochima E-30	Polytec EP 601	Polytec EP 601 LV	Polytec EP 610	Araldite 2020
Viscosity [mPa · s]	1350	460	240	800	150
Density [g / cm^3]	1.10	1.15	1.15	1.05	1.10
Pot Life	40 min	4 h	4 h	6 h	50 min
T$_{glass}$ [$^{\circ}$C]	n/a	73	65	n/a	40
T$_{degrade}$ [$^{\circ}$C]	n/a	280	280	300	200
Curing Time @23°C	16 - 72 h	24 - 48 h	16 h	24 h	16 - 25 h
Curing Time @80°C	n/a	90 min	90 min	80 min	50 min

Table 3.2 – Summary of the most relevant properties of epoxy adhesives evaluated for the production of fiber ribbons. Viscosity, density and pot life refer to the mixed state of the compounds. Values reported by vendor.

higher than room temperature. It has been thus abandoned in favor of the Polytec EP 601 and EP 601 LV products. These are epoxies with low viscosity, 460 mPa·s and 240 mPa·s respectively, specifically designed for applications in optics and fiber optics. They are also suitable for use in environments where the ambient temperature can reach up to 60°C which is expected in some regions near the Mu3e fiber detector. The initial experiments with EP 601 LV resulted in multiple miniature drops being formed on the surface of the fibers after the first layer which prevented the application of the subsequent one. In the few cases where the epoxy was almost fully absorbed through the soft cloth and a second and third layer were successfully added, the ribbon was mechanically very unstable and fibers were easily detached while lifting it off from the U-channel. Hence, the lower viscosity option was excluded and samples were produced with the EP 601 version. The flexible version EP 610 was considered in order to match the temperature expansion of the cured epoxy with that of the fibers. However, ribbons prepared with EP 610 were very soft and easily deformable, so its feasibility was not further investigated. At a later stage, the Araldite 2020 two-component cement was examined as an option for building ribbons due to its lower viscosity and tested performance in other projects involving scintillating fibers. No drops condensed on the fiber surface and the assembled ribbons exhibited sufficient rigidity to be handled without extra support materials attached to them. The Araldite 2020 is also radiation hard. It is applied for the last batch of ribbons constructed for the test beam campaigns at PSI in 2017.

Cross-section of a ribbon produced following the described methodology and glued with Araldite 2020 epoxy is shown in Fig. 3.7. Using pattern recognition algorithms, the circular cross-sections are identified. For the specific example circles are identified at the boundary between the core and the first cladding layer. The measured distance between neighboring
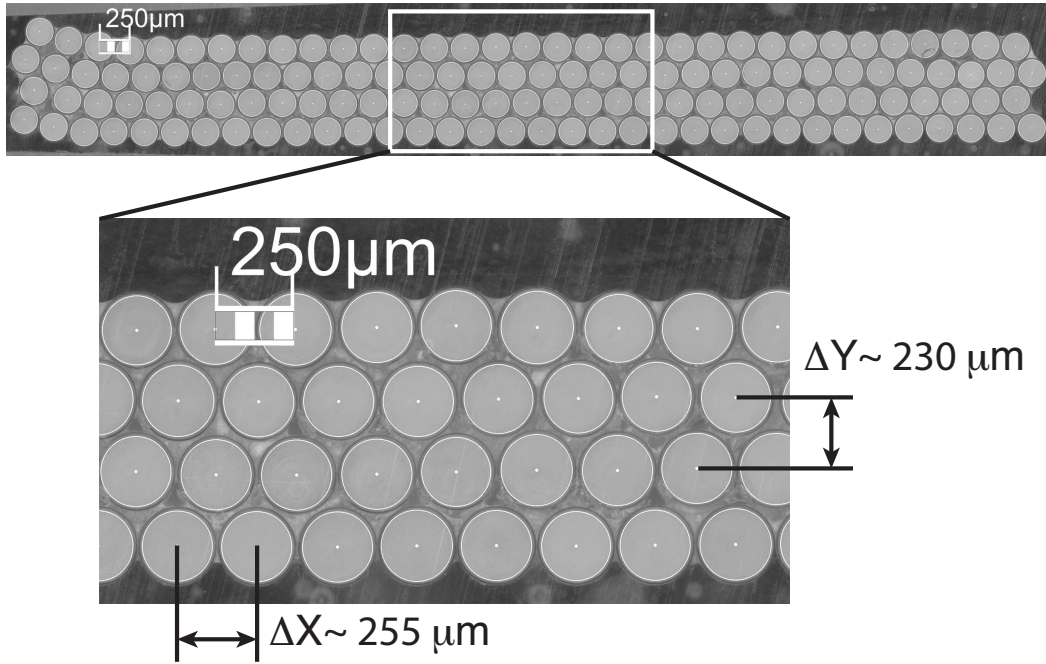
Figure 3.7 – Cross-section of an $\sim$ 8.5 mm wide ribbon with four layers. The bright epoxy visible between the fibers is ARALDITE 2020 mixed with 20 % TiO$_2$ powder. The dark gray epoxy is ARALDITE RAPID which is used only at the end of the ribbon to form a rigid mold around it which is necessary in order to machine it with a diamond tool. The bending at the left side is due to the shape of the mold used to produce the ribbon. Tape has been added to the U-channel for this particular sample which resulted in rounded corners on one side. An algorithm for detecting circles is used to locate the core of each fiber. The result from the pattern recognition is shown in white. The dark circles remaining outside are the cladding of the fibers.

fibers in one layer as well as the vertical[3] position of the fibers are shown in Fig. 3.8.

3.3.2 DETECTOR GRANULARITY

The granularity of the fiber ribbons is determined on one hand by the size of the staggered fibers, and on the other hand, by their optical readout configuration. Since the thinnest available scintillating fibers are 250 µmm in diameter/width, they are selected as the baseline option to achieve maximal segmentation. Concerning the optical readout, two possibilities are considered. In the first one, designated *single fiber readout*, each fiber is individually coupled to an independent photosensor channel. In the second one several fibers are mapped together in a column like configuration labeled *column* or *array readout*. In both cases the ribbons are produced with the winding tool described in subsection 3.3.1. For the *single fiber readout*,

---

[3]Vertical and horizontal refer to the geometrical orientations of the fibers as seen in the cross-section plot in Fig. 3.7.
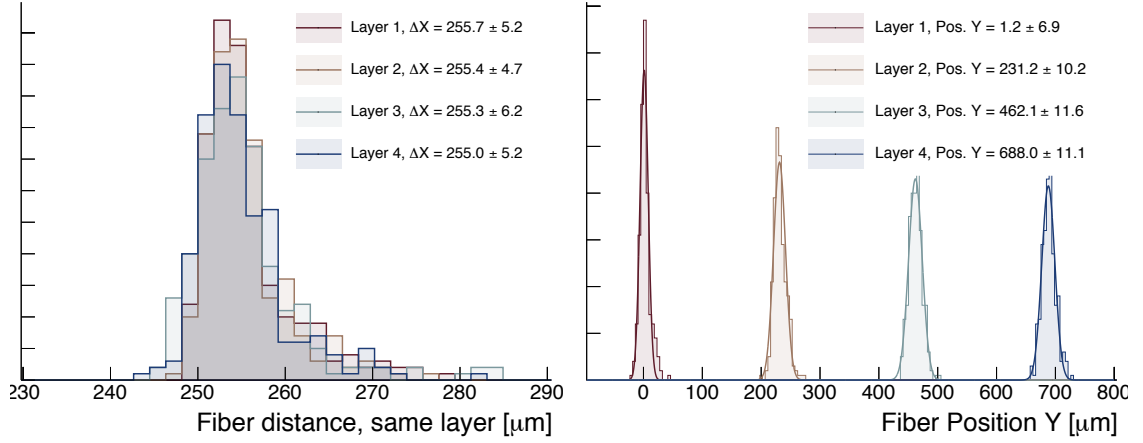
Figure 3.8 – Geometrical characteristics of a SciFi ribbon with four layers of 250 μm think fibers. A tight configuration is achieved with the proposed production technique where the average distance between neighboring fibers (Left) is about 255 μm. The vertical distance between the layers (Right) is in the order of 230 μm. The centers of the identified circular cross-sections are used as input for the plots. The ribbon is constructed using ARALDITE 2020 with 20 % TiO$_2$ powder.

however, a longer frame is used such that about 15 cm of fibers at each end of the ribbon can be kept clean of any epoxy.

3.3.2.1 RIBBONS WITH SINGLE FIBER READOUT

Once the ribbon is out of the U-channel, two plastic brackets are attached on each end of the staggered section to protect it from disassembling. Afterwards, the ribbon is straightened within a dedicated frame with the brackets being serving as holding points (see Fig. 3.10) The loose fibers are subsequently fanned out through the holes of a connector such that they align with the positions of single photosensors. In the preliminary Mu3e design each ribbon consists of 63/64 fibers per layer and a width of ≈ 16mm. The samples prepared for evaluation in this work conform to the aforementioned specification, however only a subset of 32 fibers per ribbon is fanned out in order to investigate whether this readout option is feasible. A photo of the connector with the fanned out fibers is shown in Fig. 3.9. Each hole has a diameter of 300 μm to allow smooth insertion of the fibers.

The distance of 3 mm between the fiber centers is determined by the packaging of the photosensors available at the time of production (see subsection 4.3.1). To avoid bending the fibers, the fanout connector is located 4.5 cm away from the end of the staggered section.

The final design in case the ribbons with *single fiber readout* prove to be a viable option, envisages the development of a monolithic photosensor (see chapter 4) with a custom matrix layout for the individual channels. The dimensions of a single channel would be 450 × 450 μm^2
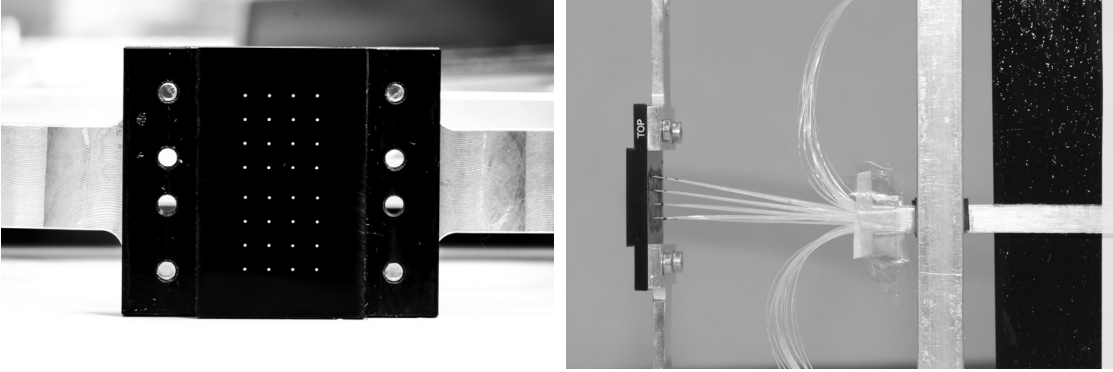
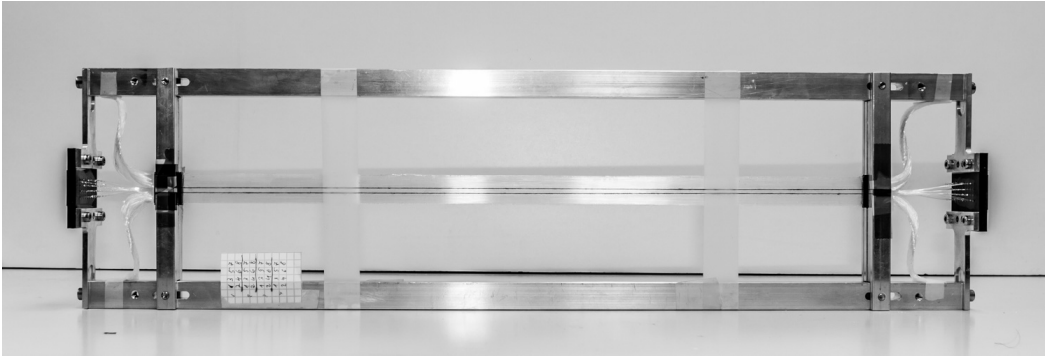**Figure 3.9** – Front (Left) and lateral (Right) view of the single fiber fanout connector.

Figure 3.10 – A full ribbon with single fiber readout.

with a 50 μm gap in between the neighboring channels and the fibers will be fanned out in a matching dense connector. The smaller fiber bending resulting from the tighter fanout configuration would allow the connector to be placed as close as 1 cm to 2 cm away from the staggered end. Since observations made during test beam studies with the *single fiber readout* samples did not lead to satisfying results in terms of efficiency and time resolution, no further action was taken to investigate the technical details of integrating such a design into the Mu3e experiment.

Nevertheless, having each fiber read out individually is beneficial in quantifying intrinsic properties of the ribbon such as the crosstalk between neighboring fibers. The samples constructed for the studies presented in chapter 6 utilize the multi-clad SCSF-81MJ fibers from Kuraray and the EP 601 epoxy.
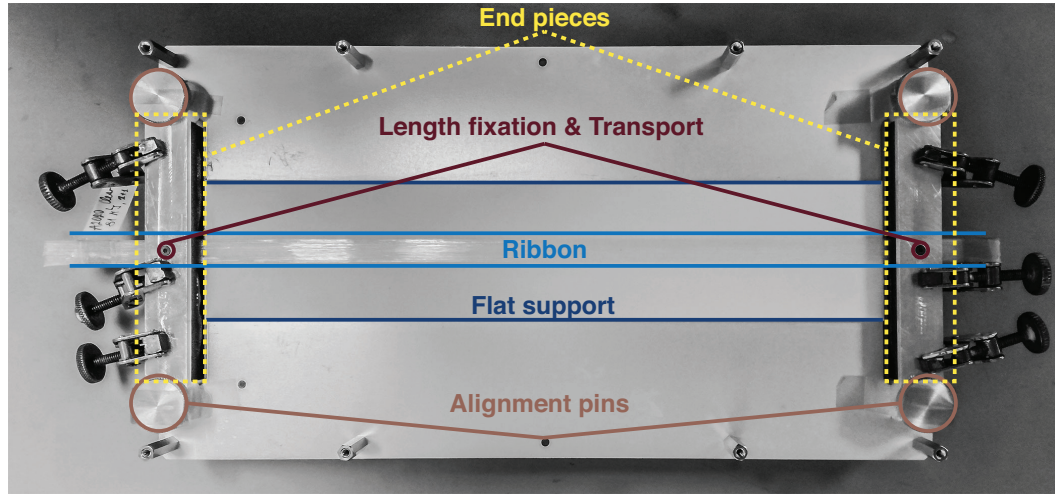
Figure 3.11 – A jig used to position the end pieces on a ribbon with *column readout*. A length fixation is attached on top of the ribbon via the threaded holes in the end connectors. The ribbon lays flattened on a teflon plate while the epoxy in the connectors hardens.
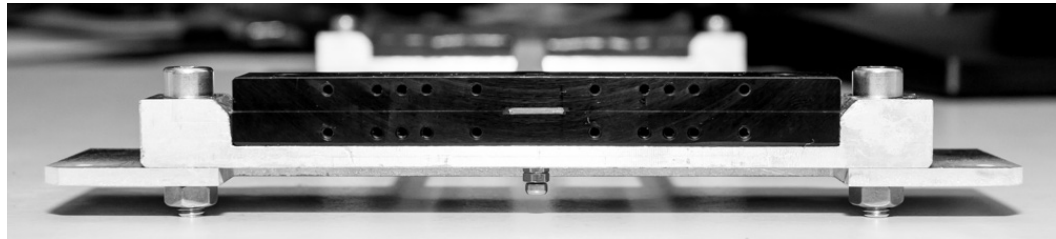

Figure 3.12 – End piece socket mounted on a ribbon with column readout. The fixation screw in the bottom attaches the black connector to the alignment aluminum bracket. The holes on the front are used for coupling with the optical photosensor.

3.3.2.2 Ribbons with Column Readout

Following the experience with the *single fiber readout* ribbons and considering the final integration of the fiber modules into the Mu3e experiment, a modular system is developed for testing the *column readout* ribbons. Similar to the brackets used to protect the staggered sections in the *single fiber readout*, a special connector is glued near the ends of the ribbon. Besides protecting the ribbon ends, it is also used to couple the optical sensor with the fibers and to attach the ribbon to external mechanical components. Fig. 3.11 shows a jig used to position the custom pieces at the ends of a ribbon and Fig. 3.12 show their cross-section (the other side is identical).

Two threaded holes on the top and bottom of the black connectors are used to fix the distance between the two ribbon ends via fixed length metal bars. The ribbon taken out of the U-channel is longer than the target distance between the end pieces e.g. for a nominal length
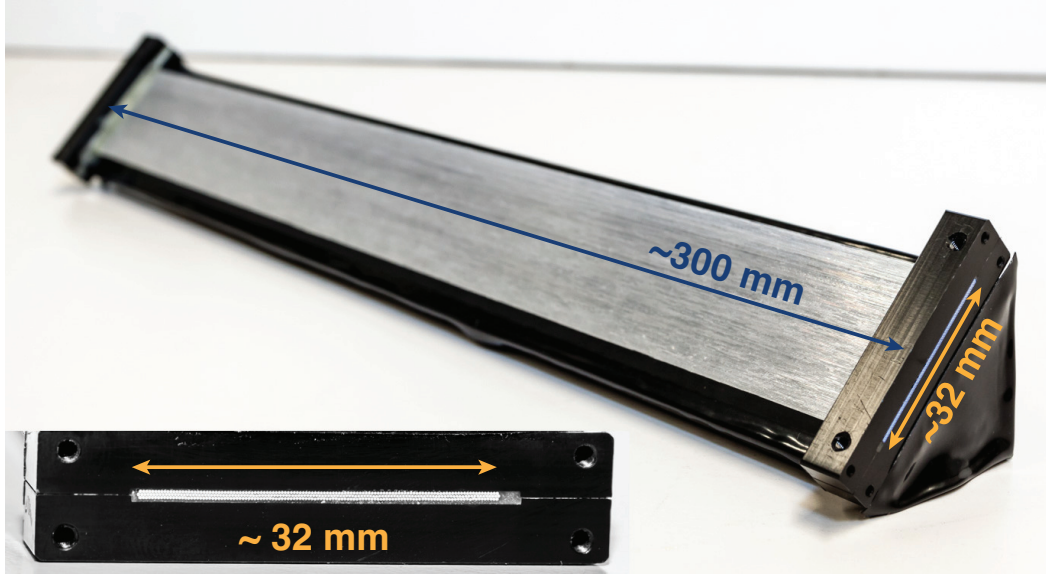
Figure 3.13 – A full size ribbon prototype produced for mechanical demonstration.

of 30 cm between the end pieces, the ribbon is between 35 cm and 38 cm. The empty space between the two target ends in the glueing version of the jig is equipped with a plate on which the ribbons is flattened and centered with respect to the upper and lower connector parts. A fast curing $\mathcal{O}($ 2-3 h) and high viscosity $\mathcal{O}(30\,\text{Pa} \cdot \text{s})$ epoxy such as ARALDITE 2011 fills in the space around the ribbon inside the connector. A thin layer is also applied at the interface between the upper and lower connector bracket. Metal clamps tighten the pieces in place while the epoxy hardens. Afterwards, the ribbon is cut using a heated saw to about 0.5 mm outside of the connector. The bottom fixation bar is then detached and the detector is stored for further processing.

A set of threaded holes at the front of the socket is used for mounting the optical sensors. Since the test samples are about 8 mm wide while the photosensors have an active width of 32 mm, several locations are foreseen such that different sections of the photosensor can be tested.

A full-size ribbon prototype with 4 fiber layers, a width of 32 mm and length 30 cm is shown in Fig. 3.13. It is intended as a mechanical prototype for the final ribbons and has not been used in any measurements.

3.3.2.3 REFLECTIVE PAINT

In an ideal environment, only fibers which lie directly on the trajectory of a traversing particle will output a signal. In the real world however, the fiber surfaces are imperfect which,

combined with the uneven distribution of the epoxy in the body of the ribbon, lead to optical cross talk between the staggered fibers. As a result, the detector granularity smears out and more channels produce an output. The occupancy of the detector increases which leads to an increase in the overall dead time of the system. Reflective coatings based on TiO_2 are often used to optically isolate scintillating components from each other [58, 59]. In an attempt to reduce the inter fiber crosstalk, a fine grained TiO_2 powder is mixed in the epoxy while building a ribbon. Once the solution is well mixed it is pressed through a filter to retain only grains with sizes bellow 5 µm. Applying the mixture evenly throughout the ribbon, however, could be achieved due to the very low amount of adhesive used in the production. Nonetheless, several samples are produced in order to measure the suppression of the cross talk. The baseline concentration is 20 % by mass i.e. 400 mg of powder are added to 2 g of epoxy. Since the effective atomic number of TiO_2 is $Z_{eff} \approx 20$, large concentrations are avoided because they deteriorate the momentum resolution of the pixel tracker due to increased multiple scattering.

Parallel to this work, another group from the Mu3e collaboration investigated the possibility of coating by sputtering individual fibers with a 100 nm thick layer of aluminum [50]. With that technology they have suppressed the optical crosstalk between fibers below 1 %. In comparison, the optical crosstalk measures in this work for ribbons prepared without any reflective compounds mixed in the epoxy is in the order of 25 %. The results from the characterization studies performed in this work and complemented by [48, 50, 51] indicate that the overhead of coating the fibers with aluminum outweighs the potential benefits.

3.3.2.4 NUMBER OF LAYERS

Lastly, the average angle at which particles will traverse the Mu3e fiber detector is $\mathcal{O}(22^\circ)$[48]. Hence the more layers a ribbon consists of, the more fibers will scintillate during a single event. The occupancy of both readout configurations is affected by the number of layers, however in the case of *single fiber readout* the number of readout channels and the data throughput also increase by 30 % when switching from 3 to 4 layers. Additionally, since measurements with *single fiber readout* did not produce convincing results to continue with that design, ribbons with 2, 3 and 4 layers have been produced only for the *column readout* setup.

3.3.3 EFFICIENCY CONSIDERATIONS

The efficiency of the full fiber detector is complex and depends on multiple components ranging from the intrinsic properties of the scintillating fibers and the photosensors, through the readout electronics and data acquisition, to the applied selection and analysis algorithms. The factors that can be controlled within the scope of this section, however, are related to the

optical coupling between the ribbons and the photosensors and the possible damages to the fibers during production.

3.3.3.1 Sources of damage during ribbon production

The 250 μm fibers are very delicate and precautions should be taken while manipulating them to build the ribbons.

Prolonged UV exposure can cause damage to the light yield of a scintillator, so all fibers used in the production of *column readout* ribbons are handled under filtered light. Wavelengths above 470 nm are suppressed by installing yellow SFLY5 Metolight foils on all light sources inside the clean room where the ribbons are constructed. The ribbons with *single fiber readout*, however, are produced without UV light protection.

Surface damage constitutes crack or scratches on the fiber surface formed as a result of excessive bending, scratching or chemical exposure. The ribbons with *single fiber readout* are most prone to breaking a fiber during the fanout process. To prevent that at least 15 cm are left for the loose fibers at the end of the ribbon. Once all fibers have been inserted at about 5 mm into the fanout connector, it is slowly moved towards the ribbon in steps of 5 mm to 10 mm. To prevent scratching of the fibers while inserting the fanout connector a small amount of low viscosity epoxy (the same as the on used in the body of the ribbon) can be applied on each fiber. The glue acts as a greasing agent. If a fiber gets stuck at some point and starts bending it is gently pulled with the help of tweezers clamping it near the end. Contact with the fibers between the staggered section and the fanout connector should be avoided due to the extremely high risk of breaking one or more of them. When the connector is secured by screws in its final position ample amount of epoxy is applied with a brush on its inner surface. The ribbon is turned vertically such that the glue can slowly flow through the holes with the fibers and seal them. The procedure is repeated on the other side once the epoxy is cured. Using a scalpel each fiber end is then trimmed to about 0.5 mm from the outer surface of the connector.

Scratching of the fiber surface can also occur when absorbing the excessive amount of glue after each layer. It is recommended to use a soft cloth with no lint and gently place it on top of the ribbon. Then using a flat plastic tool with a surface matching the width of the U-channel and a length of a 1-2 cm the cloth is pressed towards the ribbon to absorb the excess epoxy. The procedure is repeated until wet stains stop appearing on the cloth.

Finally, any cleaning of the fibers and ribbons before or after assembly should be done either with air or with a soft cloth and isopropanol. Clean water can also be used but it is ineffec-

tive in de-oiling. From the commonly used alcohols, ethanol is not recommended because it evaporates very fast while rapidly cooling the surface which can result in cracks. Additionally, grease from the fingers and palms degrades the plastic scintillators, so thee fibers should be handled with clean gloves.

3.3.3.2 OPTICAL COUPLING BETWEEN RIBBONS AND PHOTOSENSORS

A critical section in which light can be lost is the interface between the fibers in the ribbon and the photosensors. Poor geometrical alignment between the two could lead to photons escaping the sensitive surface of the optical sensors.

For both configurations realized in this text the active area of the sensors is significantly larger than the dimensions of the fiber holes or the ribbon thickness. The photodetectors used in the $single\ fiber\ readout$ have a sensitive area of 1.3×1.3 mm^2 (see subsection 4.3.1) while the diameters of the holes in the matrix connector are 0.3 mm. When soldering the optical sensor in a matrix on a PCB the margin of error in positioning is less than 100 µm, while the machining of the holes has a tolerance of 50 µm. Hence, even in the worst case scenario with opposite misalignment in both parts the fiber will still be sufficiently covered by the photosensor.

In case of the $array\ readout$, the sensitive surface of the optical sensor is 1.625×32.5 mm^2 (see subsection 4.3.2), while the dimensions of the largest tested sample are 1.0×9.0 mm^2. Variations in the positioning of the ribbon with respect to the photodetector can reach a maximum of 200 µm which is still within the acceptable limits of the sensor.

It should be noted that in both configurations the fibers are interfaced with the photosensor by mechanical contact only without any mediating substances such as optical grease or silicon pads. This means, that if a thin layer of air is left between the two, following the rules of geometrical optics, the angle of the photons exiting the fiber can reach up to $\sim 45^\circ$. As a result, the photons will be detected in a circle of larger radius than the fiber one depending on the distance to the active surface of the photosensor. Additionally, since the interface is mechanical imperfections on the surface of the fibers can lead to photons being scattered back into the fiber or away from the sensor. To minimize such type of loss the surface of the fibers coupling with the photosensors should be polished to a mirror like state. To achieve that the connectors is both configurations are first flattened in a milling machine with a sharp blade.

In case of the $single\ fiber\ readout$, the surface is then polished in three steps on a spinning machine using abrasive liquids with gradually diminishing grain sizes. At the first stage, an abrasive liquid from BIODIAMANT with a maximum particle size of 9 µm is applied on TOUCH-LAM 2TS1 polishing cloth [60]. It is a fine cloth made of natural satin-woven fibers. The socket

is polished for 7 mins at 200 rpm. Then the second stage is initiated using another abrasive liquid with maximal size 3 μm and a separate cloth plate covered with an identical silk surface. It is performed with the same angular speed of 200 rpm and lasts for 7 mins. Finally, a fine compressed wool surface TouchLam 2FL1 polishing cloths impregnated with a liquid abrasive with grains smaller than 1 μm is used to achieve a glossy surface. The large area of the fanout connector (4×5 cm^2) coupled with the long lever of the ribbon (≈ 40 cm) complicate the process . Even though a support structure is used to maintain the connector flat and parallel to the spinning disks, often minor misalignments are observed and the surface is not uniformly polished.

Following the troublesome experience with the $single\ fiber\ readout$ ribbons, a new solution is proposed for the treatment of the $column\ readout$ ribbons. After consultations with experts in the $LHCb$ SciFi collaboration, it was decided to finish the connectors with a sharp diamond tool on a computer numerical control (CNC) machine, completely eliminating the need of polishing with abrasive substances. With some experimentation the following procedure is established:

- Use a thermal cutter to pre-cut the extra fiber length coming out from the SiPM mounting connector. The cutting is at about 1 mm from the surface of the connector to avoid melting the fibers glued inside it.

- A single tooth diamond tool as shown in Fig. 3.14, is placed in contact with the end piece surface. The cutting element of the tool is a mono crystal from Wirz Diamant [61]. It is mounted on a lever at about 60 mm from the rotation center.

- With the particular CNC machine used for the polishing, a single axis translation of the ribbon is used to machine the whole surface. The extra fiber and epoxy are removed maintaining uniform speed of 200m/min as recommended by LHCb.

- Lastly, one or two finishing passes with 50 μm steps are performed.

- No lubricant is applied while machining, only dry cutting.

A photo of the diamond bit installed on a CNC machine with a ribbon being processed is shown in Fig. 3.14.
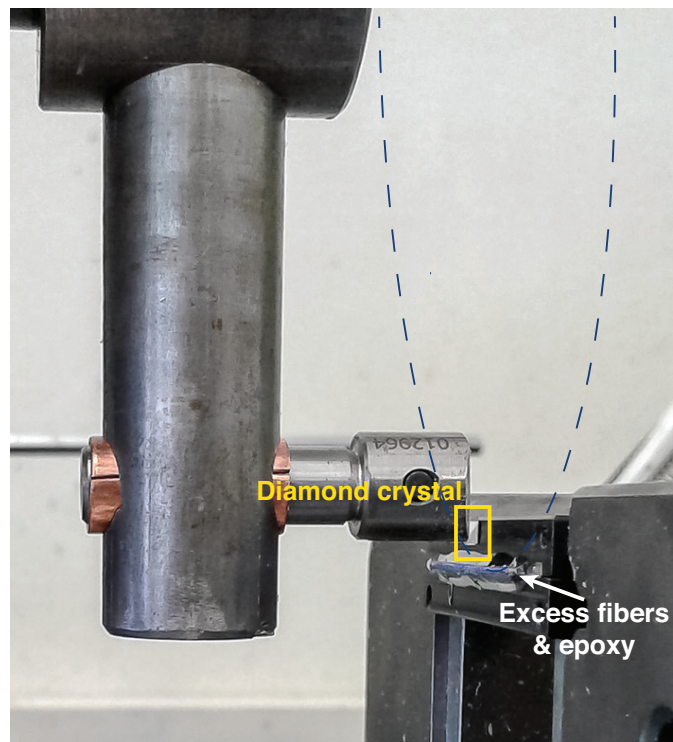
Figure 3.14 – A diamond tipped tool installed on a CNC machine with a ribbon surface being machined.

4

Silicon Photomultipliers

Silicon photomultipliers (SiPM) are solid state photon detectors. They have seen rapid development in the past two decades, partly due to the advances in the semiconductor technology and mainly due to the idea of stacking together multiple avalanche photodiodes operated in Geiger mode. The SiPMs have reached a mature state and nowadays offer high gain $\mathcal{O}(10^6)$, low time jitter $\mathcal{O}$(few 100 ps), single photon sensitivity, photo-detection efficiency (PDE) in the order of 40-50 % [62], insensitivity to magnetic fields and low operational voltages $\mathcal{O}$(50 V), while maintaining a very compact size at a reasonable price.

Due to the tight space constrains, low light flux, strict timing requirements and strong magnetic fields required for MU3E, SiPMs represent the only viable technology for the readout of the scintillating fiber and tile detectors. This section summarizes the basics of silicon photodetectors as discussed in [62–64]. Following is a description of the particular SiPM configurations used for the readout of the scintillating fiber ribbon prototypes described earlier.

4.1 PRINCIPLE OF OPERATION

The electrons in a semiconductor are divided in two groups by the energy domains they belong to, namely a valence and a conduction band. In the former they are bound to the crystal lattice unable to move around, while in the latter they are free to conduct current under an electric field. The energy separation between the two regions is called a band gap and is a crucial characteristic of a semiconductor. It represents the minimal amount of energy that an electron from the valence band needs to receive in order to get excited to the conduction band. Typical values in the most ubiquitous semiconductors are 0.66 eV for germanium (Ge) and

1.12 eV for silicon (Si) [65]. Electrons from the valence band in semiconductors with smaller band gaps need less energy to move into the conduction band. However, they are susceptive to unwanted thermal excitations manifesting as increased noise levels in the semiconductor.

With a sensitivity spanning over the full visual spectrum and a lower noise factor, Si based photodetectors are applicable for the readout of scintillating and Cherenkov light emitters.

The foundations of all solid-state photodetectors lie in the properties of a the junction formed at the boundary of a positively (p-type) and negatively (n-type) doped semiconductors. A p-type semiconductor is formed by replacing atoms in the crystal lattice of pure silicon with atoms of the elements from the IIIrd chemical group e.g. boron. The net effect is an excess of positive charge carriers called holes h. By introducing impurities of atoms from the Vth group e.g. phosphorus or arsenic, a surplus of negatively charged carriers (electrons) is created, resulting in an n-type semiconductor. When the two regions are put in contact with each other, electrons from the negatively doped side diffuse into the positively doped one and a region depleted of charge carriers is formed. The potential difference which builds up at the two sides of the joint eventually stops the recombination of carriers and the net current flow ceases (see Fig. 4.1). If an external field with a reversed polarity [1] is applied on the two sides of the junction the width of the depleted area expands as electrons tend to move toward the positive potential and away from the junction point, and vice versa for holes. A photon incident on the depletion zone interacts with a valence band electron and transfers energy to it via the photoelectric effect. When the amount of energy received is sufficient to overcome the band gap the charged carrier excites into the conduction band and is free to move under the external electric field. Consequently, a current starts flowing through the pn junction. The amplitude of the current is a measure of the incident light intensity.

4.1.1 PN and PIN Photodiodes

The most basic photodiodes are the pn diodes. They consist of a single junction formed between heavily doped p^{++} and n^{++} semiconductors. The pn diodes operate in a regime with inverted polarity of the applied voltages. The output current is proportional to the intensity of the incident light. For longer wavelengths the absorption length i.e. the depth at which $1/e$ of the initial photon flux is absorbed in the silicon, is longer - necessitating a wider sensitive area. The width of the depleted regions can be increased by inserting a silicon crystal with high purity and low number of free charge carriers between the positively and negatively doped sections. This material is known as $intrinsic$ silicon (i). The resulting photo diode Fig. 4.2 is called a PIN ($p-i-n$) diode. This device has no amplification (its gain is unity) meaning that

---

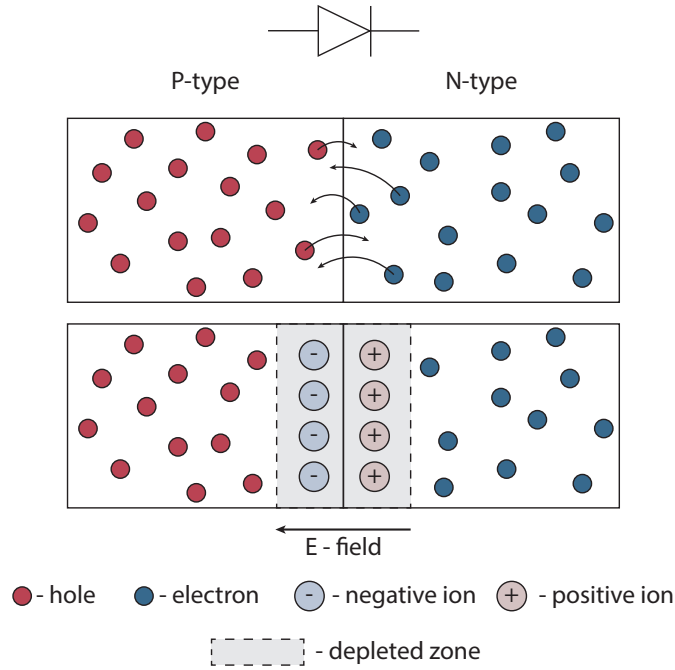[1]Reversed with respect to the dopant type.

Figure 4.1 – The excess of free electrons in the n-type semiconductor and holes in the p-type cause drift of the respective carries to the section with lower concentration. As a result, negative and positive ions are formed where holes (h) and electrons (e) have been replaced in the crystal lattice by the opposite carrier. The net effect is a volume depleted of free charges and a build-up of an electric field around the junction due to the newly formed ions.

the number of charge carriers is determined only by the intensity of the incident light flux and the number of electron-hole pairs created when photons interact in the sensitive volume. It offers high stability, but due to the lack of internal gain a light flux of at least a few thousand photons is required to achieve good signal to noise (S/N) ratio [65].

4.1.2 AVALANCHE PHOTODIODE

A step forward in increasing the light sensitivity is obtained with the avalanche photodiode (APD) - a semiconductor device with a more complex structure. It comprises a detection and an amplification stage, leading to internal charge multiplication in the order of a few tens to a few hundreds. A valence electron excited to the conduction band by interacting with an incident photon is called a photoelectron. Once produced, it gains momentum in a high intensity electric field inside the depleted zone, see Fig. 4.2, and generates additional electron-hole pairs by impact ionization[2]. The secondaries in turn also accelerate in the potential difference and

---

[2]Holes can also trigger an avalanche, however the ionization coefficient is lower compared to the electrons [66], hence the electrons are the primary avalanche triggers.
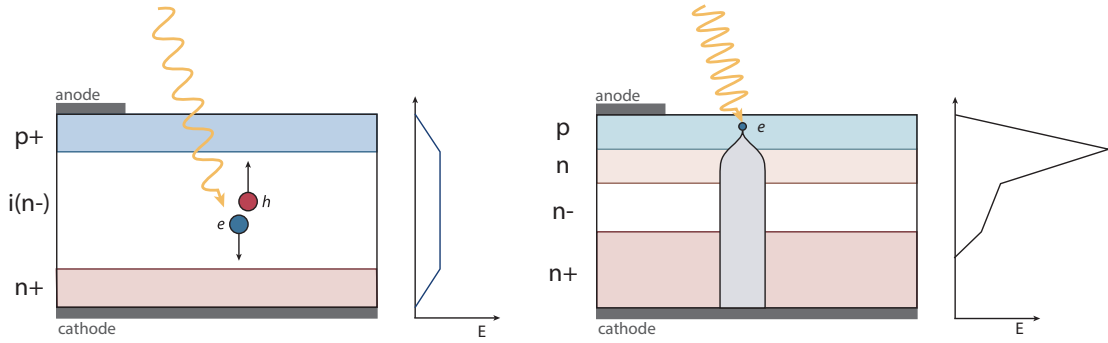
Figure 4.2 – Schematic of the electric field and doping of a PIN diode (Left) and an APD (Right). In the former the electrons and holes drift towards the cathode and anode without multiplication. In the later an avalanche proportional to the incident light flux is triggered by the electrons under the high intensity electric field at the PN junction.

produce additional free charge carriers. In the schematic shown in Fig. 4.2 the APD structure is optimized for short wavelengths in the order 420-450 nm. Photons interact with the lattice electrons in the upper section of the p layer. An avalanche is formed around the pn junction and the multiplied number of carriers than drifts through the $n^- - n^+$ section. The role of the n^- layer is to reduce the device capacitance as well as the gain dependence on the bias voltage [67]. Typically, n on p structures are used for longer wavelengths, where the absorption happens deeper into the p^- silicon. The produced photoelectrons then drift towards the junction to subsequently trigger an avalanche. The phenomenon occurs only if the electric field passes a threshold of 1.75×10^5 V/cm for electrons and 2.5×10^5 V/cm for holes in silicon [63]. The response of the device is linear with the intensity of the incident photoelectrons, however due to the indeterministic character of the avalanche process, an inherent noise manifested by the variance of the gain is observed in the signal. The avalanche multiplication factor increases with the field strength, however, it becomes unstable for values above a few hundred since both the voltage and temperature should be strictly controlled to avoid breakdown. State-of-the-art APD are capable of detecting single photons, however their S/N ratio is affected by environmental fluctuations and they need additional amplification stages for the small current generated by a single photon.

4.1.3 GEIGER MODE APD

To achieve higher single photon detection efficiency an APD can be operated in the so called Geiger mode - a regime in which the diode is reversely biased above the breakdown voltage V_{bd}) (see Fig. 4.3).

Under such conditions both an electron and a hole trigger a discharge while accelerating
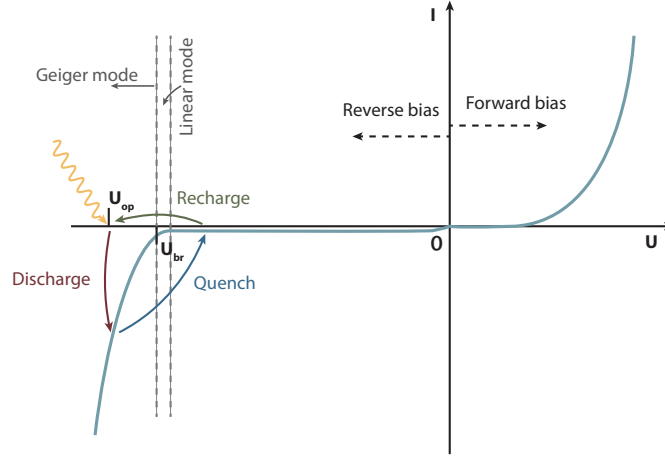
Figure 4.3 – Biasing scheme of APD cells with an accent on the processes undergoing during Geiger mode operation. When a cell is biased above the breakdown voltage, a photon interacting in the active volume triggers a Geiger discharge which is subsequently quenched via a resistor. As a result, the electric field over the PN junction drops and a short recovery time is necessary before new avalanches can be formed.

towards the anode and cathode, respectively. The high electric field ensures the process is self-sustaining and an increasing number of carriers flows continuously through the device once an avalanche is set off. This phenomenon is known as a Geiger discharge, hence the name Geiger-mode APD or G-APD. To allow detection of subsequent photons the avalanche must be stopped. A quench resistor (R_q) placed in series with the diode interrupts the chain reaction by reducing the voltage difference (V_d) over the junction when the current flow (I) increases:

$$V_d = V_{bd} + \Delta V - I \times R_q \tag{4.1}$$

where ΔV is the voltage applied over the breakdown voltage. The recovery time of the sensor is expressed in terms of the quenching resistor as $1 - e^{\left(-\frac{t}{R_q C}\right)}$ with C being the effective capacitance of the pn junction [3]. Therefore, a large resistor is beneficial for quickly inhibiting the avalanche, but has a diminishing effect on the recovery time. As a result the device performs with a longer dead time and cannot handle very high signal rates. G-APDs are competitive in single photon sensitivity to traditional photomultiplier tubes (PMT). Moreover, the G-APDs exhibit very high gain, in the order of 10^6. However, they are incapable of distinguishing between one or several incident photons if a discharge has started i.e. they are binary devices. Additionally, it is difficult to maintain large depleted areas while biased at high

---

[3]More details about the electric representation of a G-APD cell will be provided in section 4.2.

voltage due to the high probability to thermally excite electrons in the conduction band.

4.1.4 Silicon Photomultiplier

The silicon photomultiplier (SiPM), also known as a multi-pixel photon counter (MPPC), overcomes the limitations of the single cell G-APD by using a matrix of such elements in microscopic sizes grown on a monolithic silicon crystal. With this technology all pixels[4] are biased via a common cathode, while the readout is realized through a parallel connection of the individual cells, Fig. 4.4.
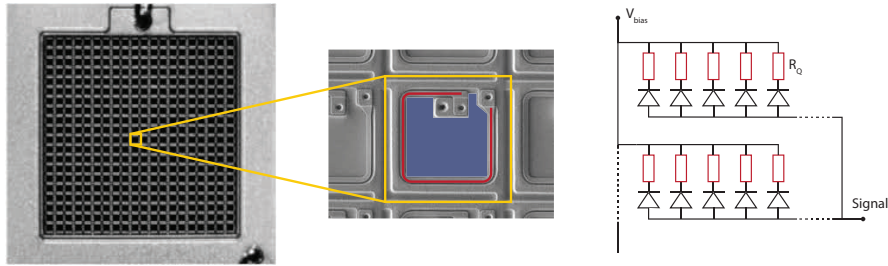
Figure 4.4 – Each cell of a single channel SiPM device can be simplified as a diode in series with a quenching resistor. A matrix of cells connected in parallel constitutes a single channel SiPM. A practical realization of the quenching resistor R_Q (—) is marked on the microscopic image of a single G-APD cell. The shaded zone (—) marks the photosensitive area of the cell. Figure adapted from [62].

The advantage of this configuration is that each cell produces a signal independently of the others and is individually sensitive to photons, hence the resulting device offers a wide dynamic range, while being sensitive to the lowest intensity light sources.

A more detailed realization of a SiPM is shown in Fig. 4.5 [62].

Photons in the blue range are absorbed in the first micrometer of the p^+ doped silicon and the electrons from the resulting electron-hole pairs accelerate in the field of the pn junction triggering a Geiger discharge in the depleted area between them. A thin layer of SiO_2 insulator which has excellent transparency for visible and UV light serves as a protector against damages on the doped silicon. The guard rings (p) around the avalanche area prevent formation of excessive electric fields and undesired discharges. The thick n layer ($\approx$ 300μm) makes the device more sturdy and easier to handle during and after production. The latest developments in the SiPM technology have seen the introduction of opaque trenches between the individual cells which reduce optical crosstalk.

4.2 Features of a SiPM

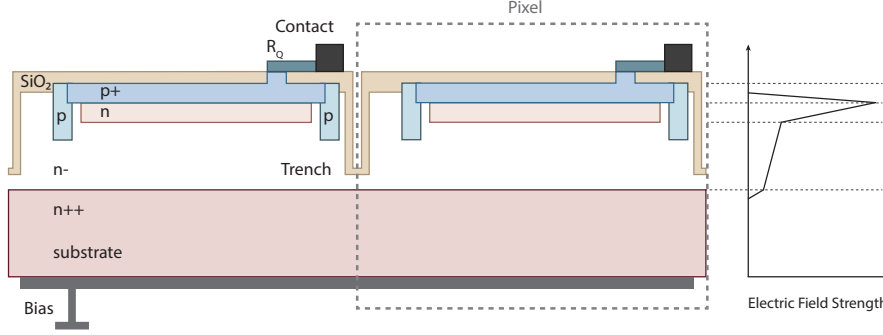[4]A G-APD cell in a SiPM matrix is often referred to a pixel or a microcell

Figure 4.5 – Detailed realization of G-APD cells arranged in an SiPM channel. The doping scheme is optimized for short wavelengths where photons interact in the upper section of the p^+ layer. Trenches between the individual cells are introduced to reduce optical crosstalk, while the SiO_2 coating protects the doped silicon layers. Anti-reflective coating consisting of layers with gradually increasing refractive indices is deposited on top of the SiO_2 to ensure maximal light transmission at the interface with the fibers. A thick substrate is used for production and handling purposes, as well as to improve the contacts with the electrode.

4.2.1 GAIN AND PULSE SHAPE

The avalanche process in a Geiger mode operated APD is such that the discharge always produces an output with a small fluctuation around the number of carriers irrespective of the triggering particle. The gain or multiplication factor of a single cell is in the order of $10^6 - 10^7$ electrons per discharge and depends only on the over-voltage $\Delta V = V_{bias} - V_{bd}$ biasing the pn junction and the pixel's capacitance C_d:

$$M_d = \frac{C_d \times \Delta V}{q_{electron}} \tag{4.2}$$

$q_{electron} = 1.6 \times 10^{-19}$ is the electron charge, while a typical junction capacitance ranges from a few tens to a few hundreds of pF.

A simplified representation to a G-APD equivalent circuit and the resulting output signal is shown in Fig. 4.6.

Initially the junction capacitor C_d is biased at V_{bias} and no current is flowing through the diode reflected in the schematic through the opened state of the conceptual switch S. When a photon or thermally excited electron triggers an avalanche the switch "closes" and the junction capacitor starts discharging via the series resistance R_s from V_{bias} down to V_{bd}. The output current grows exponentially with a time constant $R_s \times C_d$ until the voltage after the quenching resistor equates the breakdown voltage and the switch transitions in an open state. The junction capacitor recharges via the quench resistor at a much slower rate given by the time constant $R_q \times C_d$. During the so called recovery time when the capacitor is not fully charged,
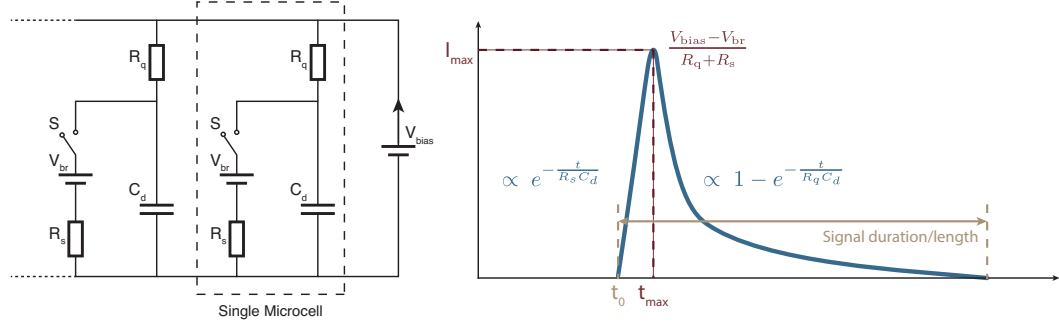
Figure 4.6 – A simplified circuit of a G-APD microcell (Left) and a sketch of its output signal (Right). If several cells in an SiPM are triggered simultaneously, the output is a linear sum of all microcell responses.

a photon can trigger an avalanche but it will have a reduced amplitude proportional to the difference in voltages between V_{bd} and the voltage over C_d. In this case, the probability to trigger an avalanche is also reduced. When several pixels fire[5] simultaneously, the total output of the SiPM channel is a direct sum of the individual microcell amplitudes.

4.2.2 DYNAMIC RANGE

If more than one photon interacts in a given pixel while a discharge is ongoing the cell will not be able to produce a distinguishable signal. To obtain a wide dynamic range i.e. being capable of counting multiple photons incident simultaneously, a SiPM should have high pixel density compared to the expected light flux. Provided that the incident photons are uniformly distributed and their number N_{ph} is much smaller than the number of pixels N_{pix} the output of the device will be to a good approximation linear in N_{ph}. This proportionality is lost, however, when the incident light becomes too intense. The response of the detector in terms of fired pixels N_{fired} is:

$$N_{fired} = N_{pix} \cdot \left[1 - e^{-\frac{PDE \cdot N_{ph}}{N_{pix}}} \right] \tag{4.3}$$

where PDE is the photo-detection efficiency. The above formula is only valid under the assumption that light is impinging homogeneously on the SiPM within a short interval of time compared to the recovery time and all noise contributions are neglected.

---

[5]Produce an avalanche discharge

4.2.3 Photo-detection Efficiency

The photo-detection efficiency of a G-APD depends on the applied over-voltage, the incident light's wavelength and the geometrical characteristics of the cell:

$$PDE(V_{ov}, \lambda) = \varepsilon_{QE}(\lambda) \cdot \varepsilon_{FF} \cdot \varepsilon_{Av}(V_{ov}) \tag{4.4}$$

$\varepsilon_{QE}(\lambda)$ is the quantum efficiency for a photon of a given wavelength interacting in silicon to generate an electron hole pair. For the emission spectra of the scintillating fibers used in this work the QE is about 80%. Geometrical inefficiencies encoded in ε_{FF} arise from various contributions which reduce the available active area e.g. quench resistors, spacing between the individual cells necessitated by the width of the guard rings and trenches. A microscope image of a single cell with an active area of $25 \times 25 \ \mu\text{m}^2$ is shown in Fig. 4.4. The absolute size of the elements causing ineffective or dead areas is almost constant for pixels of different dimensions, hence larger area cells have higher geometrical efficiency or better fill factors. Smaller pixels allow higher densities resulting in better dynamic range, however, the overall PDE drops and a compromise should be reached based on the concrete application. The average dimensions of cells used in the present work are in the order of $50 \times 50 \ \mu\text{m}^2$ and they have a fill factor in the order of 70 %. The last term in the equation, $\varepsilon_{Av}(V_{ov})$, accounts for the probability of a charge carrier to trigger an avalanche. Under normal conditions of operation, it approaches 1.

4.2.4 Dark Counts and Afterpulsing

When an avalanche is triggered in the absence of incident photons the output signal is called a dark count. Thermal excitation or quantum tunneling of electrons are the usual sources of such events. In the former, an electron gains sufficient energy via interaction with phonons in the crystal lattice and excites into the conduction band. The probability for occurrence of this process surges with inferior purity of the silicon and higher temperatures. In the case of quantum tunneling, electrons from the valence band of the p layer can tunnel through the pn-junction into the conduction band of the n layer generating free carriers. This is the dominant effect at higher electric fields around the junction and it is independent of the ambient temperature. Another contribution to the dark counts originates from the trapping of charge carriers formed during an avalanche into impurities of the lattice. They get released at a later moment, typically a few hundred nanoseconds after being captured, and also trigger a discharge, hence the name afterpulse. A large quenching resistor can mitigate the effect of an afterpulse due to the increased recovery time, however, it also amounts to a longer dead time for the detector. For modern day SiPMs the rate at which dark counts are generated at room

temperature (25°C), including afterpulses, is in the order of 100 kHz/mm^2 and it doubles for approximately every 5°C rise in temperature [62].

4.2.5 OPTICAL CROSSTALK

During a Geiger discharge, long-wavelength photons are being emitted with a probability of 2.5×10^{-5} alongside charge carriers [68]. The absorption length of these photons in silicon is sufficient for them to travel around and reach the active area of a neighboring pixel. If they interact in the high-intensity field region of a cell, they can immediately initiate an avalanche that will be indistinguishable in the output from another incident photon interacting simultaneously in a different pixel. This undesired phenomenon is called a prompt or a direct crosstalk. In the event that the secondary photon interacts in the drift region of a neighboring cell the triggered avalanche will be delayed in time and some post-processing algorithms might be used to discriminate the delayed crosstalk from true signals. To reduce crosstalk in state-of-the-art manufacturing technologies opaque trenches have been introduced between the individual SiPM cells.

4.2.6 TIME RESOLUTION

The SiPMs are characterized by inherently good time resolving capabilities due to their compact size and fast Geiger discharge. Their intrinsic time resolution depends mainly on the over-voltage generating the high intensity electric field in the avalanche region. A parameter called single photon time resolution (SPTR) is the figure of merit used to estimate the effectiveness of a SiPM to determine the arrival time of a single photon. Different groups have demonstrated excellent SPTR of Hamamatsu S13360 with cell size 50 μm × 50 μm: FWHM = 220 ± 7 ps and FWHM = 158 ± 7 ps for over-voltages of 6.1 V and 10 V, respectively. The time resolution improves with the amount of incident light due to the statistical nature of photon detection in SiPM and FWHM in the order of 50 ps is achievable in such conditions [38].

4.3 SiPM READOUT CONFIGURATIONS

Two types of SiPM have been used in this work. For the single fiber readout, a matrix of individual single channel devices has been assembled, while for the column readout - monolithic multichannel arrays have been procured from Hamamatsu.

4.3.1 SINGLE FIBER READOUT

Hamamatsu S12571-050P MPPC in surface mount packages have been soldered in a 4×4 matrix configuration on a custom designed PCB (Fig. 4.7). All 16 devices are powered via a common high voltage line on the PCB with a possibility to vary the individual bias voltages within ± 0.5 V around the baseline by soldering resistors in series with the power supply line [48]. The sensors, nevertheless, have been grouped such that their recommended operational voltages lie within ± 0.2 V of the reference voltage and no individual tinkering of the bias voltage was applied. Four such boards are used to readout 32 channels on each side of a fanned-out ribbon.
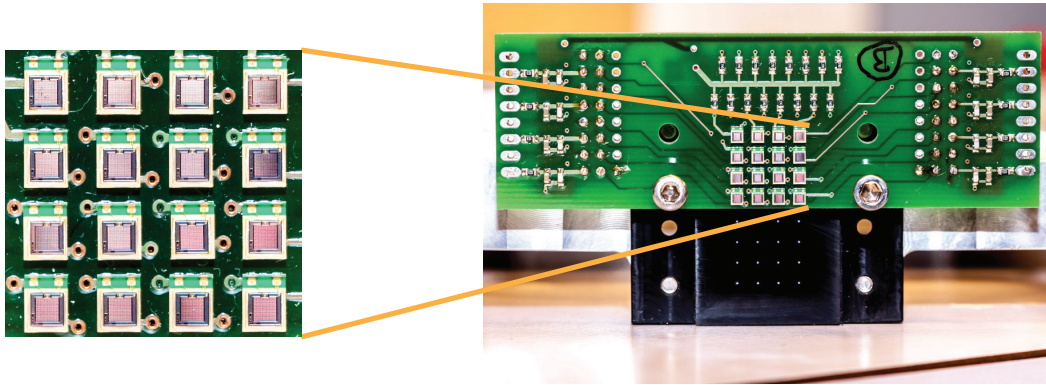
Figure 4.7 – A photo of a 4×4 matrix assembled with 16 S12571-050P MPPCs. All sensors are biased via a common voltage source while the signals are individually transmitted to an amplifier.

The active area of each sensor is 1 mm$\times$1 mm and they have been aligned within 100 μm to the fibers fanout connector. With 400 cells per channel they offer wide dynamic range and PDE in the order of 35 %. The chosen sensors have reduced afterpulses compared to the previous generation of Hamamatsu SiPMs. However, due to the lack of trenches [6] between the pixels, the crosstalk in each channel is in the order of 30 %. This number is about three times higher than the cross-talk reported for the SiPM arrays described in 4.3.2. The most notable characteristics of this class of photosensors are summarized in Table 4.1.

4.3.2 COLUMN READOUT

High density arrays consisting of two silicon dies with 64 channels per die mounted in a single package (see Fig. 4.8) are used for the column readout of the scintillating fiber ribbons.

---

[6]At the time of purchase (circa 2013) this was the state-of-the art technology and trenches were yet to be introduced.
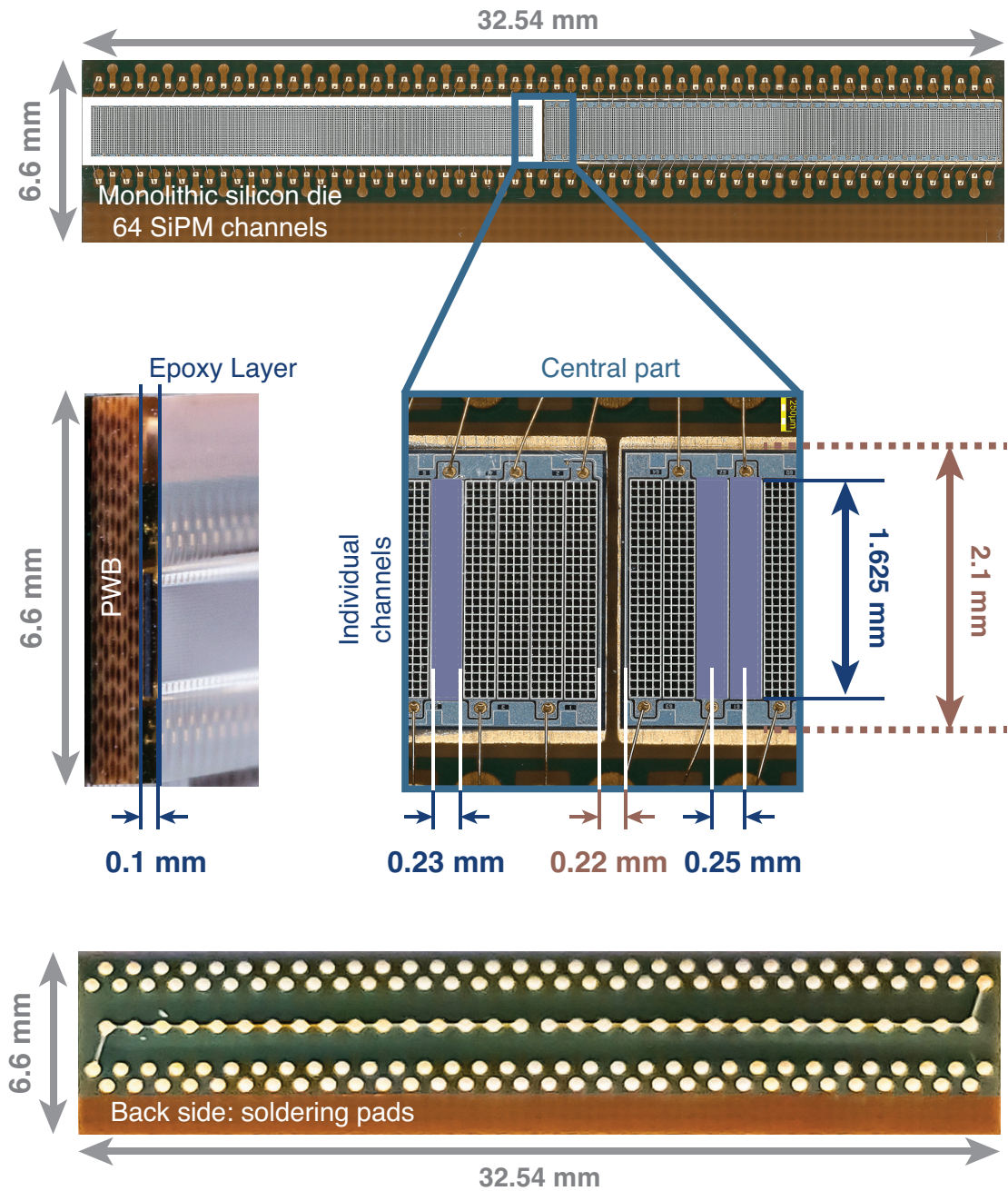
Figure 4.8 – Picture of a Hamamatsu S13552 HQR SiPM array. Two such devices are used for the column readout of the SciFi ribbons discussed in chapter 7. The Mu3e experiment will use 24 such sensor to readout 12 fiber ribbons on both sides.

Parameter per channel	S12571-050P	S10943-3183(x)	S13552-HRQ
Photosensitive area	1 mm × 1 mm	230 μm × 1500 μm	230 μm × 1625 μm
Pixel size	50 μm × 50 μm	57.5 μm × 62.5 μm	57.5 μm × 62.5 μm
N Pixels / channel	20 × 20	4 × 24	4 × 26
Geometric fill factor	62	75 %*	75 %*
Refractive index	1.55	1.55	1.55
Peak sensitivity wavelength	450 nm	480 nm	480 nm
Photo-detection efficiency	35 %	35 %	$\geq$ 40 %
Dark count rate	100 kcps	125 kcps	125 kcps
Gain	1.25×10^6	2.5×10^6	3×10^6
Recommended V_{op}	V_{br} + 2.6V	V_{br} + 3.5V	V_{br} + 3.5V
Cross-talk probability @ V_{op}	30 %	16 %	8 %

Table 4.1 – Summary of MPPC parameters for a single channel of S12571-050, S10943-3183(x) and S13552-HRQ. (*) The fill factor is extrapolated from the fill factors of square cells with size 50×50 μm^2.

Each channel of the Hamamatsu S13552-HRQ SiPMs has 4×26 pixels with dimensions 57.5 μm $\times 62.5$ μm and a gap between them of 20 μm occupying an area of 230 μm $\times 1625$ μm. They have been designed to match the granularity of the fibers with a diameter of 250 μm. The two dies are wire bonded on a single Printed Wiring Board (PWB). Soldering pads are foreseen on the backside of the PWB (see Fig. 4.8) and a 100 μm thick layer of epoxy is deposited on the front to protect the wires as well as to guarantee flat surface for coupling with the scintillating fibers.

From electrical point of view, the channels from each die share a common cathode. The optical crosstalk has been suppressed below 10 % through the implementation of the LCT5 technology with trenches in the pixel matrix and increase in the quenching resistors values to stabilize the high electric field and reduce uncorrelated noise. Using IV curves (see Fig, **??**), the variation in the breakdown voltage over 128 channels of a single device is measured at ± 0.3 V (see Fig. 4.10 (Left)), while the quenching resistors exhibit the pattern shown in Fig. 4.10 (Right).

Four SiPM arrays are characterized in terms of breakdown voltage, quenching resistor and cross talk probability within the scope of this work and the obtained results are consistent with observations made in [69].

Fig. 4.11 pictures the assembly between a SiPM array soldered on a custom PCBs developed at UNIVERSITY OF GENEVA and the fiber connector. The PCBs connect the SiPM arrays to flex prints which carry the signals out.
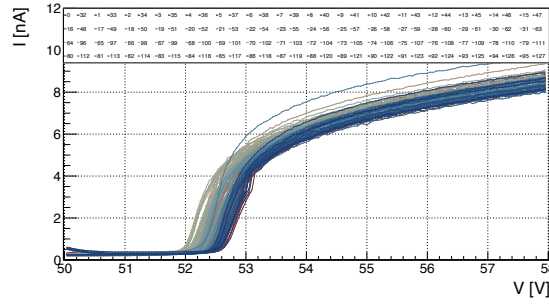
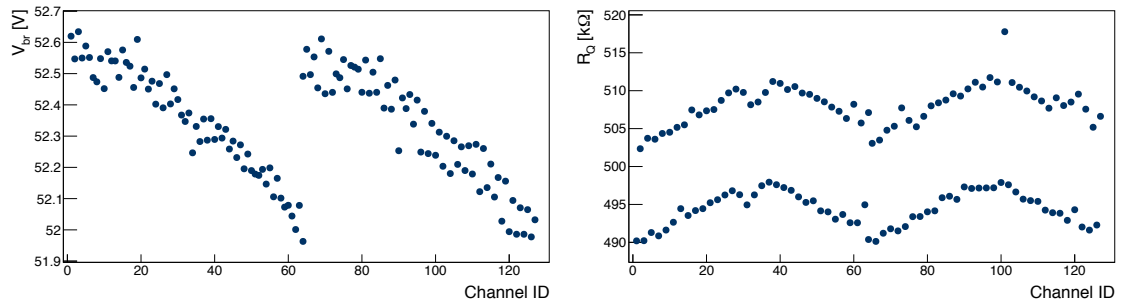**Figure 4.9** – IV curves at reverse bias of 128 channels of a Hamamatsu S13552-HRQ.

Figure 4.10 – Breakdown voltage (Left) and quenching resistor (Right) values measured for all 128 channels of a Hamamatsu S13552-HRQ. The repetitive pattern is due to the two dies constituting a single device.
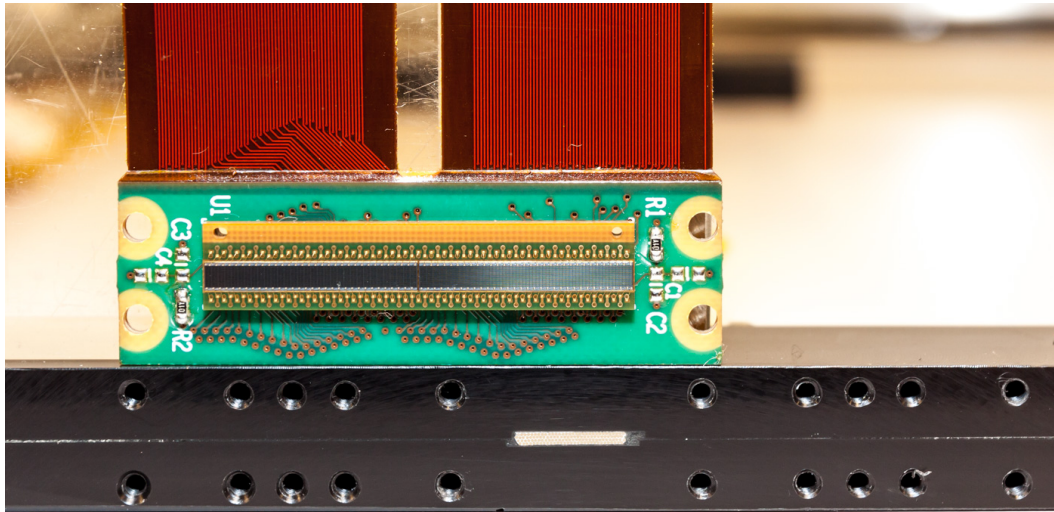

Figure 4.11 – Assembly between SiPM arrays mounted on custom PCBs and the fiber ribbon prototypes built and characterized within the current work.

4.4 SIGNAL AMPLIFICATION

The amplitude of a single cell discharge converted to voltage is in the order of 1 mV when the electron discharge is drawn over a shunt resistor of about $\approx 50~\Omega$. The data acquisition systems employed in this work require signal amplitudes in the order of a few tens of mV per photoelectron. Since the rise time of the signals is crucial for the time measurements a fast transistor-based amplifier is employed to magnify the amplitudes. The input stage of the amplifier is modeled according to the circuit shown in Fig. 4.12. It represents the electric equivalent of a SiPM channel with N cells [70].
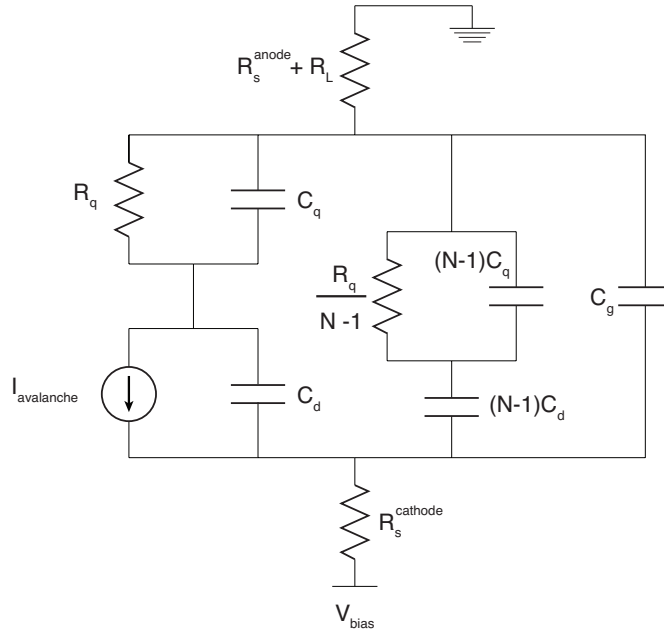
Figure 4.12 – Equivalent circuit of an SiPM with large number of N parallel-connected Geiger mode APD [70]. The values provide by the vendor HAMAMATSU for the S13552 HQR are the following: N = 104, C_d = 115 fF, C_q = 18 fF, C_g = 1 pF, R = 470kΩ, $R_s^{cathode}$ = 0.5 Ω and R_s^{anode} = 1.5 Ω.

The reported parameters are provided by the vendor and show good agreement with measurement obtained here and in [69]. A detailed discussion on the particular amplifiers used for the tests performed in this work as well as SPICE simulation results on the circuit are available in [48]. The components of the amplifier are optimized for rise-time in the order of 1 ns and recovery time of $\mathcal{O}(\lesssim 100~\text{ns})$. The gain is controlled by the collector voltage and typical values of 30 dB to 40 dB have been used where the figure of merit is the desired output amplitude with a magnitude of $\mathcal{O}(50~\text{mV/ph.e.})$. A modular system with pluggable amplifiers for each channel has been designed at the UNIVERSITY OF GENEVA for the column readout, Fig. 4.13.
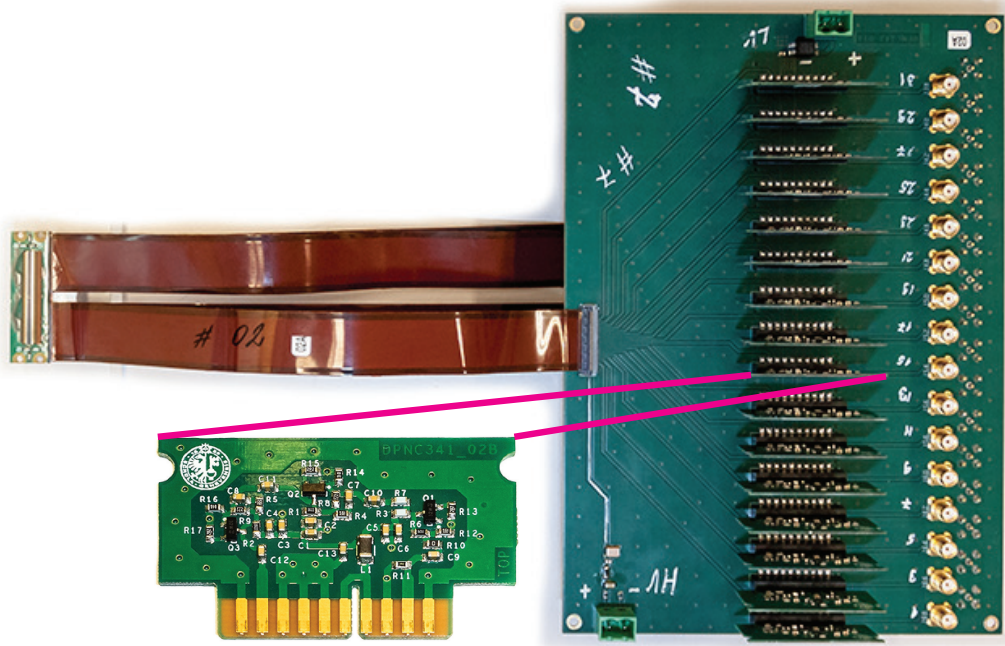
Figure 4.13 – A photo of the modular amplifier PCB developed for the array SiPMs. The board houses 32 plug-gable amplifiers, 16 on each side. A Hamamatsu S13552 array soldered on a custom PCB with four flex prints, each carrying 32 signal lines, is also connected to the amplifier board.

5

Signals Digitization

The present chapter describes the electronics components and data acquisition systems used to study the performance of the various SciFi ribbon prototypes characterized in this work. The first section is dedicated to the electronics employed in the measurement of ribbons with single fiber readout. Conventional electronic modules such as constant fraction and leading edge discriminators, charge and time to digital converters are used. For the column readout, on the other hand, a novel waveform digitizing board developed at the UNIVERSITY OF GENEVA is employed. It samples the individual waveforms from every channel and stores the full information for subsequent analysis. The author developed the software for data acquisition systems used in all measurements both with the conventional electronics and with the new waveform sampling boards. The last section describes the MuTRiG ASIC that will be used in the Mu3e detector.

5.1 CONVENTIONAL ELECTRONICS

The data acquisition systems employed in this work rely on trigger signals to initiate signal digitization and subsequent data transfer to a host computer.

In the early development stage the SciFi ribbon prototypes with single fiber readout are evaluated with a measurement setup featuring conventional electronics for particle physics experiments. In particular, for the digitization chain, the analog SiPM signals are split into two parts. One fraction is sent to a charge to digital converter (QDC) that integrates the voltage signal over a fixed period of time. The other fraction passes through a constant fraction discriminator (CFD) and enters a time to digital converter (TDC). The TDC measures the time

difference between the arrival of the discriminator output and some other reference signal e.g. the trigger signal. The digitized data is subsequently transferred to a computer for further processing, storage and analysis.

The data acquisition system can be structured in three sections: trigger, digitization and data transfer.

5.1.1 Trigger Logic

The idea of the trigger signal is to synchronize the time when data is digitized with an actual physical event i.e. a beam particle traversing the detector system. Two measurement configurations are realized within this work, see Fig. 6.1 and Fig. 7.1. In both cases pairs of crossed scintillators coupled with photomultiplier tubes are located downstream the beam axis and serve as triggers. They are labeled $PMT\,1$ and $PMT\,2$.

The outputs from the PMTs are processed through a chain of NIM[1] modules, see Fig. 5.1 $TRIGGER$. At first the signals pass through independent channels of a rise-time compensated leading edge discriminator (LeCroy 825E). The amplitude threshold is set well above the noise level such that an output is generated only in the event of a beam particle traversing the scintillator. A second threshold used for timing is chosen very close to the baseline of the signal. This threshold minimizes the time jitter induced in leading edge discriminators due to the varying slope of signals with different amplitudes, see appendix A. The width of each discriminator output is set at 20 ns. If the two PMTs emit a signal satisfying the discriminator settings within 20 ns of each other, an AND type coincidence module produces a short pulse $\mathcal{O}(10\,\text{ns})$. It then drives a pulse generator (CAEN 2255B) to output a logical signal with a user defined duration. This output is then propagated to the digitization section of the data acquisition. In case of the single fiber readout measurements, the output from the pulse generator doubles as a $gate$ for the QDC and TDC modules. It also notifies a master board communicating with the TDC and QDC modules. The master sends a blocking $VETO$ signal back to the pulse generator and prevents dispatching of new trigger signals until the data being digitized is successfully transferred to a PC. The latency between the trigger pulse and the VETO is in the order of 25 ns.

With the waveform sampling DAQ discussed in section 5.2, the output from the pulse generator initiates digitization of the sampled waveform. New triggers are vetoed whenever any of the connected boards is busy.
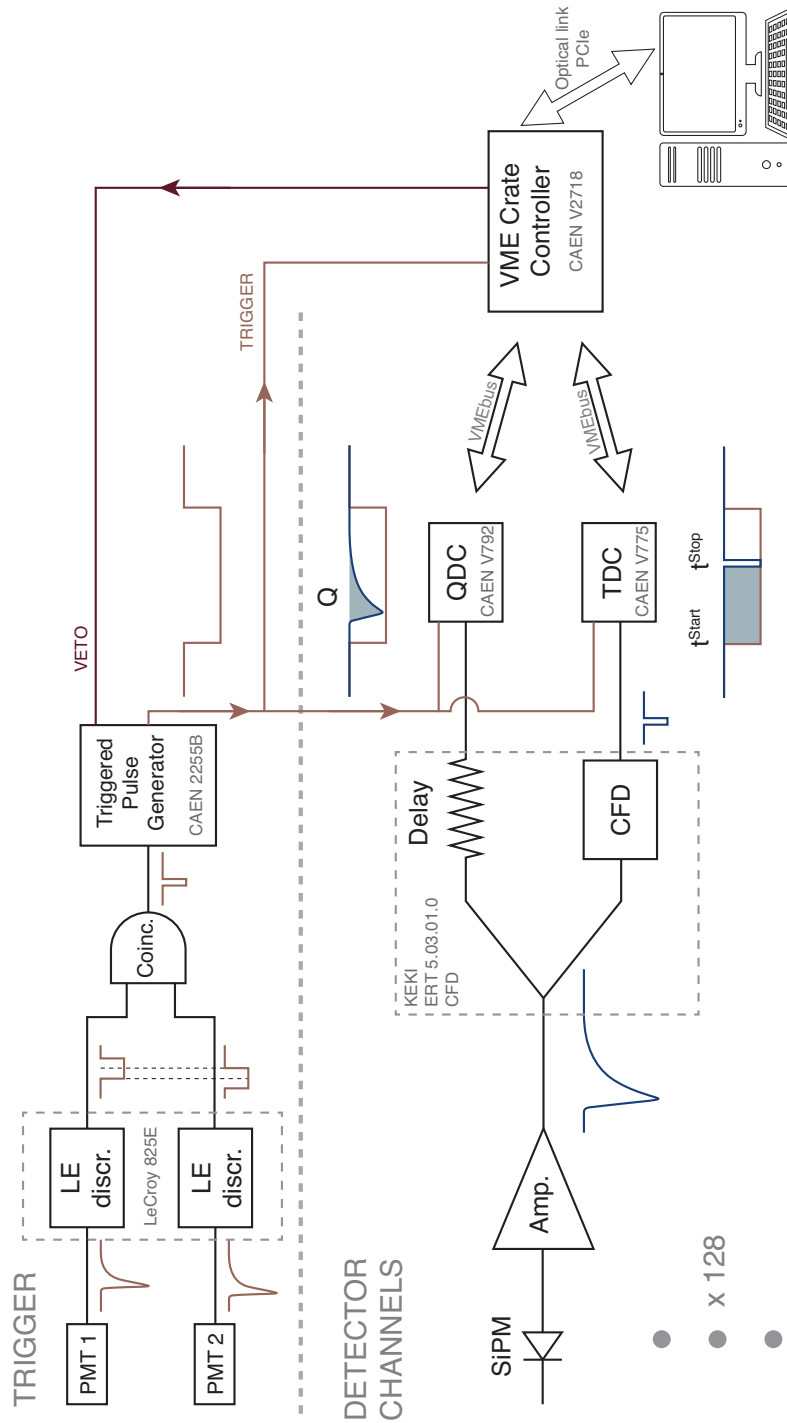
---

[1]Nuclear Instrumentation Module

Figure 5.1 – Schematic of the VME based data acquisition. The same trigger section is also used for the waveform sampling data acquisition discussed in section 5.2.

5.1.2 DIGITIZATION AND DATA TRANSFER

The lower part of Fig. 5.1 illustrates the electronics equipment used for signal processing in the single fiber readout configuration. 128 SiPM channels are recorded with the presented configuration. The discriminator modules consist of 16 individual channels each, hence a total of eight boards are used for the specified SiPM inputs. The TDC and QDC modules provide twice the number of channels per board, namely 32, hence four of each type are sufficient for the present measurements.

DISCRIMINATORS The outputs from the SiPM sensors[2] are amplified and fed to constant fraction discriminators (CFD). Details about the time extraction with this algorithm are available in appendix A. A critical parameter is the delay between the inverted signal and the fractional one. The delay in the used CFD modules is adjustable in steps of 1 ns in the range between 3 ns and 10 ns. For nominal operation, the incoming signals should have a rise time within the values selectable in the discriminator. Immediately after the amplifier the rise-time[3] of the SiPM signals, however, is in the order of 1 ns. On the other hand, before reaching the discriminators the signals travel in 60 ns long coaxial cables with finite bandwidth. High frequency components are attenuated in the cable and the resulting rise-time of the signals entering the discriminators is $\mathcal{O}(4\text{ ns})$.

An amplitude threshold is also imposed on the inputs to prevent noise events from propagating through the acquisition chain.

Each discriminator channel is equipped with an internal splitter that directs one part of the input to the timing chain and the other to the charge digitization branch.

QDC AND TDC MODULES The analog fraction of the discriminator output is digitized in a CAEN V792 QDC. The QDC input is integrated over a period of time determined by the *gate* signal produced from the pulse generator. For the presented measurements the length of the SiPMs signals is $\mathcal{O}(100\text{ ns})$. The gate signal is identical for all 32 channels in a single boards. To accommodate variations in the propagation time for signals in all 32 channels the width of the gate is set to 200 ns.

Meanwhile, a CAEN V775 TDC module operated in a *common start* mode[4] measures the

---

[2]SiPMs are used only for the readout of fiber ribbons in this setup.

[3]Historically, timing discriminators were designed to work with negative pulses delivered directly from the anodes of photomultiplier tubes. Following this convention, the "rising edge" refers to the leading edge of the pulse which, while the "falling edge" is interchangeable with the trailing edge. The rise time is defined as the time necessary to achieve the transition from 10 % to 90 % of the signal amplitude.

[4]A common signal sets the start of the time counter for all TDC channels. The length of the time interval is determined by the arrival of the measured signal. It is also possible to operate in a *common stop* mode where the start is set by the measured signal and a common end for the time interval is sent to all channels.

time between the arrival of the trigger signal and the logical output from the SiPM discriminator. Similarly to the QDC, the gate is identical for all 32 channels in a board and its start matches the start of time counting. If the SiPM input arrives outside the gate the time difference is not recorded. The CAEN V775 and CAEN V792 feature 12-bit analog to digital converters (ADCs). The bin resolution of the TDC is 35 ps, while the QDC is sensitive in the range from 0 to 400 pC with integral non-linearity of ± 0.1 %. The data from one channel is stored in a 32-bit long word. An event is the collection of all 128 inputs recorded following a single trigger. The amount of data generated per event is then $\mathcal{O}(1\ \text{kB})$ including header and footer overheads.

VME Crate Controller The QDC and TDC modules are housed in a VME crate. They communicate with a master board controller CAEN V2718 located in the crate over the VME bus. This is an asynchronous communication bus with master/slave architecture. It supports memory mapped I/O, priority interrupts and data transfer rates of up to 40 MB/s over a 32-bit data bus. The controller interfaces with a host PC via a PCIe card with optical cable connection.

Data Transfer The low level data communication between the controller and the host computer is handled via drivers provided by the vendor. A higher level library interface allows programming and reading the individual modules in the crate. The author developed the software for the data acquisition based on the CAENVMELib . It allows addressing individual boards in the crate, transferring data in large blocks of memory, configuring hardware interrupts and directing them to the computer processor. The boards readout consists of copying the digitized data from the TDC and QDC modules into the RAM of the receiving computer. The data writing from the PC memory to a hard drive is decoupled in a separate thread in the same process to minimize the dead time of the acquisition system.

The TDC and QDC modules notify the crate controller over the bus interrupt lines whenever they finish digitizing their inputs. The controller, in turn, issues a request in the form a hardware interrupt to the receiving computer. The memory from the digitizing boards is copied in the computer memory and a signal is sent back to the controller to release the VETO on the pulse generator and allow new triggers. The thread responsible for the readout enters a sleep mode and waits for the next interrupt to wake it up in order to process the new incoming data.

5.2 Waveform Digitization with the DRS4 ASIC

Contrary to the previously discussed systems, a full waveform digitized at a high sampling rate delivers maximum information about the signal of a detector. Parameters such as pulse

height, charge integral or the time of signal arrival can be extracted by processing the wave-form in real time or offline using diverse algorithms. This eliminates the drawback of having a fixed hardware design. A digitizing board based on the Domino Ring Sampler version 4 (DRS4) [71] has been developed by the DPNC electronics group for the NA61/SHINE experiment [72]. The versatility of the DRS4 makes it suitable for multiple applications including comprehensive studies of various detector prototypes.

5.2.1 PRINCIPLE OF THE DRS4 OPERATION

The DRS4 is an application specific integrated circuit (ASIC) for high speed analog signal sampling developed at PSI [71, 73]. The caveat in using such an ASIC is the slow conversion of the sampled waveform to digital data. Input signal are sampled and stored in cells of switched capacitor arrays regulated via a cyclic chain of inverters referred to as *domino wave*. Fig. 5.2 illustrates the working principle of that array.

One DRS4 chip consists of 9 differential input channels each with a depth of 1024 cells. The sampling frequency f^{sca} is determined by an externally generated sampling clock f^{sclk}. It is phase locked to a voltage controlled oscillator (VCO) in a phase locked loop (PLL) element with a frequency synthesizer. The multiplication factor of the synthesizer is 2048 leading to a sampling rate $f^{sca} = 2048 \times f^{sclk}$. The *domino wave* signal runs continuously on the voltage control line. It closes and opens simultaneously both switches around the capacitor of the corresponding cell in each of the nine channels. As the control voltage propagates through the switches, the amplitude of the input signal is stored at different points in time as a charge in the capacitors of the cells. When a readout is initiated the sampling stops[5] and each cell is sequentially discharged via the output line OUT and fed to an external analog to digital converter (ADC). By decoupling the sampling and readout stages the chip consumes less power and allows cheaper ADC components to be utilized for digitization while maintaining high number of samples per second. The sampling frequency ranges from 0.7 GSPS to 5 GSPS[6], while typical readout frequencies are in the order of $\mathcal{O}(10 \text{ MHz})$.

Fig. 5.3 is a functional diagram of the DRS4 ASIC. The outputs of the nine channels can be send in parallel to 9 ADC channels. Alternatively, they can also be multiplexed at the chip level and a single ADC channel can digitize all of them sequentially. Depending on the selected mode, the readout of the stored charges starts either at the first cell of the array (Cell 0) or the current cell at which the sampling stopped.

---

[5]The DRS4 is designed such that the domino wave can continue running and stay locked to the PLL without affecting the capacitors during readout.
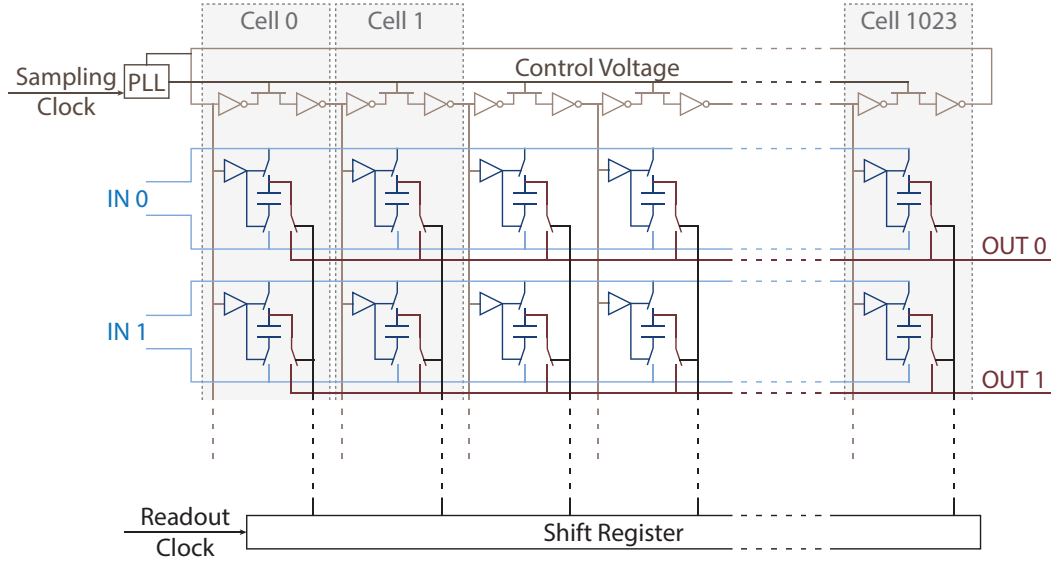
[6]Giga Samples Per Second

Figure 5.2 – A control voltage line (—) runs through an inverter chain and activates each cell's switches (—) to sequentially sample an input signal (—). Once a readout request is made, the sampling stops and a shift register (—) allows consecutive reading (—) of the charge stored in each cell's capacitor. The sampling frequency is phase locked to a precise external clock for improved stability. The shift register's clock, on the other hand, is synchronized with an external ADC's clock.

5.2.2 DPNC 342 Readout Boards

The DPNC 342 readout board features 32 input signals sampled by four DRS4 ASICs. An eight channel ADC digitizes the outputs from all four DRS4 chip. A field programmable gate array (FPGA) from the Cyclone V family of Altera®[74] executes the on board data acquisition logic and controls the communication between various components. Data transfer between the board and a host computer is realized via USB-3 connection.

A photo of the DPNC 342 PCB with annotations for the installed elements is shown in Fig. 5.4. The board is designed to match the physical dimensions of a VME 6U module. It features a VME P1 connector in the rear with modified pin layout to supply power at ± 6 V, as well as various control signals for the DRS4 readout and synchronization between multiple boards. Following is a USB-blaster for communications with the FPGA during development. An RJ45 socket is foreseen for external communications and data transfer. Further down a 34-pin connector provides differential pairs designated for general purpose usage linked directly to pins on the FPGA. Eight pairs are currently implemented as inputs and eight as outputs. A coaxial LEMO 00 series input accepts externally generated signals for time calibration.

At the top of the front panel is located a two pole LEMO F/RA interconnect for the domino wave clock. It is followed by two 34-pin connectors for 2×16 single ended signal inputs
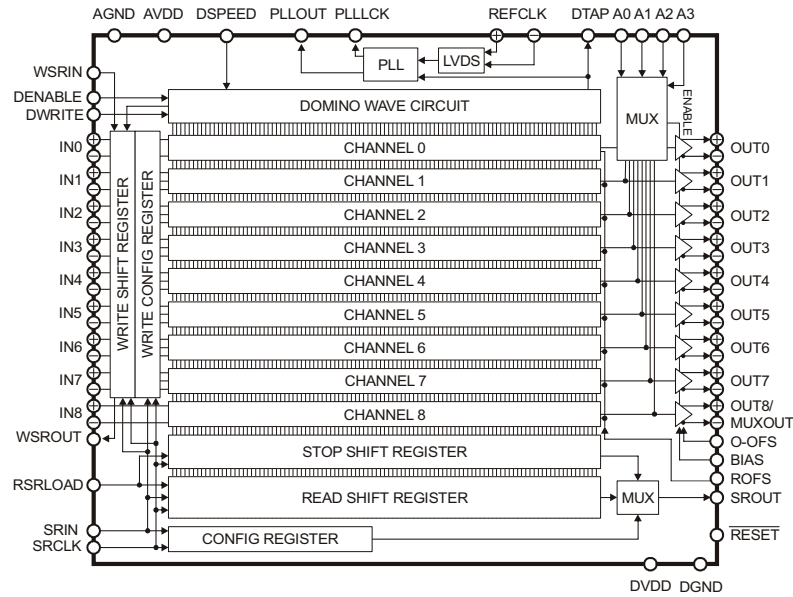
Figure 5.3 – A functional diagram of the DRS4 ASIC [73]. The write signal for the sampling cells is generated by a chain of inverters on the chip and stabilized by a PLL. The content of the sampling cells can be send either to a multiplexed or individual output lines from where it is digitized with an external ADC.

terminated at 50 Ω. In the middle of the panel two coaxial LEMO 00 series connectors are installed for trigger input and busy output. Lastly, a USB type B interconnect compatible with the USB-3 standard serves for communication with a host computer during data taking.

Identification of the board is realized via the three rotatable switches labeled "Addressing Switches" in Fig. 5.4. The FPGA is programmed via a JTAG connector.

A simplified schematic of the DPNC 342 readout board components communication is shown in Fig. 5.5. The input signals arriving at each of the DRS4 channels are controlled by an analog frontend stage (AFE). On one hand, the AFE inverts and shifts the amplitudes of the front panel inputs from the allowed spectrum between -1 V and 0 V to the dynamic range of the DRS4 inputs, namely -0.1 V to 0.9 V. On the other hand, a set of switches controlled by the FPGA selects between the front panel inputs and a group of dedicated calibration signals. All inputs to the DRS4 chips first pass through the AFE stage. A source for the amplitude calibration is a 16-bit digital to analog converter (DAC) LTC2600 programmable via the FPGA. For the time calibration there are two foreseen options: a 100 MHz sine wave provided by an onboard crystal oscillator with a precision of 25 ppm or an external signal delivered through the rear LEMO connector. In version 02.01C of the board[7] eight channels of the available nine from

---

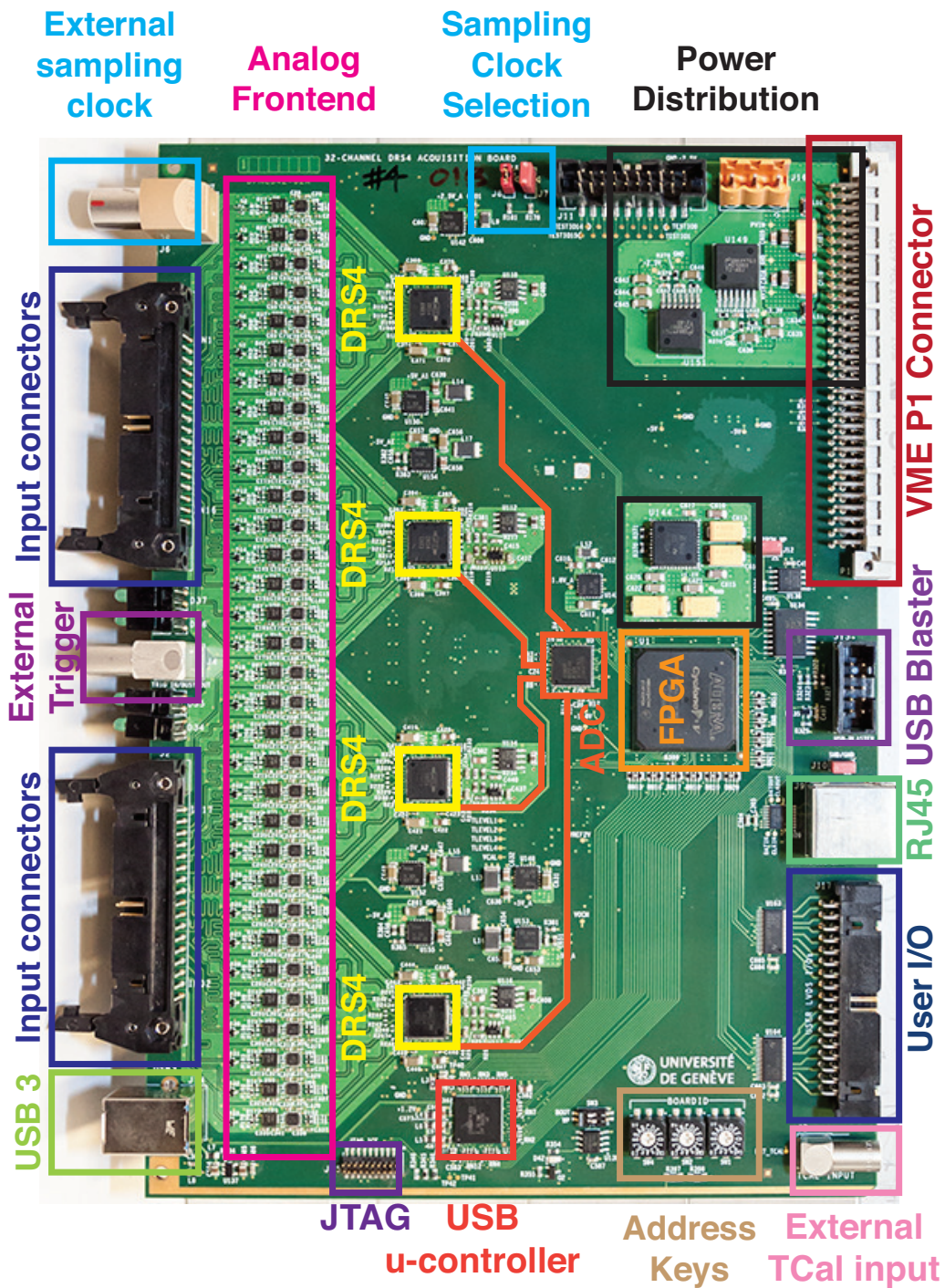[7]The one used for measurements discussed in chapter 7

Figure 5.4 – A photo of the DPNC342 v2 readout board with annotations for the various components.

each DRS4 chip are connected to their respective analog frontend. In subsequent versions, the ninth channel will be used for time synchronization through a dedicated circuit distributing an identical signal to each chip. Four of the available eight channels from a 12-bit AD9637 analog to digital converter (ADC) are used to digitize the multiplexed outputs from each DRS4 chip. The readout clock frequency f^{ro} is specified through the FPGA and is set to 16.5 MHz matching the DRS4 read shift register clock.[8] During readout the waveform sampling is inactive and the system accumulates dead time. When all 8 channels (N^{chs}) per chip with the full depth of 1024 cells (N^{cells}) are digitized at the aforementioned rate the contribution to the dead time is approximately 500 μs, estimated with the formula:

$$t^{dead} = N^{\mathrm{chs}} \times N^{\mathrm{cells}} \times \frac{1}{f^{\mathrm{ro}}} = 8 * 1024 * \frac{1}{16.5 \text{ MHz}} \tag{5.1}$$

The ADC data is stored in the dual port random access memory (DPRAM) allocated on the FPGA for subsequent retrieval. Furthermore, the DRS4 states are controlled and monitored through two registers programmed into the FPGA (see subsubsection 5.2.2.1). The front panel trigger input is reprocessed there as well, and the state of the system is forwarded to the busy output. A EZ-USB®FX3™ micro-controller by Cypress realizes the data exchange with a host computer during data acquisition.

A crystal oscillator with a frequency of 2.4576 MHz and stability of 50 ppm is available on the board to generate the *domino wave* clock. With a PLL multiplication factor of 2048 a sampling rate of 5.033 GSPS is achieved. The front panel LVDS clock or the backplane of the crate can be used when multiple boards need to be synchronized via an external clock unit or when other sampling frequencies are desired. The clock source is determined by a combination of the $J7$ and $J8$ jumpers on the PCB.

$$
\begin{aligned}
J8: \quad &\text{IN} \quad \rightarrow \quad \text{onboard clock} \qquad\qquad J7: \quad \text{IN} \quad \rightarrow \quad \text{front panel input}\\
&\text{OUT} \quad \rightarrow \quad \text{external clock} \qquad\qquad\qquad\quad\ \text{OUT} \quad \rightarrow \quad \text{backplane input}
\end{aligned}
$$

Four temperature sensors ADT7301 located below the DRS4 chips are periodically read by the FPGA.

---

[8] A nominal readout frequency of 33 MHz is reported in [71, 73] and achieved in other application, however they employed a fine tuning between the phases of the ADC and the shift register clocks to eliminate signal artifacts arising under certain conditions. This functionality is not supported in the current firmware revision for the DPNC 342 board, so it is not explored for the measurements reported in this work.
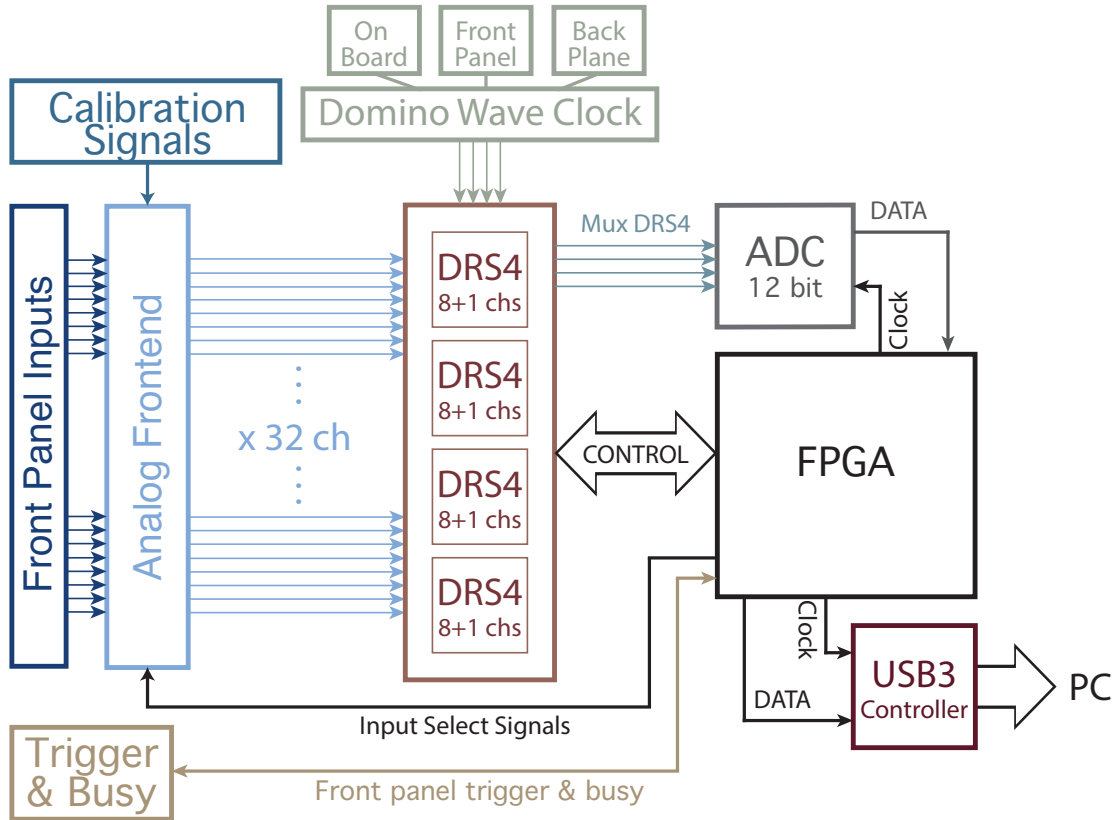
Figure 5.5 – Simplified schematics of the DPNC 342 readout board.

5.2.2.1 FIRMWARE DISCUSSION

This section provides a brief explanation of the firmware implemented on the FPGA and the USB-3 micro-controller. It is relevant for the software development of the data acquisition realized in the present work.

USB-3 MICRO-CONTROLLER

The communication between a DAQ computer and the FPGA on each board is realized through the EZ-USB®FX3™ micro-controller. It features several peripheral hardware blocks GPIF II, USB, UART, SPI etc. Each of them has access to an internal system RAM through dedicated unidirectional connection points called sockets. For the chosen device, the available system memory is 512 kB.[9] It is shared between data buffers and programming code. A fully configurable parallel general programmable interface (GPIF II) provides means of com-

---

[9]This is the memory on the USB micro-controller. It should not be confused with the FPGA resources.

77

munication with an external processor such as an FPGA. In particular, a synchronous interface accessing a FIFO buffer allocated in the micro-controller memory has been implemented on top of the GPIF II. A direct memory access (DMA) engine built into the FX3™ device allocates the FIFO buffers at a firmware level and maintains the data flow between them and the FPGA once the FPGA initiates a transfer. Data exchange between the micro-controller and the FPGA is triggered by a command received through the host computer. This command is always written to a control register in the FPGA which decodes it and based on the programmed logic initiates an action. The host command consists of a key word encoding the data direction, an address of memory in the FPGA address space and a length of the data to be retrieved or written. Once, the command is decoded by the FPGA the data flow proceeds. A 66 MHz clock generated on the FPGA drives the interface. The FIFO pointer in the FX3™ buffer is incremented on each rising edge of the clock and a 32-bit word is propagated to the data bus from(to) the FPGA. The data flow between the FPGA memory and the FX3™ buffers is realized through unidirectional producer(consumer) channels. A host computer can then access the buffers through the USB interface.

FPGA Memory

Resources on the FPGA are distributed in different blocks depending on their designated purpose. On the chosen device - Cyclone V E - there is a total of 7 696 kbit of system memory. A fraction of it is allocated for storage of the digitized DRS4 samples and configured as a dual port random access memory (DPRAM). Two registers built of adaptable logic units (ALU) control and store the state of the full waveform readout. The control register consists of fifteen 32-bit words and is programmed for both read and write access. Not all bits are used, but the ones that are, are directly linked to general purpose input/outputs (GPIO) pins of the FPGA. They control the DRS4 chip states. The status register, which has sixteen 32-bit words stores the state of the DAQ e.g. idle, busy, running, etc., as well as information such as number of triggers, DAC levels, stop cell in each DRS4 chip, temperature measurements, identifying data, etc. The 12-bit ADC data from the waveform digitization is recorded in 16-bit words. A buffer with capacity for one full readout of all the 32 channels is foreseen in the DPRAM. It is prepended by a copy of the control and status registers defining a contiguous block of 65 664 bytes that is transferred to the FX3™ buffers upon request.

Readout State Machine

Under normal mode of operation the DRS4 chip is sampling continuously and awaiting the arrival of a trigger signal. At this point the "writing" to the capacitors is disabled and

the system prepares for readout. The domino wave is kept running to maintain the stability of the system and to avoid dead time accumulated for locking the PLL to the external clock at every trigger. It takes in the order of a $\mathcal{O}$(few ms) per event to lock to the external clock. Accepting new triggers is disabled and the FPGA DPRAM is cleared. Meanwhile a transition in the state of various digital components in the DRS4 ASIC occurs which draws excessive power from the chip's power supply. A short stabilization period $\mathcal{O}(10~\mu s)$ is required after entering the readout state to prevent misreading of the capacitor charges. Once the driving voltage VDD stabilizes, the ADC is synchronized with the readout shift register and the outputs from each cell in all channels of one chip are sequentially digitized. The multiplexed outputs from the four chips are digitized in parallel by four of the ADC channels. When the ADC data is successfully stored in the FPGA memory the status register is updated such that a host PC can read it and request data transfer through the USB interface. Meanwhile, sampling in the DRS4 restarts, however no triggers are accepted until a user generated signal (from the FPGA) is received by the ASIC.

5.2.2.2 DATA ACQUISITION

The data acquisition is executed on a dedicated DAQ computer. To achieve maximum data transfer rate, each DPNC 342 readout board is connected to an independent USB-3 micro-controller installed in the host PC.. The PEXUSB3S44V 4-Port PCI Express USB 3.0 offers four USB-3 ports interfaced with four independent PCIe lanes each with maximum data transmission rate of 5 GT/s.[10] Up to four such card can be installed on the used host computer[11] supporting data acquisition with a maximum of 16 DPNC 342 readout boards or up to 512 readout channels.

In the current application of critical importance is the integrity of data transferred over USB. A brief overview of the USB-3.0 standard is presented to explain the design choices made in defining DAQ software.

USB-3.0 STANDARD

The USB-3.0 standard [75] defines three communication layers - physical, link and protocol. The physical layer represent the actual physical connection between two ports. It receives 8 bit data from the link layer, scrambles it to reduce EMI, encodes the scrambled data into 10 bit

---

[10]GT/s - giga transfers per second; the rate of usable data is $\approx$4 Gbit/s (500 MB/s) due to overhead from 8b/10b encoding.

[11]The number of cards is determined by the available PCIe lanes on the installed CPU and the PCIe slots available on the motherboard. For the current station Intel Core i7-7800X series processor with 28 PCI lanes has been mounted on an ASUS Prime X299-Deluxe motherboard with 4(+2) PCIe slots.

symbols, and serializes the data to be sent over the cable. At the receiving end, the reverse operation is performed. The link layer handles data integrity checks, packet acknowledgement and error recovery, packet flow control, and link power management.

The building blocks of the USB-3.0 protocol layer are called packets and communication between a host and a connected device is realized through the exchange of such structures. Each packet consist of a header section encoding identifying information about the designated sender/receiver. Additionally, depending on the transfer type a packet can also carry a payload representing the data that needs to be exchanged. The USB-3.0 specification guarantees integrity of the packet headers during a transfer. Depending on the transfer type - control, bulk, isochronous or interrupt - the integrity of the payload is not guaranteed. Only the bulk transfers retry getting the payload if data checks fail. They have the lowest priority with respect to the others and utilize only whatever bandwidth is leftover from the remaining three. In the present system that does not pose a concern since bulk transfers are the only type utilized by the data acquisition, so they benefit from the full bandwidth in their PCIe lane.

A transfer is realized between a host and a device via so called pipes - software abstractions relating to a specific device function. The physical buffer serving a particular role on the USB connected device is called an endpoint. Each software pipe is associated with a designated device endpoint. Data flow proceeds only after a request by the host. The term OUT transaction refers a packet moving out of the host to a device while IN specifies the opposite direction.

A radical change introduced in the USB-3 standard with respect to older versions is the possibility of parallel bidirectional data transfer. To initiate incoming transactions with the current firmware implementation, the host sends an output data packet containing the address of the FPGA memory it expects to receive data from. Upon arrival in the FPGA registers, the FPGA decodes the command and starts pushing data to the micro-controller FIFO buffers accessible by the USB interface. Meanwhile, the host sends an IN token and opens a pipe to receive the incoming data from the device. If the IN token is scheduled immediately after the OUT transfer an acknowledge (ACK) for the out transaction is sent from the device simultaneously with the following IN due to the double data lines introduced in the standard. Compared with the previous revision i.e. USB-2 where on each transfer (including ACK) the same data line is used and its direction should be specified, the USB-3 revision speeds communication significantly. Nevertheless, the minimal interval between subsequent transfers is 125 µs, unless burst sequencing is used, which negates the need for acknowledgment after each transfer. Burst sequences, however, are limited to 16, afterwards a new handshake should be negotiated between the host and the device. The 125 µs limitation should be considered when designing the software such that any unnecessary transaction are avoided to minimize the dead time.

With the current software implementation between 10 and 12 transactions (including both

IN and OUT) occur per event per readout board. About half of them proceed while checking whether the sampled DRS4 data is digitized and transferred to the FPGA memory. The rest consist of the actual event data transfer over the USB and subsequent commands sent to restart data taking and release the busy state of the DPNC 342 boards.

BOARDS INITIALIZATION

The first step in starting the data acquisition is to initialize the readout boards.

The implemented software operates on a Linux system and uses the LIBUSB-1.0 library [76] to send packets over the USB. Using this library, a list of all USB devices currently connected to the host computer can be retrieved. Each device, including the DPNC 342 board exposes information about its vendor ID. This number is to identify all DPNC 342 boards and to send them a configuration command. Querying the status of the board returns its address as set by the hardware rotational switches, see Fig. 5.4. Consequently, the devices discovered by the library can be linked with the hardware address on each DPNC 342 board and accessed for subsequent operations throughout the software.

All settings are transmitted to the board by writing to the FPGA control register. In most cases a single bit needs to be switched on or off in order to enable a specific option. A peculiarity of the current FW revision requires a read cycle to be executed on the control register after updating it in order to disconnect the analog outputs on the FPGA.

The boards can be reconfigured at any point via the control register. In the present software implementation their readout mode and specific acquisition options are defined before a data run starts and remain constant until the end of the run.

There are three main modes of operation - data taking, voltage calibration and time calibration. They differ in the source of inputs linked to the DRS4 channels via the analog front end. In order to perform a voltage calibration ($VCal$) the $acalib$ bit should be set to 1. It takes precedence over the time calibration ($TCal$) controlled by the tca_ctrl value. Hence, the $acalib$ should be disabled if time calibration is desired. Both flags, on the other hand, should be set to zero in order to accept inputs from the front panel interconnects ($Data$ mode).

Another important element concerns the readout mode of the DRS4 chip. Depending on the value of $readout\_mode$ - 1 or 0 - the cells in each channel are digitized either by starting from the cell at which the $domino\ wave$ reached when the sampling stopped ($stop\ cell$) or always by the first physical cell of the capacitor array ($Cell\_0$). In the latter, the $stop\ cell$ is not recorded, hence proper reconstruction of the waveform is not possible. The default mode of operation is $readout\_mode$ = 1 - when the readout starts from the stop cell.

Table 5.1 summarizes the most relevant settings which should be considered when operating

Register Name	Data run value	Description
start_trig	1	1: starts the domino wave
reinit_trig	1	1: stops and resets the DRS chip
enable_trig	1	1: enable accepting triggers in the the DRS4
reset_trig_count	1	1: reset trigger and readout counters
adc_active	1	0/1: keep ADC clocked all the time
tca_ctrl	0	0/1: disable/enable time calibration
enable_trigger	1	0/1: disable/enable hardware triggers
readout_mode	1	0/1: start from first cell / domino stop
acalib	0	0/1: disable/enable calibration voltage (DAC4)
dactive	1	0/1: stop domino wave/keep it running during read-out
reduced_readout	0	0/1: 1024/512 cells readout
dmode	1	0/1: domino wave single shot/continuous cycling
pllen	1	0/1: disable/enable PLL in DRS

Table 5.1 – A summary of the most relevant FPGA control registers used when operating the DPNC 342 boards. With the exception of enable_trig, all other registers should be initialized once at the beginning of each data run. enable_trig should be set to 1 after each readout of the DPNC 342 board, so that new triggers can be accepted by the DRS4 ASIC and it can stop sampling. Sending a 0 to any of the top four registers has no effect. Hardware triggers are expected from the front panel LEMO connector or the backplane.

the DPNC 342 boards.

Data Collection

In the current software implementation the readout of each DPNC 342 board is handled in an independent thread. Each thread polls the status of its respective DPNC 342 board and initiates transfer once the ADC data is written in the FPGA memory. The recorded waveform is transferred over the USB-3 using a bulk type of transaction to ensure data integrity. Once the data is copied in the host memory, a command enabling the triggers in the DRS4 is sent back to the device.

To synchronize the events in all boards an external veto mechanism is used. Each board outputs a busy signal at the LEMO connector on its front panel the moment a trigger is received by the DRS4 and the sampling is stopped. The busy output stays high until the enable triggers command is received by the device. A logical Fan-IN NIM module concentrates the busy outputs of all boards and keeps its output high if any of them is still busy. This module vetoes the triggered pulse generator discussed in subsection 5.1.1. As a result, new triggers

are synchronously distributed to all DPNC 342 boards.

5.2.3 SYSTEM CALIBRATION AND PERFORMANCE

The digitized data needs to be calibrated in order to reflect the actual input voltages and time scales. Despite being identically designed, differences in the manufacturing of integrated circuits on silicon result in small variations in the output of each DRS4 cell. A set of known signals is sent to the DRS4 inputs in order to estimate the cell responses. Depending on the sampling frequency and environmental conditions the behavior of the cells varies, hence they should be calibrated whenever a change occurs. Nevertheless, once calibrated the outputs remain stable over time. In the present work calibration coefficients extracted several months apart proved to be still valid when the boards are operated under identical conditions. The performance results discussed in this section are relevant for operation under nominal sampling frequency f^{SCA} = 5.033 GHz. The measurements presented in chapter 7 are conducted under the same conditions.

5.2.3.1 VOLTAGE CALIBRATION

Precisely known[12] constant voltage levels driven by the 16-bit onboard DAC are fed into the DRS4 inputs. For each cell the recorded ADC values are then mapped to the reference inputs. To account for statistical fluctuations a few hundred samples are recorded at each voltage level. As recommended in [77], a straight line is used to match the averaged $\overline{\text{ADC}}$ values to the applied voltage. The deviation of the recorded voltage level with respect to preset input is measured at multiple points. To assert the quality of the calibration, the observed cumulative nonlinearity of all cells is thus examined, see Fig. 5.6. The calibration coefficients are optimized for the region between 10 mV and 800 mV which coincides with the expected pulse heights used in chapter 7. Since the nonlinearity observed with the linear fit exhibits a quadratic behavior with the applied reference voltage, a quadratic function is also evaluated for calibrating the response. Fig. 5.6 demonstrates the measured offsets w.r.t. a reference voltage in 64 channels from 8 DRS4 chips when either a first or a second degree polynomial is used.

The large deviations observed at 0 V are due to the floating levels of the DRS4 inputs when no input voltage is present. Additionally, the chip is known to have nonlinear behavior at the upper boundary. The calibration coefficients are obtained by sampling the input voltage in steps of 50 mV and using only the points in the range [50 mV, 850 mV]. Other, combinations of endpoints and voltage steps are also explored but they lead to worse overall performance,

---

[12]With a precision much better than the expected cell resolution.
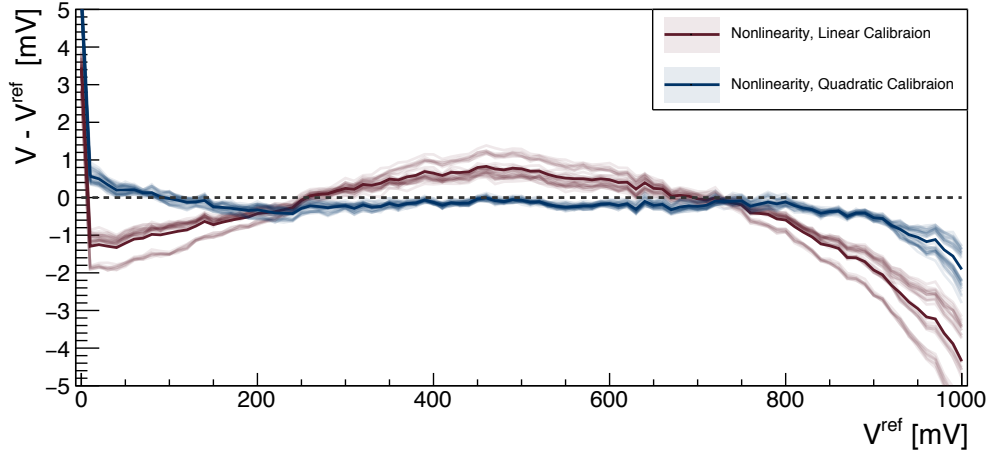
Figure 5.6 – Nonlinearity of the voltage calibration depending on the model used for mapping the voltage value to the recorded ADC outputs. Using a quadratic function lead to better matching to a reference input signal. The data is from 64 channels in 8 DRS4 chips. A constant level reference signal is used for each point.

especially when reference values of 0 V or more than 900 mV are included in the fits. Smaller intervals between the levels do not show improvement or degradation of the calibration, while larger ones result in higher nonlinearities.

Fig. 5.7 illustrates the variation in cell responses. The shown calibrated data corrects only the offsets in each cells. The fine tuning discussed earlier is too small to be observed in this plot. Additionally, the overall baseline offset is not subtracted to illustrate the span of a single waveform in the ADC values.

5.2.3.2 Time Calibration Algorithm

Once the voltage calibration is completed the time width of each cell can be precisely determined. Following the algorithm described in [77], the time calibration proceeds in two stages - the so called *local* and *global* time calibration. A sine wave fed to each channel is the source signal for both calibrations. An onboard crystal oscillator generates a 100 MHz square wave which is subsequently filtered to a quasi sinusoidal wave with the same frequency. It is then distributed to the analog front end of each channel and used as a source for the time calibration. The sine amplitude delivered to the DRS4 inputs is $\mathcal{O}(350 \text{ mV})$ and the offset is at $\approx$600 mV.

As mentioned, due to the nature of the manufacturing processes in silicon, turning on and off the write switches for each cell does not happen at equal intervals despite the constant
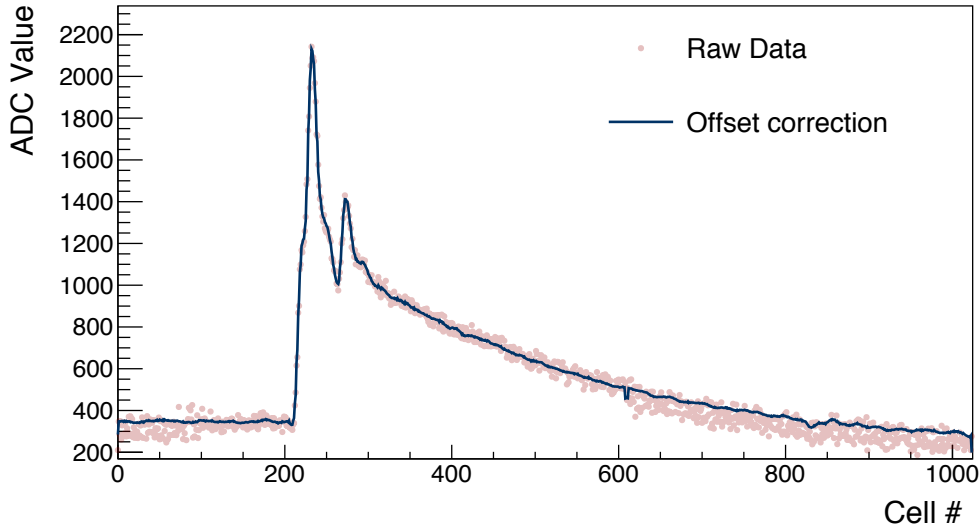
Figure 5.7 – Comparison of a recorded waveform with and without voltage calibration. The shown calibrated data corrects only the offsets in each cells. However, the common baseline shift is not subtracted in order to illustrate the span of a single waveform in the ADC values. The scaling of the amplitude to voltage is omitted since it does not affect visible the shape of the shown result. The amplitude of the signal is about 500 mV.

sampling frequency. Nonetheless, the time widths are constant over time and can be measured. The *local* time calibration exploits the linear relation between the differential change in the voltage measured in two consecutive cells and their time width. To a good approximation the points immediately around the mean value of a sine function lie on a straight line. The widths of the time bins are adjusted using the slope of the function as shown in Fig. 5.8.

At the next stage, thanks to the periodic nature of the input, additional fine corrections can be applied. The idea is to sum the time bins between two rising (falling) edge crossings at the mean value and compare them to the expected period of the reference signal, see Fig. 5.9. The ratio between the sum and the period is then equally distributed to all cells in the corresponding subset.

Fig. 5.10 illustrates the effect of time calibration applied to channels in three different DRS4 ASICs. The same input signal is propagated to all inputs. The default values for the time bins assume identical width of 200 ps.

5.2.3.3 SYSTEM TIME RESOLUTION

To verify the time resolution of the system after calibration a split signal test is employed, see Fig. 5.11. The calibration is quantified by the time difference resolution between any two channels. Measurements are performed with two sources. In one case, an external square
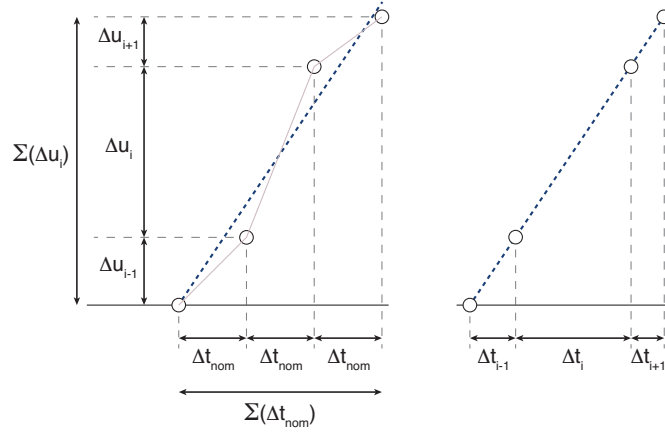
Figure 5.8 – Illustration of the local time calibration algorithm [77]. Knowing the difference between voltage levels allows time intervals to be adjusted such that the point in the figure lie on a straight line. The shape of the line is known because the calibration happens only in the sections of the sine signal that can be approximated well by a straight line.
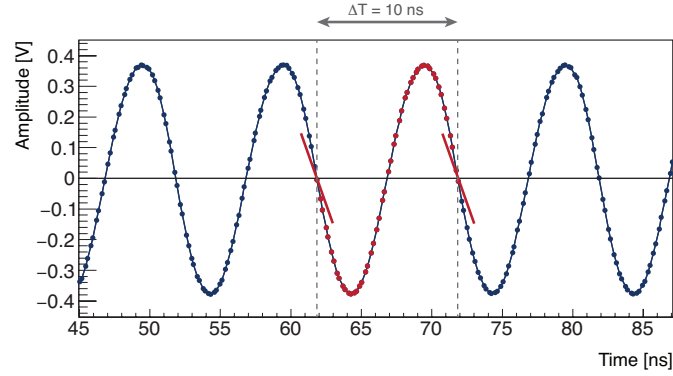
Figure 5.9 – Illustration of the global time calibration algorithm [77]. The period of the sine is fixed. Any deviation of the measured period from the expected one is factored as a small correction to all time intervals between the start and end of a period.

impulse split through a low jitter fan-out unit is directed to the analog inputs on the front panel. Alternatively, the sine wave generated onboard and replicated to all 32 channels per board can be used. The two methods are independent.

The time difference is always determined with reference to the time in $Cell\_0$ because it is synchronized with the external clock locking the *domino wave* via the DRS4 PLL. The *trigger* that stops the sampling propagates from the FPGA to the different ASICs with a jitter of $\approx$200 ps, hence the stop cells will inherit this jitter. Additionally, by the time each DRS4 stops sampling a time jitter of several cells can be accumulated. Indeed, a time resolution in the order of 1 ns is observed between channels on two chips when the stop cell time is used.
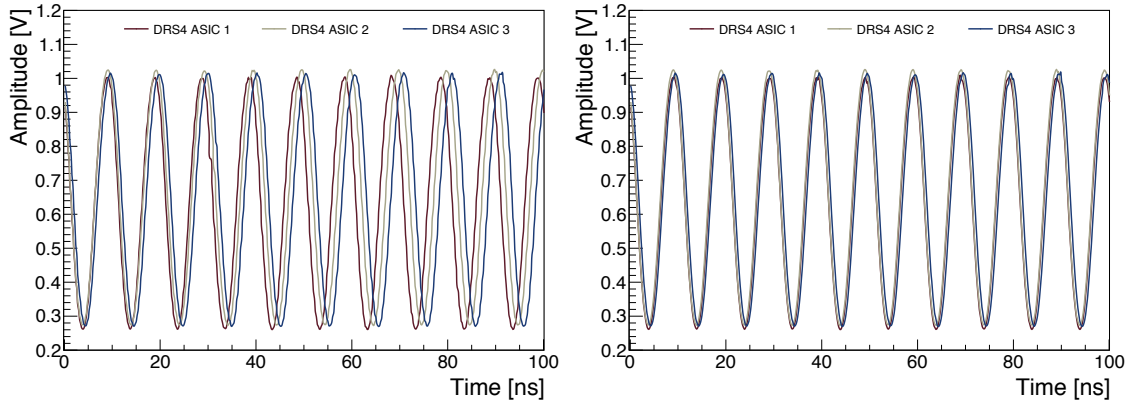
Figure 5.10 – An identical sine signal distributed in three DRS4 channels in different ASICs. The width of each cell is set at 200 ps (Left) prior to calibration. The same signal with widths extracted following the time calibration (Right).
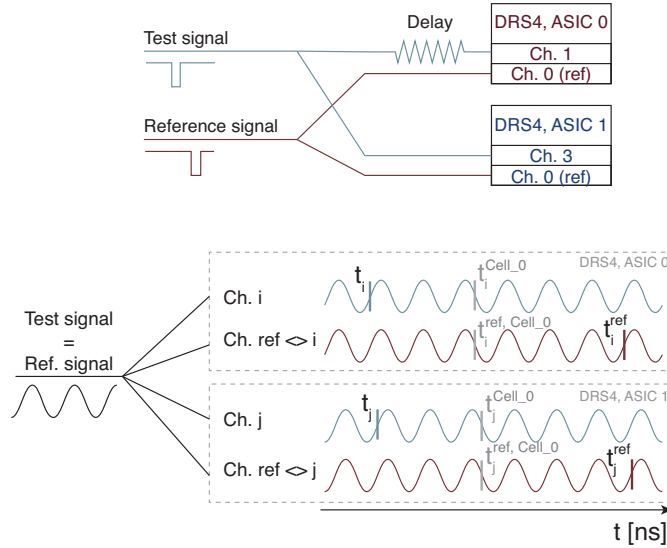
Figure 5.11 – Two configurations with well defined input signals are realized in order to evaluate the time resolution of the DPNC 342 boards. (Top) A test signal is replicated through a low-jitter fan-out to the inputs of different DRS4 chips. One input in each ASIC receives an independent reference signal that is also replicated in a low-jitter fan-out. (Bottom) Alternatively, the sine wave generated in each board can be used for timing studies. Annotated are sample time measurement points. The plotted waveforms illustrate the output recorded in the different DRS4 ASICs. The start of each waveform is at the stop cell. To keep the plot simple, only four channels from two DRS4 chips are shown.

If the same external clock synchronizes the *domino wave* on several boards the main source of time jitter is in the locking of the PLL element for each chip. It amounts to a resolution

between 25 ps and 60 ps[13] while the typical jitter between channels on the same ASIC is $\mathcal{O}(3\,\text{ps})$.

Hence, to achieve optimal time resolving capabilities an external reference signal can be delivered to one channel in each DRS4 chip and used for offline correction. Fig. 5.12 presents the effect of the discussed synchronization mechanisms on the time difference between two channels in different chips. Using the reference signal alone (without the $Cell\_0$ time) the jitter is reduced from about 200 ps RMS to about 15 ps. Adding the $Cell\_0$ corrected resolution improves ten times from about 40 ps to 4 ps RMS. The time difference ΔT_{ij} between channels i and j is expressed with the formula:

$$
\begin{aligned}
\Delta T_{ij} \quad = \quad & [(t_i^{ref,Cell\_0} - t_i^{ref}) - (t_j^{ref,Cell\_0} - t_j^{ref})] \\
& - [(t_i^{Cell\_0} - t_i) - (t_j^{Cell\_0} - t_j)]
\end{aligned}
\tag{5.2}
$$

t_i, t_j - time stamps from main signal waveforms

$t_i^{Cell\_0}$, $t_j^{Cell\_0}$ - time stamps for $Cell\_0$ of channel i, j

t_i^{ref}, t_j^{ref} - time stamps from waveforms of reference signals in the chips of channels i, j

$t_i^{ref,Cell\_0}$, $t_j^{ref,Cell\_0}$ - time stamps for $Cell\_0$ of reference signals

Fig. 5.13 presents the time resolution dependence on the time difference between the reference signal and the measured point. It is derived through the sine wave signal that is generated for time calibration and spread through the DPNC 342 inputs. For the characterization studies discussed later in chapter 7, the reference signal is displaced by 120 ps to 140 ps from the point of interest, contributing a systematic uncertainty $\mathcal{O}(7\,\text{ps})$ to the time difference. The synchronization is realized via a copy of the trigger signal.

5.3 MᴜTRɪG

To accommodate the stringent time and rate requirements imposed on the Mᴜ3ᴇ timing detectors a custom designed ASIC called Muon Timing Resolver with Gigabit link (MᴜTRɪG) is being developed by the Kirchhoff-Institute of Physics at Heidelberg University. It features an analog section with 32 input channels, integrated time to digital converters (TDC) and a dedicated digital logic for processing and data transmission. With the latest implementation

---

[13]Using the $Cell\_0$ time as a reference.
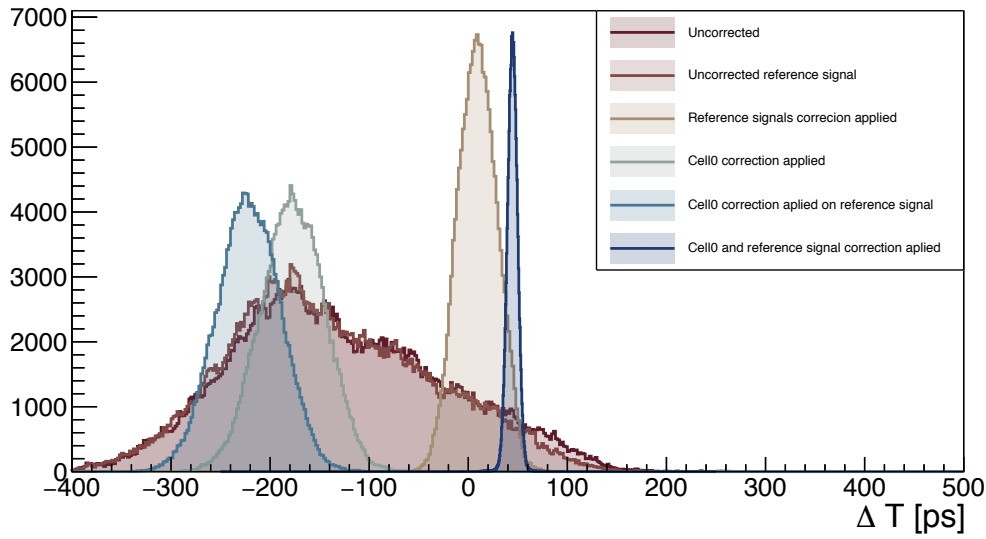
Figure 5.12 – Time difference between channels on two different DRS4 chips. The uncorrected histogram (—) shows the time difference between two channels in two DRS4 chips using their time information without any correction ($t_i - t_j$). The time difference between the two reference signals in the corresponding DRS4 chips is also shown (—) ($t_i^{ref} - t_j^{ref}$). Adjusting the time in each of the test signals relatively to the reference signals and then taking the time difference result in the "Reference signals correction applied" histogram (—). By adjusting the time stamps in each of the channels with respect to the $Cell\_0$ and then taking the time difference the "Cell 0 corrected" plots are obtained (—) and (—). Applying both the $Cell\_0$ and reference signal relative corrections result in the last histogram (—) which exhibits the smallest time jitter.

of the chip [43], hit rates of up to 1.1 MHz per channel are supported and the time resolving capabilities are defined by 50 ps fine counters of the TDC.

A MUTRIG channel diagram is shown in Fig. 5.14. The analog front end consists of an input stage, timing and energy branches and a hit logic unit. The input stage accepts SiPM signals in differential or single ended connection modes. It transforms the current from the SiPMs to voltage signals used in the timing and energy branches. Additionally, the DC voltage at the input terminals can be varied within a range of 900 mV to compensate for small variations in the nominal bias voltages of different SiPM channels. Both the timing and energy branches consist of amplifiers and level comparators. The hit logic unit encodes the two discriminator outputs into a single combined signal and sends it to the TDC module. The data from the TDC is buffered in on-chip memory banks and is subsequently transferred out. The analog processing components, the TDC, and the digital modules are programmed via a Serial Peripheral Interface (SPI).

Fig. 5.15 illustrates the principle of operation in the MUTRIG analog stage. A single input signal is used to illustrate the idea of the signal processing to avoid overloading the figure with
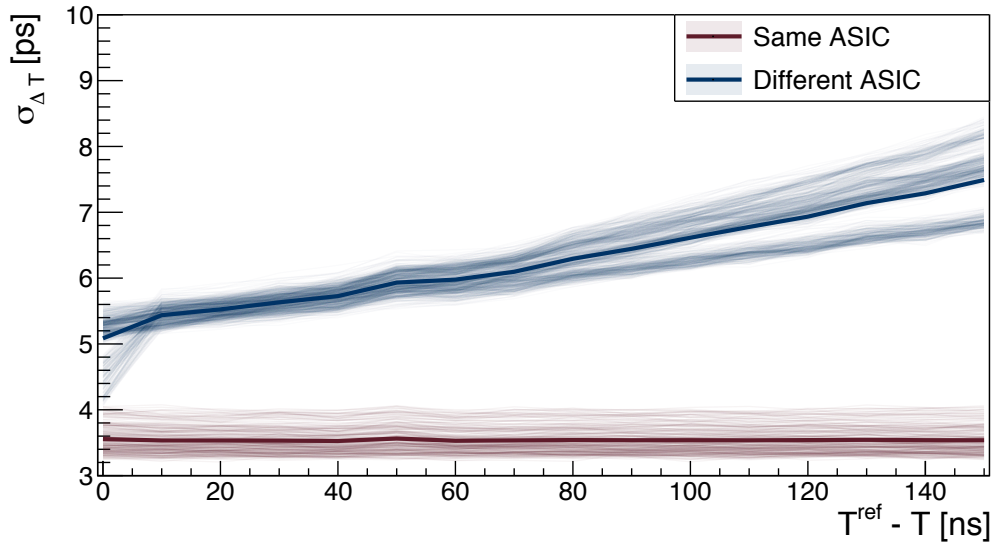
Figure 5.13 – Time difference jitter scan as a function of the distance to the reference signal and the measured one. The jitter is expressed as the value of the standard deviation in Gaussian fitted time difference histograms. Depending on the relative time displacement between the reference signal and the test signal a small increase in the jitter is observed.
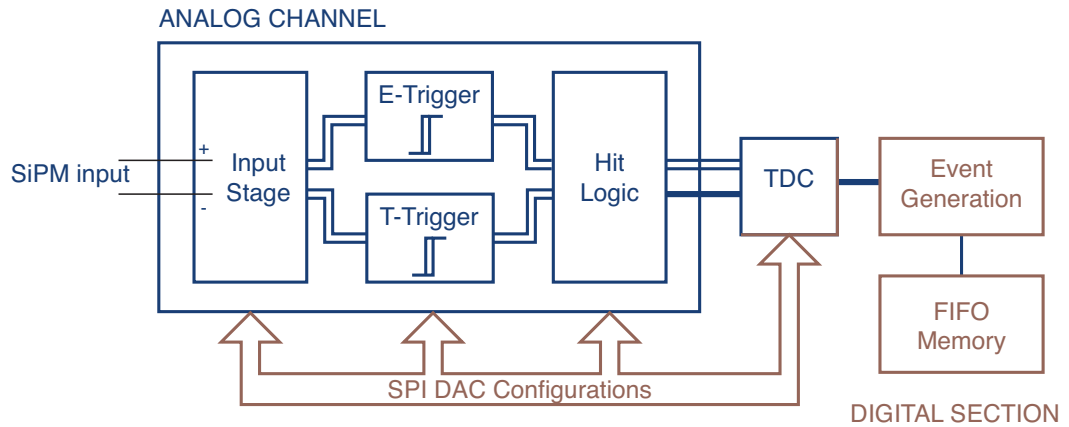
Figure 5.14 – Block diagram of a single MuTRiG channel. Figure adapted from [43].

the two signal paths - energy and timing. A fast leading edge discriminator determines the arrival of the signal at the $time$ threshold level. Another discriminator produces an output whenever the signal is above a second $energy$ threshold. The two signals are combined with an XOR operation to produce a single input for the TDC. The first leading edge of the encoded signal is digitized through a fine counter section with a bin width of 50 ps. The second rising edge corresponds to the end of the energy discriminator output. It is digitized only in

the coarse section of the TDC. The arrival time of the signal is determined with respect to a reference time t_0 driven by an external reset clock with a frequency of 625 MHz. The difference between the two time stamps - from the time and energy edges - results in a linearized time over threshold measurement.
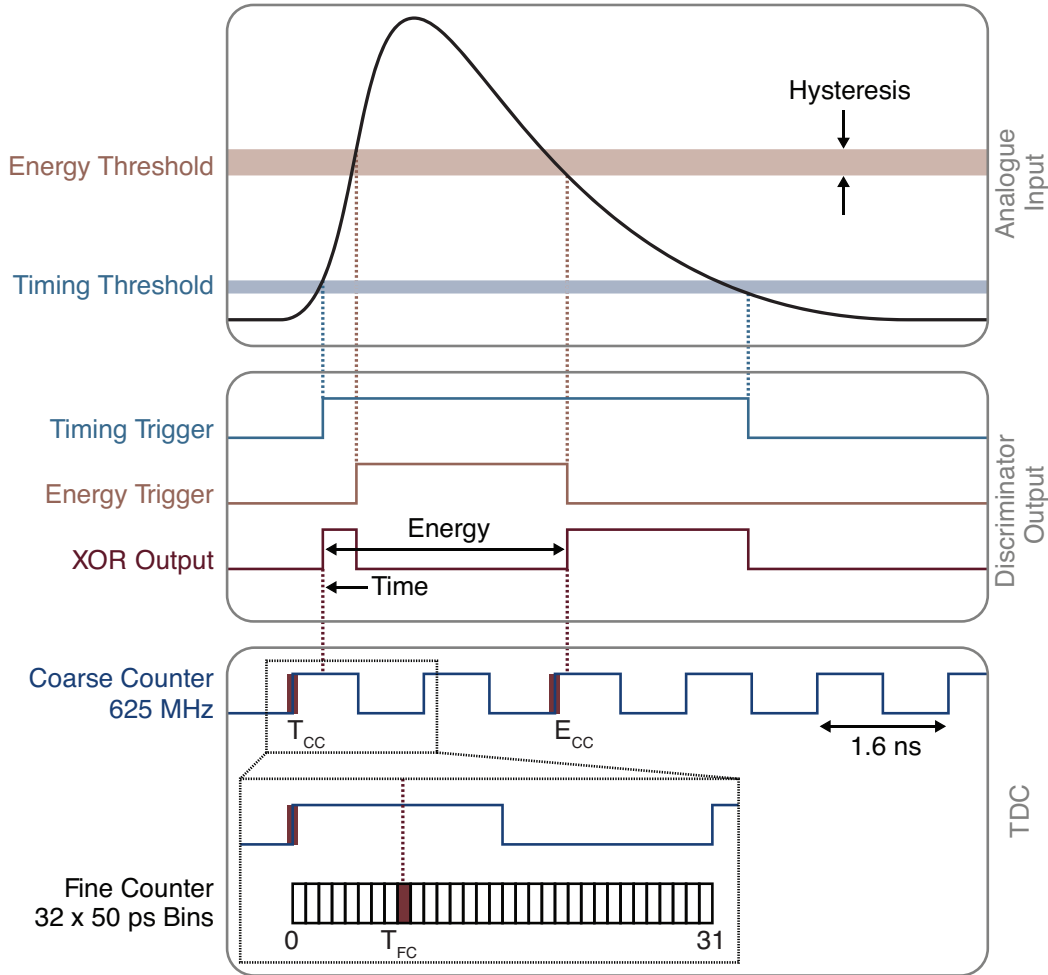
Figure 5.15 – Operational principle of the MuTRiG ASIC. Two thresholds in fast leading edge discriminators are used to extract time and energy information from the input signal. The outputs from the discriminators are combined such that a single TDC channel can digitize the result and provide time stamps for both measurements.

The resolution of the energy measurement is in the order of a few photoelectrons, hence it is only useful for the tiles detector where hundreds of photoelectrons are fired in each event. The expected output from the fiber detector is $\mathcal{O}(10 \text{ ph.e.})$. This renders the energy information unusable. Furthermore, meaningful energy thresholds for the fiber detector would be 1.5 ph.e. or 2.5 ph.e., see chapter 7. To save bandwidth the data from the energy branch is not transferred

for the fiber detector. Optionally, a flag indicating whether the threshold is reached can be set, however a finer tuning of the energy level is required. Events from the fiber detector including only the timestamps for the arrival time and an energy flag are encoded in 27 bits. Including the full energy information, as required for the tiles, results in 48 bits of data per channel. The result is encoded in 8b/10b scheme and transferred out of the MuTRiG over a LVDS link with a transmission rate of 1.25 Gbit/s.

6

Single Fiber Configuration

The present chapter describes the characterization measurements and analysis procedures used in testing scintillating fiber ribbons with single fiber readout. The performance of four prototypes with 250 μm thick fibers fanned out to individual photosensors at both ends is evaluated in an accelerated proton beam. Additionally, three ribbons equipped with SiPM arrays on one side are simultaneously tested and used as a beam telescope. The obtained results are summarized at the end of the chapter.

6.1 Experimental Setup

A schematic of the experimental setup utilized for the studies of scintillating fiber ribbons with single fiber readout is shown in Fig. 6.1. Trigger signals for the data acquisition are generated by a cross of two scintillating bars coupled to photomultiplier tubes (PMTs) located downstream along the beam axis. The overlapping sections of the trigger define an active area of 10 mm×10 mm in the $\vec{y}\times\vec{z}$ plane transverse to the beam direction.

A group of three scintillating fiber ribbons equipped with silicon photomultiplier arrays on one side form a particle tracker with a vertical pitch of 250 μm. The detectors are labeled $Array\_0$, $Array\_1$ and $Array\_2$. The distance along the beam between the first two modules is 30 cm while the second and third array ribbons are located 60 cm apart. A ribbon with individual fiber readout is placed in the middle between $Array\_1$ and $Array\_2$. Throughout this text the ribbon with single fiber readout is also referenced as the Device Under Test, DUT or $Ribbon\_SF$. Since the thickness of the ribbons seen by the beam is $\mathcal{O}(1\text{ mm})$, a module can be regarded as a plane.
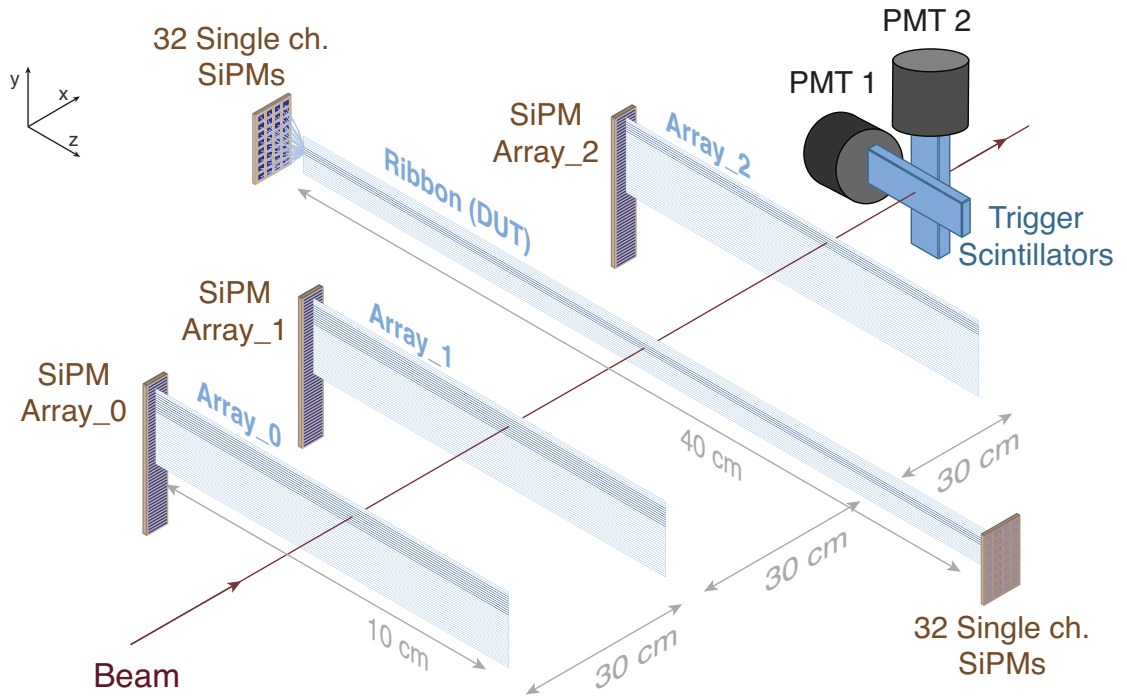
Figure 6.1 – Schematic of the setup used for measurements of single fiber readout prototypes. Three ribbons read out on one side only by column like arrays of SiPM sensors form a particle tracker - $Array\_0$, $Array\_1$ and $Array\_2$. The Device Under Test (DUT) is a ribbon with individual fibers fanned out to individual SiPM photosensors - $Ribbon\_SF$ (see subsection 3.3.2). It is placed after the second tracker module along the beam direction. The shaded areas in each ribbon represent the part of the detector that is digitized and used in the subsequent analysis. The figure is not to scale.

The length of the tracker ribbons is 10.0 cm and their width (along the vertical axis $\vec{\mathbf{y}}$) is about 30 mm. The ribbon with single fiber readout, on the other hand, is 40 cm long and 16 mm wide. The active area of each detector (darkened in the figure), however, spans only a subset of the fibers in a ribbon. It is limited by the electronics available for digitizing the SiPM channels.

In the present configuration, the sensitive parts of the $Array\_0$ and $Array\_1$ are 6.25 mm wide, while the channels digitized from $Array\_2$ correspond to a width of 3.5 mm. The fibers fanned out to individual SiPM sensors in the DUT correspond to a width of 2 mm.

All ribbons discussed in this chapter are constructed of staggered scintillating fibers with round cross-section and a diameter of 250 μm. One of the tracker ribbons is composed of two layers, while the remaining contain five fiber layers. The single fiber ribbon is made of four staggered layers and eight fibers of each layer are fanned out to individual SiPM sensors, see subsection 3.3.2.

The SiPM sensors attached to the tracker ribbons are S10943-3183(x) produced by HAMA-MATSU [78]. They are an earlier prototype version of the final device that will be used in MU3E and that is employed for the measurements in chapter 7. The arrays consist of column shaped channels with a size of 230 μm × 1.5 mm arranged next to each other in an array fashion, see subsection 4.3.2. A dedicated connector maps the individual fibers from the $Ribbon\_SF$ to HAMAMATSU MPPCs S12571-050P photosensors with an active area of 1×1 mm^2, see Figure 4.7.

During the test beam campaign conducted in the scope of this work four ribbons with single fiber readout are tested. Two of them are constructed with SCSF-81 fibers by KURARAY, exposed to UV light over an unknown period of time and two are produced with a newly purchased fibers of the same type. Ribbons of the former are referred to as $exposed$, while the later are labeled new throughout this text. Additionally, for each fiber type two distinct epoxy mixtures are used - one without any reflective components added to it and one with 20 % of TiO$_2$ powder.

Table 6.1 summarizes the types of ribbons characterized in this chapter. The first tracker ribbon set at the zero of the $\vec{\mathbf{x}}$ axis in the coordinate system shown in Fig. 6.1.

6.1.1 PROTON BEAM AT SPS

The measurements for this work are performed at the H2 beam line [79]. It is located in the north area (NA) of the CERN accelerator complex and receives intense proton beam with momentum of up to 400 GeV/c accelerated in the super proton synchrotron (SPS). The beam is delivered in spills with extraction time of 4.8 s to 9.6 s. The resulting particle content reaches $\mathcal{O}(10^8$ protons/spill). The ribbon tests are conducted with a proton beam of momentum

Label	Readout Mode	N Layers	Epoxy	Pos. $\vec{X}$ [cm]	MPPC Model
$Ribbon_{Clear}$	Single Fiber, Both sides	4	Clear	60	S12571-050P
$Ribbon_{TiO_2}$	Single Fiber, Both sides	4	20% TiO_2	60	S12571-050P
$Ribbon_{Clear}^{Exp}$	Single Fiber, Both sides	4	Clear	60	S12571-050P
$Ribbon_{TiO_2}^{Exp}$	Single Fiber, Both sides	4	20% TiO_2	60	S12571-050P
$Clear\_5L$	Column, One side	5	Clear	0, 30 or 90	S10943-3183
TiO_2_5L	Column, One side	5	10% TiO_2	0 or 30	S10943-3183
$Clear\_2L$	Column, One side	2	Clear	0 or 30	S10943-3183

Table 6.1 – A list of the detectors characterized within chapter 6.

150 GeV/c and an intensity $\mathcal{O}(10^5$ protons/s/cm$^2)$.

The energy deposited in polystyrene[1] by such protons is in the order of 230 keV/mm. On the other hand electrons with momentum $\mathcal{O}(50$ MeV/c) deposit about 217 keV/mm. Hence, the aforementioned proton beam is a suitable source for characterizing the performance of the fiber detectors in light of the expected Mu3e environment.

Additionally, the multiple scattering of 150 GeV/c protons passing through 1 mm of plastics[2] at these energies is negligible. Using Eq. 2.2, the width of the angular distribution is $\theta_{MS} \approx 3.6 \times 10^{-6}$. Thus hits in the fiber detectors can be consistently matched to particle trajectories of straight lines.

6.2 Data Taking

The first step in the data taking process is aligning the detector planes such that the protons reaching the trigger traverse the sensitive sections of the ribbons placed before it. While visual inspection and lasers are helpful, the precise location of the active fibers in a ribbon is known only to a few millimeters. Hence, the detector planes are aligned using the trajectories of the beam particles.

The success of the operation depends on two conditions. Firstly, the precision with which the position of particle interacting in a ribbon can be determined. With the present setup this is in the order of the diameter of the fibers i.e. 250 μm. Secondly, the precision with

---

[1]The core material of the scintillating fibers.

[2]The thickness of the scintillating fiber ribbons along the beam axis.

which module positions can be adjusted vertically, along the $\vec{\mathbf{y}}$ axis. In the current setup the ribbons are mounted on frames that can be moved up and down only manually. As a result, the alignment precision is in the order of 1 mm.

ALIGNMENT PROCEDURE

When a particle traverses a detector plane several fibers scintillate and generate signals in one or more SiPM channels. The number of photoelectrons produced in an SiPM channel is linearly proportional to the QDC value recorded by the data acquisition, see chapter 5. As a first approximation the position where the particle interacts with the ribbon is determined by the channel with largest QDC value. A correlation plot is constructed between the hits in every two planes. The x axis corresponds to the position of a hit in one of the planes and the y axis to hit locations in the other plane. An entry in the z axis is added when hits are observed in both planes within a time window of 60 ns. If two planes are aligned with one another the maximum of the correlated entries is in the center of the plot. Once a pair of detectors is aligned, the next ribbon is adjusted such that its correlation plots with the other two also show a maximum of entries in the middle of the histogram. The procedure is applied to all planes in order to reach an optimal configuration of the system.

Due to the poor resolution in adjusting the positions of the frames manually, the alignment is only partially successful. While the *Array_0* and *Array_1* have sufficiently large active areas $\mathcal{O}$(6 mm) to achieve overlap, the same is not true for the fanned out ribbon with 2 mm of active area. In fact, the detailed offline analysis after the test beam shows that the first three planes - namely *Array_0*, *Array_1* and the *Ribbon_SF*- are aligned and can be used for characterization. However, *Array_2* is not properly correlated with any of the remaining three and it is thus excluded from the analysis.

6.3 ANALYSIS

More sophisticated algorithms are developed for the data analysis after the test beam. The current section details the steps in extracting usable information from the collected data.

6.3.1 INDIVIDUAL CHANNELS

At first, the data is analyzed at the level of individual SiPM channels. A correlation plot between the digitized charge integral and its corresponding time stamp for one SiPM channel is shown in Fig. 6.2.
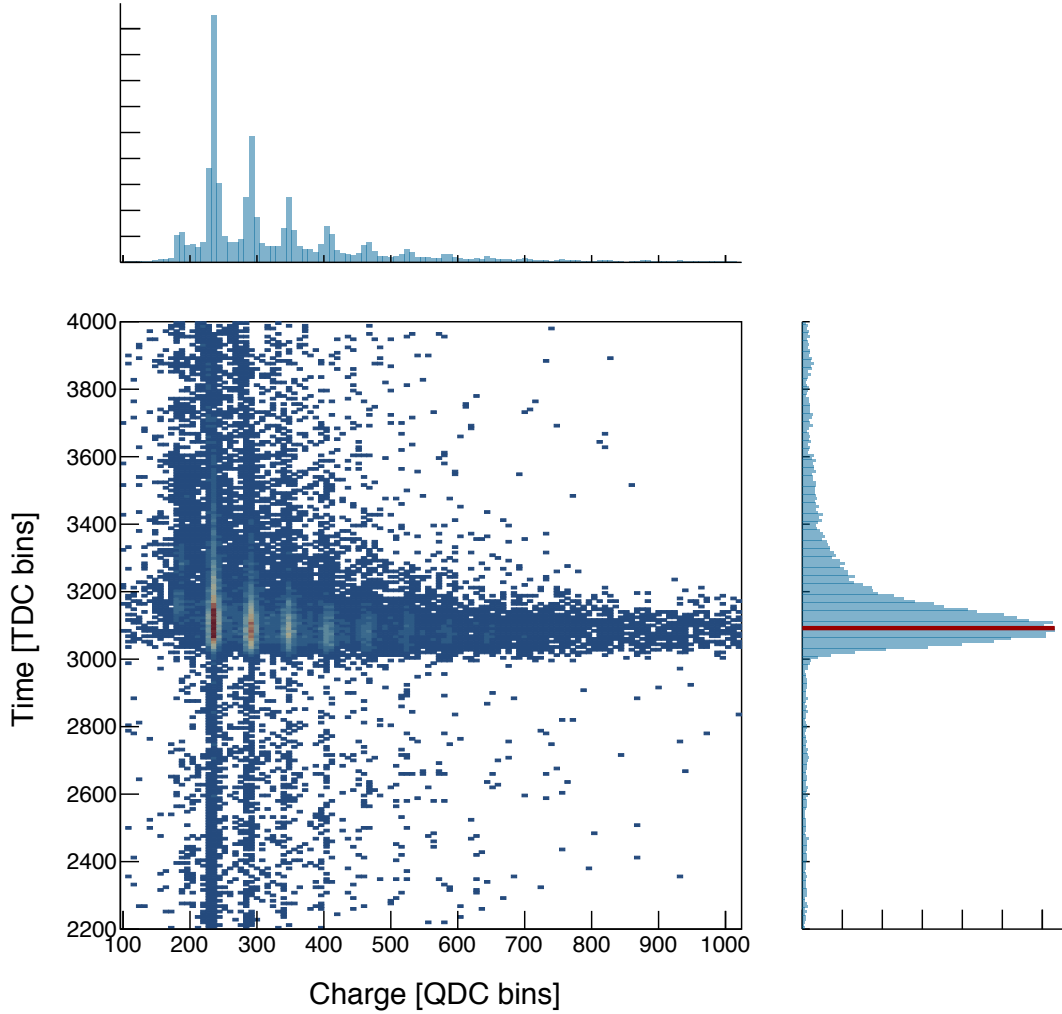
Figure 6.2 – Correlation plot of the digitized charge (QDC) and arrival time (TDC) parameters recorded for a single SiPM channel. The time projection (Right) is used to distinguish signal from background events based on their timestamps. Events with timestamps of ≤ 3000 TDC bins are the result of dark counts, hence they are treated as noise. The peaks in the charge projection (QDC) correspond to individual photoelectrons generated in the SiPM, with the highest one representing 1 ph.e. The correlation is generated by a fiber placed in the path of a 150 GeV/s proton beam. The photosensor is Hamamatsu S12571-050P biased at 67.5 V or +2 V above the breakdown.

The islands visible in the plot translate to photoelectron peaks in the QDC projection. The time stamps, on the other hand, are clustered around a single peak in the TDC projection. They represent the relative response of the channel with respect to the time of the DAQ trigger.

When a particle traverses both the fibers matching the channel under discussion and the trigger a timestamp is added to the TDC peak. Uniformly distributed timestamps, e.g. in the TDC bins below 3000, are the result of randomly discharged SiPM cells (i.e. dark counts) The centroid of the peak is fixed by the routing of the signal through the electronic circuits. The broadening, on the other hand, is governed by physical processes such as the Poissonian nature of scintillating light production, the inherent jitter in the response of the various detectors - PMTs and SiPMs, as well as by any noise superimposed on the signals which deteriorates the timing precision of the discriminator. Depending on the algorithm used to extract the time stamp, a jitter in the measured time can be observed. It typically manifests itself when leading edge discriminators are used and for PMT signals it is suppressed if the constant fraction algorithm is applied. The phenomena driving the response to light in an SiPM, however, are somewhat different from those in a PMT, hence a small variation with the amplitude is observed in the time measurements even when a constant fraction discriminator is adopted.

TIME WALK CORRECTION is the procedure that accounts for time jitter caused by differences in the amplitude[3] of the input signal. The effect is stable over time when the same algorithm for time extraction is used and can be corrected for. At first, timestamp projections corresponding to exactly 1, 2, 3 and so on photoelectrons are generated. Then the centroids of the time peaks are plotted against the number of photoelectrons[4] and the relation is modeled with a function of the form $f(t) = A + B * \sqrt{charge}$. In the subsequent steps of the analysis timestamps are corrected using the obtained A and B coefficients for each channel.

THE NUMBER OF PHOTOELECTRONS is extracted from the charge projection. Each peak is fitted with a Gaussian function and the centroid is mapped to the number of photoelectrons, see 7.7. In section 7.2 the SiPM charge is extracted from recorded signal waveforms and subsequently converted to number of photoelectrons. The procedure followed here is identical, albeit the charge is already available from the data acquisition and the waveform processing is handled by the electronics. In both cases the relation between the charge and the number of photoelectrons is linear.

---

[3] A linear relation exists between the amplitude and the integral of a signal from an SiPM channel, hence, for the current chapter only, the two terms are interchangeable.

[4] The number of photoelectrons is linearly proportional to the QDC values.

6.3.2 Layer and Plane Alignment

As discussed in section 3.2, a relative shift between fibers fanned out from different layers in the same ribbon is expected due to the inherent difficulty in seeing the individual fibers of an already constructed ribbon without damaging them. When a proton crosses a ribbon it deposits energy in a small subset of neighboring fibers. To reconstruct the displacement of fanned out fibers in a ribbon $2D$ hit histograms are created for each individual fiber. Entries are added to a histogram only if its ID matches that of the fiber, $F^{maxPh.e.}$, with highest number of photoelectrons registered in the given event. Each fiber that has produced a signal concurrently with the $F^{maxPh.e.}$ contributes to the histogram. Samples of the resulting hit maps for two fibers are shown under the *expected* labels in 6.3. The z axis of the histograms measures the number of hits at a given fiber position normalized to the number of hits in the fiber with maximal intensity. The topology observed in the *expected* plots cannot be produced from a proton traversing the fibers. The energy deposited in such an interaction is localized, hence the maximal hit intensity in each layer should appear at the same position along the $\vec{\mathbf{y}}$ axis. The position of the layer containing the fiber $F^{maxPh.e.}$ is chosen as a reference and the rest are aligned with respect to it. Repeating the procedure for all generated histograms demonstrates consistent behavior and the position reconstruction results are shown under the *true* labels in Fig. 6.3.
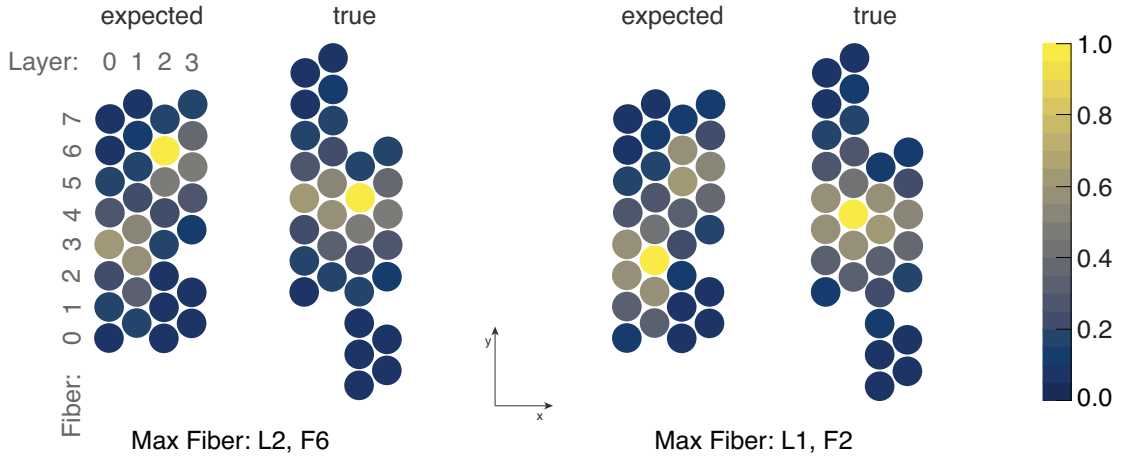
Figure 6.3 – An example of a ribbon where the fibers that have been chosen for the fanout are not staggered as expected. By looking at the hit distribution intensity in neighboring fibers the true positions of the fanned out fibers are reconstructed. This cross-section is produced with the $Ribbon_{Clear}$ ribbon.

The positions of fibers in each detector plane are recorded in a coordinate systems local to each plane such that the lower edge of the sensitive region corresponds to the beginning of the respective local $\vec{\mathbf{y}}_i$ axis. In order to use the fiber detectors as a tracker a coordinate system is

defined such that the zero of the new $\vec{\mathbf{y}}$ axis coincides with the bottom edge of the active region of $Array\_0$. The relative positions of the remaining two detectors are reconstructed under the assumption that protons traversing all three ribbons follow a straight line trajectory. The width of the angular distribution of protons with momentum of 150 GeV/c scattering through 3 mm of polystyrene is $\theta_{MS} \approx 6.3 \times 10^{-6}$. The distance along the beam between detector planes in the current setup is 30±5 cm, hence the trajectory deviation of protons passing through two planes is $\Delta y = \mathcal{O}(2\ \mu\text{m})$. The value is much lower than the precision of the fiber alignment within a ribbon, thus any effects arising from multiple scattering are negligible compared to the geometrical configuration of the ribbons.

Fig. 6.4 illustrates the alignment algorithm. Histograms are created for each of the detector planes with entries corresponding to the relative displacement of hits in the given detector with respect to the hit in the reference detector. Entries are added to the histograms only if interactions are detected in all three planes within a time window of 20 ns. A hit is valid if a ribbon has at least two neighboring channels with more than 0.5 ph.e. in each.
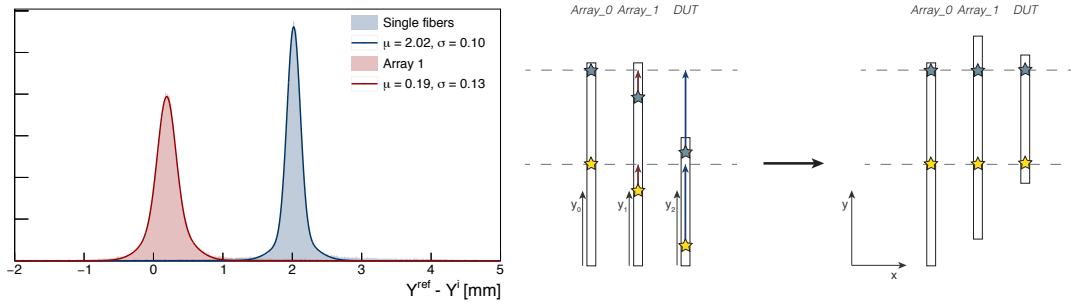
Figure 6.4 – The plane of $Array\_0$ is chosen as a reference and the alignment of the remaining two - $Array\_1$ and the DUT - is reconstructed in software using the deviations between hit positions in each plane with respect to the reference.

6.3.3 EFFICIENCY

Once the detector planes are aligned, tracks reconstructed from the hits in $Array\_0$ and $Array\_1$ are used to measure the efficiency of a ribbon with a single fiber readout.

The response of the detectors is displayed in Fig. 6.5 with cuts applied on the slope of tracks reconstructed from the coincidence in hits between $Array\_0$ and $Array\_1$. A single channel with at least 0.5 ph.e. in both arrays is required for a positive entry in this plot. The algorithm is however prone to falsely labeling a track as valid due to the high dark count rate $\mathcal{O}(100\ \text{kHz})$ of the SiPM channels reading out the arrays.

TRACKS CONDITIONS with conservative requirements are thus imposed on the hits in *Array_0* and *Array_1* in order to eliminate the probability of accidental coincidences that would underestimate the overall efficiency. The following criteria should be fulfilled concurrently for a track to be accepted:

$$
\begin{aligned}
\text{Cluster multiplicity:} && Mult^{A0} &\geq 2 && \cap && Mult^{A1} &\geq 2 \\
\text{Cluster light yield:} && NPhe^{A0} &\geq 3.5 && \cap && NPhe^{A1} &\geq 3.5 \\
\text{Coincidence time window:} && |T^{A0} - T^{A1}| &\leq && 20\ ns \\
\text{Track slope:} && |Y^{A0} - Y^{A1}| &\leq && \sigma_{\text{align}}^{A1}(\approx 0.13\ mm)
\end{aligned}
$$

Only then, any hits in the ribbon are considered. As discussed in the alignment section, the coordinate system is chosen such that the proton trajectories are parallel to the beam axis $\vec{\mathbf{x}}$. Hence, each valid track generates an entry in the histogram Array0 ∩ Array1 in Fig. 6.6. The position is set to the predicted value for a hit in the plane of the DUT. An entry is added to the second histogram if a hit is detected in the last ribbon together with a valid track and the deviation from the expected hit position is less than 0.5 mm (see Fig. 6.7). Finally, the efficiency is calculated for every bin as

$$
\varepsilon_i = \frac{k_i}{N_i} \tag{6.1}
$$

where k_i is the number of hits in the ribbon and N_i are the number of tracks selected under the afore stated conditions.

Fig. 6.8 is an example of an efficiency profile scan along $\vec{\mathbf{y}}$ for the $Ribbon_{TiO_2}$ ribbon. The data is modeled with a convolution of a square impulse function and a Gaussian. The smearing at the edges is consistent with the Gaussian variances observed in both the alignment histograms in Fig. 6.4 and the residual plot in Fig.6.7. The measured value $\sigma^{\Delta Y}$ = 160 µm is an upper estimate on the position resolution of the fiber detector.

6.3.4 CLUSTERING

Clustering is performed on an event basis for all signals in a given detector plane. A nearest neighbor algorithm is implemented. Channels are considered for clustering and added as cluster candidates if they have a minimum number of photoelectrons Th^{all}. Clusters are formed around a *seed* fiber defined as the one that outputs the highest number of photoelectrons in a
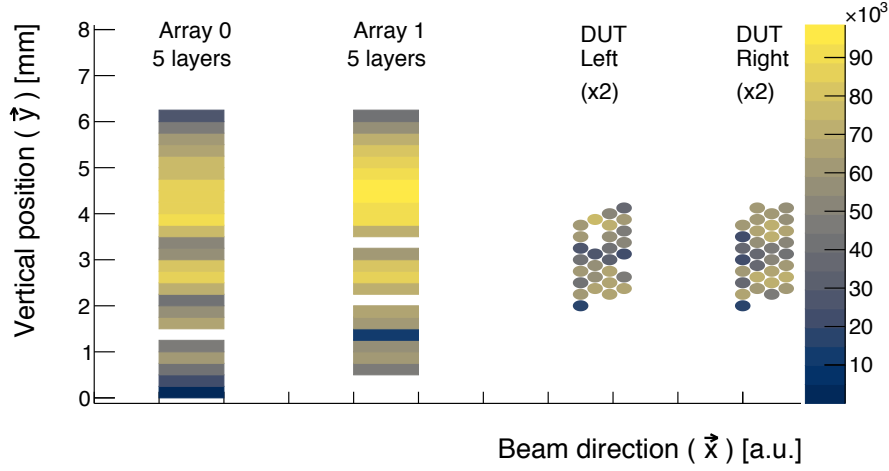
Figure 6.5 – Number of hits recorded in each detector channel during one run. The arrays exhibit higher number of hits per channel due to the larger effective area of the photosensor which couples to several fibers per channel while in the single fiber readout individual fibers are matched to separate SiPM channel. The DUT is $Ribbon_{TiO_2}$ ribbon and the S12571-050P photosensor are reverse biased at V_{br} + 2 V.
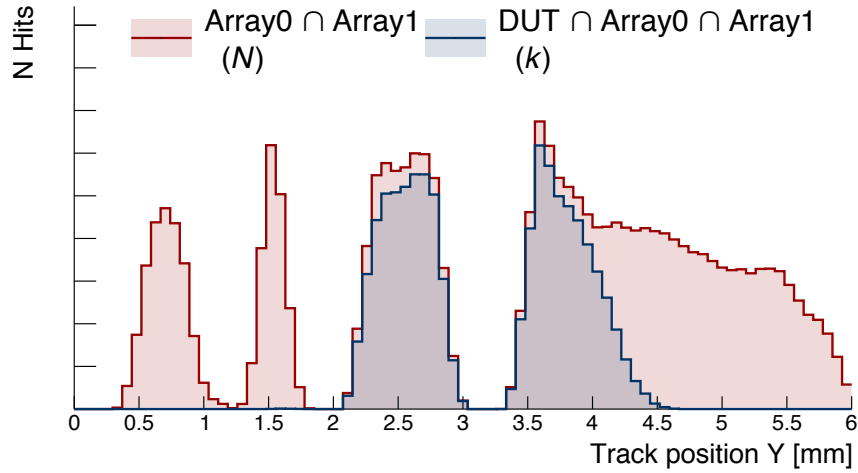
Figure 6.6 – Number of tracks (—) defined using conservative cuts (see text) on the hits of $Array\_0$ and $Array\_1$. Hits in the DUT matched with tracks (—) if the deviation from the track predicted position for the hit is within 0.5 mm. The empty regions correspond to locations with dead channels in either of the arrays.

given detector. The cluster building proceeds if the number of photoelectrons in at least one fiber surpasses the specified threshold labeled Th^{seed}. Immediate neighbor from the candidates list are then added to the cluster. If a cluster with a predefined minimal multiplicity is formed the hit in the detector is considered valid.

A special criteria is considered for labeling an event as valid in the single fiber readout.
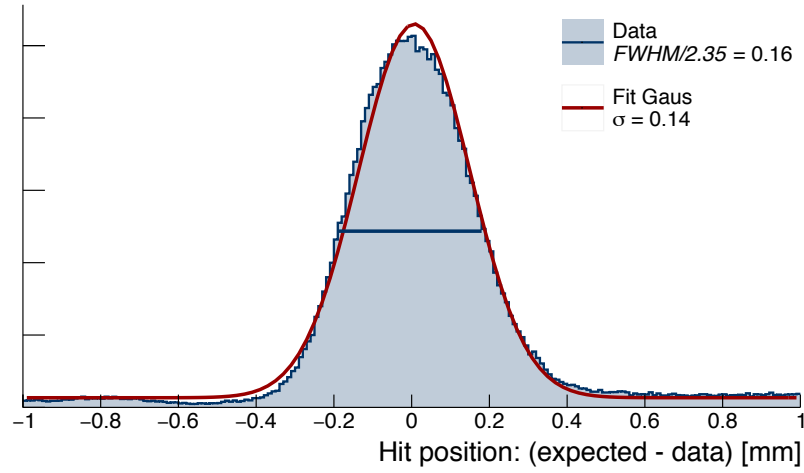
Figure 6.7 – Deviation between the predicted position of a hit in the DUT and the actually observed one. Only hits with residuals in the range (-0.5 mm, 0.5 mm) are used in the subsequent efficiency studies.
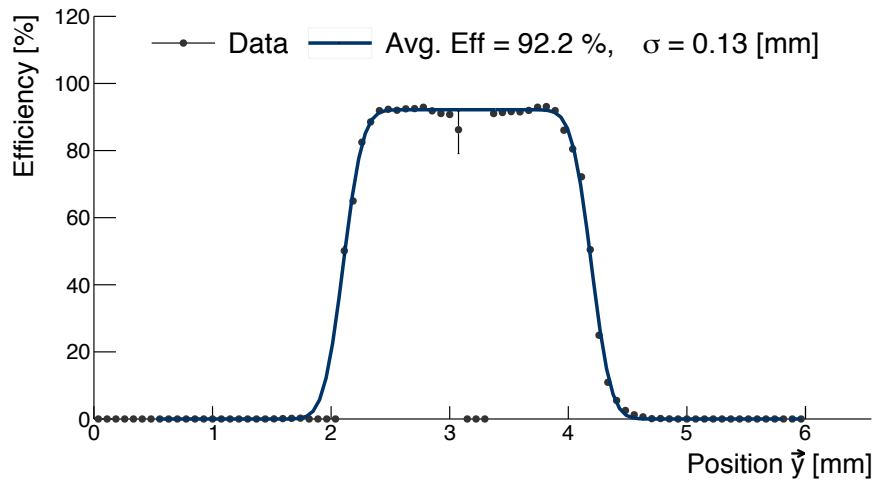
Figure 6.8 – Sample efficiency profile scan along $\vec{\mathbf{y}}$ for New_TiO_2 ribbon. The data is modeled as a convolution between a square impulse and a Gaussian. The reported value of $\sigma = 0.13$ mm is consistent with the position resolution of the tracker observed in previous plots.

Depending on whether or not a cluster is formed on both sides of the ribbon the following coincidence conditions are defined:

OR –   a cluster is reconstructed at either side of a detector

AND –   clusters on both sides of a detector are required simultaneously

In the OR configuration the seed threshold Th^{seed} needs to be true for only one fiber in

any of the two clusters (left or right). This means that a clusters can be formed with different seed thresholds in both sides, one of them being the lower candidates threshold. In the AND configuration the seed threshold requirement is imposed for each side independently, hence two channels - one from each side - should have registered sufficient number of photoelectrons.

CHOOSING THE CLUSTERING PARAMETERS

The quality of the clustering algorithm is assessed based on how well it suppresses the false positive hits while preserving the highest possible ribbon efficiency. Two of the detectors are used with stringent conditions to provide track hits. The cluster parameters in the third detector are varied to optimize the algorithm.

The ribbon efficiency and the noise level shown in Fig. 6.9 are the quantities used for comparison between different parameter sets. The hits in the device under test are not restricted geometrically for the efficiency. This means that if a noise event occurs in the detector simultaneously with a hit expected outside of its sensitive area, the entry will be added at the expected position. The active width of the ribbon measured for this plot is about 2 mm and it corresponds to the area with the highest measured efficiency. No true hits are expected in the DUT at positions below 1 mm and above 5 mm for this setup due to the strict geometrical requirements for the tracks.
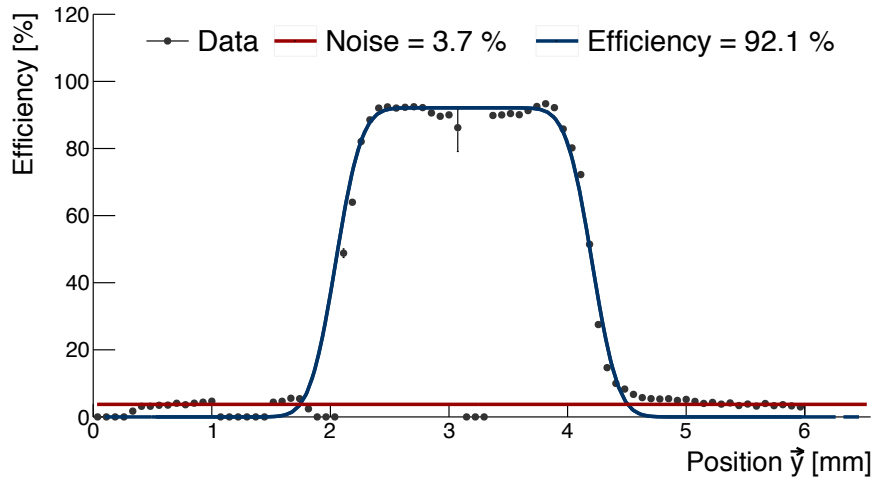
Figure 6.9 – Tracks constructed with strict cuts applied on the hits in $Array\_0$ and $Array\_1$ are used to scan a ribbon with active width of ≈ 2 mm. The overlapping sensitive fractions of $Array\_0$ and $Array\_1$ cover ≈ 6 mm. Points in the central section represent the measured efficiency in the DUT while at positions below 1 mm and above 5 mm no true hits are expected, hence they are used to identify falsely accepted hits due to the discrimination capabilities of the clustering algorithm. The sections where the efficiency is zero are caused by dead channels in the data for one (or both) of the arrays.

105

Table 6.2 summarizes the performance of the clustering algorithm under varying parameters for ribbons with single fiber readout. Unless otherwise specified, evaluation and comparison of all four ribbons characterized in these test measurements are conducted with the set of parameters PSet ID = 9. If the readout electronics does not allow for double thresholds e.g. in the case of MuTRiG, the preferred clustering algorithm would be PSet ID = 6. As the measurements in this section are performed before finalizing the design for the readout electronics, freedom is allowed on the number of amplitude thresholds. Moreover, the PSet ID = 6 will consistently underperform for configuration with only two active layers as is the case for some sections of $Ribbon_{Clear}$.

PSet ID	$\mathrm{Th}^{\mathrm{all}}$ [N Ph.e.]	$\mathrm{Th}^{\mathrm{seed}}$ [N Ph.e.]	Cl. Mult. $\geq$	Coinc. Type	Noise [%]	Efficiency [%]
1	0.5	0.5	1	AND	3.04 ± 0.08	89.88 ± 0.10
2	0.5	0.5	2	AND	1.60 ± 0.06	66.04 ± 0.15
3	0.5	0.5	3	AND	0.89 ± 0.05	30.93 ± 0.15
4	0.5	0.5	1	OR	30.23 ± 0.22	93.40 ± 0.08
5	0.5	0.5	2	OR	4.32 ± 0.10	92.04 ± 0.10
6	**0.5**	**0.5**	**3**	**OR**	$\mathbf{2.33 \pm 0.07}$	$\mathbf{89.10 \pm 0.11}$
7	0.5	1.5	1	AND	2.13 ± 0.07	76.98 ± 0.14
8	0.5	1.5	1	OR	12.77 ± 0.16	93.66 ± 0.09
9	**0.5**	**1.5**	**2**	**OR**	$\mathbf{3.56 \pm 0.09}$	$\mathbf{92.14 \pm 0.10}$
10	1.5	1.5	1	AND	2.23 ± 0.07	77.92 ± 0.14
11	1.5	1.5	1	OR	13.76 ± 0.17	94.75 ± 0.09
12	1.5	1.5	2	OR	2.64 ± 0.08	86.99 ± 0.11

Table 6.2 – Various parameters in the clustering algorithm are varied in order to achieve optimal performance in terms of background suppression while maximal efficiency is preserved. The study is performed on a ribbon with single fiber readout and is relevant for such configurations only. Unless otherwise specified, the default parameter set is PSet ID = 9.

The light yield spectrum of the fiber with maximum number of photoelectrons in a cluster is shown in Fig. 6.10. On top of applying the same track conditions for hits in $Array\_0$ and $Array\_1$, the absolute value of the residual between the expected hit position and the measured one in the DUT is confined to ≤ 0.3 mm. The results are extracted using clustering algorithms with OR coincidence, $\mathrm{Th}^{\mathrm{all}} = \mathrm{Th}^{\mathrm{seed}} = 0.5$ ph.e. and multiplicity either ≥ 1 or ≥ 2.
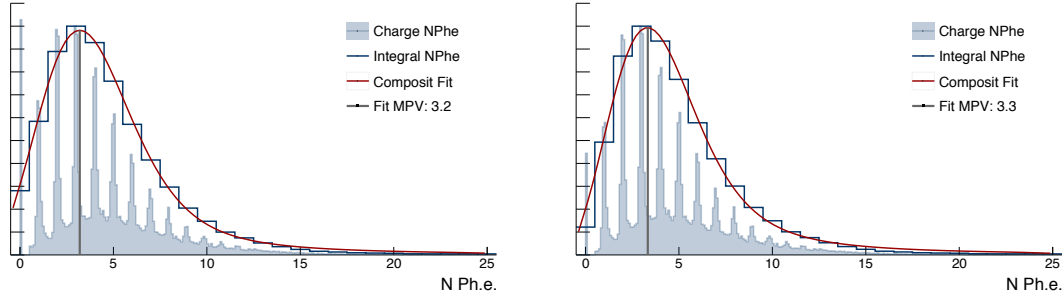
Figure 6.10 – Photoelectron spectra of fiber with maximum charge per cluster for one side of a ribbon with a single fiber readout. Clustering algorithm assumes OR coincidence, Th^{all} = Th^{seed} = 0.5 ph.e. and multiplicity $\geq$ 1 (Left) or multiplicity $\geq$ 2 (Right). The data is generated with $Ribbon_{TiO_2}$ ribbon.

The spectrum provides insight about the rapidly decreasing efficiency of the DUT when higher number of photoelectrons are imposed at the Th^{all} and Th^{seed}. As the shape is representative for both sides, requiring more fibers with higher collected charge per channel significantly decreases the efficiency.

6.3.5 Features Comparison

Scintillating fiber ribbons are compared in terms of cluster light yield, time resolution, efficiency and fiber cross talk.

With exception of the optical cross talk between fibers, the rest of the parameters are extracted for particle trajectories crossing the DUT at positions (along $\vec{\mathbf{y}}$) where fibers in all four layers are equipped with photosensors and at most one channel is inactive. The restriction is necessary for ribbons such as $Ribbon_{Clear}$ where half of the active area is only covered by two photosensitive layers.

Light yield is reported as a sum of the recorded number of photoelectrons in all cluster channels.

Time resolution is compared in terms of the observed time difference between cluster timestamps on both sides of a $Ribbon\_SF$[5]. While each channel bears its own timestamp, the cluster time can be selected through multiple considerations. Among the following four algorithms, the one that results in the narrowest time difference distribution is preferred.

- **TFirst** - the arrival time of the first photon is set as the cluster time i.e. the channel with the smallest timestamp defines the cluster time

---

[5]When using a clustering algorithm with OR coincidence type, only events in which clusters are formed on both sides are considered for the timing.

- **TMaxPhe** - the arrival time of the channel with the highest number of photoelectrons in the cluster is used

- **TMeanW** - mean time of all cluster channels weighted by the number of photoelectrons in each one

- **TMean** - unweighted mean time of all cluster channels

Fig. 6.11 is an example of a time difference distribution obtained using the **TFirst** algorithm on the $Ribbon_{TiO_2}$ ribbon. Simulation studies [48] on the time difference between the two ends of a single fiber when the arrival time of the first photon is used as a time stamp indicate the shape of the distribution can be modeled with a symmetric exponential function such as the Laplace distribution:

$$f(t) = c \cdot e^{-\frac{|t|}{\tau}} \tag{6.2}$$

It is a direct consequence of the Poissonian nature of the scintillating process. The parameter τ scales as $\propto 1/(Nph.e.)$ with the number of produced photons. Since the efficiency of the SiPMs is $\mathcal{O}(35\ \%)$ the first photon is not always detected. Moreover, jitter in the time difference is also introduced by the electronics, hence for the data observed in Fig. 6.11 the Laplace distribution is smeared with a Gaussian. An "equivalent" standard deviation σ^{equiv} is introduced to compare the distribution with the design parameters of Mu3e where Gaussian distribution is assumed for the time difference.

$$\sigma^{equiv} \approx \frac{\text{FWHM}^{\text{conv}}}{2.35} + \sigma^{\text{conv}} = \frac{2\tau^{\text{conv}}\ln(2)}{2.35} + \sigma^{\text{conv}} \tag{6.3}$$

The same argument holds when reporting the $\frac{\text{FWHM}}{2.35}$ of the raw distribution.

The proposed cluster time algorithms are investigated on the same dataset and their performance is summarized in Table 6.3. Time resolution of the fiber detectors compared in this chapter is extracted using **TFirst** method as it delivers the best results.

6.3.6 FIBER CROSS TALK

Cross talk between fibers is observed when scintillating photons originating from one fiber are trapped and propagated to a photosensor through another, usually neighboring fiber. To quantify the effect light sharing between adjacent fibers in the same ribbon layer is investigated. Tracks with expected position along the full active area of a $Ribbon\_SF$ are selected and only fibers matched to a cluster are analyzed. To account for inefficiencies in the the photosensor, the maximal distance between a fiber already assigned to a cluster and a candidate
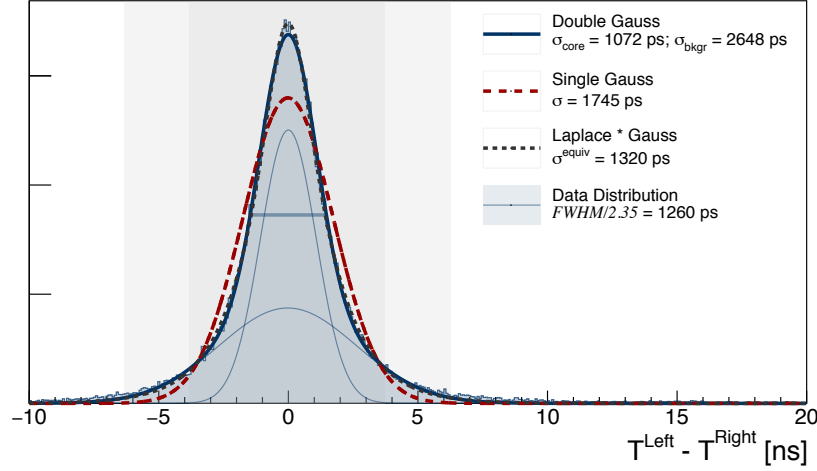
Figure 6.11 – Time difference distribution using the **TFirst** algorithm on the $Ribbon_{TiO_2}$ ribbon. The data is best modeled with a convolution of a Laplacian and Gaussian, however, a double Gaussian (sum of two Gaussian distributions) is also an acceptable function and offers an intuitive interpretation of the fit parameters.

Time Algorithm	$\frac{FWHM}{2.35}$ [ns]	σ^{equiv} [ns]	σ^{Gauss} [ns]	$\sigma^{D\ Gauss}_{core}$ [ns]	$\sigma^{D\ Gauss}_{bkgr}$ [ns]	N^{core}/N^{bkgr}
TFirst	1.26	1.32	1.74	1.07	2.64	1.15
TMaxPhe	1.77	1.79	2.61	1.35	3.59	0.71
TMeanW	2.31	2.47	3.53	1.73	4.83	0.63
TMean	2.01	2.05	2.88	1.54	3.94	0.75

Table 6.3 – Comparison of the algorithms for choosing the cluster time.

fiber is set at two fiber diameters i.e. not only immediate neighbors but also the next neighbors are added to the cluster if they have produced sufficient amount of light. The primary point of interaction is set in the fiber with the highest number of photoelectrons per layer. If photons are registered from a second fiber in the same layer they are added to a histogram bin reflecting the vertical offset with respect to the main fiber (see Fig. 6.12). The main fiber contributes to the bin with a center at 0.

The overall event multiplicity[6] is also affected by the optical cross talk and is an additional parameter that assesses the effect of adding TiO_2 powder to the epoxy. Fig. 6.13 shows the event multiplicity distribution in $Ribbon_{Clear}$ and $Ribbon_{TiO_2}$ ribbon. The data is modeled with a convolution of Gaussian and Landau distributions. The most probable value from the

---

[6]Event multiplicity is the total number of cluster candidate channels.
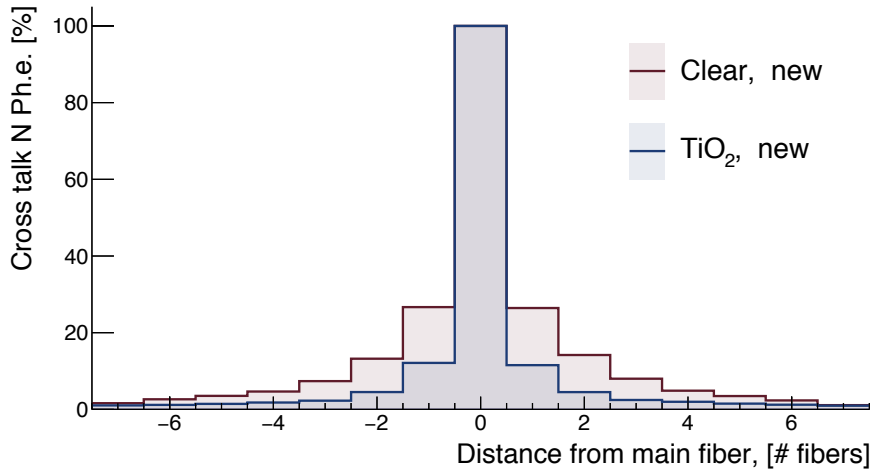
Figure 6.12 – Percentage of light registered through fibers in one layer. The central bin corresponds to the main fiber in every event where the highest number of photoelectrons is recorded. Adding 20 % TiO$_2$ powder to the epoxy while gluing the fibers into a ribbon reduces the crosstalk. The data is obtained from the two ribbons with *new* fibers.

fit is reported in the results section.
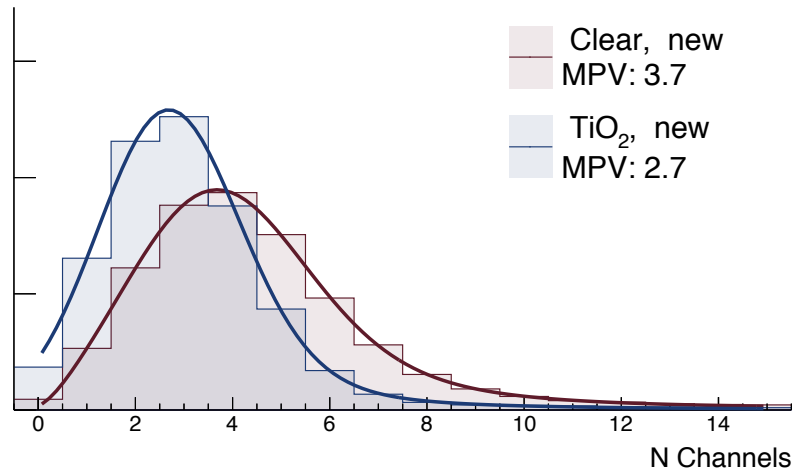
Figure 6.13 – Event multiplicity as seen on one side of the ribbons with *new* fibers. The photoelectron threshold is 0.5 ph.e. Entries in the zero bin are added only if a cluster is found on the opposite side but not in the currently analyzed one. The data is modeled with a convolution of a Gaussian and Landau distributions with the MPV of the fit reported in comparisons between samples.

6.3.7 Column Readout

The present setup is also suitable for studies of the column readout configuration, albeit somewhat limited since only one side of each ribbon is equipped with a photosensor. By reconstructing tracks with one of the $Array\_0(1)$ planes and the $Ribbon\_SF$ the other can be evaluated. Light yield, efficiency and crosstalk are extracted independently for each detector plane under test. The time resolution, however, is estimated from the time difference between the two $Array$ planes.

6.4 Results

The principal goal of this test beam campaign is to investigate the feasibility of ribbons with single fiber readout for the Mu3e experiment. Hence the time resolution of the detector should conform to the design requirement of ≤ 0.5 ns, while the efficiency should be in excess of 95 %. Both parameters are directly dependent on the light yield of the fibers.

Cross talk effects in the inner ($L1$ and $L2$) and outer layers ($L0$ and $L3$) are examined independently to assess differences arising from their respective position in the ribbon. No significant variations ($\leq 5\%$) are observed between the four layers of a sample, neither between the left and right sides. Table 6.4 summarizes the results for all tested $Ribbon\_SF$ detectors. The entries are averaged in both sides and all layers of a SciFi ribbon. Differences in the crosstalk suppression observed in the ribbons with added TiO_2 are attributed to uncontrolled distribution of the reflecting powder during production.

Ribbon Distance	$Ribbon_{Clear}$	$Ribbon_{Clear}^{Exp}$	$Ribbon_{TiO_2}$	$Ribbon_{TiO_2}^{Exp}$
0	100.0 %	100.0 %	100.0 %	100.0 %
1	24.7 %	22.0 %	12.0 %	15.4 %
2	12.6 %	11.8 %	4.4 %	5.9 %
3	7.1 %	6.8 %	2.4 %	3.3 %
4	4.4 %	4.2 %	1.7 %	2.2 %
5	3.0 %	3.5 %	1.3 %	1.6 %
6	1.9 %	2.4 %	1.1 %	1.2 %
7	1.5 %	2.0 %	1.0 %	1.0 %

Table 6.4 – Single fiber cross talk summary. The entries represent the fraction of photoelectron detected N fibers away from the main interaction fiber per layer.

Summary The single fiber readout configuration offers unique environment to study the cross-talk between individual fibers in the SciFi ribbons. However, the overall performance of the tested prototypes is at the upper limit and of the early days requirements for the Mu3e experiment[7]. The efficiency results are also not very promising. While results from the column readout (see chapter 7) show that the SCSF-81MJ is not the most efficient fiber, further studies with the single fiber readout are not conducted. On one hand the very tight space constrains for the SciFi detector make it difficult to fit a ribbon with additional 2 to 3 cm of fanout for the single fibers. On the other hand, the high risk of damage during construction and handling of the SciFi ribbon increases the cost of the project, mainly in human hours. Additionally, using the single fiber readout would require the development of a custom SiPM arrays and 3 to 4 times more readout channels, depending on the number of layers. The eventual cost outweighs significantly the potential gains from having a detector with such granularity.

Ribbon Type	Efficiency [%]	Time res. [ps] $\frac{\text{FWHM}}{2.35}$	Light Yield [MPV] Left	Right	Ev. Multipl. [MPV] Left	Right
$Ribbon_{Clear}$	80.0 ± 0.2	1395 ± 38	7.8 ± 1.7	4.9 ± 1.2	3.9 ± 0.4	2.8 ± 0.2
$Ribbon_{Clear}^{Exp}$	79.0 ± 0.3	1362 ± 53	6.4 ± 1.7	5.5 ± 1.5	3.3 ± 0.4	3.2 ± 0.3
$Ribbon_{TiO_2}$	91.5 ± 0.1	1260 ± 23	6.0 ± 1.2	6.0 ± 1.4	2.6 ± 0.2	2.8 ± 0.2
$Ribbon_{TiO_2}^{Exp}$	82.8 ± 0.5	1328 ± 74	4.7 ± 1.1	3.4 ± 1.0	2.3 ± 0.3	2.0 ± 0.3

Table 6.5 – All results are obtained using the default clustering algorithm requiring at least one channel with $\geq$ 1.5 ph.e. from one of the sides, OR coincidence and cluster multiplicity $\geq$ 2. For the time resolution, light yield and event multiplicity additional cuts are applied on the track to ensure trajectories crossing four layers equipped with photosensors are traversed. The efficiency is extracted at the maximum of a profile fit modeled as a convolution between a Gaussian and a square impulse. The photosensors remain identical through all measurement and they are biased at V_{br} + 2 V.

---

[7]While in the latest specification the expected time resolution from the SciFi detector should be better than 350 ps per side, in the early days of the R&D phase, the criteria were more relaxed, requiring a time resolution better than 1 ns.

Position	Ribbon Type	Efficiency [%]	Time res. [ps] $\frac{FWHM}{2.35}$	Light Yield [MPV]	Ev. Multipl. [MPV]
$Array\_0$	$Clear\_2L$	71.2 ± 0.2	1075 ± 34	5.5 ± 1.3	3.0 ± 1.2
$Array\_1$	$Clear\_5L^1$	90.1 ± 0.2		10.0 ± 2.4	3.8 ± 1.2
$Array\_0$	TiO_2_5L	87.6 ± 0.2	953 ± 16	9.3 ± 2.5	3.4 ± 0.9
$Array\_1$	$Clear\_5L^2$	78.0 ± 0.2		9.2 ± 2.2	4.2 ± 1.2

Table 6.6 – Default clustering parameters are used i.e. multiplicity ≥ 2 and at least one channel with ≥ 1.5 ph.e. Since the ribbons with column readout are coupled to photosensors only at one side, the time resolution is extracted from the time difference between hit in $Array\_0$ and $Array\_1$. In both runs the SiPMs are reverse biased at V_{br} + 2.5 V. $Clear\_5L^1$ and $Clear\_5L^2$ designate two different ribbon samples with identical number of layers and coating. The difference in the efficiency is attributed to a dead channel in $Array\_1$ coinciding with the active area of the $Ribbon\_SF$ detector, hence affecting the clustering algorithm.

7

Column Configuration

This chapter presents the characterization of scintillating fiber ribbons coupled to monolithic SiPM arrays. Following is a discussion on the analysis algorithms and the obtained results. Various materials, shapes and coatings are examined to reach a conclusion on the design of the Mu3e fiber detector.

7.1 Experimental Setup

A schematic of the experimental setup used for characterization of the SciFi prototypes with column readout is depicted in Fig. 7.1. The Device Under Test (DUT) is a scintillating fiber ribbon with a width of ≈ 8 mm (along $\vec{y}$), a length of ≈ 300 mm (along $\vec{z}$) and a thickness of ≈ 1 mm (along $\vec{x}$) equipped on both sides with Hamamatsu S13552-HQR SiPMs for optical readout. The ribbon and the sensors are mechanically attached to a common motorized frame movable vertically (along the $\vec{y}$ axis) and rotatable around the horizontal axis $\vec{z}$. The DUT is sandwiched between a trigger detector downstream the beam axis and an optional single scintillating fiber upstream. The active areas of the two instruments is much smaller than that of the ribbon. Thus they form a simplified beam telescope suitable for efficiency measurements.

7.1.1 Triggering

The role of the trigger detector is to select particles whose trajectories are confined within a narrow region of space. For this purpose two thin scintillating fibers, 1 mm in diameter each, have been arranged in a cross configuration and placed in a close proximity behind the DUT.
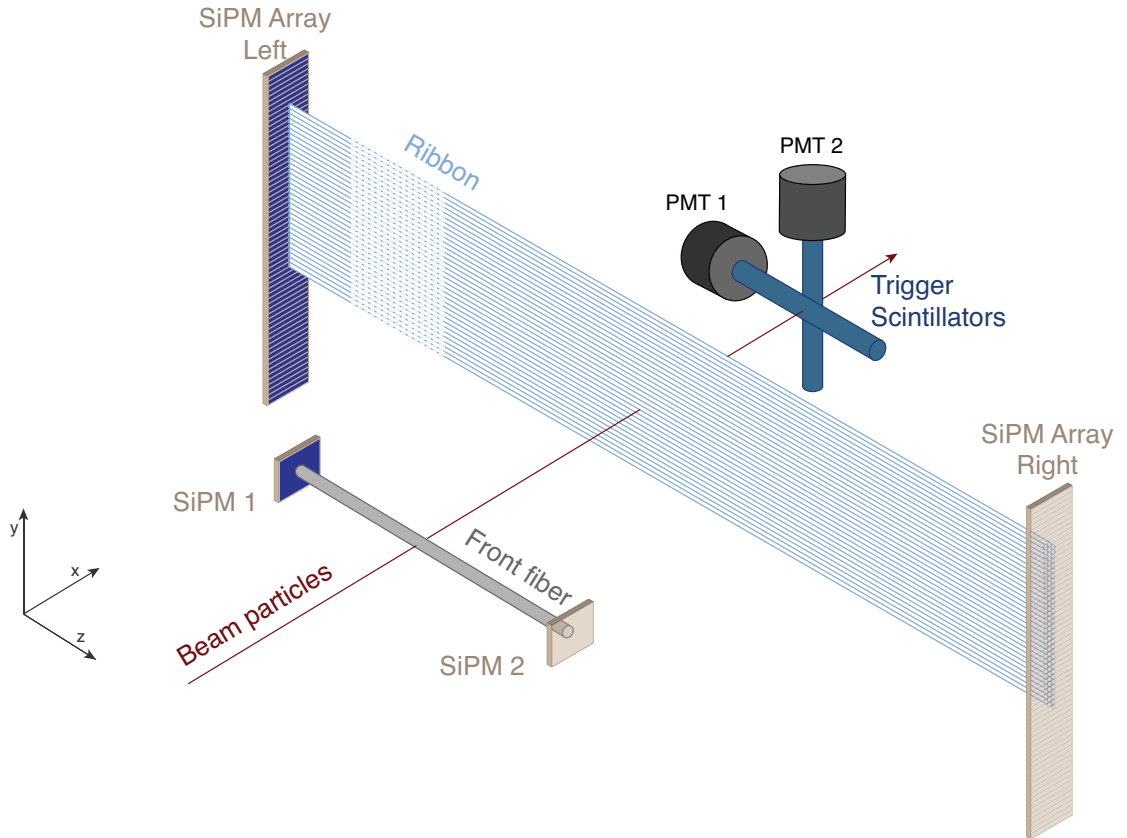
Figure 7.1 – Experimental setup for characterization of the SciFi ribbons with column readout. Two crossed scintillating fibers (—) placed closely behind the ribbon (—) under test serve as a trigger for incoming beam particles (—). An additional fiber (—) in front of the ribbon is used in some of the measurements to form a simplified beam tracking telescope with the triggers. Both sides of the ribbon are equipped with multichannel SiPMs (—). The front fiber is also coupled to two single channel SiPMs (—) on both sides, while the trigger scintillators are readout by conventional PMTs (—)

Each trigger fiber is connected on one side with a compact PMT [48]. The PMT outputs are independently passed through a level discriminator. It generates a positive logical output when the amplitude of the input signal is above a predefined threshold. Afterwords, a coincidence unit determines if the two logical signals occurred concurrently within a window of 10 ns. In case of a positive outcome the data acquisition receives a start signal and the waveforms are recorded with the DRS4 based digitizing boards. As explained in chapter 5, new trigger arrivals are blocked while the digitization is ongoing. The single fiber in front of the DUT has a diameter of 500 μm and is readout on both sides by Hamamatsu S13360-1375CS with an active area of 1.3 mm × 1.3 mm. It is positioned at a distance of only a few centimeters ($\approx$ 2 cm) upstream the DUT. The combined trigger and front fiber system has an efficiency $\mathcal{O}(10\ \%)$ relative to the cross only. Since many fiber comparisons can be achieved without the telescope setup and higher number of events is preferred, the front fiber signals were recorded for offline processing only and not used in the online trigger.

7.1.2 ELECTRON SOURCES

The main part of the measurements are carried out at the πM1 testbeam area in PSI, while some cross validation and additional SciFi ribbons are characterized in lab conditions with a radioactive source.

πM1 TESTBEAM AREA

The πM1 line at PSI delivers a mixed beam of electrons, pions and muons with an optional choice of the polarity. The momentum of the particles can be tuned between 100 MeV/c and 500 MeV/c. Depending on the selected energy, the concentrations of each particle type vary. Positrons dominate $\mathcal{O}(60\ \%)$ the mixture at momenta below $\lesssim$ 170 MeV/c[1]. For the measurements performed in this work a beam of positively charged particles was used and the momentum was fixed at 161 MeV/c. Due to their different masses electrons, muons and pions with the same momenta can be identified via their time of flight over a fixed distance. In this case, protons accelerated in the PSI cyclotron impinge on the facility's carbon target M at intervals of 19.74 ns determined by the radio frequency (RF) of the accelerating cavities (50.63 MHz). The pions extracted at the interaction between the protons and the target quickly decay into muons and electrons and the mixture is directed towards the testbeam area. The distance of $\approx$ 21 m between the target and the trigger cross is sufficient to allow particle identification. To this goal the time difference between the RF signal and the trigger is used. Both signals

---

[1]The momentum boundary is about $\lesssim$ 220 MeV/c for electrons to be the main beam component at negative polarities

are recorded for offline analysis. Fig. 7.2 shows the resulting time difference distribution for one data run where the three particle type can be clearly distinguished. A cut starting at 2σ before the maximum of the electron peak and extending until the end of the histogram range (≈ 24 ns) can be applied in the analysis to select only electrons. The particle identification procedure described here is first used in [48].
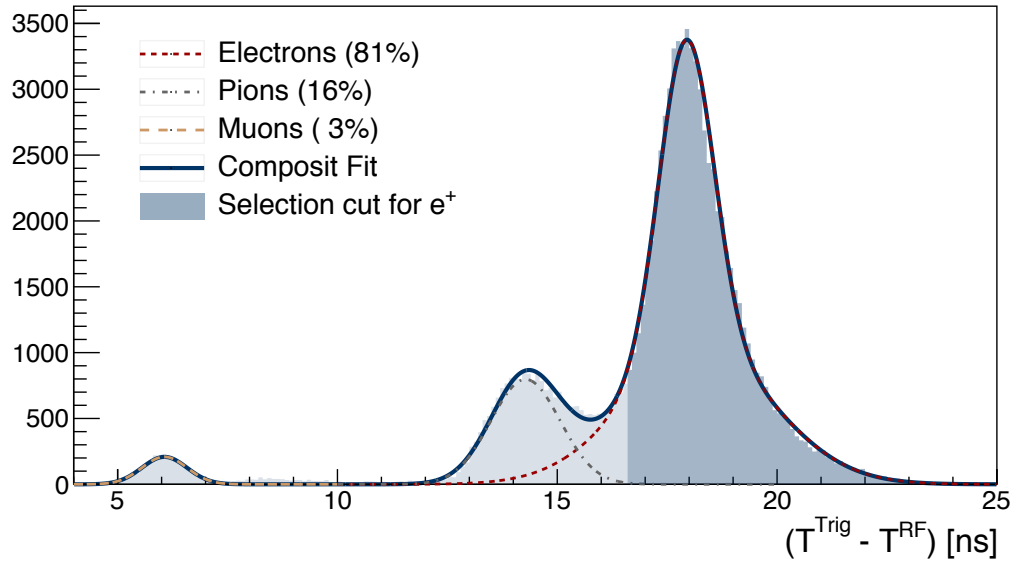
Figure 7.2 – The πM1 beam consists of pions, muons and electrons in different ratios depending on their momentum. For the 161 MeV/c beam particles the above time of flight between the trigger cross and the πM1 production target is recorded. Particle concentrations are extracted after a composite fit of four Gaussian functions. The shaded area represent the cut applied to select only electrons.

^{90}Sr Radioactive Source

The radioactive element strontium-90 (^{90}Sr) is a source of β^- radiation with a half-life time of 28.8 year [80] It decays to yttrium-90 (^{90}Y) via emission of an electron with an end point momentum (maximum momentum) of 0.546 MeV/c. The daughter nucleus ^{90}Y is also unstable and emits electrons with a maximal kinetic energy of 2.28 MeV/c while decaying to the stable zirconium-90 ^{90}Zr with a half-life of 64 hours [80]. A radioactive source with activity of 1 MBq is used for the lab tests carried out in this work. It is placed in a heavily shielded plastics and lead container, with a collimator of 1 mm in diameter.

The energy loss of electrons in polystyrene is shown in Fig. 7.3. Assuming the average density of polystyrene is 1.05 g/cm^3, the typical energy deposited by an electron with momen-
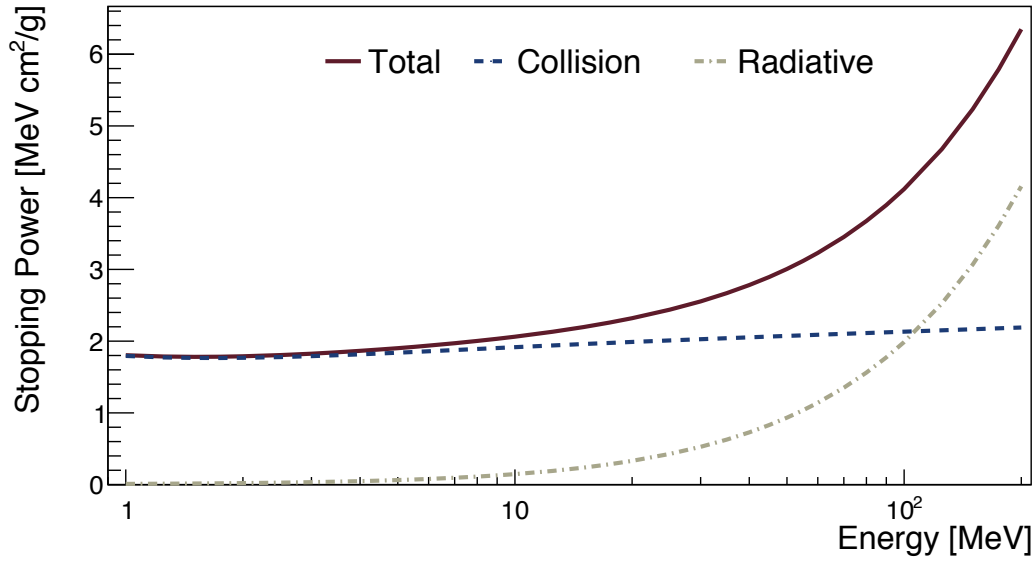
Figure 7.3 – Stopping power of electrons in polystyrene. Figure produced with data from [81].

tum 161 MeV/c is 228 keV/mm[2] while for 1.5 MeV/c electrons it is 186 keV/mm. Due to this difference a small variation is observed in the performance of the scintillating fibers in the two environments, however the results are comparable.

7.2 ANALYSIS ALGORITHMS

The recorded raw waveforms are subjected to a series of algorithms in order to extract useful information about the characteristics of the tested SciFi ribbons. The current section details the particular steps followed in the analysis of datasets collected during a testbeam at PSI and in subsequent laboratory studies.

7.2.1 WAVEFORM PROCESSING

When a trigger signal is received all DRS4 boards digitize their current state and transfer the data to a computer. Thus a single event is produced. The plot shown in Fig. 7.4 represents a partial event[3] registered in one of the DRS4 digitizing boards. A reference signal multiplexed through a low jitter fan out module is fed into one channel of each DRS4 chip for time synchronization. The rest of the available inputs are used for signals coming from individual SiPM

---

[2]This is the energy deposited via collisions in polystyrene. The photons emitted via radiative energy escape the thin plastic scintillators and do not contribute to the production of scintillating light.

[3]It is partial because the data is from a single digitizing board representing 32 channels, while a full event consists of 96 or 160 channels in the test beam and lab configurations, respectively.

array channels. The relevant sections of the waveforms, shaded in green in the plot, can be adjusted along the time axis via external cable delays. Their position has been fixed in time such that the reference signals are sufficiently far away from the critical sections in order to avoid interference due to electrical crosstalk. Each waveform is then treated independently of the others following the procedure described hereafter. Due to electrical fluctuations the baseline of the signal is offset from zero in arbitrary direction for each event. To account for such variation a region at the beginning of the waveform without a signal is chosen and its mean amplitude is calculated (see the shaded area labeled *Normalization* in Fig. 7.4).
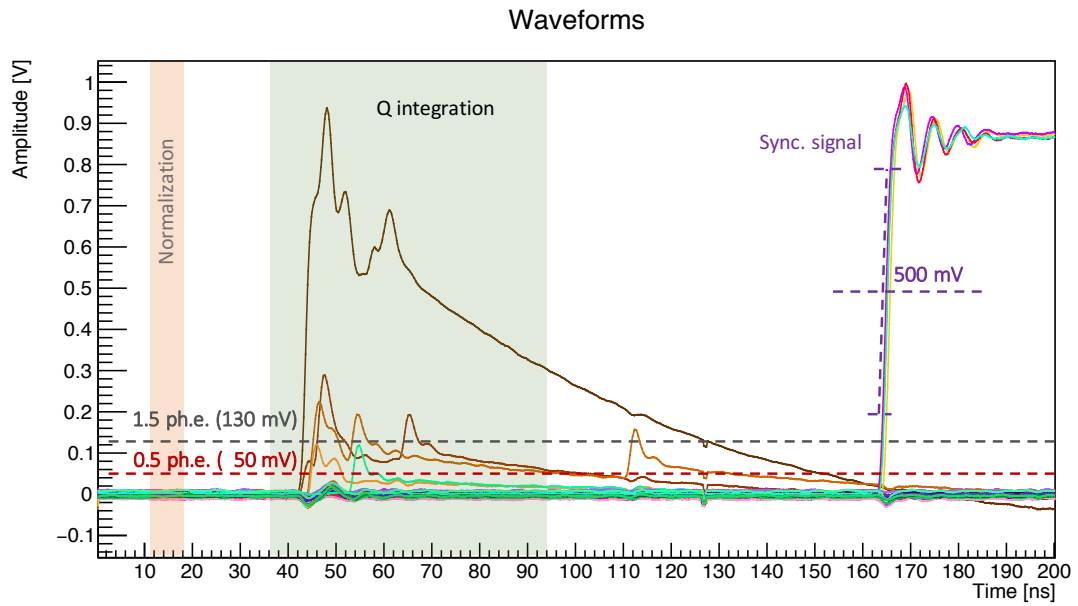
Figure 7.4 – A sample set of waveforms recorded during one event. The area labeled "Normalisation" is used for baseline correction, while the main part of the signals are integrated over the shaded region "Q Integration". Visible on the right are the signals used for synchronisation of the data from the different DRS4 chips. The dashed lines labeled 0.5 ph.e. and 1.5 ph.e. are the levels of the corresponding thresholds for the current operational settings. The individual peak in a single waveform represent photons arriving at different moments of time.

The amplitudes at each point of the waveform are then corrected for and a histogram containing the maximal amplitudes from the integration area *Q integration* is generated (Fig. 7.5).

The first and second peak in this histogram correspond to 1 ph.e. and 2 ph.e. while the lines mark the 0.5 ph.e., 1.5 ph.e. and 2.5 ph.e. levels which will be needed afterwords. Once the thresholds are determined, the beginning of the signal is defined at the crossing point of the waveform edge with the 0.5 ph.e. minus 4 ns. An integral under the curve is then calculated in
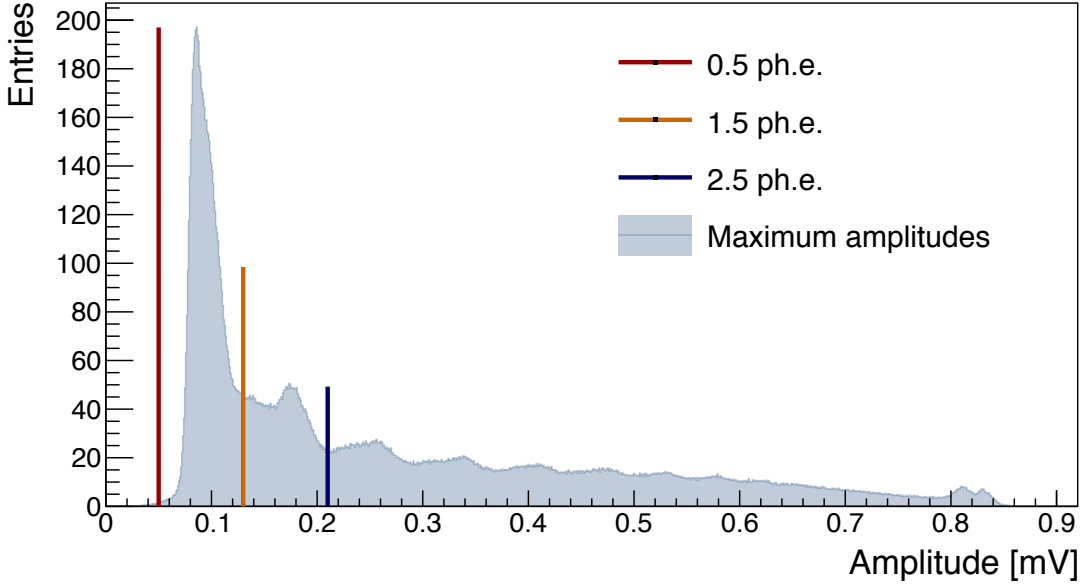
Figure 7.5 – Spectrum of the maximal amplitudes from a single dataset. The thresholds corresponding to 0.5 ph.e. (——), 1.5 ph.e (——) and 2.5 ph.e (——). have been selected based on this plot.

a region with a length of 60 ns [4] starting at the begging of the signal. As it can be seen in the correlation plot of the charge integral vs. the maximal amplitude shown in Fig. 7.6 the integral characterizes better the number of photoelectrons produced in a given event. Any noise superimposed on the amplitude affects its quality for distinguishing individual photoelectrons, while the integral cancels most of the fluctuations and presents a cleaner outcome.

At this phase of the analysis timestamps are also extracted based on two algorithms. On one hand, a digital leading edge discriminator with thresholds at 0.5 ph.e. and 1.5 ph.e. mimics the performance of the MuTRiG. And on the other, a constant fraction algorithm with fraction equal to 0.3 simulates the discriminators used in chapter 6.

From Charge Integral to Number of Photoelectrons

The charge integral spectrum in each dataset differs slightly due to small changes in the environmental conditions e.g. temperature variations in the order of $\pm 3^\circ$ C. As a result the positions of the photoelectron peaks in Fig. 7.7 (Left) exhibit marginal shifts. A more stable and meaningful feature than the integral is the actual number of photoelectrons it corresponds to. For each set of data runs the peaks in the charge spectrum are detected and fitted to individual Gaussian functions. The centroids of these fits are then mapped to the number of

---

[4]The length was chosen to produce well defined charge spectrum while avoiding long integration intervals.
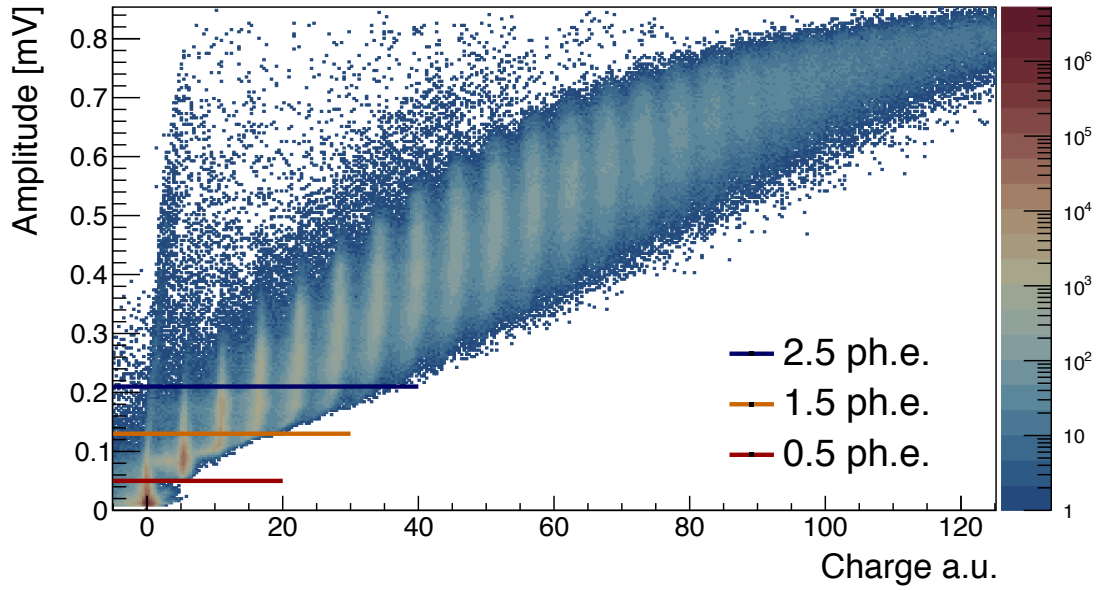
Figure 7.6 – Charge vs maximum amplitude for all 32 SiPM channels attached to one side of a SciFi ribbon. The current sample present events collected when the active area of the SciFi ribbon has been traversed by beam particles. The thresholds corresponding to 0.5 ph.e. (—), 1.5 ph.e. (—) and 2.5 ph.e (—) have also been marked.

photoelectrons by a linear function $y = A_0 + A_1 * x$, see Fig. 7.7.
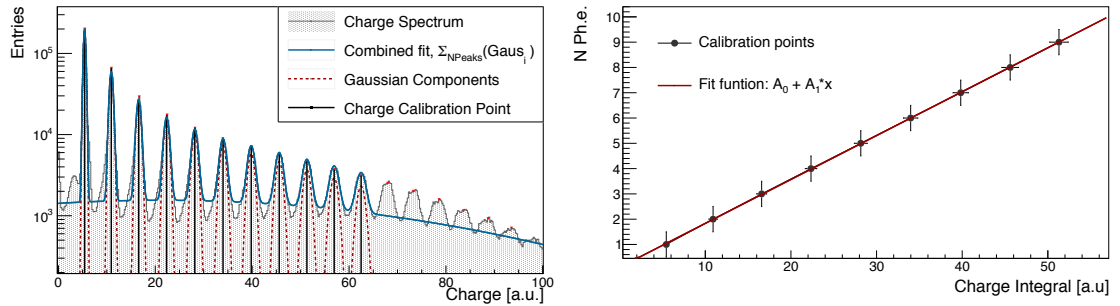
Figure 7.7 – (Left) The charge projection of 7.6. Each peak is fitted with a Gaussian function and the centroid of the result is used as an input for the photoelectron calibration. (Right) The integrated SiPM signal shows expected linear proportionality to the generated number of photoelectrons.

In most data sets the area of the ribbon coincident with the trigger hits occupies only a small subset of channels. Because of that, in cases where the number of events per channel is limited, e.g. outside the central region in Fig. 7.8, it is difficult to achieve adequate conversion to photoelectron numbers.

On the other hand, the response variation between SiPM channels from the same die is
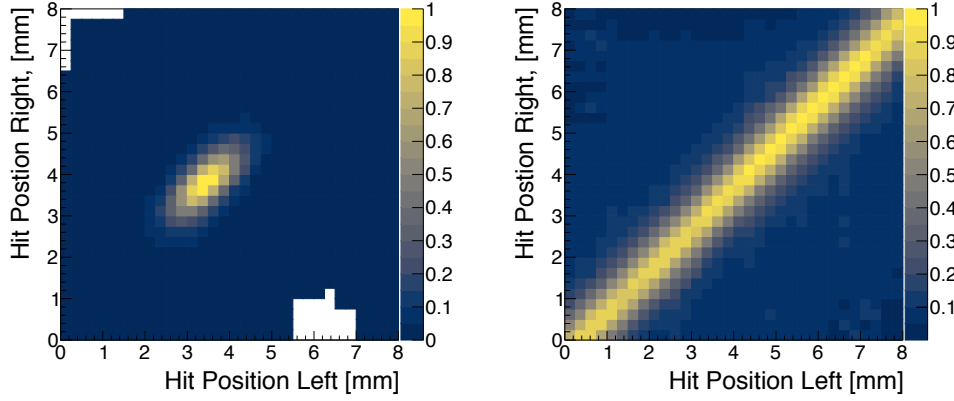
Figure 7.8 – Correlation between the hits generated in the two SiPMs on each side of a ribbon when irradiated in πM1 with the default trigger configuration (Left). The correlation plot (Right) is obtained when only the vertical trigger fiber is used, i.e. there is no restriction along the $\vec{y}$ axis. Each column represents an individual SiPM channel that fired a signal during an event. The points are weighted by the number of photoelectrons generated in the corresponding channel. The active area of the trigger cross $\mathcal{O}(1 \text{ mm} \times 1 \text{ mm})$ behind the ribbon can clearly be distinguished (Left).

small, at the order of 5 %. Additionally, digitizing boards show excellent linearity (see chapter 5). Thus, the charge and amplitude spectra of all 32 equipped channels per side can be combined to extract the photoelectron calibration coefficients and amplitude thresholds. In fact, the plots shown in Figs. 7.5, 7.6, 7.7 represent data points from groups consisting of 32 channels. A comparison between the photoelectron calibration coefficients calculated when the procedure is applied individually on each channel and for a group of 32 channels is shown in Fig. 7.9. The uniformity of the SiPM channels response is evident.
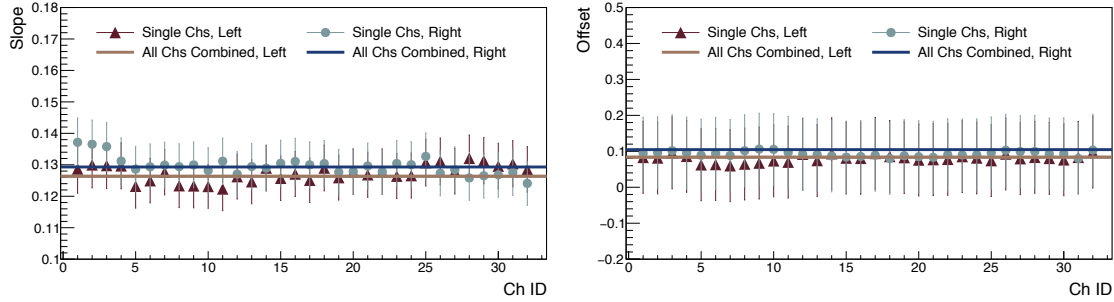
Figure 7.9 – (Left) Slope A_1 and (Right) offset A_0 coefficients obtained when running the calibration procedure for each channel individually. The straight lines represent the slope and offset extracted when the charge spectra of 32 channels in one SiPM are combined.

7.2.2 CLUSTERING ALGORITHM

Fig. 7.10 is a simplified illustration of signals generated in a single event. When a particle traverses the ribbon it deposits energy in the fibers and causes scintillation. The emitted photons travel through the fibers and impinge on the SiPM spreading at an angle of about 45° relative to the fiber axis . Scintillating light triggers avalanches in several pixels per channel resulting in signals with amplitudes proportional to its intensity. Due to light scattering at the optical junction, crosstalk between the SiPM channels and dark count effects (discussed in chapter 4), fake signals might appear in other non signal channels. The goal of the clustering algorithm is to group signals caused by an ionizing particle together while eliminating any unwanted contribution from accidentally fired SiPM channels.
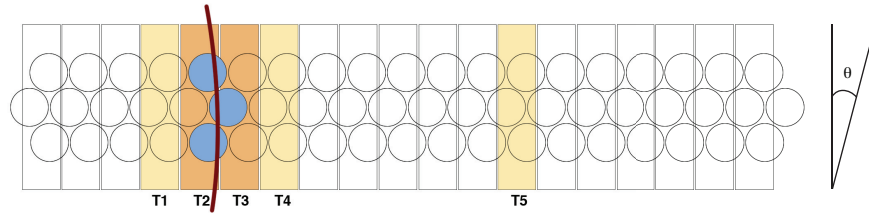
Figure 7.10 – Transverse view of a three layered ribbon mapped to a SiPM array. A particle (—) traversing the ribbon generates scintillating light in some fibers (—) which can trigger signals in several SiPM channels (▮,▮). A "dark" count signal which is identical to a real event signal (▮) should be excluded from the main cluster. Channels are first grouped by proximity and afterwords sorted by their timestamp.

The first step in building a cluster is to select candidate channels which fulfill the following physically significant constraints:

- The amplitude should pass a predefined threshold level e.g. 0.5 ph.e., 1.5 ph.e., etc.

- The timestamp should belong to a specific time window with a width of 20 ns.

A test of proximity selecting only nearest neighbors is imposed on the prepared set of candidates and they are placed in clusters. The multiplicity of the cluster is another parameter used to eliminate noise events, usually at the lowest amplitude threshold at least two channels are necessary to form a cluster. If more than one cluster is found after all the cuts are applied, the "true" group is chosen to be the one with the fastest time of arrival. The cluster time is set to the first timestamp of the channels assigned to it. For the sake of completeness, other parameters e.g the cluster multiplicity or the channel with the maximum amplitude or charge were also explored for sorting multiple clusters per event. However, they did not lead to significantly different results and since information for the latter two sorting parameters will not be available in the Mu3e readout, sorting by time of arrival was chosen for the analysis.

A dataset collected in the absence of ionizing particles from a ribbon coupled to two SiPMs is used to estimate the efficiency of the clustering algorithm to discriminate noise events.
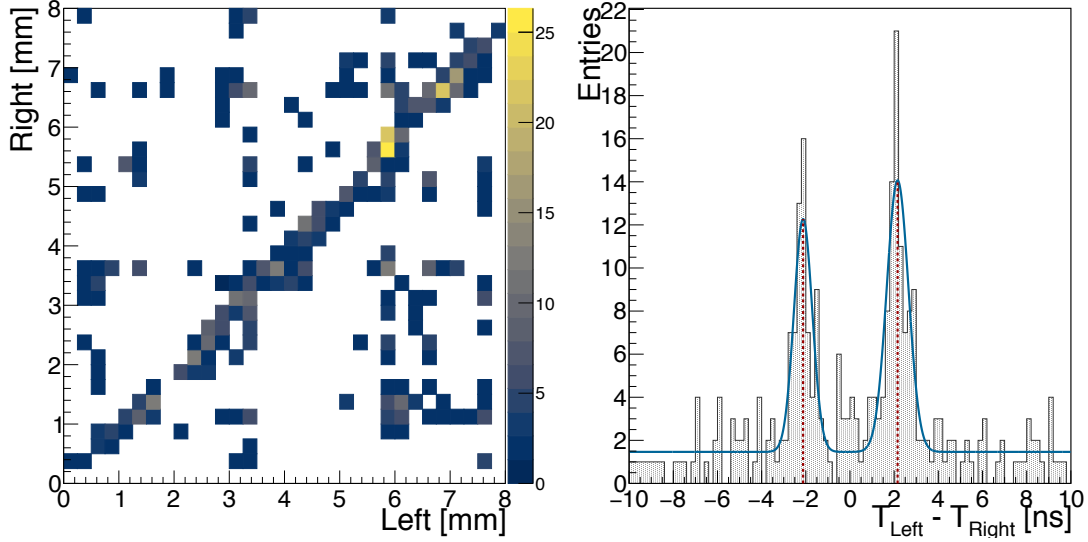
Figure 7.11 – (Left) Charge correlation and (Right) time difference between SiPMs channels placed on both sides of a SciFi ribbon when no particles are traversing it. The uniform charge distribution off the diagonal is due to randomly generated noise signals over time in each SiPM channel. Light emitted during an avalanche by a SiPM pixel on one side is propagated to the other via the fiber and causes the correlated pattern observed in the charge and time spectra. The time difference between the two peaks on the right is indicative of the length of the optical fiber coupling the two SiPMs.

Threshold [N ph.e.]	Distance [mm]	Min Multiplicity	N Triggers	N Accid. Coinc.	False [%]
0.5	0.25	1	10^5	150	0.150
0.5	0.50	1	10^5	150	0.150
1.5	0.25	1	10^5	5	0.005
1.5	0.50	1	10^5	5	0.005
0.5	0.25	2	10^5	1	0.001
0.5	0.50	2	10^5	4	0.004
1.5	0.25	2	10^5	0	0.000
1.5	0.50	2	10^5	0	0.000

Table 7.1 – Cluster efficiency for discriminating accidental coincidences from true events. The varied parameters are the amplitude threshold level, the maximal distance between two channels to be considered neighbors and the minimal cluster multiplicity (inclusive i.e. Multiplicity 1 means $\geq$ 1 channel). A distance of 0.25 mm signifies direct neighbors, while 0.50 mm means there might be a channel that did not produce a signal between two neighbors.

Based on the numbers in Table 7.1, viable combinations of parameters for the clustering algorithm are the ones with a low threshold of 0.5 ph.e and high multiplicity e.g. two or more or a threshold of 1.5 ph.e. or more and a multiplicity of one or more. Besides noise rejection, the clustering algorithm should also be optimized for efficiency and timing. The implications on the latter two parameters resulting from the choice of threshold level and multiplicity are discussed in subsection 7.2.3 and section 7.3.

7.2.3 Time Resolution

The time resolution achievable with the fiber detector is of utmost importance for the background rejection in the Mu3e experiment, see chapter 2. To extract the performance parameters in the tested SciFi ribbon-SiPM prototypes, the distribution of the time difference ΔT between the left and right side of a ribbon is exploited. The time resolution $\sigma_{T^{side}}$ of one side is derived under the following assumptions:

- Any two channels have approximately identical intrinsic time resolution.

- The generated signals from both sides occur independently of each other.

- The timestamps at each side are Gaussian distributed.

Based on the above considerations, the time resolution achievable at one side of the SciFi detector is extracted from the time difference distribution:

$$\Delta T = T^{Left} - T^{Right}$$
$$\sigma_{\Delta T} = \sqrt{\sigma_{T^{Left}}^2 + \sigma_{T^{Right}}^2} = \sqrt{2 \cdot \sigma_{T^{Side}}^2} \qquad (7.1)$$
$$\sigma_{T^{Side}} = \frac{\sigma_{\Delta T}}{\sqrt{2}}$$

Furthermore, in the framework of the Mu3e experiment, both sides of the ribbon will be synchronized to a precise reference clock and their timestamps will represent two independent measurements of the same particle crossing event. Hence, the time resolution σ_{FDet} of the fiber detector will be improved as[5]:

$$\sigma_{FDet} = \frac{\sigma_{T^{Side}}}{\sqrt{2}} = \frac{\sigma_{\Delta T}}{2} \qquad (7.2)$$

Fig. 7.12 shows a sample time difference distribution obtained from a ribbon prepared with four layers of SCSF-81MJ fibers. Trials with fitting the measured points to different models

---

[5]Provided that the light propagation time in the fiber is linearly dependent on the hit position

have shown that a sum of two Gaussians is the best suited function. For completeness, a single Gaussian fit is also plotted. The parameter chosen for comparison between different fibers is the FWHM/2.355. It converges to a Gaussian standard deviation should the data be exactly Normally distributed. This is the case for ribbons which exhibit higher light yields where the contribution of the wide component in the double Gaussian diminishes.
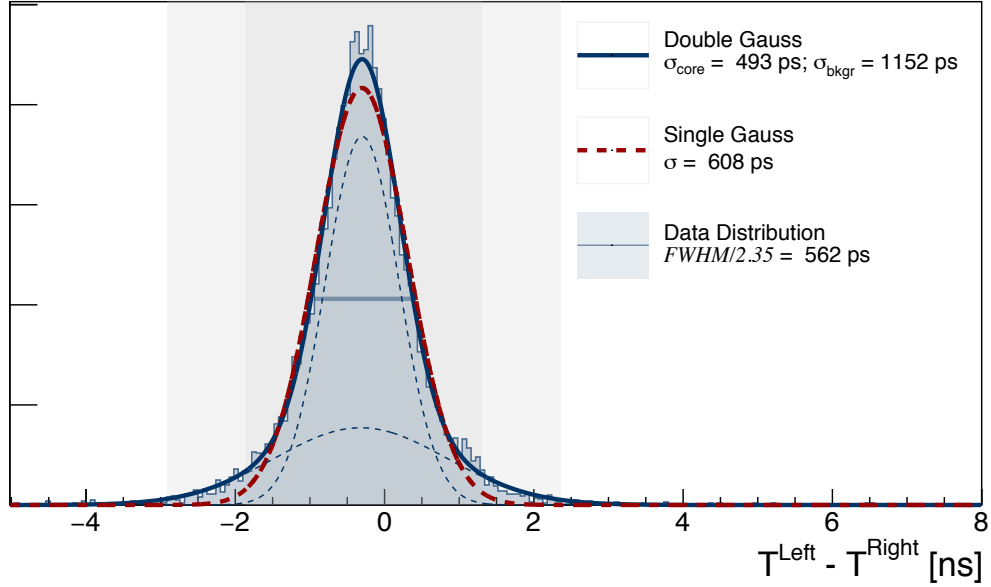
Figure 7.12 – Time difference distribution from a four layers SciFi ribbon made of SCSF-81MJ fibers. Two models based on a single Gaussian function (—) and a sum of two Gaussians (—) are fitted to the data and the results are displayed. In ribbons with higher light yield the core component of the double Gaussian dominates strongly and the fit approaches the single Gaussian. The FWHM/2.35 of the distribution (—) will be used for the time resolution comparisons between ribbons. The shaded rectangles indicate the boundaries of $\pm 3\sigma_{core}$ (▫) and $\pm 5\sigma_{core}$ (▫) around the centroid which will be used to select events for the efficiency estimates.

CLUSTER TIME

The timestamp for each SciFi ribbon side is extracted from the corresponding main event cluster. Depending on the algorithm widely varying values have been observed for the time resolution. Ordering the timestamps by arrival time and using only the first one from the cluster yields the best outcomes. The mean time of all channels in a cluster (either weighted by the number of photoelectrons or not) is also investigated as a candidate estimator. However, it does not produce satisfying results in its non-weighted variant that resembles the capabilities of the MuTRiG ASIC, see section 5.3.

Ph.e. Thr.	Mult. Chs	WF Alg.	Cl. Time Alg.	$\frac{\text{FWHM}}{2.35}$ [ps]	σ_{single} [ps]	σ_{core} [ps]	σ_{bkgr} [ps]	$N_{\text{core}}/N_{\text{bkgr}}$
0.5	2	CF, 10%	First T	391	475	338	625	1.08
0.5	2	CF, 30%	First T	451	525	375	682	1.03
0.5	2	LE, 0.5	First T	400	469	327	612	0.99
1.5	1	LE, 0.5	First T	400	475	336	637	1.12
1.5	1	LE, 1.5	First T	468	560	399	752	1.12
1.5	2	LE, 1.5	First T	460	549	382	711	0.94
0.5	2	LE, 0.5	Mean T, W	536	602	461	780	1.25
1.5	1	LE, 1.5	Mean T, W	647	729	567	986	1.51
0.5	2	LE, 0.5	Mean T	1166	1208	1119	1499	3.47
1.5	1	LE, 1.5	Mean T	1217	1278	767	1354	0.18

Table 7.2 – The cluster time algorithm based on the fastest arrival time is chosen to compare the performance of the waveform time extraction with constant fraction (CF) and leading edge (LE) algorithms. The numbers cited next to each of the two algorithms represent the corresponding parameter - fraction of the amplitude for the CF and the amplitude level at the specified number of photoelectrons. Mean time cluster time algorithms are compared using LE for the waveforms.

Waveform Time

From algorithmic point of view, several factors influence the time resolution. The leading edge algorithm is susceptible to jitter induced at the threshold level due to differences in the slopes of signals with varying amplitudes. Constant fraction algorithms, on the other hand, take advantage of the constant shape of the signal irrespective of the amplitude and produce lower time jitter. Additionally, depending on the minimal cluster multiplicity and threshold, noise events can contribute to the time estimation and deteriorate the result. In systems where information about the amplitude is available the time walk can be corrected for, however, this will not be the case with the MuTRiG ASIC[6]. The constant fraction algorithm has been designed for signals which exhibit a fixed rise time[7] independent of the amplitude. It exploits this property by always taking the time at fixed fraction of the amplitude, thus eliminating the time walk from the fixed amplitude threshold, see appendix A.

Table 7.2 summarizes the outcomes from various combinations of cluster and waveform timing algorithms.

Since there is a single level in the MuTRiG chip sensitive enough to be adjusted at the level of single photoelectrons both the cluster and time thresholds will coincide. As a result a com-

---

[6]The MuTRiG can provide amplitude information, however the resolution is in the order of 10 ph.e., which is not sufficient for the fiber detector.

[7]The rise time is used as a synonym of the leading edge of the signal, not the tail.

promise should be sought between occupancy and time resolution, with the former improving while the later worsens at higher amplitude cuts.

7.2.4 LIGHT YIELD

The various scintillating fiber materials and epoxy mixtures used in the preparation of the ribbons, as well as the number of fiber layers, affect the intensity of scintillating light reaching the SiPMs. With the detailed waveforms available from the current measurement setup, a comparison between the relative light yield of the tested SciFi ribbons can be made[8]. This information is useful in understanding the observed performance and choosing an optimal clustering algorithm, as well as for tuning the parameters in the Mu3e simulation software.

Fig. 7.13 presents a charge spectrum obtained by summing the number of photoelectrons per event detected in all SiPM channels that have been assigned to a valid cluster on one side of the ribbon.
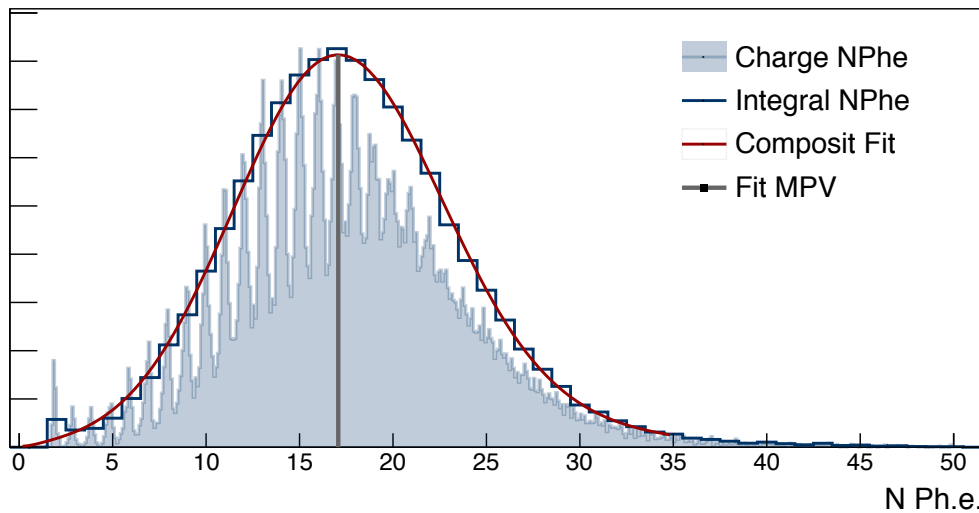
Figure 7.13 – Cluster light yield of a three layered SCSF-78MJ fiber ribbon prepared with clear epoxy. The integral (—) NPhe is obtained by summing the charge in a region of ± 0.5 ph.e. around each integer. A convolution of a Gaussian and a Landau is used to fit the data (—) and the most probable value (MPV) is marked with a line —.

The high resolution charge spectrum with fractional number pf photoelectrons is reduced to an integral representation by summing all entries in a region of ± 0.5 around each integer with the goal of extracting higher level features of the data. A convolution of a Gaussian and a Landau distribution is used to fit the integral representation. It is motivated by the distribution

---

[8]Measuring the absolute light yield of a SciFi ribbon is a complex task requiring dedicated equipment which is beyond the scope of the present work.

of energy deposited in a thin layer of material $\mathcal{O}(1\text{ mm})$ modeled with a Landau distribution [82] and the Poissonian nature of scintillating light generated and further detected in the SiPM pixels[9] The most probable value of the fitted distribution is taken as a figure of merit for the light yield of different ribbons.

7.2.5 EFFICIENCY

Since the trigger has a cross section of 1 mm×1 mm in the $\vec{\mathbf{y}} \times \vec{\mathbf{z}}$ plane perpendicular to the beam direction and the front fiber has a width of 500 µm along the vertical $\vec{\mathbf{y}}$ axis and they are located about 10 cm apart along $\vec{\mathbf{x}}$, simultaneous hits in both detectors guarantee particle trajectories are confined within a narrow window of dimensions close to the trigger area along the $\vec{\mathbf{y}}$ axis. When a fiber ribbon with a width of 8 mm (in $\vec{\mathbf{y}}$) is centered between the two detectors its efficiency can be estimated from the number of detected events in the ribbon and the number of all hits observed in the triggers. Following the method described in [83], the efficiency estimator is taken as the mode of the probability distribution $P(\varepsilon|k, N, I)$ where k are the observed events out of N trials and the term I encodes any knowledge that might be available for the efficiency distribution prior to the experiment. The maximum of the selected distribution is always at

$$\hat{\varepsilon} = \frac{k}{N} \tag{7.3}$$

where in the sense of the current measurements

$$k := (\text{Ribbon Hit}) \wedge (\text{Cross Trigger Hit}) \wedge (\text{Front Fiber Hit})$$

$$\tag{7.4}$$

$$N := (\text{Cross Trigger Hit}) \wedge (\text{Front Fiber Hit})$$

The errors of the estimator are taken at the boundaries of the shortest interval with a specified probability content. In this case a confidence level of 68.27 % is used. At low number $\mathcal{O}(1000)$ of trial and observed events, the boundaries of the interval are slightly asymmetrical around the mode of the distribution, however they approach the $\mu \pm 1\sigma$ region of a Normal distribution at larger numbers.

A more conservative estimate of the efficiency is proposed where the number of successful events k is additionally restricted by taking only events whose time difference does not deviate from the mean value by more than $3 \times \frac{\text{FWHM}}{2.355}$.

---

[9]At the observed mean value of photoelectrons in the cluster, the Poissonian distribution approaches Gaussian, hence the fit is a convolution between Gaussian and Landau distributions.

7.3 ANALYSIS RESULTS

7.3.1 OCCUPANCY

The occupancy of a detector is defined as the number of hits per second in a given readout channel. If this number exceeds the capabilities of the electronics, the system will be inefficient or blind for a fraction of the events, which is in general undesirable.

The factors that affect the occupancy of the fiber detector include the angle at which a particle traverses a SciFi ribbon, the number of ribbon layers and their light yield, the SiPM dark count rate etc. The results obtained in this work combined with the simulation software provide a general guidance towards the expected number of hits per readout channel and can be used as a reference in the design of the MuTRiG chip.

According to the full Mu3e simulation with a muon stopping rate of 1×10^8 muons/s, the expected hit rate per fiber is $\mathcal{O}(165\text{ kHz})$ and the hit rate per readout channel at 0.5 ph.e. threshold is $\mathcal{O}(600\text{ kHz})$ [51] for a SCSF-78MJ ribbon with 4 layers.

Fig. 7.14 is a comparison between cluster multiplicity measured during the PSI testbeam and a simulated response of the detector to 161 MeV/c electrons within the Mu3e simulation framework. The cluster threshold is set at 0.5 ph.e. in both cases. In the presented simulation results, effects stemming from the noise in the SiPM sensors, e.g. dark count rate (DCR), are omitted. More details about the parameters used to produce the concrete example are available in [51]. The event multiplicity on the other hand, reflects the combined properties of the fiber detector and can be used to estimate the increase in the expected hit rate per channel. The average difference between cluster and event multiplicity for the selected threshold is in the order of 30 %, hence under stable conditions with a temperature of 26±3 degrees, the expected event rate per channel can rise to $\mathcal{O}(780\text{ kHz})$. Besides that, radiation damage to the photo sensor throughout the operation of the experiment will further increase the DCR and thus the occupancy per channel. During the test beam at PSI the effect of ionizing particles on a single channel SiPM have manifested in a ten fold increase of the DCR accompanied by significant deterioration of the amplitude after only a few hours in the beam, so it is another point to be considered in the choice of the clustering algorithm parameters. Systematic studies are currently ongoing [84], aiming to characterize the effect of radiation on both the SiPM sensors and the scintillating fibers that will be used in the final detector.

REFLECTIVE COATING

In an attempt to reduce the average occupancy, SciFi ribbons produced with optically isolating epoxy compounds have been studied. More specifically, sets of ribbons with identical
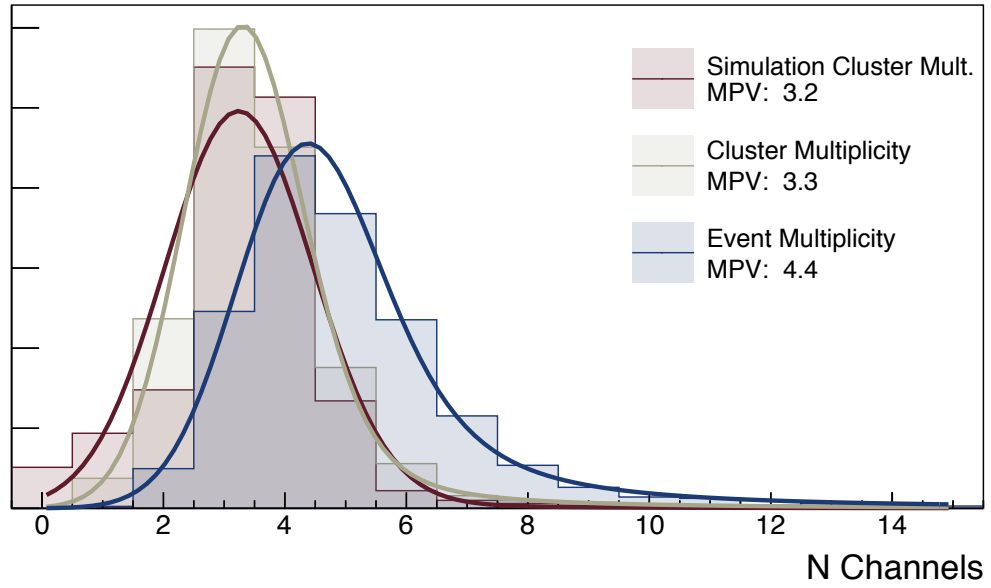
Figure 7.14 – The cluster multiplicity obtained during the test beam at PSI (━) is reproduced through simulation (━) with the main Mu3e simulation framework. The event multiplicity (━) tends to be larger by approximately 30 %. The figure is adapted from [51] with test beam data provided by measurements performed in this work. A ribbon of four layers SCSF-78MJ is used in both studies.

fibers were produced where transparent epoxy is used for one ribbon and a mixture of epoxy and 20 %[10] TiO_2 powder for the other, see subsection 3.3.2.

Due to limited beam time and changes of the test setup throughout the process only two pairs of ribbons were evaluated under conditions allowing direct comparison. Fig. 7.15 shows the results from measurements obtained with SCSF-78MJ and NOL-11 fiber materials. A reduction in the order of $\mathcal{O}(10\,\%)$ is observed in the number of fired channels when TiO_2 is added to the adhesive. This number is consistent with the results obtained in the single fiber configuration, see section 6.4. The benefit from it, however, is outweighed by the increased multiple scattering in the fiber detector degrading the momentum resolution, which is crucial for the Mu3e experiment.

A possible option to reduce the multiplicity is to use SciFi ribbons with fewer layers e.g. three or even two. The latter has the disadvantage of being inefficient for particles traversing at an angle of about 20°which is close to the most probable angle (22°) at which electrons will cross the SciFi detector in the experiment. Having a ribbon with three layers reduces the multiplicity by a factor of about 30 % relative to the a SciFi ribbon with four layers of the same material. The occupancy is then brought down to a number comparable with the

---

[10]The compound proportion is taken by mass.
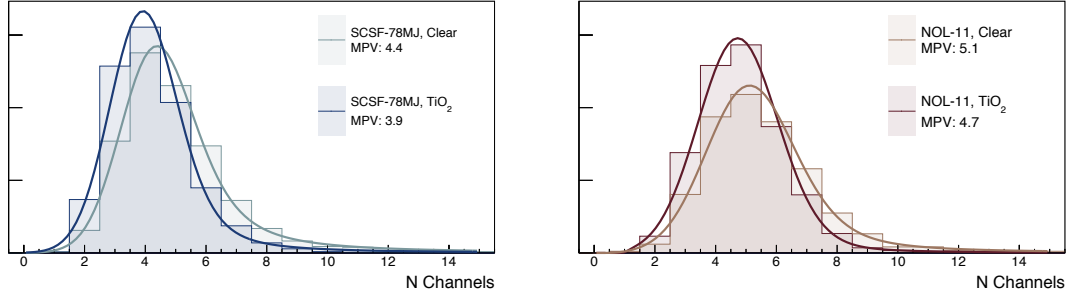
Figure 7.15 – Event multiplicity at one side of a ribbon with four layers of SCSF-78MJ (Left) and four layers of NOL-11 (Right). Adding a TiO$_2$ powder in the epoxy with 20 % concentration by mass leads to reduction of the occupancy by $\mathcal{O}(10 \%)$ for 4 layer SciFi ribbon. The data is for particles traversing the ribbons at an angle of 0° and cluster threshold set at 0.5 ph.e.

simulation results where the DCR of the SiPMs is not accounted for. See Fig. 7.16 and Fig. 7.15 for comparison between three and four layer SciFi ribbons produced with SCSF-78MJ fibers without any reflective material added in the epoxy.

The final decision for the number of layers in a ribbon has not be reached, however, based on results from this work three layers of SCSF-78MJ are a viable candidate. The plots in Fig. 7.16 are obtained with a ^{90}Sr source and are intended as a reference in tuning the main Mu3e simulation parameters.

7.3.2 Ribbons Comparison

Both time resolution and efficiency are strongly dependent on the light yield of the fibers in a SciFi ribbon and the corresponding number of layers. The SCSF-81 fibers were the primary choice of material for testing prior to the present studies. It was motivated by using the fibers with the shortest decay time available at the time. Additionally, no concrete data was available about the light yield of these fibers with respect to the SCSF-78MJ ones, except for a vague statement from the vendor that the latter have a higher one. From Fig. 7.17 it is evident that the divergence between the two is rather large and could be as much as a factor of 2.[11] Since the SCSF-81 spool used for the preparation of the ribbons was exposed to UV light originating from fluorescent lamps in the lab and weakly filtered sunlight, a conclusive statement cannot be made on whether the SCSF-81 produce indeed twice less scintillating photons than the SCSF-78MJ. However, tests with intentionally exposed ribbons of SCSF-78MJ and NOL-11 fibers have failed to provide proof that after a week under direct sunlight and a conventional light bulb the light yield has degraded, see Table 7.4. The novel NOL-11 fibers which are advertised for their

---

[11]The NOL-11 fibers exhibit similar light yield as the SCSF-78MJ.
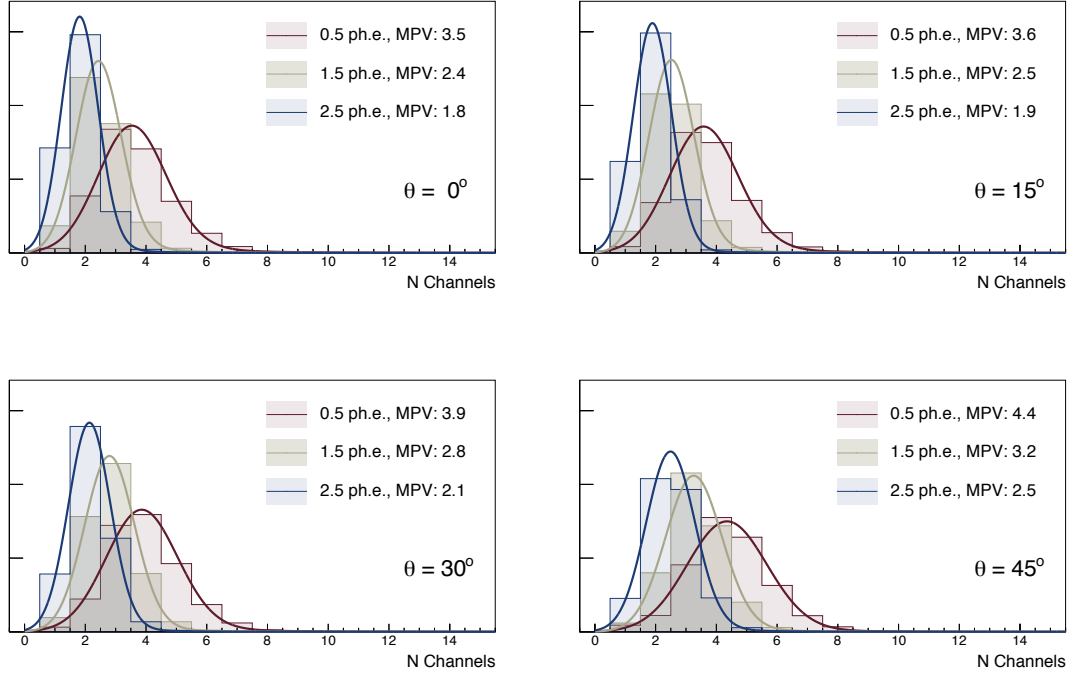
Figure 7.16 – Event multiplicity at one side of a ribbon in terms of SiPM channels. The ribbon is rotated horizontally around the $\vec{z}$ axis. The angle is relative to the beam axis, see Fig. 7.10 and Fig. 7.1. The MPV is obtained from a fit with a convolved Gaussian and Landau functions as in 7.14. The data is from a three layer SciFi ribbon prepared of SCSF-78MJ fibers with transparent epoxy (ARALDITE 2020). A radioactive ^{90}Sr source emits the electrons used in the measurement. The average occupancy decreases with increasing the amplitude threshold and increases with the trajectory crossing angle.

fast decay time $\mathcal{O}(1\ \text{ns})$ [54] deliver as many photons as the SCSF-78MJ ones. The prototype with aluminized BCF-12 fibers results in the least number of photoelectrons measured in the SiPMs.

Larger number of photons generated in the process of scintillation implies that sufficient amount of them will be emitted in a short time interval, thus reaching the optical sensor with minimal jitter. Additionally, the clustering algorithm benefits from the increased number of neighboring channels firing a signal due to the higher light intensity. Fig. 7.18 compliments the results from Fig. 7.17 by demonstrating a strong correlation between the light yield of a ribbon and the observed time resolution and efficiency. The data in both figures is extracted with the default cluster parameters, namely a threshold at 0.5 ph.e. for both cluster candidates and waveform time, the fastest arrival marks the cluster time and the minimal multiplicity is 2 channels.

Fiber Type	Layers, Coating	Test Env.	N Ph.e. [MPV]	Ev. Mult. [MPV]	$\frac{FWHM}{2.35}$ [ps]	Efficiency [%]
NOL-11	3, TiO_2	Sr90	17.1 ± 0.8	4.83 ± 0.29	467 ± 32	$94.3^{+0.5}_{-0.5}$
NOL-11	3, TiO_2	TB	18.2 ± 1.1	5.59 ± 0.50	382 ± 13	$93.7^{+0.2}_{-0.2}$
NOL-11	4, Clear	Sr90	21.7 ± 1.8	4.69 ± 0.14	425 ± 29	$96.0^{+0.2}_{-0.3}$
NOL-11	4, Clear	TB	22.7 ± 2.0	5.10 ± 0.28	391 ± 34	$94.1^{+0.6}_{-0.7}$
SCSF-78MJ	4, Clear	Sr90	21.9 ± 0.8	3.79 ± 0.13	433 ± 27	$91.2^{+0.2}_{-0.2}$
SCSF-78MJ	4, Clear	TB	26.0 ± 3.2	4.36 ± 0.34	408 ± 10	$95.2^{+0.3}_{-0.4}$

Table 7.3 – Characterization parameters such as light yield, time resolution and efficiency have been compared for ribbons measured under both test beam and lab conditions. Event multiplicity and MPV of the number of photoelectrons are for one side of the ribbon. The small differences in the obtained values are attributed to the less energy deposited in the ribbons in the case of electrons produced by ^{90}Sr.

7.3.3 MEASUREMENTS REPEATABILITY AND STABILITY

Stability over time of various parameters is studied in large datasets by subdividing them into small sets of events and extracting the features of interest from each one of them. The size of each subset is limited to 10 000 triggers corresponding to a data taking time of approximately 150 sec. The results shown in Fig. 7.19 are collected over 4 h 40 min for a SciFi ribbon made of four layers SCSF-78MJ fibers without any TiO_2 added to the epoxy. The stable behavior of estimated parameter values is verified in other data sets from the same test beam campaign. A similar plot obtained for a NOL-11 ribbon with four layers is available in [51].

Part of the measurements taken with ribbons during the πM1 test beam are subsequently repeated with a β source using the same readout electronics. Table 7.3 summarizes the observations for a select subsample of ribbons. Slightly lower light yield and hence worse time resolution is systematically observed in all samples when irradiated with ^{90}Sr source. It is attributed to the lower energy deposited by the electrons in the fibers due to their lower momentum. Nevertheless, the results allow studies of new SciFi ribbons to be compared with the ones obtained in the test beam. Hence, two more prototypes are characterized only with a ^{90}Sr source. Additionally, first measurements using the MuTRiG ASIC have been completed and presented in [51]. Even though the time resolution is the only available parameter for comparison the measurement has shown good agreement with the observations derived here.

LIGHT YIELD ALONG THE SCIFI RIBBON WIDTH

During the test beam campaign two ribbons consisting of three and four layers of NOL-11 fibers with 20 % TiO_2 in the epoxy are scanned along their width ($\vec{y}$). The uniformity of their light yield is measured in steps of approximately 1 mm. Fig. 7.20 presents the results of the study. The position of each channel in a valid cluster is weighted by the number of photoelectrons and used to generate a hit profile. The coordinates for the mean hit position are determined from the hit profile in each subset. The standard deviation of the profile histogram is in the order of 450 μm reflecting the dimensions of the trigger cross located behind the SciFi ribbon. As discussed in subsection 7.2.4, the discrete cluster charge spectrum is modeled according to a convolution between a Gaussian and a Landau and the MPV is reported for the light yield. The error corresponds to the Gaussian sigma of the fit. The dip in the light yield of the four layer ribbon observed on both the left and the right side suggests an inferior quality in the central region of the ribbon, rather than inefficiency in the optical sensors. Furthermore, no such behavior is observed in the other device tested under the same conditions.

PARTICLES CROSSING ALONG THE SCIFI RIBBON LENGTH

The time difference between the right and left side of a ribbon can be used to estimate the location along the length of the SciFi ribbon ($\vec{z}$ axis) where a particle has traversed the ribbon. Such information is instrumental in identifying the upstream or downstream section of the fiber detector where an electron has crossed. It facilitates track matching with the pixel tracker. The position resolution of a SciFi ribbon with three layers of SCSF-78MJ fibers is measured by moving a collimated ^{90}Sr radioactive source along the ribbon length ($\vec{z}$). A plot with the results is shown in Fig. 7.21. The centroid of the time difference distribution at each point is taken with the error bars equal to $\pm\frac{\text{FWHM}}{2.355}$. For the tested SciFi ribbon with a mean time resolution $\mathcal{O}(\frac{\text{FWHM}}{2.355}$=500ps) a position resolution of $\sigma_{\Delta z}$ = 3.8 cm is determined.

SUMMARY

If the temperature at which the SiPMs will be operated in the MU3E experiment is higher than the one maintained throughout the presented measurements, triggering at 0.5 ph.e. might not be feasible due to the too high rate. The efficiencies and time resolutions obtained at varying cluster parameters for a few select ribbons are presented in Fig. 7.22. The samples are chosen purely to illustrate the overall performance of a given type of scintillating fiber material. For ribbons with high light yield a threshold of 1.5 ph.e. worsens the time resolution by approximately 100 ps. However, setting the cluster multiplicity at ≥ 2 combined with a

1.5 ph.e. threshold significantly reduces the efficiency achievable with any of the ribbons with three layers. The only viable options in this case are the SCSF-78MJ and NOL-11 fibers for SciFi ribbons with four layers whose efficiencies estimated are about 95 %.

A complete list of the characterized ribbons with their respective performance parameters is available in Table 7.4. Due to the poorer performance of BCF-12 and SCSF-81[12] observed here and in [48, 50], there are no further prototypes produced to evaluate the effect of various coatings or number of layers on their performance.

The NOL-11 fibers clearly outperform the rest of the tested materials. However, they are not commercially available and research activities are still ongoing for their development. Hence, the only feasible option left is to use the SCSF-78MJ scintillating fibers in the final production of the Mu3e fiber detector. The decision on the number of layers will be taken after detailed simulations of the environment in which the detectors should operate, mainly in terms of temperature, have been done. Additionally, studies on the radiation damage of the SiPMs and the fibers under the running conditions of Mu3e are being prepared [84]. They should be concluded before any final statement is reached. From the point of view of the tracking detector, the three layers are the preferred option offering smaller thickness, ergo reduced multiple scattering. Provided the performance of both SiPMs and fibers remains close to nominal throughout the radiation damage tests, a ribbon with three layers SCSF-78MJ will be the baseline design solution.

---

[12]Relative to the other available materials.

Fiber Material	N Layers	Coating	Test Env.	Light Yield [MPV] Left	Right	Ev. Multipl. [MPV] Left	Right	Time res. [ps] $\frac{FWHM}{2.35}$	Efficiency [%]
NOL11	2	TiO$_2$	TB	10.3 ± 1.3	10.8 ± 1.3	4.21 ± 0.65	3.97 ± 0.63	433 ± 16	$86.4^{+0.3}_{-0.3}$
NOL11	3	TiO$_2$	TB	18.2 ± 1.1	18.3 ± 1.7	5.59 ± 0.50	5.61 ± 0.58	382 ± 13	$93.7^{+0.2}_{-0.2}$
NOL11	3	TiO$_2$	Sr90	17.1 ± 0.8	18.2 ± 0.8	4.83 ± 0.29	5.11 ± 0.22	467 ± 32	$94.3^{+0.5}_{-0.5}$
NOL11	4	Clear	TB	22.7 ± 2.0	22.7 ± 2.2	5.10 ± 0.28	5.05 ± 0.27	391 ± 34	$94.1^{+0.6}_{-0.7}$
NOL11	4	TiO$_2$	TB	21.5 ± 1.9	20.7 ± 3.0	4.70 ± 0.12	4.60 ± 0.22	348 ± 16	$96.6^{+0.2}_{-0.2}$
NOL11	4	Clear	Sr90	21.7 ± 1.8	21.0 ± 1.5	4.69 ± 0.14	4.56 ± 0.11	425 ± 29	$96.0^{+0.2}_{-0.3}$
MJ81	4	TiO$_2$	TB	11.9 ± 1.0	12.5 ± 1.3	3.56 ± 0.27	3.55 ± 0.34	544 ± 26	$88.4^{+0.3}_{-0.3}$
MJ78	3	Clear	Sr90	16.5 ± 0.5	17.2 ± 0.6	3.30 ± 0.09	3.48 ± 0.12	484 ± 23	$89.7^{+0.3}_{-0.3}$
MJ78	4	TiO$_2$	TB	21.9 ± 1.1	22.4 ± 1.5	3.88 ± 0.21	3.77 ± 0.31	365 ± 14	$94.2^{+0.2}_{-0.2}$
MJ78	4	Clear	TB	26.0 ± 3.2	24.1 ± 1.6	4.36 ± 0.34	4.62 ± 0.45	408 ± 17	$95.2^{+0.3}_{-0.4}$
MJ78	4	Clear	Sr90	21.9 ± 0.8	22.7 ± 0.7	3.79 ± 0.13	3.83 ± 0.11	433 ± 27	$91.2^{+0.2}_{-0.2}$
BCF12	3	Al	Sr90	6.2 ± 1.4	5.9 ± 1.3	1.97 ± 0.02	2.02 ± 0.02	747 ± 26	$58.9^{+0.5}_{-0.5}$
BCF12	4	TiO$_2$	TB	50.0 ± 0.7	3.6 ± 0.6	2.32 ± 0.27	2.04 ± 0.30	756 ± 34	$49.5^{+0.5}_{-0.5}$

Table 7.4 – The most important parameters of ribbons measured in both test beam and lab conditions are summarized. In all presented results the front fiber was used to extract the efficiency estimates. Event multiplicities are reported in conjunction with the efficiency cuts on the front fiber. The time resolution is extracted from the FWHM of the time difference histograms using leading edge algorithm for the timestamps and fastest arrival for the cluster time. The MPV for the light yield is derived from the integrated cluster charge at each event.
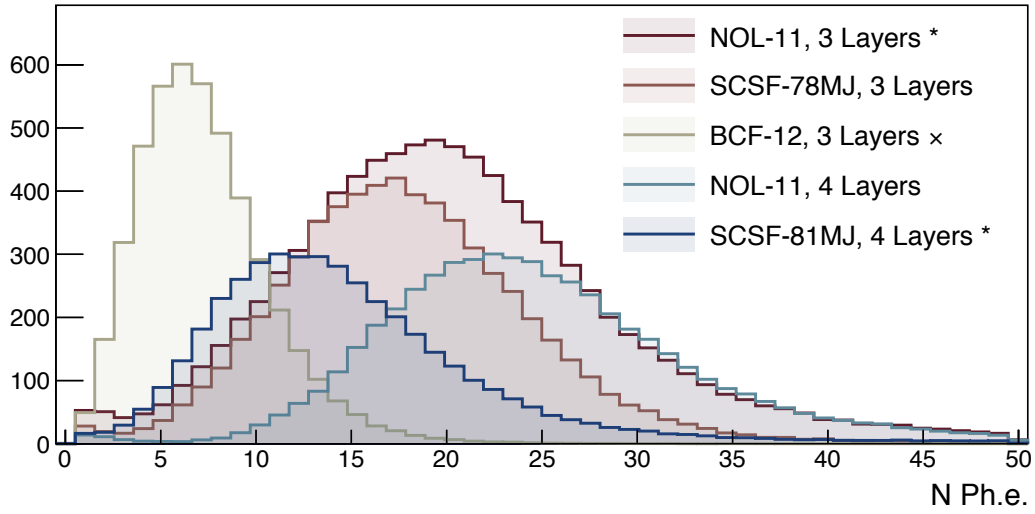
Figure 7.17 – Light yield at one side of select ribbons. The number of photoelectrons is the charge sum of all channels in a cluster at one side matched to a track. The minimal cluster multiplicity is of two neighboring channels with an amplitude of at least 0.5 ph.e. The histograms are normalized by their integral. (*) - ribbons with 20 % TiO_2 added to the glue. ($\times$ - individual fibers coated with $\mathcal{O}(100$ nm) of Al.
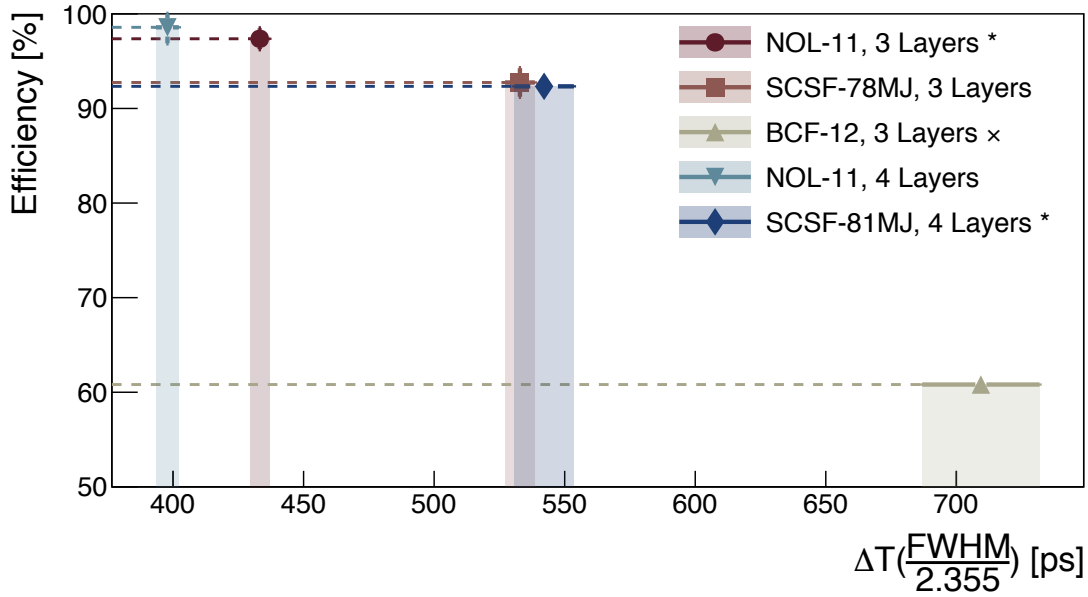
Figure 7.18 – Select ribbon efficiencies vs their respective time-difference resolutions. The efficiency is estimated for an AND configuration and the minimal cluster multiplicity is two neighboring channels with an amplitude of at least 0.5 ph.e. Events are considered valid if they fall within the area of $\pm 3 * \frac{\text{FWHM}}{2.355}$ around the centroid of the distribution. The estimates are conservative and represent a lower limit on the efficiency. (*) - ribbons with 20 % TiO_2 added to the glue. ($\times$ - individual fibers coated with $\mathcal{O}(100$ nm) of Al.
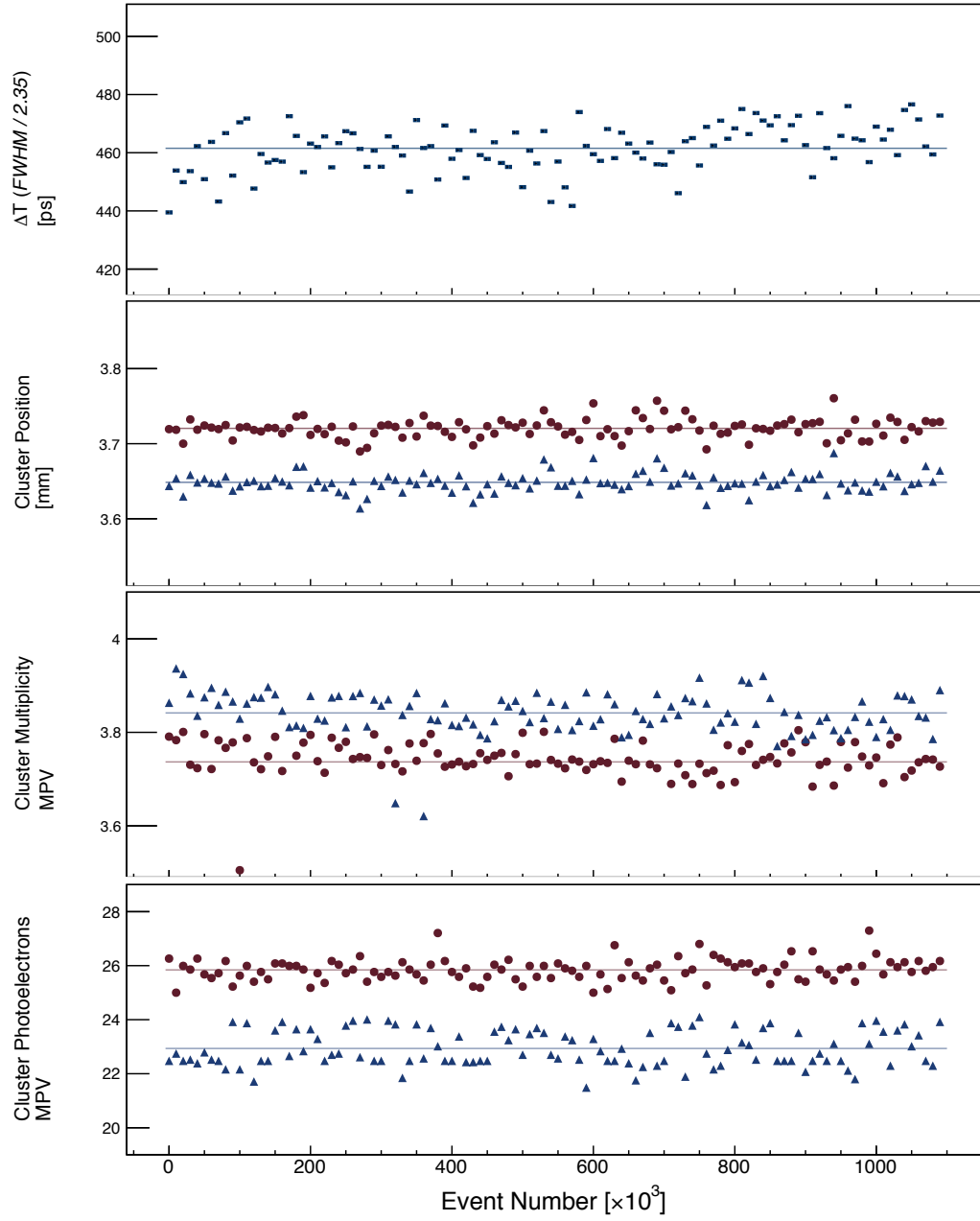
Figure 7.19 – Stability of various ribbon characterization features over time. The samples are collected over 4h 40min with a four layered ribbon of SCSF-78MJ fibers during the test beam campaign at πM1. The plotted values are extracted from subsets of 10 000 triggers corresponding to an average data taking time of 2 min 30 sec. The time difference resolution is shown in the top most graph (—). The remaining plots include feature values obtained for both the left (●) and right (▲) side of the ribbon.s
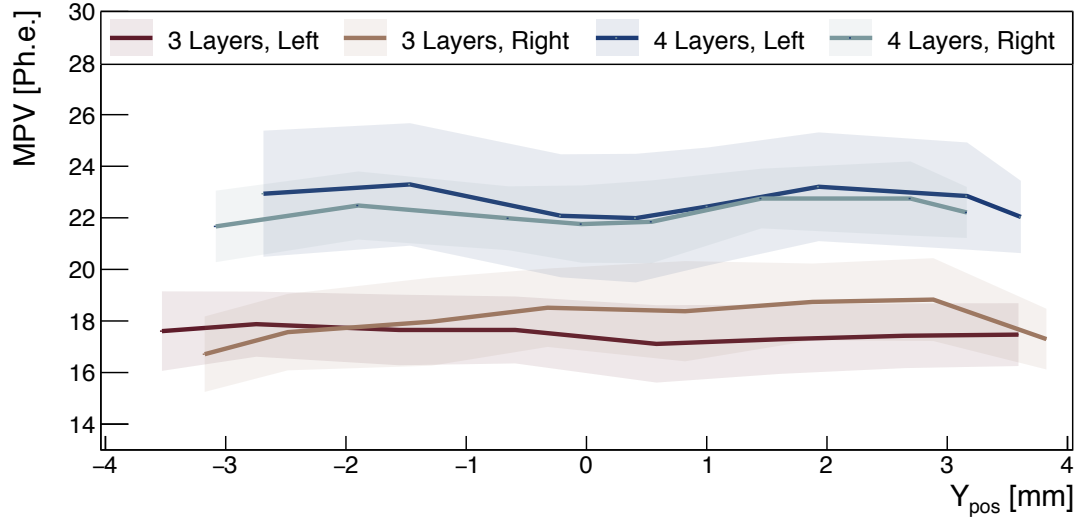
Figure 7.20 – Cluster light yield for different ribbon positions scanned along the width of a SciFi ribbon. The left and right sides of two ribbons are plotted. One is composed of three and the other of four layers NOL-11 fiber, both prepared with 20 % TiO_2 in the epoxy mixture.
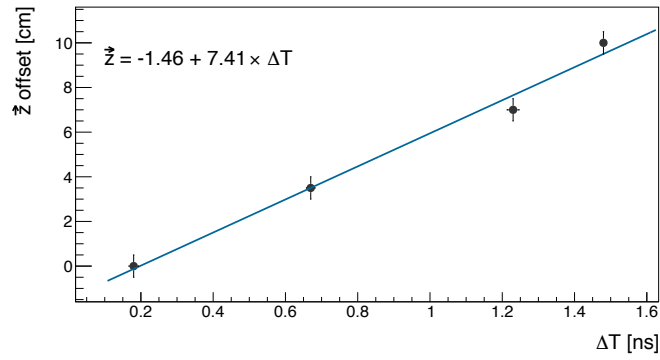
Figure 7.21 – Time difference offset caused by particles traversing the ribbon at different offsets along $\vec{z}$. The zero position is the middle of the ribbon. Results are acquired using a three layer SciFi ribbon made of SCSF-78MJ fibers.

141
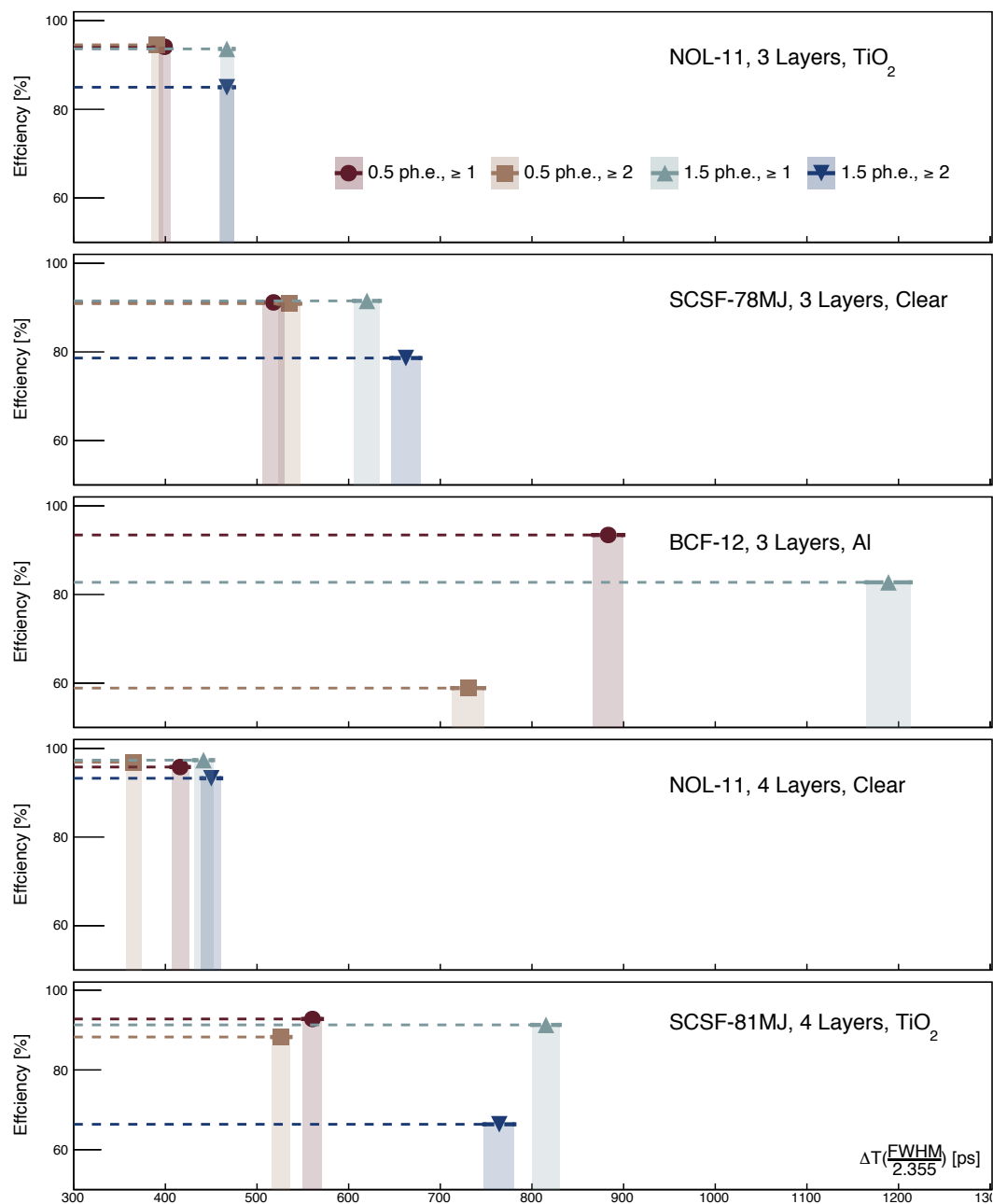
Figure 7.22 – Efficiency and time resolution for select ribbons as a function of the cluster threshold and minimal multiplicity. The time threshold is the same as the cluster one.

8

Mechanical Integration

A design for the mechanical integration of the scintillating fiber detecter into the full Mu3e experiment is proposed in this chapter. The CAD drawings[1] are based on input following the SciFi ribbons production and characterization studies. the integration steps in the proposed design are described after a brief discussion on the space and environment requirements,

8.1 Detector Requirements

The requirements for the fiber detector are determined by space constrains imposed from the surrounding detectors and environment conditions under which the detector should operate.

8.1.1 Space Constrains

As discussed in subsection 2.2.6, the scintillating fiber (SciFi) timing detector will be located immediately under the third pixel layer. The dimensions of the SciFi detector are determined by the geometrical acceptance of the Mu3e experiment. Fig. 8.1 illustrates the limitations stemming from the mechanical design of the inner and outer pixel layers. The sensitive region is defined by the direct line of sight from the outer most pixel sensor in the fourth pixel layer and the center of the target. The mechanical support for the inner pixel layer is also taken into account when defining the axis. Any non-active material in the SciFi detector should be located outside of the yellow shaded region in Fig. 8.1. The inner and outer radii of the geo-

---

[1]Produced by Franck Cadoux at the University of Geneva

metrical envelope holding the fiber detector are determined by the beam pipe underneath and the geometrical acceptance above. In the developed design the outer radius R_{out} is 67.9 mm, while the distance between opposing sides of the beam pipe is 67.8 mm. The total length of the detector, including electronics, is set at 339 mm, see Fig. 8.2.
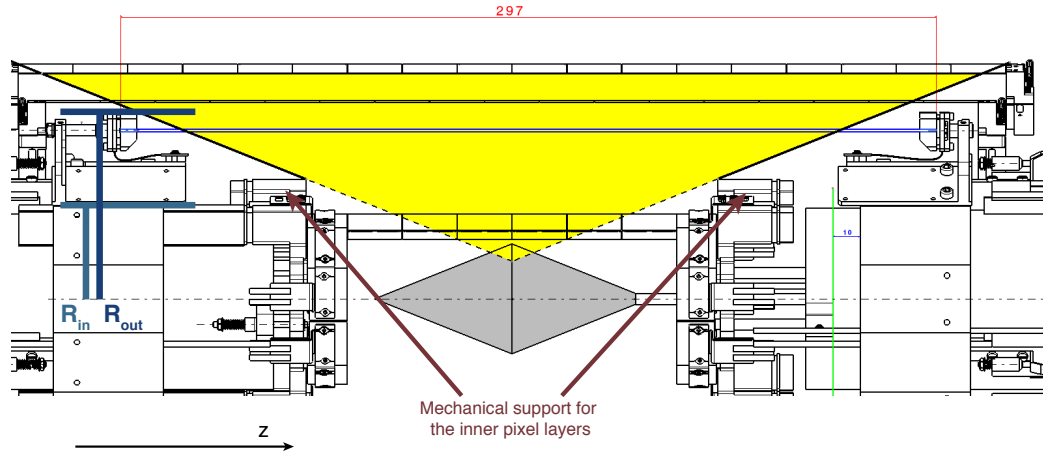
Figure 8.1 – Geometrical acceptance of the Mu3e central detector. A direct line of sight from the outer most pixel sensor in the fourth pixel layer and the center of the target determines the acceptance region. Any non-active components of the SciFi detector should be located outside of this region. The R_{in} and R_{out} radii illustrate the dimensions of the geometrical envelop holding the fiber detector.
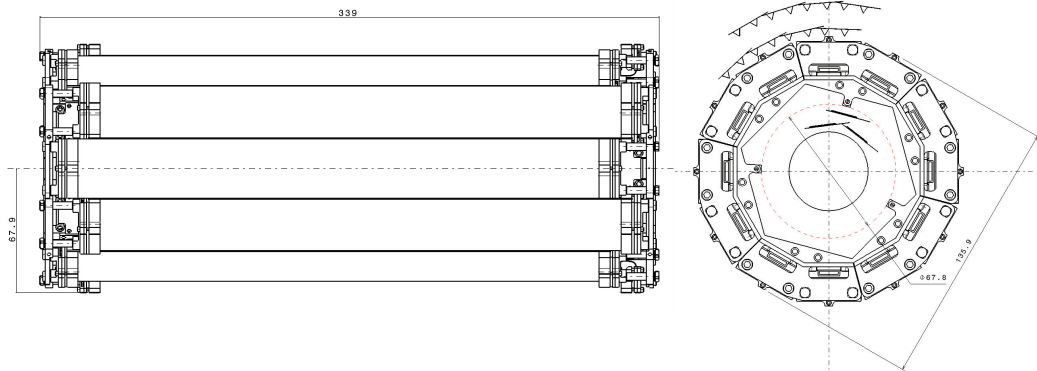
Figure 8.2 – Dimensions of the SciFi detector. The length of 339 mm is fixed by the outer pixel support and the tiles detector. The hexagonal beam pipe and the third pixel layer determine the inner (33.9 mm) and outer (67.9 mm) radii of the detector components. Module elements from each of the outer and inner pixel layers are shown in the cross-section view for reference.

8.1.2 ENVIRONMENT CONDITIONS

The experiment is operated in a helium atmosphere under pressure of approximately 1 bar. Gaseous flow of helium running at a speed of about 0.5 m/s between the fiber detector and the third pixel layer cools down the MuPix sensors. However, expected temperature gradients along the beam axis for the fiber detector can reach 40°C with a minimum value above 25 °C. While the thermal specifications are not yet finalized, the highest temperature at which the fiber detector should be operational is estimated at 40 °C. The upper limit of the ambient atmosphere for the SciFi detector when it is not collecting data is about 60°C in order to prevent damage to the scintillating fibers. At 40°C, the thermal expansion of a fiber ribbon's length is in the order of 2 mm where an expansion coefficient of 80×10^{-6}/K is considered [51]. The mechanical support should accommodate such variations and ensure the fiber ribbons do not sag.

High ambient temperatures are also critical for the operation of the SiPMs. The dark count rate doubles for approximately every 5°C rise in temperature [62]. This can significantly impair the detector's performance, hence a cooling system is being developed to keep the SiPMs below 10°C. An additional cooling system is required for the MuTRiG ASICs which dissipate in the order of 30 mW per channel summing up to $\mathcal{O}$(50 W) per side [43].

Finally, since the fiber ribbons are not coated with any light blocking material the volume in which the SciFi detector is operated should be light proof. Any light emitting sources used for detector alignment and checks should be switchable and turned off during operation.

8.2 MECHANICAL DESIGN

The Mu3e experiment is designed with a modular structure in mind such that inner sections of the detector subsystems are easily accessed without destroying outer components. A drawing of the scintillating fiber detector integrated in the Mu3e experiment is shown in Fig. 8.3. It consists of twelve cylindrically arranged ribbons with an active length of 297 ± 0.5 mm and a width of 32.5 ± 0.1 mm. The ribbons are mounted on six detachable modules each consisting of two ribbons staggered along the beam axis. To better illustrate the arrangement of all subsystems one module is removed from the central drawing in Fig. 8.3. The two ribbons in a module are longitudinally displaced with respect to one another by approximately 10 mm in order to accommodate the mounts for the optical sensors, see Fig. 8.4.

A support ring for the the SciFi detector is installed around the hexagonal beam pipe. Water cooling flanges for the MuTRiG chips are running inside the ring. The ribbon modules attach statically on top of the it via heat conducting L-shaped structures made of aluminum, see Fig.

145
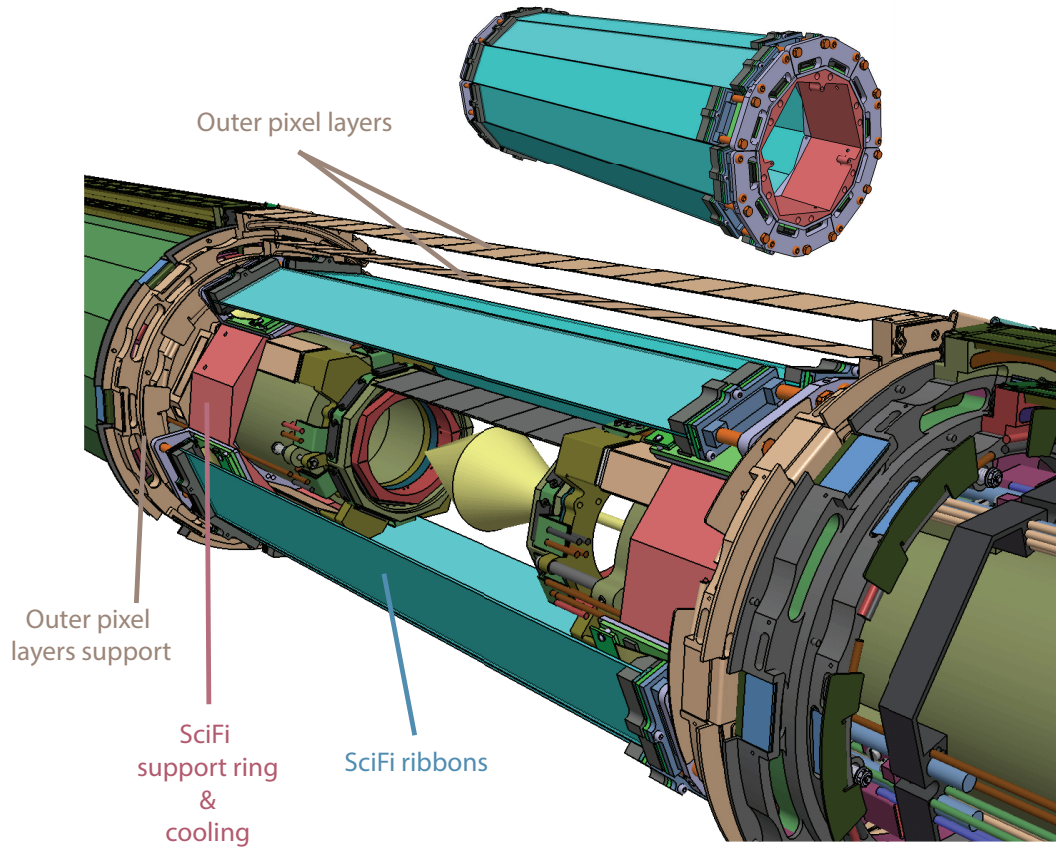
Figure 8.3 – A CAD rendering of the full scintillating fiber detector. Twelve ribbons are arranged in a cylindrical shape and coupled to SiPM sensor on both sides.

8.5 The modules are assembled outside of the detector volume before installing them over the cooling plates.

' Two SciFi front-end electronic (FEE) boards are first mounted on the L-shaped frames - one for each ribbon's end. One FEE board houses four MuTRiG chips supplying a total of 128 readout channels. The SiPMs, soldered in advance on PCBs with integrated flex prints, connect electrically to the MuTRiG carrying boards via high density Z-RAY[85] interposers. The final thickness of the interposer is not yet determined, however a single compression 4 mm thick option is considered in order to prevent the SiPM flex prints from touching the hot MuTRiG packages. Afterwords, the SiPM is sandwiched between a SciFi ribbon and a stiffener, see Fig. 8.6.

Three screws secure the optical coupling between the SiPM and the ribbon, while two spring loaded screws put the fiber mat under tension to avoid sagging due to thermal expansion. The metal plate behind the SiPM separates the optical connection from the spring loading system,
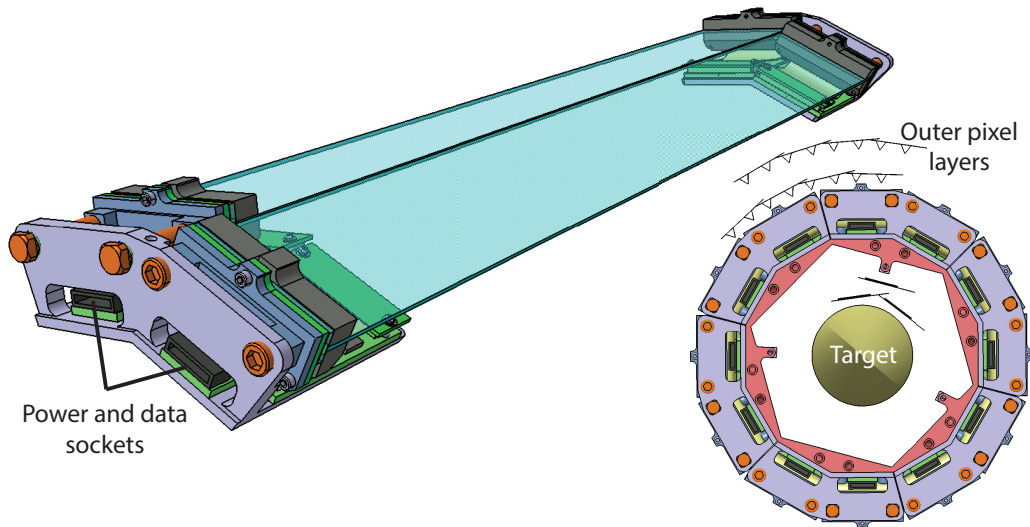
Figure 8.4 – A SciFi detector module holding two ribbons staggered longitudinally to accommodate the SiPMs mounts. Six such modules arrange on top of the SciFi support/cooling ring.
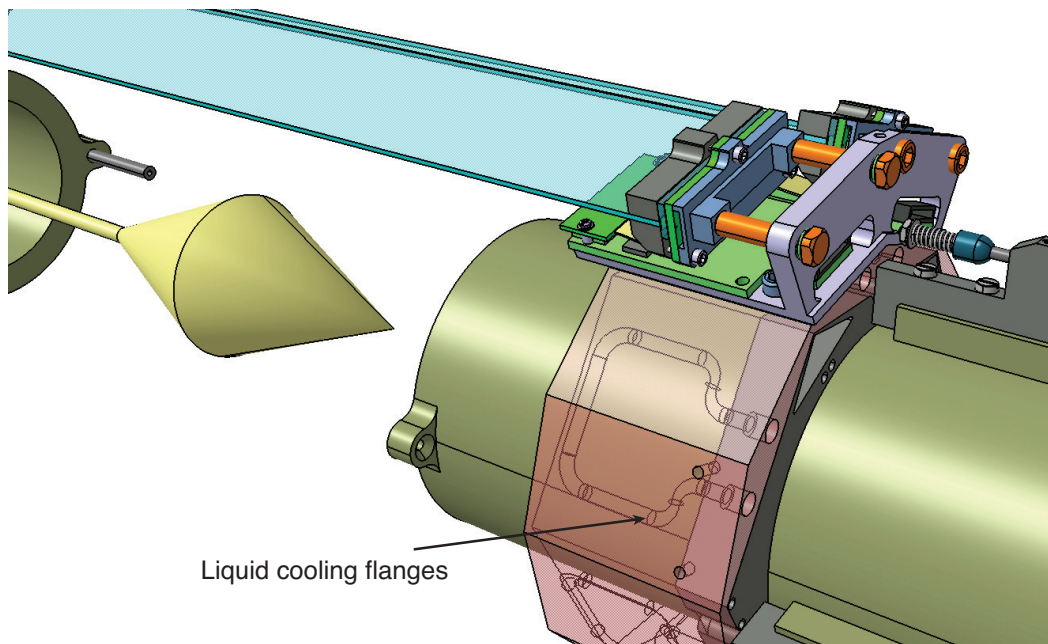
Figure 8.5 – The SciFi modules assembled in advance attach rigidly to the support ring. The cooling flanges running inside the ring are also shown.

on one hand. On the other, it cools the SiPM through the L-shaped support structure and the spring loaded screws. The spring loading is realized only on one end of a ribbon, the other side is rigidly fixed to the L-shape support. The two fixation types are interchanged on the up and
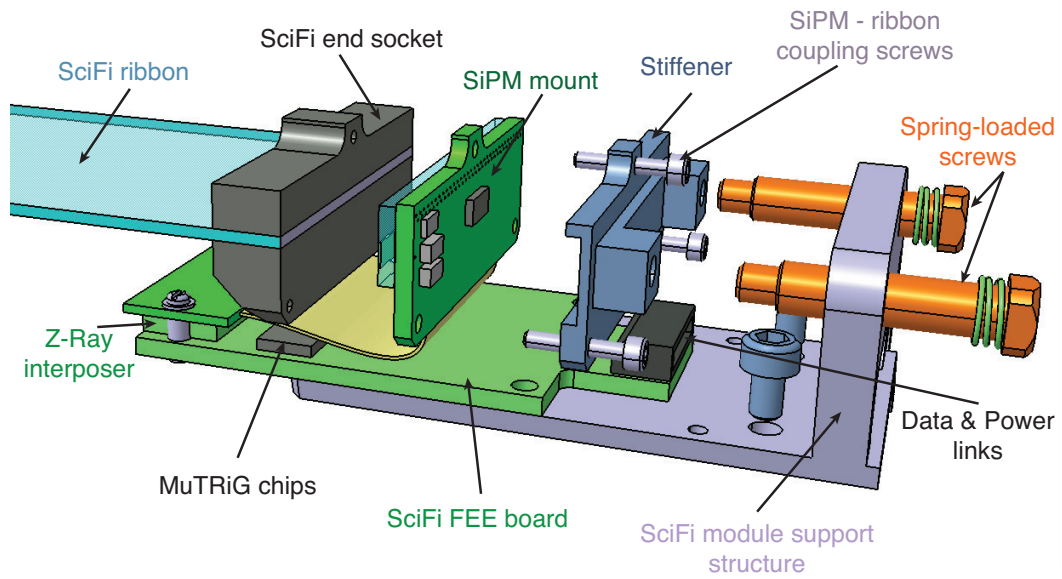
Figure 8.6 – An exploded view showing the end piece assembly of one ribbon in a fiber module. The coupling between the SiPM and the polished ribbon surface is static, while the large spring loaded screws prevent sagging of the fiber mat under thermal expansion. The SciFi ribbon is installed on one side of the L-shape module support.

downstream side of the module such that if one of the ribbons is spring-loaded at upstream end the other is spring-loaded at the downstream end. Holes on top of the support structure are foreseen for handling and transport tools that keep the distance between the two fiber ends fixed to avoid breakage.

9

Summary and Outlook

With a proposed sensitivity of 1 in 10^{15} muon decays for its first phase, Mu3e aims to improve the current experimental limit on the $\mu \rightarrow$ eee process by three orders of magnitude. Due to the very small branching ratio of $\mathcal{B} \approx 10^{-54}$ predicted by the extended Standard Model, any observation of this decay will be a clear sign for new Physics. In the more realistic scenario, where no $\mu \rightarrow$ eee events are found, many Beyond Standard Model theories will benefit from this measurement to constrain the allowed values for their parameters.

To reach such sensitivity in a reasonable timescale $\mathcal{O}(100 \text{ days})$, the Mu3e experiment requires about 2×10^8 muons/s to decay at rest inside the sensitive volume of its detectors. PSI is currently the only facility worldwide that can deliver a continuous muon beam with sufficient intensity to satisfy the needs of Mu3e. While some R&D activities to improve the transmission of the beam line are still ongoing, the latest tests performed in 2018 show promising stopping rates of 6.2×10^7 muons/s at the Mu3e target. An upgrade to a high intensity muon beam (HIMB) line is also investigated and scheduled in the coming years. It will provide muons for the second phase of the Mu3e experiment where the target is to reach a sensitivity of 1 in 10^{16} muon decays.

To detect such high muon rates novel instruments are developed and optimized for minimal material and maximal efficiency. The core of the Mu3e experiment is an electron spectrometer placed in a solenoidal magnetic field. It consists of a state-of-the-art pixel tracker based on the HV-MAPS. Time information about the electrons passing the detector is provided by two sub-detectors utilizing scintillating fibers and tiles. The current work investigates the production of the scintillating fiber detector and studies its performance in various configurations.

The pixel tracker requires minimal material along the electron trajectories in order to achieve the best possible momentum resolution. Moreover, the Mu3e fiber detector will be located between the pixel layers, thus its material budget should be minimized. On the other hand, the time resolution and the efficiency of the fiber detector benefit from having more material traversed by the electrons. Adding more layers in the fiber ribbons also increases the occupancy of the detector and leads to longer dead times. Hence, the goal of the current work is to investigate the possible solutions, evaluate their performance and reach a conclusion about the final detector design. To this end, high-granularity ribbons with different readout options and materials are produced using staggered 250 μm thick scintillating fibers. The ribbons are equipped with optical sensors on both ends.

Scintillating Fiber Ribbons

Concerns about the occupancy of the detector motivated the production of the first ribbon prototypes, where each fiber end is individually attached to an independent SiPM sensor. The higher granularity is also considered advantageous when matching tracks between the pixel tracker and the fiber detector. The first set of prototypes was made of SCSF-81MJ fibers by Kuraray. Details about the tools developed for the ribbon production and the challenges in constructing ribbons with single fiber readout are provided in section 3.3. The characterization studies discussed in chapter 6, as well as measurements by other members of the Mu3e fiber detector group[48, 50], showed that the time resolution $\mathcal{O}(1\,\text{ns})$ achieved with this configuration is on the verge of the Mu3e requirements. Therefore, ribbons with column readout are explored in the present work. Along with that, more fiber materials were tested - notably prototypes built with four layers of the novel NOL-11 fibers have demonstrated time difference resolution of $\frac{\text{FWHM}}{2.35} = 380\,\text{ps}$ which translates to 270 ps per ribbon side. This value exceeds the Mu3e requirements of 500 ps time resolution for the SciFi detector. Since the NOL-11 fiber are not yet commercially available, the next best material SCSF-78 will be used for the initial production of the Mu3e fiber detector. Ribbons with three layers of SCSF-78MJ fibers have shown a time difference resolution of $\frac{\text{FWHM}}{2.35} = 550\,\text{ps}$ and efficiency above 90 %. Thanks to the modular construction discussed in chapter 8, the fiber ribbons can be exchanged once sufficient length of the NOL-11 fibers is procured to construct the full detector with them.

SiPM Arrays

The scintillating fibers comprise only part of the detector. The rapid development of SiPM technology with decreased afterpulsing, cross-talk and dark count rates and improved photodetection efficiency contributed significantly to the successful operation of the fiber detec-

tors. The S13552-HRQ by Hᴀᴍᴀᴍᴀᴛsᴜ used for the latest column ribbon measurements will also be employed for the final Mᴜ3ᴇ fiber detector. The expected occupancy per SiPM column when triggered at 0.5 ph.e. for a ribbon with four fiber layers is in the order of 600 kHz. This number excludes dark count rates and cross-talk in the SiPM which can reach a few hundred kHz after irradiation and when operated at higher than room temperatures. The Mᴜ TRɪG chips will not be able to handle such rate. In this case, triggering at a higher threshold such as 1.5 ph.e. should be considered. The collected data shows that such an option is viable and the fiber detector can still yield acceptable results. If the energy threshold in the Mᴜ TRɪG ASIC can be controlled with a good enough precision, a scheme where the time is extracted at a lower threshold can be used, while a flag on the energy can be set at 1.5 ph.e. to reduce the occupancy.

Dᴀᴛᴀ Aᴄǫᴜɪꜱɪᴛɪᴏɴ Sʏꜱᴛᴇᴍꜱ

Custom data acquisition systems were developed to study the performance of various prototypes. Established electronics component such as discriminators, QDC and TDC modules housed in VME crates were useful for the initial testing. However, their capabilities are restricted by the hardware inside and they are subject to higher failures due to the many distinct modules involved in the acquisition chain.

A more sophisticated system allowing high-rate sampling and storing of the full input waveforms was developed to study in detail the performance of the fiber prototypes. The readout software for the DPNC342 boards featuring DRS4 sampling ASICs is a product of this work. The data acquisition has been successfully employed for the PSI beam test and the subsequent column readout measurements in laboratory conditions. Due to the generic nature of the DPNC342 board design, the system can be used in multiple situations with different detectors. An example is the NA61/SHINE experiment which benefited from the developed readout solution.

Tʜᴇ Mᴜ3ᴇ Fɪʙᴇʀ Dᴇᴛᴇᴄᴛᴏʀ Rᴏᴀᴅᴍᴀᴘ

The current work proves the feasibility of a scintillating fiber detector with as little as three layers for the needs of the Mᴜ3ᴇ experiment. The analysis algorithms with the sampled waveforms show results consistent with the preliminary measurement, obtained using the Mᴜ TRɪG ASIC [51]. However, the explored SiPM readout schemes are not the ones that will be used in the final detector, as the full chain of the detector and its integration in the Mᴜ3ᴇ DAQ is still ongoing. Reading out several fiber ribbons with the Mᴜ TRɪG on both sides is the goal of

several beam tests that are scheduled for the summer and autumn of 2019. This will further explore the readout chain and obtain better efficiency estimates with the full system.

The mechanical integration of the detector is close to completion and the Mu3e SciFi fiber ribbons are being produced following the procedure established in the current work.

A

Timing Algorithms

The primary function of a timing discriminator is to mark the arrival of detector signals consistently with high precision. Depending on the shape of the input signal different techniques can be used to extract the arrival time.

Fig. A.1 illustrates the algorithms used for time extraction in various stages of this work. The quality of the algorithm is judged based on the variation of time outputs when inputs with different amplitudes are expected. Noise contributions on top of the signal deteriorate the performance of all presented timing algorithms, hence they are not considered for the comparison.
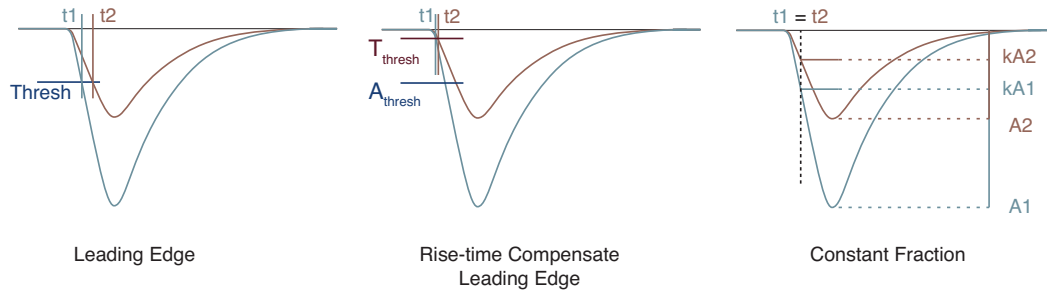
Figure A.1 – Algorithms for extraction of arrival time for detector pulses.

The simplest leading edge (LE) algorithm detects a signal at the time it crosses a predefined amplitude threshold. It suffers from the so called time-walk induced jitter. If information about the full amplitude of the signal is available together with the time measurement, the time value can be corrected to reduce the effect of this jitter. In the absence of amplitude information, the

time walk can only be reduced by setting the threshold at a smaller amplitude value closer to its baseline.

An improvement on the LE edge algorithms is the rise-time compensated leading edge discriminator, where two thresholds are employed to suppress low amplitude signals while maintaining a minimal time walk. The T_{thresh} is used to extract the arrival time, while the A_{thresh} sets the minimum amplitude of signals for which an output pulse is generated. The main advantage of this algorithm is that it works well for signals with varying rise times and amplitudes.

Finally, the constant fraction (CF) algorithm exploits the fact that signals with identical rise-times take the same time to reach a specific fraction of their full amplitude. This algorithm is widely used for outputs from photomultiplier tubes which by design have almost constant rise time for different amplitudes.

Fig. A.2 illustrates the realization of a CF in an electronics board. The input signal is divided in two. One part represents a copy of the input scaled down by the desired fraction. The other part is identical to the input, albeit with inverted polarity. The inverted input is delayed in time such that when it is summed with the scaled input the zero crossing of the new signal matches results in a time measurement as if a leading edge threshold was set at the specific fraction of the amplitude.
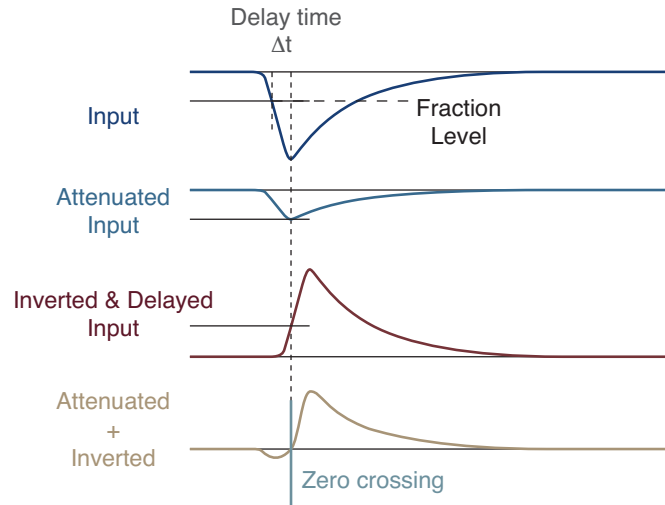
Figure A.2 – Signal processing steps in fast electronics boards for constant fraction time thresholds.

Bibliography

[1] Steven Weinberg, Abdus Salam and Sheldon Lee Glashow. The Nobel Prize in Physics 1979 is awarded "for their contributions to the theory of the unified weak and electromagnetic interaction between elementary particles, including, inter alia, the prediction of the weak neutral current. NobelPrize1979.

[2] David J. Gross, H. David Politzer and Frank Wilczek. The Nobel Prize in Physics 2004 is awarded "for the discovery of asymptotic freedom in the theory of the strong interaction.". NobelPrize2004.

[3] François Englert and Peter W. Higgs. The Nobel Prize in Physics 2013 is awarded "for the theoretical discovery of a mechanism that contributes to our understanding of the origin of mass of subatomic particles, and which recently was confirmed through the discovery of the predicted fundamental particle, by the ATLAS and CMS experiments at CERN's Large Hadron Collider.". NobelPrize2013.

[4] G. Aad *et al.*, "Observation of a New Particle in The Search for the Standard Model Higgs Boson with the ATLAS Detector at the LHC," *Physics Letters B*, vol. 716, no. 1, pp. 1 – 29, 2012. `doi:10.1016/j.physletb.2012.08.020.`

[5] S. Chatrchyan and others., "Observation of a New Boson at a Mass of 125 GeV with the CMS Experiment at the LHC," *Physics Letters B*, vol. 716, no. 1, pp. 30 – 61, 2012. `doi:10.1016/j.physletb.2012.08.021.`

[6] A.-K. Perrevoort, " Sensitivity Studies to New Physics in the Mu3e Experiment and Development of Firmware for the Front-End of the Mu3e Pixel Detector ," Ph.D. dissertation, Ruperto-Carola-University of Heidelberg, 2018. `doi:10.11588/heidok.00024585.`

[7] Y. Fukuda *et al.* [Super-Kamiokande], "Evidence for Oscillation of Atmospheric Neutrinos," *Phys. Rev. Lett.*, vol. 81, pp. 1562–1567, 1998. `doi:10.1103/PhysRevLett.81.1562.`

[8] Q. R. Ahmad *et al.* [SNO], "Measurement of theRate of $\nu_e + d \rightarrow p + p + e^-$ InteractionsProduced by ^8B Solar Neutrinos at the Sudbury Neutrino Observatory," *Phys. Rev. Lett.*, vol. 87, 071301, 2001. `doi:10.1103/PhysRevLett.87.071301.`

[9] K. Abe *et al.* [T2K Collaboration], "Indication of Electron Neutrino Appearance from an Accelerator-produced Off-axis Muon Neutrino Beam," *Phys. Rev. Lett.*, vol. 107, 041801, 2011. `doi:10.1103/PhysRevLett.107.041801`.

[10] F. An *et al.* [Daya Bay Collaboration]. (2012) Improved Measurement of Electron Antineutrino Disappearance at Daya Bay. arXiv:1210.6327v2.

[11] B. Pontecorvo, "Electron and Muon Neutrinos," *Sov. Phys. JETP*, vol. 10, pp. 1236–1240, 1960, [Zh. Eksp. Teor. Fiz.37,1751(1959)].

[12] A. Ceccucci and others. (2018, January) CKM Quark-Mixing Matrix. http://pdg.lbl.gov/2019/reviews/rpp2018-rev-ckm-matrix.pdf.

[13] K. Nakamura and S. Petcov. (2017, November) Neutrino Masses, Mixing, and Oscillations. http://pdg.lbl.gov/2017/reviews/rpp2017-rev-neutrino-mixing.pdf.

[14] F. Capozzi *et al.*, "Global Constraints on Absolute Neutrino Masses and Their Ordering," *arXiv*, 2017. `doi:10.1103/PhysRevD.95.096014`.

[15] M. Tanabashi and others. [Particle Data Group], "Review of Particle Physics," *Phys. Rev. D*, vol. 98, 030001, Aug 2018. `doi:10.1103/PhysRevD.98.030001`.

[16] P. A. R. Ade *et al.* [Planck Collaboration], "Planck 2015 Results. XIII. Cosmological Parameters," *Astron. Astrophys.*, vol. 594, A13, 2016. `doi:10.1051/0004-6361/201525830`.

[17] A. de Gouvea and P. Vogel, "Lepton Flavor and Number Conservation, and Physics Beyond the Standard Model," *Prog.Part.Nucl.Phys.*, vol. 71, pp. 75–92, 2013. `doi:10.1016/j.ppnp.2013.03.006`.

[18] P. J. Mohr and others., "CODATA Recommended Values of the Fundamental Physical Constants: 2014," *Rev. Mod. Phys.*, vol. 88, no. 3, 035009, 2016. `doi:10.1103/RevModPhys.88.035009`.

[19] J. C. Bernauer *et al.* [A1 Collaboration], "High-Precision Determination of the Electric and Magnetic Form Factors of the Proton," *Phys. Rev. Lett.*, vol. 105, 242001, Dec 2010. `doi:10.1103/PhysRevLett.105.242001`.

[20] S. L. Glashow, D. Guadagnoli, and K. Lane, "Lepton Flavor Violation in B Decays?" *Phys. Rev. Lett.*, vol. 114, 091801, 2015. `doi:10.1103/PhysRevLett.114.091801`.

[21] F. Borzumati and A. Masiero, "Large Muon- and Electron-Number Nonconservation in Supergravity Theories," *Phys. Rev. Lett.*, vol. 57, pp. 961–964, Aug 1986. doi:10.1103/PhysRevLett.57.961.

[22] H. Dreiner and others., "New Bounds on Trilinear R-parity Violation from Lepton Flavor Violating Observables," *Phys.Rev.*, vol. D86, 015003, 2012. doi:10.1103/PhysRevD.86.015003.

[23] Y. Kuno and Y. Okada, "Muon Decay and Physics beyond the Standard Model," *Rev. Mod. Phys.*, vol. 73, pp. 151–202, 2001. doi:10.1103/RevModPhys.73.151.

[24] A. Crivellin *et al.*, "Renormalisation-group Improved Analysis of $\mu \rightarrow e$ Processes in a Systematic Effective-Field-Theory Approach," *JHEP*, vol. 05, 117, 2017. doi:10.1007/JHEP05(2017)117.

[25] W. J. Marciano and others., "Charged Lepton Flavor Violation Experiments," *Ann.Rev.Nucl.Part.Sci.*, vol. 58, pp. 315–341, 2008. doi:10.1146/annurev.nucl.58.110707.171126.

[26] V. Khachatryan and others., "Search for Lepton Flavour Violating Decays of the Higgs boson to $e\tau$ and $e\mu$ in Proton–Proton Collisions at $\sqrt{s} = 8$ TeV," *Physics Letters B*, vol. 763, pp. 472 – 500, 2016. doi:10.1016/j.physletb.2016.09.062.

[27] G. Aad and others., "Search for Lepton-Flavour-Violating Decays of the Higgs and Z Bosons with the ATLAS Detector," *The European Physical Journal C*, vol. 77, no. 2, 70, Feb 2017. doi:10.1140/epjc/s10052-017-4624-0.

[28] A. M. Baldini *et al.* [MEG], "Measurement of the Radiative Decay of Polarized Muons in the MEG Experiment," *Eur. Phys. J.*, vol. C76, no. 3, 108, 2016. doi:10.1140/epjc/s10052-016-3947-6.

[29] U. Bellgardt *et al.* [SINDRUM Collaboration], "Search for the Decay $\mu^+ \rightarrow e^+e^+e^-$," *Nucl.Phys.*, vol. B299, 1, 1988. doi:10.1016/0550-3213(88)90462-2.

[30] W. H. Bertl *et al.* [SINDRUM II Collaboration], "A Search for Muon to Electron Conversion in Muonic Gold," *Eur.Phys.J.*, vol. C47, pp. 337–346, 2006. doi:10.1140/epjc/s2006-02582-x.

[31] R. Akhmetshin *et al.* [COMET Collaboration]. (2012) Experimental Proposal for Phase-I of the COMET Experiment at J-PARC. https://j-parc.jp/researcher/Hadron/en/pac_1207/pdf/E21_2012-10.pdf.

[32] M. Aoki and others. [DeeMe Collaboration], "An Experimental Search for Muon-Electron Conversion in Nuclear Field at Sensitivity of 10^{-14} with a Pulsed Proton Beam," *AIP Conf.Proc.*, vol. 1441, pp. 599–601, 2012. `doi:10.1063/1.3700628.`

[33] R. Abrams *et al.* [Mu2e Collaboration]. (2012) Mu2e Conceptual Design Report. arXiv:1211.7019.

[34] A. Baldini *et al.*, "MEG Upgrade Proposal," *e-Print*, Jan. 2013, arXiv:1301.7225.

[35] A. Blondel *et al.* [Mu3e Collaboration], "Research Proposal for an Experiment to Search for the Decay $\mu \rightarrow eee$," *e-Print*, Jan. 2013, arXiv:1301.6113v1.

[36] R. Abramishvili1 *et al.* [COMET Collaboration], "COMET Phase I Technical Design Report," KEK, Tech. Rep., 2016, Online: http://comet.kek.jp/Documents_files/PAC-TDR-2016/COMET-TDR-2016_v2.pdf.

[37] L. Bartoszek *et al.* [Mu2e Collaboration], "Mu2e Technical Design Report," *e-Print*, 2014, arXiv:1501.0524.

[38] Mu3e Collaboration, "Technical Design of the Phase I Mu3e Experiment," in preparation, internal Document.

[39] R. Akhmetshin *et al.* [PSI]. (2014) The Proton Accelerator at the Paul Scherrer Institute: Forty Years of Top-Flight Research. https://www.psi.ch/en/media/our-research/the-proton-accelerator-forty-years-of-top-flight-research.

[40] F. A. Berg, "CMBL - A High-Intensity Muon Beam Line & Scintillation Target with Monitoring System for Next-Generation Charged Lepton Flavour Violation Experiments," Ph.D. dissertation, ETH Zurich, 2017. `doi:10.3929/ethz-b-000213470.`

[41] I. Perić, "A Novel Monolithic Pixelated Particle Detector Implemented in High-Voltage CMOS Technology," *Nucl.Instrum.Meth.*, vol. A582, 876, 2007. `doi:10.1016/j.nima.2007.07.115.`

[42] L. Huth, "A High Rate Testbeam Data Acquisition System and Characterization of High Voltage Monolithic Active Pixel Sensors," Ph.D. dissertation, Ruperto-Carola-University of Heidelberg, 2018. `doi:10.11588/heidok.00025785.`

[43] H. Chen, "A Silicon Photomultiplier Readout ASIC for the Mu3e Experiment," Ph.D. dissertation, Universität Heidelberg, 2018. `doi:10.11588/heidok.00024727.`

[44] D. vom Bruch, "Pixel Sensor Evaluation and Online Event Selection for the Mu3e Experiment," Ph.D. dissertation, Ruperto-Carola-University of Heidelberg, 2017. doi:10.11588/heidok.00023689.

[45] S. Ritt, P. Amaudruz, and K. Olchanski. (2001) Maximum Integration Data Acquisition System. http://midas.psi.ch.

[46] A. Herkert, "Gaseous Helium Cooling of a Thin Silicon Pixel Detector for the Mu3e Experiment," Master Thesis, Heidelberg University, 2015.

[47] M. Zimmermann, "Cooling with Gaseous Helium for the Mu3e Experiment," Bachelor Thesis, Heidelberg University, 2012.

[48] R. Gredig, "Scintillating Fiber Detector for the Mu3e Experiment," Ph.D. dissertation, University of Zurich, Faculty of Science, 2016. doi:10.5167/uzh-127074.

[49] E. Ripiccini, "An Active Target for the MEG Experiment," Ph.D. dissertation, Rome U., 2015, Online: http://inspirehep.net/record/1494142/files/Ripiccini.pdf.

[50] G. Rutar, "In Search of Charged Lepton Flavor Violating Decays at PSI," Ph.D. dissertation, ETH Zurich, 2017. doi:10.3929/ethz-b-000174750.

[51] S. Corrodi, "A Timing Detector based on Scintillating Fibres for the Mu3e Experiment," Ph.D. dissertation, ETH Zurich, 2018. doi:10.3929/ethz-b-000299260.

[52] L. Collaboration, "LHCb Tracker Upgrade Technical Design Report," http://cds.cern.ch/record/1647400, CERN, Tech. Rep. CERN-LHCC-2014-001. LHCB-TDR-015, Feb 2014.

[53] J. Birks, *The Theory and Practice of Scintillation Counting*, ser. International series of monographs on electronics and instrumentation. Pergamon Press, 1964. doi:10.1016/C2013-0-01791-4.

[54] O. Borshchev and others., "Development of a New Class of Scintillating Fibres with Very Short Decay Time and High Light Yield," *Journal of Instrumentation*, vol. 12, no. 05, P05013, 2017. doi:10.1088/1748-0221/12/05/P05013.

[55] S. A. Ponomarenko and others., "Nanostructured Organosilicon Luminophores and Their Application in Highly Efficient Plastic Scintillators," *Scientific Reports*, vol. 4, 6549, 2014. doi:10.1038/srep06549.

[56] https://www.kuraray.com/products/psf, Kuraray, Plastic scintillating fibers (PSF).

[57] https://www.crystals.saint-gobain.com/products/scintillating-fiber, Saint-Gobains, Scintillating Fiber.

[58] C. Joram and others., "LHCb Scintillating Fibre Tracker Engineering Design Review Report: Fibres, Mats and Modules," https://cds.cern.ch/record/2004811, CERN, Geneva, Tech. Rep. LHCb-PUB-2015-008. CERN-LHCb-PUB-2015-008, Mar 2015.

[59] R. Asfandiyarov and others., "The Design and Construction of the MICE Electron-Muon Ranger," *Journal of Instrumentation*, vol. 11, no. 10, pp. T10 007–T10 007, oct 2016. doi:10.1088/1748-0221/11/10/t10007.

[60] L. Plan. TOUCHLAM polishing cloths. TOUCHLAM Polishing Cloths.

[61] W. Diamant. Wirz Diamant: Nos marques et produits. http://www.wirzdiamant.ch/Products/products_fr.php.

[62] A. Ghassemi and others., "A technical guide to silicon photomultipliers (mppc)," https://hub.hamamatsu.com/jp/en/technical-note/sipm-mppc-technical-note/index.html, 2018, accessed: 2019-04-09.

[63] D. Renker and E. Lorenz, "Advances in Solid State Photon Detectors," *Journal of Instrumentation*, vol. 4, no. 04, P04004, 2009. doi:10.1088/1748-0221/4/04/p04004.

[64] P. Eckert, "The Mu3e Tile Detector," PhD thesis, Heidelberg University, 2015. doi:10.11588/heidok.00018763.

[65] S. M. Sze and K. K. Ng, *Physics of Semiconductor Devices*, 3rd ed. John Wiley & Sons Inc., 10 2006.

[66] V. M. Robbins and others., "Electron and Hole Impact Ionization Coefficients in (100) and in (111) Si," *Journal of Applied Physics*, vol. 58, 4614, 1985. doi:10.1063/1.336229.

[67] K. Deiters and others. [CMS Collaboration], "Response of avalanche photo-diodes of the CMS Electromagnetic Calorimeter to neutrons from an Americium-Beryllium source," https://cds.cern.ch/record/1316926, CERN, Geneva, Tech. Rep. CMS-NOTE-2010-016, Oct 2010.

[68] R. Mirzoyan, R. Kosyra, and H.-G. Moser, "Light emission in Si avalanches," *Nuclear Instruments and Methods in Physics Research Section A: Accelerators, Spectrometers, Detectors and Associated Equipment*, vol. 610, no. 1, pp. 98 – 100, 2009. doi:10.1016/j.nima.2009.05.081.

[69] K. Axel and others. [LHCb Collaboration], "Characterization of the Hamamatsu MPPC Multichannel Array for the LHCb SciFi Tracker v.11.2016," EPFL, Tech. Rep., 2017, Online: http://lphe.epfl.ch/publications/2017/LPHE-2017-001.pdf.

[70] F. Corsi and others., "Modelling a Silicon Photomultiplier (SiPM) as a Signal Source for Optimum Front-End Design," *Nuclear Instruments and Methods in Physics Research Section A: Accelerators, Spectrometers, Detectors and Associated Equipment*, vol. 572, no. 1, pp. 416 – 418, 2007, frontier Detectors for Frontier Physics. doi:10.1016/j.nima.2006.10.219.

[71] S. Ritt, "Design and Performance of the 6 GHz Waveform Digitizing Chip DRS4," in *2008 IEEE Nuclear Science Symposium Conference Record*, Oct 2008, pp. 1512–1515. doi:10.1109/NSSMIC.2008.4774700.

[72] NA61/SHINE Collaboration, "Status Report to the Proposal SPSC-P-330: Report from the NA61/SHINE Experiment at the CERN SPS," European Laboratory for Particle Physics, Tech. Rep., 2016, Online: https://cds.cern.ch/record/2222876/files/SPSC-SR-197.pdf.

[73] S.Ritt, "DRS4 Datasheet rev 0.9: 9 Channel, 5 GSPS Switched Capacitor Array," https://www.psi.ch/sites/default/files/import/drs/DocumentationEN/DRS4_rev09.pdf, PSI, Villigen, Tech. Rep., 2008.

[74] Intel. Cyclone V Device Overview. https://www.intel.com/content/dam/www/programmable/us/en/pdfs/literature/hb/cyclone-v/cv_51001.pdf.

[75] Universal Serial Bus 3.0 Specification. https://www.usb3.com/whitepapers/USB%203%200%20(11132008)-final.pdf.

[76] A Cross-Platform User Library to Access USB Devices. http://libusb.sourceforge.net/api-1.0/.

[77] D. Stricker-Shaver, S. Ritt, and B. J. Pichler, "Novel Calibration Method for Switched Capacitor Arrays Enables Time Measurements With Sub-Picosecond Resolution," *IEEE Transactions on Nuclear Science*, vol. 61, no. 6, pp. 3607–3617, Dec 2014. doi:10.1109/TNS.2014.2366071.

[78] K. Axel and others. [LHCb Collaboration], "Characterization of the Hamamatsu MPPC multichannel array for the LHCb SciFi Tracker v.9.2014," EPFL, Tech. Rep., 2015, Online: http://lphe.epfl.ch/publications/2015/LPHE-2015-001.pdf.

[79] (2017) The H2 Secondary Beam Line of EHN1/SPS. http://sba.web.cern.ch/sba/BeamsAndAreas/h2/H2manual.html.

[80] Interactive Chart of Nuclides. https://www.nndc.bnl.gov/nudat2/.

[81] M. Berger, J. Coursey, M. Zucker, , and J. Chang, "(2005), ESTAR, PSTAR, and ASTAR: Computer Programs for Calculating Stopping-Power and Range Tables for Electrons, Protons, and Helium Ions (version 2.0.1)," [online] National Institute of Standards and Technology, Gaithersburg, MD, 2005, available: http://physics.nist.gov/Star Star [2018, February 8].

[82] L. Landau, "56 - ON THE ENERGY LOSS OF FAST PARTICLES BY IONISATION," in *Collected Papers of L.D. Landau*, D. T. Haar, Ed.   Pergamon, 1965, pp. 417 – 424. doi:https://doi.org/10.1016/B978-0-08-010586-4.50061-4.

[83] M. Paterno. Calculating Efficiencies and Their Uncertainties. https://home.fnal.gov/~paterno/images/effic.pdf.

[84] L. Gerritzen, "Internal MU3E collaboration meetings."

[85] S. Corporation, "Ultra-low profile micro arrays," Catalogue.

List of Figures

165

List of Tables

Acknowledgments